



HAL
open science

Resonant dynamics of Super-Earth systems

Gabriele Pichierri

► **To cite this version:**

Gabriele Pichierri. Resonant dynamics of Super-Earth systems. Astrophysics [astro-ph]. COMUE Université Côte d'Azur (2015 - 2019), 2019. English. NNT : 2019AZUR4054 . tel-02438364

HAL Id: tel-02438364

<https://theses.hal.science/tel-02438364>

Submitted on 14 Jan 2020

HAL is a multi-disciplinary open access archive for the deposit and dissemination of scientific research documents, whether they are published or not. The documents may come from teaching and research institutions in France or abroad, or from public or private research centers.

L'archive ouverte pluridisciplinaire **HAL**, est destinée au dépôt et à la diffusion de documents scientifiques de niveau recherche, publiés ou non, émanant des établissements d'enseignement et de recherche français ou étrangers, des laboratoires publics ou privés.

THÈSE DE DOCTORAT

Dynamique résonante des systèmes de Super-Terres

Gabriele PICHIERRI

Laboratoire J.-L. Lagrange (UMR 7293), Observatoire de la Côte d'Azur

Présentée en vue de l'obtention du grade de docteur en Sciences de la Planète et de l'Univers de l'Université Côte d'Azur

Dirigée par : Alessandro Morbidelli

Co-encadrée par : Aurélien Crida

Soutenue le : 23 Septembre 2019

Devant le jury composé de :

Konstantin Batygin, Professeur, Caltech

Émeline Bolmont, Professeur assistant, Université de Genève

Aurélien Crida, Maître de Conférences, avec HDR, OCA

Daniel Fabrycky, Professeur Associé, Université de Chicago

Jacques Laskar, Directeur de recherche, IMCCE Observatoire de Paris

Anne Lemaître, Professeur, Université de Namur

Alessandro Morbidelli, Directeur de Recherche, OCA

Richard Nelson, Professeur, Queen Mary College

Dynamique résonante des systèmes de Super-Terres

Resonant dynamics of Super-Earth systems

Jury :

Rapporteurs

Daniel Fabrycky, Professeur Associé, Université de Chicago
Anne Lemaître, Professeur, Université de Namur

Examineurs

Konstantin Batygin, Professor, Caltech
Émeline Bolmont, Professeur assistant, Université de Genève
Jacques Laskar, Directeur de recherche, IMCCE Observatoire de Paris
Richard Nelson, Professeur, Queen Mary College

Directeur de thèse

Alessandro Morbidelli, Directeur de Recherche, Observatoire de la Côte d'Azur

Co-directeur de thèse

Aurélien Crida, Maître de Conférences, avec HDR, Observatoire de la Côte d'Azur

Résumé et mots clés

Abstract and keywords

Titre : Dynamique résonante des systèmes de Super-Terres

Résumé : Les observations de centaines de systèmes d'exoplanètes nous ont fourni un large échantillon de configurations orbitales. Les périodes orbitales figurent parmi les données les mieux connues et les plus étonnantes. Les Super-Terres, ces planètes caractérisées par une masse entre 1 et 20 masses terrestres et une période typiquement de moins de 100 jours, sont présentes autour de la plupart des étoiles. La distribution des rapports de leurs périodes orbitales défie les astrophysiciens : pendant leur formation et migration au sein de leur disque protoplanétaire, elles devraient former des chaînes de résonances de moyen mouvement, c'est-à-dire que les rapports des périodes orbitales de planètes voisines devrait être proches de fractions simples. Toutefois, la plupart des systèmes de Super-Terres ne sont pas résonants. Dans cette thèse, je traite les aspects clés des chaînes résonantes : leur formation, leur évolution et leur stabilité. Premièrement, j'introduis les idées modernes en théorie de formation planétaire, et les méthodes utilisées dans la thèse : la mécanique Hamiltonienne, le problème planétaire et la théorie perturbative. Deuxièmement, je présente le processus de capture en résonance de moyen mouvement du premier ordre $k : k - 1$ par migration convergente des planètes, avec une nouvelle description analytique de l'évolution planétaire qui en suit, et je décris la dynamique résonante dans le plan orbital commun. La description analytique est confirmée par des intégrations N -corps qui incluent les interactions disque-planète. Ensuite, je me base sur des résultats existants concernant l'évolution dissipative de deux planètes en résonance qui engendre la divergence de leurs demi-grands axes. Par une approche similaire, je présente une méthode statistique qui permet de déterminer dans quelle mesure l'architecture observée d'un système de trois planètes est compatible avec une histoire dynamique résonante dissipative. Je considère par la suite la stabilité des chaînes résonantes. Des études antérieures ont montré que l'absence de systèmes exoplanétaires résonants n'est pas en contradiction avec le modèle de capture en résonance par migration dans le disque, si une phase d'instabilité est très commune après la disparition du disque. On observe un taux d'instabilité plus élevé dans les systèmes synthétiques plus compacts et peuplés par des planètes plus massives. Des simulations N -corps dédiées à l'étude de la stabilité des chaînes résonantes ont montré qu'il y a une masse planétaire maximale qui garantit la stabilité; cette masse limite diminue si les planètes sont plus massives et/ou si la chaîne résonante est plus compacte. J'étudie la stabilité des chaînes résonantes de planètes en fonction de leur masse commune, et j'examine de façon analytique et numérique des cas spécifiques de systèmes comprenant deux ou trois planètes. Je découvre un mécanisme dynamique qui peut déclencher une excitation du système, et qui mène à une phase de rencontres proches et collisions. Ce mécanisme se généralise à différents nombres de planètes et/ou à des chaînes résonantes plus ou moins compactes, et donne une prédiction analytique de la masse critique qui est en accord qualitatif avec les expériences numériques mentionnées précédemment. Enfin, je décris un scénario dynamique qui peut expliquer la pollution des naines blanches en éléments lourds. Les systèmes planétaires compacts peuvent devenir instables pendant la phase de perte de masse qui marque la fin de l'évolution stellaire, et les impacts entre planètes génèrent des débris. En m'appuyant sur des résultats précédents, je montre que l'excentricité orbitale des débris qui résident en résonance de moyen mouvement avec une planète externe peut devenir suffisamment élevée pour que les débris soient engloutis par l'étoile, ce qui peut expliquer la pollution observée.

Mots clés : Exoplanètes – Mécanique céleste – résonance de moyen mouvement – stabilité – évolution dynamique – formation planétaire

Title: Resonant dynamics of Super-Earth systems

Abstract: Observations of hundreds of exoplanetary systems have produced a huge sample of orbital configurations, and the orbital periods are one of their better constrained and most astonishing properties. A common type of exoplanets are the Super-Earths, which have a mass between 1 and 20 Earth masses and a typical period of less than 100 days. The period ratio distribution of these planets poses a challenge to astrophysicists: during their formation, still embedded in the protoplanetary disc, we expect them to form chains of mean motion resonances, where the period ratio of neighbouring planets is close to a low-integer ratio. However, most Super-Earth systems are not close to resonance. In this thesis, I discuss key dynamical aspects of resonant chains: their formation, their evolution and their stability. I first give an overview of our current understanding of planetary formation, and an introduction of the methods used in the thesis: the tools of Hamiltonian dynamics, the planetary problem and perturbation theory. Then, I present the process of capture of planets migrating in protoplanetary discs into first order $k : k - 1$ mean motion resonances, including a novel analytical description of the corresponding planetary evolution, and I describe the relevant aspects of resonant dynamics in the planar approximation. The analytical treatment is supported by numerical N -body simulations which include the planet-disc interactions. Next, I expand on previous results on two-planet dissipative evolution in mean motion resonance and the resulting divergence of the planets' semi-major axes. With a similar approach, I present a statistical method which allows to determine to what extent the observed architecture of a three-planet system is compatible with a dissipative resonant dynamical history. I then address the main problem of the stability of resonant chains. Previous works have shown that the over-all lack of resonances in the exoplanet sample is not in contradiction with resonant capture, if a post-disc phase of planetary instabilities is extremely common. Higher rates of instabilities are observed in synthetic systems where planets are most massive and the configurations most compact. Specific N -body experiments on the stability of resonant chains found that there is a critical planetary mass allowed for stability, which decreases with increasing number of planets and/or increasing value of k in the chain. The origin of these instabilities was however not discussed. I study the stability of resonant chains of equal-mass planets in terms of their mass, investigating analytically and numerically specific cases of two- and three-planet systems. I find a dynamical mechanism which can trigger an excitation of the system, leading to mutual close-encounters and collisions. This can be generalised to an arbitrary number of planets and/or value of k in the resonant chain, and gives an analytical prediction for the critical mass allowed for stability which agrees qualitatively with the aforementioned numerical experiments. Finally, I describe a dynamical scenario that can explain the pollution of White Dwarfs with heavy elements. The idea is that compact planetary systems become unstable during the mass-loss phase characterising the end of the stellar evolution, so that impacts among planets lead to the generation of collisional debris. Expanding on previous works, I show that debris residing in mean motion resonance with an outer planetary perturber can have their orbital eccentricity excited to large-enough values to be engulfed by the host star, causing the observed pollution.

Keywords: Exoplanets – Celestial Mechanics – mean motion resonance – stability – dynamical evolution – planet formation

I am immensely grateful to Alessandro Morbidelli (Morby) who advised my work with great academical and personal attention. Thank you for the inspiring three years that lead to the writing of this manuscript, whose quality would be diminished if it were not for your frequent suggestions and accurate insights. It has been a privilege to learn the beautiful ways of Celestial Mechanics under your supervision.

I am also grateful to Aurélien Crida, co-advisor and friend, who has assisted me in my first steps in the planetary science world, and continued to do so, with unique positivity and enthusiasm.

It has been a pleasure working with Morby and Aurélien, who have helped me from the very beginning and up until the very end, and I surely hope that our collaboration will not stop here.

I am grateful to Konstantin Batygin, who hosted me for four amazing months in Caltech, and showed me first that science can be a lot of fun, and second that everything else can also be a lot of fun. He is a true rockstar of planetary science and I hope to collaborate with him again (on scientific papers, but also next to an amplifier).

I thank Clément Robert and Tobias Hertel for proofreading parts of the manuscript, thus improving its readability.

I thank the personnel of the administration, in particular Rose Pinto, who has always been extremely efficient and has made many practical aspects of my life at the Observatory much easier. I also thank Khaled, who feeds us up here in Mont Gros: your meals and your attitude are among the best things at the Observatory.

I also wish to thank Antonio Giorgilli, my former Master advisor, without whom I would not have started this journey.

~

I thank my girlfriend Annelore, who brought love, affection and friendship, and supported me (sometimes both in the French and in the English meaning of the word) during the last two years. These are the best gifts the universe can provide.

I finally thank all my fellow colleagues, my friends, my family, and all the people who helped me along the way.



This work is licensed under the Creative Commons Attribution 4.0 International License. To view a copy of this license, visit <http://creativecommons.org/licenses/by/4.0/> or send a letter to Creative Commons, PO Box 1866, Mountain View, CA 94042, USA.

Contents

1	Introduction	1
1.1	A brief history of Planetary Science	1
1.1.1	The discovery of exoplanetary systems	2
1.1.2	The exoplanets sample	2
1.1.3	The Solar System in perspective and implications of the exoplanets sample	3
1.2	Planetary formation	4
1.2.1	Protoplanetary discs	4
1.2.2	Building the planets: Overview of accretion processes	6
1.2.3	Shaping the planets' orbits during the disc phase: Planetary type-I migration and eccentricity damping	8
1.3	This thesis in context	11
2	Hamiltonian mechanics and the planetary problem	15
2.1	Hamiltonian systems	15
2.1.1	Link with Lagrangian formalism	16
2.1.2	Dynamical variables	17
2.1.3	Canonical transformations	19
2.1.4	Integrable dynamics and action-angle variables	20
2.1.5	Equilibrium points and linear stability	22
2.1.6	Basic examples of Hamiltonian systems	24
2.2	Planetary systems in Hamiltonian mechanics	29
2.2.1	The two-body problem	29
2.2.2	The planetary problem	34
2.3	Elements of Hamiltonian perturbation theory	38
2.3.1	First order perturbation theory	38
2.3.2	An introduction to adiabatic theory	40
2.3.3	Application of the adiabatic theory to resonant capture	42
3	Two planets – The structure of resonant pairs and capture into mean motion resonance	45
3.1	Structure of first-order mean motion resonances	45
3.1.1	First and higher order expansions of the Hamiltonian in the eccentricities	47
3.1.2	Equilibrium points of the averaged Hamiltonian	47
3.1.3	Frequencies in the limit of small amplitude of libration	49
3.2	Capture into resonance by type-I migration	52
3.2.1	Convergent inward migration in disc and resonant capture	53
3.2.2	Planet-disc interactions and evolution in mean motion resonance	56
4	Three-planet systems and the near-resonant population	63
4.1	The near-resonant population	63
4.1.1	Methods and physical setup	64
4.2	Analytical model for three resonant planets	66
4.2.1	Resonant equilibrium points	68
4.2.2	Resonant repulsion for three-planets systems	69
4.3	A scenario for dissipative evolution of three-planet systems	70
4.3.1	Choice of systems	70

4.3.2	Analytical maps	71
4.3.3	Numerical simulations	73
4.4	Results	77
4.4.1	Probabilistic measure of a resonant configuration in Kepler-305, YZ Cet and Kepler-31	77
4.4.2	The 5:4 – 4:3 resonant chain on Kepler-60 and other near-resonant systems with $k > 3$	78
4.5	Conclusions	78
5	The onset of instability in resonant chains	81
5.1	Introduction	81
5.2	2 Planets	82
5.3	3 Planets	88
5.3.1	Numerical stability maps for $N = 3$ and $k = 3$	88
5.3.2	Numerical and analytical investigation of the phenomenon	89
5.3.3	Rescaled Hamiltonian and new set of canonical variables	90
5.3.4	Purely resonant dynamics	93
5.3.5	The synodic contribution	95
5.3.6	Dependence on k	106
5.4	N Planets	108
6	Extreme secular excitation of eccentricity inside mean motion resonance	111
6.1	Small bodies driven into star-grazing orbits by planetary perturbations	112
6.2	Planetary Hamiltonian	113
6.3	Studying the averaged Hamiltonian	115
6.4	Effect of short-range forces	118
6.5	Results	119
6.6	Conclusions	124
7	Conclusions	127
7.1	Future perspectives	129
A	Integrable approximation for two-planet mean motion resonant dynamics	141
B	Reduced Hamiltonian to a common planetary mass factor for three resonant planets	145
C	Some useful Mathematica code snippets for perturbation theory	147
D	Mathematica code used in Chapter 6	149
E	List of symbols and notations	157

Chapter 1

Introduction

1.1 A brief history of Planetary Science

The study of dynamics was triggered by the need to understand the movement of the planets in our Solar System, our astronomical home. There have been a few major milestones in our understanding of their motion. The first was heliocentric theory, put forth as early as the 3rd century BC by Aristarchus of Samos but gaining scientific and historical significance in the 16th century with Nicolaus Copernicus, who showed that orbits centred at the Sun provide a much simpler description of the motion of the planets. The second innovation was the introduction of Kepler's laws of planetary motion by Johannes Kepler between 1609 and 1619. They are three empirical laws that describe the motion of the planets around the Sun on elliptical orbits, an approximation valid at least on short timescales. The third innovation was given by Newtonian theory, derived by Isaac Newton and first published in 1687 in his *Philosophiæ Naturalis Principia Mathematica*. Newton's laws of motion, his law of universal gravitation and the techniques of differential and integral calculus allowed him to derive Kepler's laws, even introducing some corrections and developments, like the fact that parabolic and hyperbolic motion are also allowed. Newton also realised that the planets' mutual interactions may be responsible for significantly modifying their orbits over time. Theoretical applications of Newtonian theory have been very successful and enlightening, such as the Lagrange-Laplace theory on the secular evolution of the planets' orbits in the 1770's. Moreover, they drove the development of perturbation theory, and yielded theoretical results such as Poincaré's proof around 1900 of the non-integrability of the three-body problem and the coexistence of order and chaos even in seemingly ordered systems, which completely changed our understanding of dynamical systems. One last improvement in the understanding of gravitational interactions was Einstein's 1916 theory of general relativity, which gives a geometrical description of the origin of the gravitational force (a question which Newton admitted he could not address) and an explanation for a few quirks of the dynamics of the planets, most notably the precession of Mercury. Nonetheless, classical Newtonian dynamics is very accurate and adequate to describe the motion of the planets and small bodies of the Solar System. It should suffice to say that Newtonian theory was not only able to prove Kepler's empirical laws in describing why the planets move as they do, but it even allowed to predict with astonishing accuracy the position of unseen planets, as in the case for Neptune, discovered by Le Verrier "with the point of his pen" (as F. Arago put it) and observed by J. G. Galle and H. L. d'Arrest in Berlin in 1846 following Le Verrier's calculations.

It is worth recalling our classification of the orbiting bodies of the Solar System, with the definitions given in 2006 by the International Astronomical Union. A *planet* is a celestial body that orbits around the Sun, has a large enough mass that it has an approximately spherical shape due to its own gravity, and dominates the local dynamics around its orbit. There are 8 planets known in our Solar System, some of which having natural satellites (moons) around them: they are Mercury, Venus, Earth, Mars, Jupiter, Saturn, Uranus and Neptune in order of their distance to the Sun, usually measured in terms of the semi-major axis of their Keplerian ellipse. Additionally, there are the dwarf planets (like Pluto, Eris, Ceres, Makemake, Haumea, some of which having moons of their own) and a vast number of additional small Solar System bodies, such as the comets, the asteroids, the trojans and the trans-Neptunian objects. In a way, the task of Celestial Mechanicians is to verify that Newtonian theory can explain all the aspects of the dynamics of these orbiting bodies that we observe and to understand the dynamical features of the Solar System. And indeed, this task is still not complete, as many details of the dynamics exhibited by our Solar System need to be investigated and explained, such as the orbital distribution of the distant Kuiper belt objects, which has been proposed as evidence for an additional, yet unseen ninth planet orbiting our Sun. However, in the last 20 years the attention of many astronomers has turned far, far away from our Solar System.

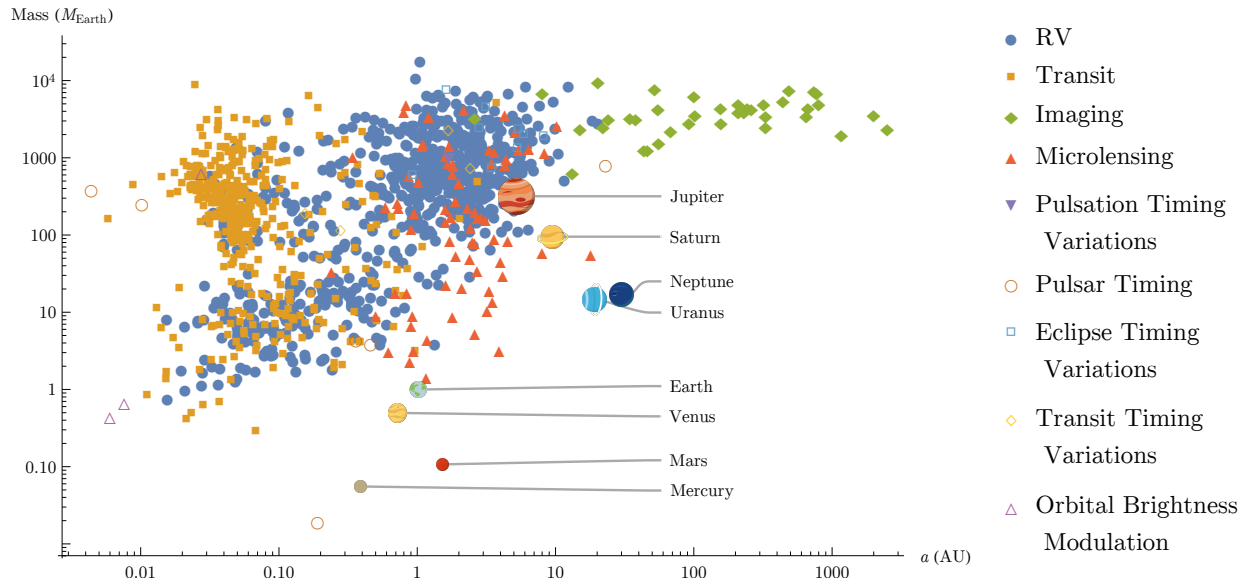


Figure 1.1: Semi-major axes a and masses of detected exoplanets (the coloured markers). The semi-major axis is measured in Astronomical Units (AU), with 1 AU being the semi-major axis of Earth’s orbit. The colours and markers indicate the different detection methods (see legend on the right), most planets having been detected by the Radial Velocity (RV) or Transit method (see main text). The Solar System planets are also shown for comparison. Data was obtained from the Nasa Exoplanet Archive <https://exoplanetarchive.ipac.caltech.edu/>.

1.1.1 The discovery of exoplanetary systems

Until very recently, the Solar System was the only known planetary system, and as far as we could tell even the only existent one. This unlikely possibility was ruled out by observations in 1995, with the detection of a doppler-shift signal in the movement of the star 51 Pegasi (a method called Radial Velocity, see below), the first evidence of an exoplanet orbiting a main sequence G-type star and thus modifying its motion in a detectable way¹ [Mayor and Queloz(1995)]. The planet 51 Peg b has a mass at least half that of Jupiter and an orbital period of only about 4.2 days. As such, it is the prototype of the now called *hot Jupiters* which, as the name suggests, are Jupiter-like planets which orbit very close to their host star. The possibility that a planet similar to Jupiter could have such a narrow orbit came as a shock to astronomers, who thought that other planetary systems, if they existed, would be more or less like ours. Soon enough, it was realised that the Solar System is not the typical planetary system. For example, observations now indicate that more than 50% of stars have planets that do not have analogues in the Solar System [Morbidelli(2018)], while only $\sim 1\%$ of observed systems have a gas giant planet relatively far away and on a low eccentricity orbit like Jupiter [Winn and Fabrycky(2015)].

These statements have been made possible by more than two decades of observations of exoplanetary systems. The number of planets discovered every year has been growing exponentially, with a doubling time of about 2 years. As of 21 June 2019 there are 4003 confirmed exoplanets, with 1704 planets found in 678 multi-planetary systems. This represents a massive sample, telling us that planets can be much more diverse than we could ever imagine, and opening completely new physical and dynamical questions, all the while giving us many more clues in the process of planetary formation and evolution. There are of course many interesting aspects that emerge from the study of the current exoplanet population, but in the interest of brevity we review below those which are most significant in the context of this thesis.

1.1.2 The exoplanets sample

Figures 1.1 and 1.2 show the detected exoplanets up until 21 June 2019, in terms of planetary mass versus semi-major axis of their orbit or orbital period. Each marker is a detected planet, and the Solar System planets are included for comparison. From these figures, especially Figure 1.2, one can make out the different classes of exoplanets. The so called *hot Jupiters* (such as the already mentioned 51 Peg b) are massive planets, with masses

¹The discovery was made on 6 October 1995 by M. Mayor and D. Queloz using observations gathered at the Observatoire de Haute-Provence. Even earlier, on 9 January 1992 an exoplanet was detected orbiting the pulsar PSR 1524-29 [Wolszczan and Frail(1992)].

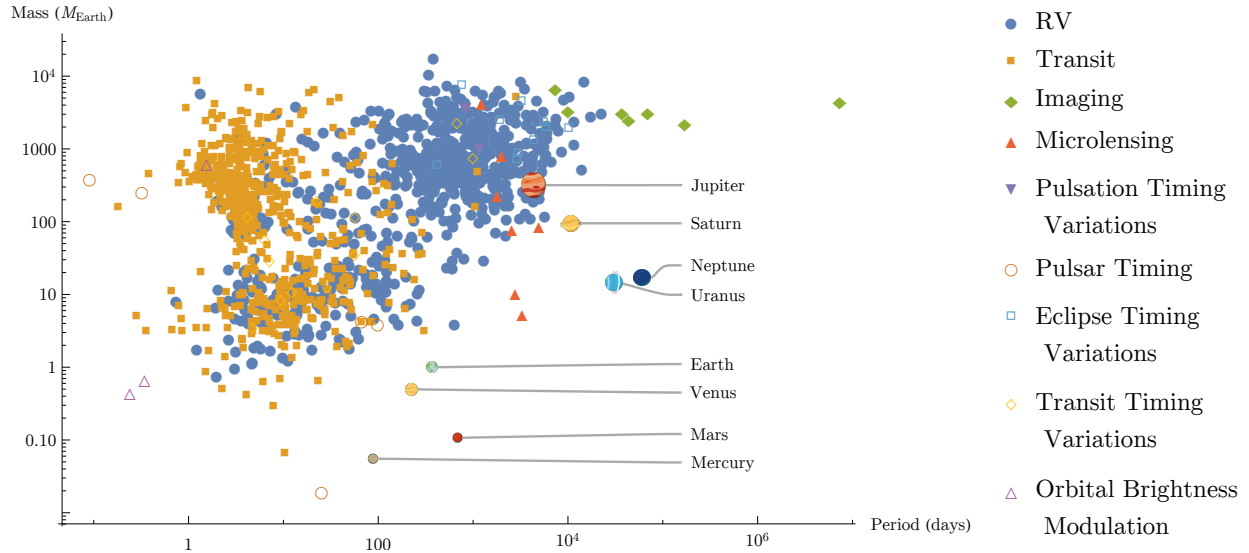


Figure 1.2: Same as Figure 1.1, but with the orbital period measured in (Earth’s) days on the horizontal axis.

ranging from $10^2 M_{\oplus}$ to a few $10^4 M_{\oplus}$ ($1 M_{\oplus} = 1$ Earth mass), with a very short orbital period between 1 and 100 days, which are thought to be physically similar to our gas giants Jupiter and Saturn, and occupy the top left corner in both plots. Although they were the first planets to be detected (as they are the easiest ones, being so massive and with a short orbital period), more recent data suggests that only less than a few percent of stars host a hot Jupiter [Howard et al.(2012), Wright et al.(2012), Winn and Fabrycky(2015)]. The top right corner is populated by the *cold* or *normal Jupiters*, and we see that our Jupiter actually falls within the boundaries of this group. The planets in the bottom left corners have masses between about 1 to a few tens of Earth’s masses and a period of less than about 100 days, and are called *Super-Earths* or *Mini-Neptunes*, depending on their composition (see Section 1.3). These planets are thought to orbit up to 50% of Sun-like stars ([Mayor et al.(2011)]; [Howard et al.(2012)]; [Fressin et al.(2013)]; [Petigura et al.(2013)]), therefore posing an enormous constraint on planet formation and evolution models, and their dynamics will be the main subjects of this thesis. The rest of the parameter space (where all of the Solar System’s planets except Jupiter are located) is left empty, but mostly because of our limitations in detecting these planets.

The different colours/markers in Figures 1.1 and 1.2 represent the detection methods used to discover the planets. So far, the two main detection methods are the Radial Velocity (RV) and the Transit photometry methods. The RV method (also called Doppler spectroscopy) exploits the fact that the gravitational pull of a massive enough body orbiting a star will force said star to orbit around the system’s centre of mass, and cause a detectable periodic Doppler shift of the star’s spectrum. With the transit method, one essentially observes eclipsing planets which cause a small, regular decrease in the brightness of the star. The two surveys from NASA’s Kepler and K2 missions have been extremely successful in finding thousands of planets in only a few years, and missions such as TESS and PLATO will expand on this legacy. Other detection methods include direct imaging, microlensing, and astrometry (thanks to the Gaia mission), and are expected to yield in the future a large amount of new data which will allow us to fill the current observational gaps still present in Figures 1.1 and 1.2, and to better describe the nature of exoplanetary systems.

1.1.3 The Solar System in perspective and implications of the exoplanets sample

Observing thousands of planetary systems has many consequences. On the one hand it puts our own into context, and on the other it actually allows us to better understand the processes that shaped the Solar System. For example, we did not expect that planets like hot Jupiters could exist, and since the possibility that they formed where they are now may seem unlikely, processes like orbital transport within the protoplanetary disc become now conceivable (e.g. [Lin et al.(1996), Kley and Nelson(2012), Beaugé and Nesvorný(2012)]; however, see also e.g. [Batygin et al.(2016), Bailey and Batygin(2018)]). As we shall see, this so-called *planetary migration* is indeed thought to play a major role in shaping the orbits of planets such as Super-Earths and Mini-Neptunes. This and many other realisations come from the study of the physical processes acting on distant planetary systems, and

leak into the understanding of the formation and evolution of our own.

It is important to realise that different exoplanet detection methods allow to obtain different physical and orbital parameters, and are more or less sensitive to different regions of parameter space, which is why the two plots in Figures 1.1 and 1.2 show some differences. For example, RV detections usually yield the planetary mass m_{pl} only via $m_{\text{pl}} \sin I$ (where I is the angle between the normal to the orbital plane and the line-of-sight of the observer²), the orbital period, the eccentricity and the direction of the periastron (the point along the orbit that is closest to the star) of the planet’s orbit from the signal’s amplitude, periodicity, shape and phase respectively. Instead, transit detections allow to get the orbital period from the periodicity of the signal and the radius of the planet from the shape of the signal. More precisely, these two methods give the planetary mass and radius with respect to that of the star. Moreover, if an additional unseen planet is disturbing the transiting one, small Transit Time Variations (TTV) in the signal of the observed planet can allow the indirect discovery of the undetected one. In some cases one can observe the same system with multiple methods. Or, if one is not interested in specific systems but on the general distribution of the physical and orbital parameters of exoplanets, statistical methods can be used (e.g. assuming a uniform distribution of $\cos I$ to extract the distribution of planetary masses from RV detections, or breaking the mass-eccentricity degeneracy in the TTV signals [Wu and Lithwick(2013)]). In any case, making a complete exoplanet demographics study is very hard and one needs to be extremely careful before drawing absolute conclusions. Moreover, planetary systems like our own are not yet detectable, since all planets but Jupiter are either too small or have too large orbital periods to be observed.

However, it remains clear from Figures 1.1 and 1.2 that any model of planetary formation must be able to explain the formation of planets very different from those of our Solar System. Then, the observed architecture of planetary systems challenges the Celestial Mechanician to explain how these orbital configurations can emerge. I therefore recall in the next section the main points in our current understanding of planetary formation and early evolution, while I give in Section 1.3 the motivation for the dynamical investigations that are described in this thesis.

1.2 Planetary formation

Planetary formation is a byproduct of star formation. Molecular clouds that are massive enough collapse gravitationally to form protostars in so-called star forming regions. While a protostar is forming, by conservation of angular momentum some material does not fall into the protostar but forms a relatively flat, rotationally supported disc around it. In the mostly credited core-accretion scenario [Pollack et al.(1996)], planets are then thought to form from the material contained in such a disc: the rocky planets or the cores of the gas giants are accreted from the rocky components while giant planets’ atmospheres represent gaseous material that has been accreted by sufficiently massive cores formed within the lifetime of the disc. For this reason, the discs observed routinely around young stars are called *protoplanetary discs*. Very recently, in [Keppler et al.(2018)], the first evidence of a forming planet with a mass around 2 – 20 Jupiter masses observed still embedded in and interacting with its ~ 5 Mys old disc was announced (see also [Müller et al.(2018)]).

The growth from the micron-sized dust particles detected in these young discs to fully formed planets is usually divided into steps corresponding to different physical processes: from dust to small pebbles, to planetesimals, to planetary embryos, to planetary cores, to planets in all their shapes and forms. We give a quick review of these accretion processes in Subsect. 1.2.2. However, before we delve into the question of the formation of the actual planets, it is important to realise that the protoplanetary discs set the stage for planet formation, which is why it is crucial to understand the physical properties and mechanisms that control their structure and evolution. This is still a topic of vast research, and a full discussion is beyond the scope of this text. We shall recall below the most important concepts that are needed in the context of this thesis.

1.2.1 Protoplanetary discs

The idea of a flat disc of material orbiting our Sun from which the planets formed dates back to the eighteenth century with thinkers such as Kant and Laplace. Nowadays, discs of gas and dust are detected regularly around young stars, either because of the infrared excess in the observed spectral energy distribution coming from the forming star, or by direct imaging with instruments such as ALMA, SPHERE and GPI. Measuring the disc frequency against stellar age yields a lifetime of protoplanetary discs of around 3 – 10 My [Hernández et al.(2007)].

²This is because we only measure the movement of the star that happens along our line-of-sight, so we cannot tell apart a small planet whose apparent motion takes place along the line-of-sight ($I \simeq 90^\circ$), or a massive planet whose orbit appears to be almost face-on ($I \simeq 0^\circ$).

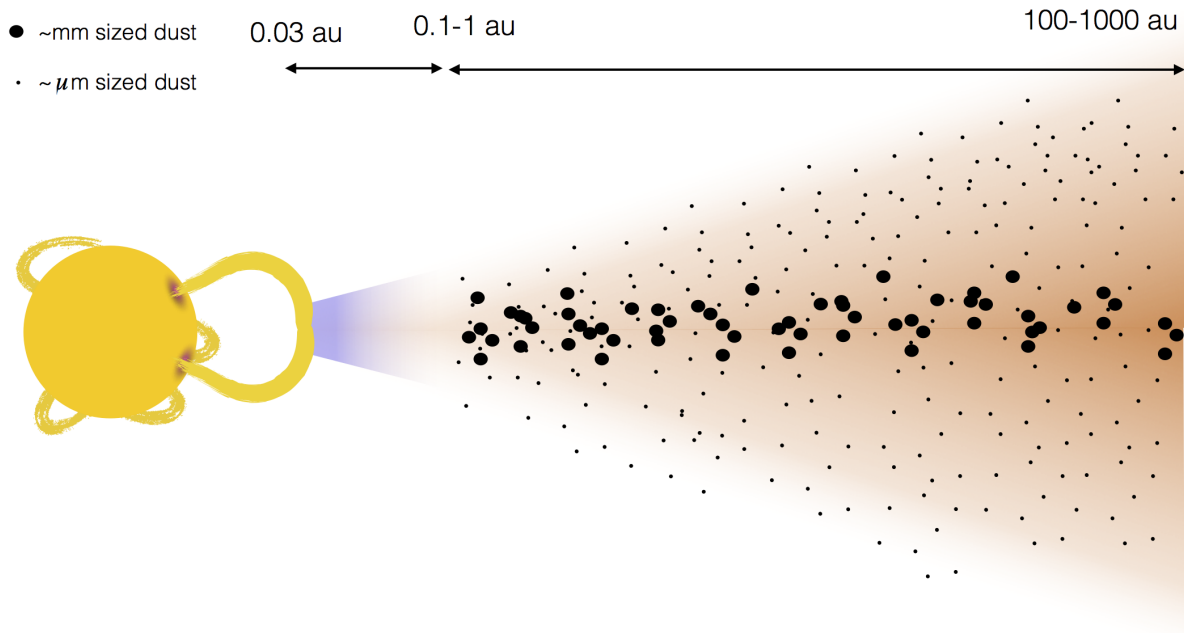


Figure 1.3: Diagram of a protoplanetary disc (adapted with permission from [Lesur(2018)]).

The typical structure of protoplanetary discs is shown in Figure 1.3. Their bulk composition is mostly *gas* (mainly H/He), with only $\sim 1\%$ of their mass being made of *dust* (micron-sized grains). The gas feels a pressure in addition to the star's gravity, and so gas molecules rotate around the star with an orbital velocity that can be slightly different from the Keplerian velocity $v_K = \sqrt{\mathcal{G}M_*/r}$ (where \mathcal{G} is the gravitational constant, M_* is the mass of the central star and r is the radial distance from the star), and this influences the motion of small solid particles dynamics by aerodynamic coupling, as we shall see. Moreover, locally there can be enhancements in the solid-gas ratio which allow for different accretion processes to take place. Ultimately, the 1% dust is what makes the telluric planets and the gas giants' cores, so the study of how the dust particles can clump together and interact with the surrounding gas is of great interest. In the description of the equilibrium structure of protoplanetary discs, two simplifications are helpful [Armitage(2010)]. The first is the assumption that the disc's mass is negligible compared to that of the star, so self-gravity can be neglected (however this may not always be the case, especially early in the formation of the protostar). The second is that the vertical thickness of the disc $H(r)$ is small (of the order of a few percent, see below) compared to the orbital radius r (this is true in conditions of relatively low temperatures, as we see below).

Concerning the radial structure of the disc, probably the most important parameter is the vertically averaged *surface density* $\Sigma = \int \rho dz$, where ρ is the density and z is the direction normal to the disc. In truth, one cannot always avoid the presence of azimuthal structures such as vortices (which might play a role in planetesimal formation, see next subsection), spiral waves (important in the treatment of planet-disc interactions and migration, see Subject. 1.2.3), eccentric cavities due to binary companions to the main star, etc. However, to first approximation in an undisturbed, (nearly) radially symmetric disc rotating in equilibrium around a single star, one considers $\Sigma = \Sigma(r)$ as function of r alone. In the most simple case one imagines a power law profile $\Sigma(r) = \Sigma_0(r/r_0)^{-\alpha_\Sigma}$, for some constant $\alpha_\Sigma > 0$ and some reference orbital separation r_0 . In the case of the Solar System, one approach to obtain such a density profile has been to divide up the space around the Sun in rings centred at the location of the planets, and use the amount of material now present in these rings rescaled to solar abundances to give a lower bound to the original surface density. This yields the so-called Minimum-Mass Solar Nebula (MMSN) prescription $\Sigma(r) \simeq 1.7 \times 10^3 \text{ g cm}^{-2} (r/1 \text{ AU})^{-3/2}$ (e.g. [Hayashi(1981)]); integrating over a reasonable extension of the disc one would get a total disc mass of $\simeq 0.01M_\odot$, consistent with the assumption that the gravity of the Sun is dominant. However, we now know there's no reason that the initial material should not move radially during the disc's lifetime

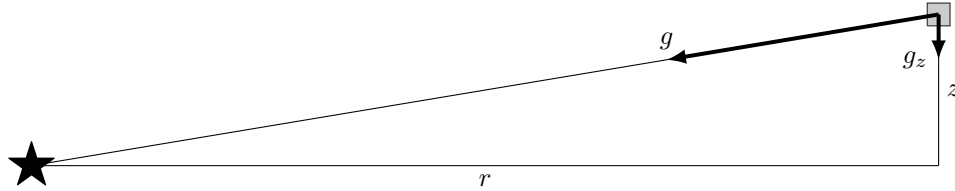


Figure 1.4: Vertical structure of a thin protoplanetary disc. A parcel of gas (in grey) at a radial distance r and a height z feels a vertical gravitational force $g_z \sim (\mathcal{G}M_*/r^3)z$ for $z \ll r$. This is balanced by the pressure gradient under vertical hydrostatic equilibrium.

so different power law profiles cannot be excluded. Note moreover that a power law is always an approximation for $\Sigma(r)$, and we now have observational evidence that rings and gaps do form routinely in protoplanetary discs thanks to ALMA (e.g. [Dullemond et al.(2018)]).

Concerning the vertical structure of the disc, consider a gas parcel at radial distance r and height z from the disc mid-plane (Figure 1.4). The vertical component of the gravitational force is $g_z = ((\mathcal{G}M_*)/(r^2 + z^2))(z/\sqrt{r^2 + z^2}) \sim (\mathcal{G}M_*/r^3)z$ for $z \ll r$. Assuming that the gas is in vertical hydrostatic equilibrium so that the gravitational force due to the star is balanced by pressure, we get $(\mathcal{G}M_*/r^3)z = -(1/\rho)dP/dz$ where ρ is the density and P the pressure. Assuming a perfect gas law $P\mu = R\rho T$ as an equation of state for the pressure, μ being the mean molecular mass, R the ideal gas constant and T the temperature, we solve the force-balance equation and get a *vertical density profile* $\rho(z) = \rho_0 \exp(-z^2/(2H^2))$ with $H(r) = (R/(\mu T r^3))^{1/2}$, called the *vertical scale-height* of the disc, which depends on the disc's physical parameters. Notice that now one can write $\rho_0 = 1/\sqrt{2\pi}(\Sigma/H)$. If the disc is vertically isothermal the equation for the pressure can be written as $P = \rho c_s^2$, where c_s is the sound speed, so the scale-height becomes $H = c_s/\Omega_K$, where $\Omega_K = \sqrt{\mathcal{G}M_*/r^3}$ is the Keplerian orbital frequency at the radial distance r . One also defines $h = H/r = c_s/v_K$ called the *aspect ratio* of the disc. This parameter gives the vertical geometrical thickness of the disc, and depends on the temperature $T(r)$. The temperature profile is usually sculpted by viscous heating at small distances from the central star and by stellar irradiation at larger distances. Assuming a power law for T one gets $h(r) = H/r = z_{\text{scale}}(r/r_0)^{\beta_f}$. The exponent β_f is usually positive for T distributions shallower than $1/r$, as those resulting from viscous and irradiation heating; it is called *flaring index*. Calculations of the equilibrium temperature of the disc lead to values of $h(r)$ of the order of a few to several percents, in agreement with observations of discs, and validating the approximation $h \ll 1$.

Other physical parameters of the disc (such as the viscosity, turbulence, ionisation fraction, opacity), and the effect of magnetic phenomena are also important. This is the subject of a vast research, and I refer to [Turner et al.(2014), Armitage(2015), Lesur(2018)] for an extensive treatment of these processes. With the basic understanding of disc structures outlined above, we can now turn to the problem of planetary formation in protoplanetary discs.

1.2.2 Building the planets: Overview of accretion processes

To go from microscopic dust to planets we need to grow ~ 13 orders of magnitude in size, or ~ 40 orders of magnitude in mass. The details of the accretion processes at play are usually split up in stages according to the different scales at which they occur. In general, these processes have to be efficient and fast [Morbidelli(2018)], and models of planetary formation must explain the presence of planets in all their shapes and forms (terrestrial, gas giants, ice giants, Super-Earths, Mini-Neptunes, ...): this is clearly a difficult problem. For this thesis, we will not need to go too much into the details, and we will concentrate mainly on the formation up to Super-Earths/Mini-Neptunes.

We start with the micron-sized dust particles which are observed in discs around young stars, and may originate from interstellar medium and/or condense in the disc itself. The aerodynamic coupling between solid particles and gas is important, and it is usually measured by the *stopping time* $t_s = m\Delta v/|F_{\text{drag}}|$, where m is the particle's mass, Δv is its velocity relative to that of the gas, and F_{drag} is the aerodynamic drag force acting in the opposite direction to Δv ; notice that $|F_{\text{drag}}|$ is generally $\propto \Delta v$ for a given particle, so that t_s only depends on the particle's properties and not on its velocity. The *dimensionless stopping time* or *Stokes number* $\tau_s = t_s\Omega_K$ is also used to measure the stopping time relative to the orbital timescale at the location of the particle [Armitage(2015)]. Micron dust grains are well coupled to the gas, but in the meantime they can collide with each other and stick together (a process called *coagulation*) to form larger and larger particles, and there is no impediment to forming \sim mm- to

cm-sized particles/pebbles/grains. These particles are less strongly coupled with the gas, so they do not follow the gas streamlines: they start to settle vertically towards the disc’s midplane and drift radially by aerodynamic drag, caused by the difference between their Keplerian velocity and the gas’ velocity. By increasing the dust density near the midplane, particles can grow bigger and sediment more. This process is however halted by a number of barriers: the bouncing barrier, the fragmentation barrier, the drifting barrier (see e.g. [Birnstiel et al.(2016)]). The next step is to make *planetesimals*, which are large enough objects (typical size of \sim few tens to 100 km) that their mutual gravitational interactions are more important than the aerodynamic coupling with the gas, and therefore avoid significant radial drifting towards the star due to gas drag. Going from small grains to planetesimals requires overcoming the various barriers mentioned above; in any case, we know that planetesimals necessarily formed since they are still found in the Solar System as asteroids and Kuiper belt objects, and we know that they probably formed relatively big (size of order 100 km, [Johansen et al.(2015), Simon et al.(2016)]), but the details of their formation are still not fully understood. Processes such as particle sticking, concentration at pressure maxima, various instabilities (such as gravitational instabilities [Safronov(1969), Goldreich and Ward(1973)], Kelvin-Helmoltz instability [Cuzzi et al.(1993)], streaming instability [Youdin and Goodman(2005), Johansen et al.(2015)] and turbulent concentration [Cuzzi et al.(2008)] have been proposed as viable ways or important factors in the formation of planetesimals, and some combination of them may come into play.

Then, the growth from planetesimals to *planetary embryos* (objects of the size of the Moon or Mars) is considered. The traditional model was that of planetesimal accretion, which suggests that the growth from planetesimals to larger bodies can happen via mutual collisions and accretion. The accretion process at this scale is aided by gravitational focusing, where the collisional cross section is enhanced from being simply the geometrical cross section R to $b = R\sqrt{1 + \Theta}$, where $\Theta = (v_{\text{esc}}/v_{\text{rel}})^2$ is the *focusing* (or Safronov) *parameter*, defined in terms of $v_{\text{esc}} = \sqrt{2Gm/R}$ the escape velocity of the accreting body of mass m and radius R , and v_{rel} the relative velocity between the two planetesimals. This process is usually divided in a first phase of so-called *runaway growth* where the biggest object in a region of the disc accretes material at a larger rate than the smaller ones, which can happen if the system is relatively cold dynamically so that $v_{\text{rel}} \ll v_{\text{esc}}$; this in turn leads to a second phase of *oligarchic growth* where the biggest objects excite the other planetesimals so that $v_{\text{rel}} \sim v_{\text{esc}}$ and now the accretion tends to grow at comparable rates these larger bodies (called *oligarchs*) at regular intervals in semi-major axis until they clear out their feeding zones. This process has however been shown not to be efficient enough to form the giant planet cores within the lifetime of the gas in the disc. A possible solution is the *pebble accretion model* [Lambrechts and Johansen(2012)]. The pebble accretion scenario invokes the fact that pebbles, when sufficiently deflected during a close encounter with the planetesimal, end-up spiralling towards its surface, because of the effects of gas drag. This makes the planetesimal cross-section for accretion of pebbles much larger than that for the accretion of other planetesimals.

Finally, larger objects (mass $> M_{\oplus}$) may be formed, which one may well call planets or *planetary cores*. The final accreted mass of these bodies depends on the accretion process and the parameters of the disc or of the host star. In the case of pebble accretion a *pebble isolation mass* is defined, which is the mass at which the planet starts to carve a gap sufficiently deep in the gas profile to stop the pebble flux at the pressure bump generated at the outer edge of the gap. The pebble isolation mass is found to depend on local properties of the protoplanetary disc (viscosity, aspect ratio and radial pressure gradient) as well as of the Stokes number of the particles [Bitsch et al.(2018)], and yields Neptune-mass planets or smaller in disc conditions consistent with observations [Lambrechts and Johansen(2014)]. This narrative then extends to explain the formation of gas giants and terrestrial planets. For the gas giants, the idea is that once a massive enough core is generated and is still embedded in the protoplanetary disc, it may start accreting a gas envelope. Bigger bodies are able to sustain a bigger envelope, and a slow phase ensues (called *hydrostatic growth*) where the core keeps accreting both solids and gaseous material, in a self-regulated fashion under hydrostatic equilibrium. If the process stops here, the resulting body would be very similar to the ice giants of the Solar System, Uranus and Neptune. When a critical condition is reached (when the core and the envelope masses are comparable) a quick *runaway gas accretion* phase follows [Mizuno(1980), Pollack et al.(1996)], where now the limit of mass is set by how much gas is available near the planet (in the pebble accretion scenario, reaching the pebble isolation mass cuts the infall of solids onto the core, hence the addition of energy, which can trigger this phase [Lambrechts et al.(2014)]). Accretion can be limited by the radial transport of gas or by the dissipation of the disc itself. Other smaller bodies (such as planetary embryos) may be produced by planetesimal-planetesimal collisions and/or pebble accretion without reaching pebble isolation mass within the lifetime of the disc. The terrestrial planets would then be formed from these embryos after the disc has dissipated, in a phase of giant impacts [Morbidelli et al.(2012)].

I will not go further into the details of planetary formation. Recently, three papers [Izidoro et al.(2019), Lambrechts et al.(2019), Bitsch et al.(2019)] have been published, which together attempt to develop a “unified

model to explain the formation of rocky Earth-like planets, hot Super-Earths and giant planets from pebble accretion and migration” [Izidoro et al.(2019)], and I refer to them and the references therein for the interested reader. However, it is now time to introduce the last of the three fundamental ingredients mentioned in [Izidoro et al.(2019)], which is the so-called planetary migration: the possibility of orbital transport of forming planets within the disc. Indeed, one must realise that when massive enough planetary embryos are formed, the coupling with the disc of gas becomes important again, not because of aerodynamic effects but because of planet-gas gravitational interactions. Torques can be generated that act on the planet and therefore change its radial distance from the star. The so-called *type-I migration* pertains to planets with a mass roughly between Mars and Saturn, while more massive planets can change substantially the disc’s structure, open a gap around their orbit, so that a different migration regime applies traditionally called *type-II migration* [Lin and Papaloizou(1986), Dürmann and Kley(2015), Kanagawa et al.(2018), Robert et al.(2018)]. We will not expand on type-II migration, while I give a more detailed description of type-I migration in the next Section since it significantly shapes the Super-Earth population.

1.2.3 Shaping the planets’ orbits during the disc phase: Planetary type-I migration and eccentricity damping

When an accreting planet embedded in the protoplanetary disc becomes massive enough, with a mass m_{pl} of the order of Mars’ mass, its gravitational influence on the disc (albeit not strong enough to change significantly the radial surface density of the disc described in Subsect. 1.2.1 – e.g. opening gaps) can cause significant axial asymmetries in the disc’s density profile. In turn, by the action-reaction principle, there is a force felt by the planet and caused by the disc: this results in a torque, which changes the planet’s orbital angular momentum $\mathcal{L} = m_{\text{pl}}\sqrt{\mathcal{G}M_*r_{\text{pl}}}$ (where again \mathcal{G} is the gravitational constant and M_* is the mass of the central star) and therefore changes its radial distance from the star r_{pl} (we assume here that the orbit is nearly circular). This orbital displacement is referred to as *planetary migration*. Migration can be inward, that is towards the star, or outward (or vanishing if there is no net torque), but it is generally inward. There are different types of torques acting on the planet, which correspond to different ways in which the planet interacts with the orbiting material present in the disc. One effect is generated at orbital separations which extend inside and outside the planet’s orbit, while another takes place around the planet’s *corotation region*, a narrow ring centred at the planet’s orbital separation r_{pl} containing the planet’s so-called *horseshoe region*, where the disc material executes horseshoe turns relative to the planet. I briefly describe below the origin of these torques.

Outside the corotation region, in a coordinate frame rotating with the planet, the gravitational pull of the planet on the gas causes an overdensity which trails the planet in the region exterior to its orbit (where the material is rotating with a lower orbital speed than the planet’s), and a second overdensity which leads the planet in the region interior to its orbit (where the material is rotating with a higher orbital speed than the planet’s). These overdensities are generated as multi-arm spiral waves at the so-called *Lindblad resonances*, which are the first-order mean motion resonances in the disc, expressed in rotating coordinates [Goldreich and Tremaine(1979), Goldreich and Tremaine(1980)]. Summed together, they give rise to a single-armed spiral density wave, called the *wake*, which appears stationary in the frame co-rotating with the planet (see Figure 1.5 panel (a)). Since the planet is accelerating gas material external to its orbit thereby increasing the material’s angular momentum, the back-reaction is a negative torque felt by the planet; the exact opposite occurs for the material internal to the planet’s orbit, which therefore exerts a positive torque on the planet. The two torques could in principle cancel out, if it were not for the fact that the gas’ angular velocity is slightly sub-Keplerian, causing a shift of the planet’s corotation region and of the Lindblad resonances which fall inward closer to the central star [Ormel and Shi(2013)]: this causes the outer torque to win over the inner torque whatever the steepness of the decaying radial profile of the disc’s surface density [Ward(1997)], and the net effect is a total negative torque felt by the planet, called the *Lindblad torque*. The Lindblad torque Γ_L is found to be given by

$$\gamma\Gamma_L/\Gamma_0 = -2.5 - 1.7\alpha_T + 0.1\alpha_\Sigma, \quad \Gamma_0 = \Sigma_{\text{pl}} \left(\frac{m_{\text{pl}}}{M_*} \right)^2 h_{\text{pl}}^{-2} \Omega_{\text{pl}}^2 r_{\text{pl}}^4, \quad (1.1)$$

where α_Σ sets the surface density profile, $\Sigma \propto r^{-\alpha_\Sigma}$, α_T sets the temperature profile, $T \propto r^{-\alpha_T}$, $\Omega_{\text{pl}} = \sqrt{\mathcal{G}M_*r_{\text{pl}}^{-3}}$ is the Keplerian orbital frequency at the location of the planet (also called mean motion in the jargon of Celestial Mechanics), and γ is the adiabatic index of the disc [Baruteau et al.(2014)]. Equation (1.1) states that the change in specific orbital angular momentum $\mathcal{L}/m_{\text{pl}}$ of the planet is proportional to the gas surface density $\Sigma_{\text{pl}} = \Sigma(r_{\text{pl}})$, to the planet’s mass m_{pl} , and inversely proportional to the square of the aspect-ratio $h_{\text{pl}} = H(r_{\text{pl}})/r_{\text{pl}}$, all quantities being evaluated at the location r_{pl} of the planet. Using the expression for the orbital angular momentum in the

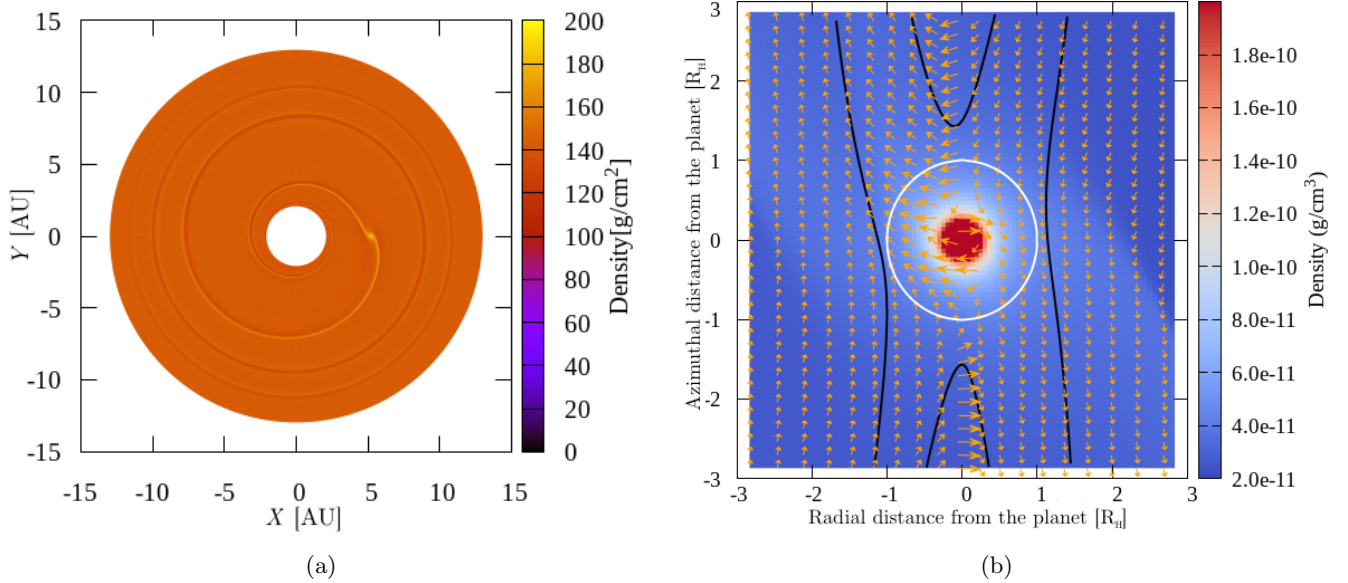


Figure 1.5: Planet-disc interactions in the case of type-I migration. Panels (a) and (b) are the result of hydrodynamical simulations of a planet of mass $m_{\text{pl}} = 1 \times 10^{-5} M_*$ embedded in a protoplanetary disc, and show the resulting density profile of the disc. In panel (a), the single-armed spiral density wave (called *wake*) is visible, which is a modification of the density profile of the disc caused by the presence of the planet. These overdensities are in turn responsible for the *Lindblad torque*, the back-reaction felt by the planet because of its interaction with the disc. Panel (b) is a zoom to the region close to the planet. Near the planetary orbit, the disc material performs U-turns in the frame of reference co-rotating with the planet: the orange arrows show the direction of the flow of the disc’s material (note: the arrows are not to scale), and in black a few flow lines are also marked. The two U-turns shown here actually connect through the other side of the disc, giving this trajectory a horseshoe shape. This planet-disc interaction generates the so-called *corotation torques*, see main text for details. Units of length in panel (b) are in Hill radii $r_{\text{H}} = (m_{\text{pl}}/(3M_*))^{1/3} a$, indicated by the white circle around the planet. The hydrodynamical simulations and the images were provided by Elena Lega.

circular case, $\mathcal{L} = m_{\text{pl}} \sqrt{GM_* r_{\text{pl}}}$, and that $d\mathcal{L}/dt = \dot{\mathcal{L}}$ equals the torque, the torque factor Γ_0 yields a timescale for the relative change of r_{pl} given by

$$\tau_0 = \frac{r_{\text{pl}}}{|\dot{r}_{\text{pl}}|} = \frac{1}{2} \frac{M_*}{m_{\text{pl}}} \frac{M_*}{\Sigma_{\text{pl}} r_{\text{pl}}^2} h_{\text{pl}}^2 \Omega_{\text{pl}}^{-1}, \quad (1.2)$$

where we use the notation $\dot{r}_{\text{pl}} = dr_{\text{pl}}/dt$. Assuming a MMSN-like surface density, a solar mass star and an aspect ratio of 5%, the timescale of migration in years at 1 Astronomical Unit (AU) is given approximately by M_*/m_{pl} : an Earth-mass planet would migrate in $\sim 3 \times 10^5$ years while a Neptune-mass planet would migrate in $\sim 2 \times 10^4$ years [Baruteau et al.(2014)]. These timescales are some orders of magnitude shorter than the typical lifetime of the disc, so the effect of the Lindblad torque cannot be neglected in the context of the formation of Super-Earth and Mini-Neptune systems.

Another type of torques arises from the interaction of the planet with the material located in the planet’s horseshoe region (Figure 1.5 panel (b)), and they are called *corotation torques*. There are different types of corotation torques, depending on the physics involved. The *vortensity-driven corotation torque*³ emerges from the purely gravitational effect of the planet pushing inward the outer material that is performing the horseshoe U-turn and pushing outward the inner material performing the U-turn [Ward(1992), Masset(2001)]; if the density profile $\Sigma \propto r^{-3/2}$ (as for the MMSN) the net torque is zero, if it is steeper the net effect is a negative torque, if it is flatter there is a positive torque. However the libration of co-orbital material tends to establish a local density profile with a $-3/2$ radial slope, which would vanish the torque (a process denoted *co-orbital torque saturation*). So, the vortensity-driven corotation torque can be maintained only if the internal forces of the disc (e.g. viscosity) restore a density profile with a slope different from $-3/2$. The *entropy-driven corotation torque* takes into account the fact that a steep local temperature profile causes hotter inner material that is pushed outwards to expand and

³The *vortensity* is the ratio between a fluid’s vorticity (the curl of the flow’s velocity field) and its density.

cold outer material that is pushed inwards to contract, causing a density imbalance which can generate a positive torque [Paardekooper and Mellema(2006)]. It is also prone to saturation if the libration timescale of the horseshoe material is much faster than the cooling/heating timescale of the gas in the new medium [Kley and Crida(2008)]. The *dynamical corotation torque* considers that in low-viscosity discs the inward migrating planet carries along its co-orbital material without mixing with the local disc, which causes a feedback on planetary migration which is positive if the surface density of the disc is steeper than $1/r^{3/2}$, and negative otherwise.

To summarise, the Lindblad torque is typically negative. Instead, corotation torques can give rise to a positive net torque, but they are more complicated as they are subject to saturation unless certain conditions in the disc are met [Kley and Nelson(2012)], and they are also fragile, since if the eccentricity or inclination of the planet increase (as can be the case if other planets are present in the disc and they excite each other’s orbits) the corotation torques decrease exponentially [Fendyke and Nelson(2014), Cossou et al.(2014)]. The easiest way to probe the resulting torques is to fit their formulas to hydrodynamical simulations. One can construct a disc model and calculate the resulting torques, building so-called *migration maps* which show in which region of parameter space there is inward or outward type-I migration; in between these regions are the locations where the net torque is zero, which are called *planet traps*, since a protoplanet would tend to migrate towards this location in the disc (e.g. [Bitsch et al.(2013), Bitsch et al.(2015), Baillié et al.(2015)]).

Another important effect for the Super-Earth/Mini-Neptune population is the torque that is generated at the inner edge of the protoplanetary disc, where the surface density experiences a radial jump and inside of which the disc is relatively empty (see the region closest to the star in Figure 1.3). In this circumstance, the resulting direction and strength of the Lindblad and corotation torques have been investigated for example in [Masset et al.(2006)]. They find that, if the inner region is almost empty, a planet orbiting the central star at the disc’s edge experiences a total Lindblad torque which is essentially equal to the negative outer contribution. Instead, the corotation torque (which is very sensitive to the local gradient of the disc surface density) is positive and much stronger than in a power-law disc, provided that the jump occurs radially over a few H . Moreover they find that “the corotation torque largely dominates the differential Lindblad torque on the edge of a central depletion, even a shallow one” and that “a disk surface density jump of about 50% over 3-5 disk thicknesses suffices to cancel out the total torque”. Therefore, a planet that has undergone inward type-I migration all the way to the inner edge of the disc will stop migrating. [Mulders et al.(2018)] used their *Exoplanet Population Observation Simulator* to estimate the characteristic architecture of exoplanetary systems based on Kepler data, and found a clustering of the innermost planets of multi-planet systems at ~ 0.1 AU, reminiscent of the location of the inner edge of protoplanetary discs.

In the above treatment, we considered the case of a nearly circular planetary orbit in the same plane as the disc of gas, which need not be always the case, for example in the presence of other planets which can excite each other’s orbit. In the more general case of an eccentric planet and/or a planet which is inclined with respect to the gas, the effect of the gas on the planet is to damp the eccentricity and/or inclination of the planet, which happens on timescales which are much shorter than the migration timescale [Cresswell and Nelson(2008)]. For this reason, planets are expected to be nearly circular and coplanar during the disc phase, in a relatively dynamically cold configuration. Then, one should also consider the effects of type-I migration on a planetary system’s architecture when multiple planets are embedded in the same disc. Considering two planets, *convergent migration* occurs if the outer planet migrates inward at a higher rate than the inner one, either because it is more massive (cfr. Equation (1.1)) or because the inner planet has halted its migration at the inner edge of the disc. As we review in Chapter 3, a result of convergent migration of Super-Earth/Mini-Neptunes is the formation of chains of mean motion resonances, where the period ratios between neighbouring planets is close to a low integer ratio such as 2:1, 3:2, etc. (see also the next section). Before the disc’s disappearance, the resonant interaction enhances the eccentricities against the disc’s damping effect; this can lead to an equilibrium configuration when the two effects cancel out (in some cases, the acquired resonant configuration may be destabilised due to the overstability of the captured state caused by dissipative effects still generated by the disc [Goldreich and Schlichting(2014), Deck and Batygin(2015)]). However, after the disc phase, when the gas is not present anymore to damp out any dynamical excitations of the system, dynamical instabilities could be responsible for generating high eccentricities and mutual inclinations (which are indeed observed in the exoplanet sample), and to break the resonant chains that were formed under the supervision of the disc. For this reason, it is important not only to have an understanding of the physical processes that shape the formation of planetary systems during the disc’s lifetime, but also of their subsequent long-term dynamical evolution, which, as we will see, can change completely the types of orbital configurations that we can expect to find in the end. This is the general context in which this thesis is developed. In the next section, I therefore introduce the specific questions that we wish to address, I recall the observational constraints which need to be taken into consideration, and I explain how we have proceeded in our investigation, giving the layout of this document.

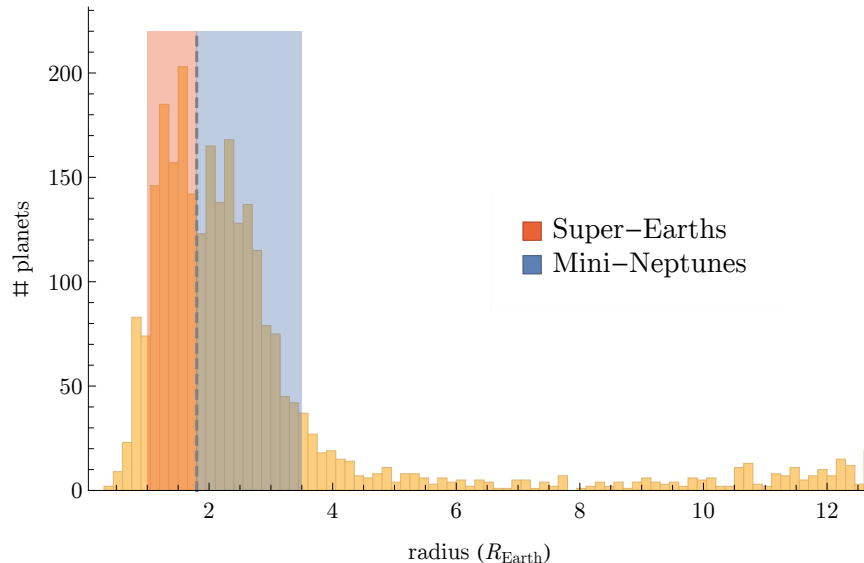


Figure 1.6: Distribution of the radii of detected exoplanets with orbital periods less than 100 days. The two red and blue vertical bands show the distinction between the more rocky Super-Earths and the Mini-Neptunes, which are thought to host a gaseous envelope which significantly shapes their observed radius. Data was obtained from the Nasa Exoplanet Archive <https://exoplanetarchive.ipac.caltech.edu/>.

1.3 This thesis in context

Despite our limited knowledge on the real nature of exoplanetary systems, there are some trends in the exoplanet sample which impose constraints on formation scenarios. These include the radius distribution (in particular the dip at $\simeq 1.8R_{\oplus}$, known as the Fulton gap [Fulton et al.(2017)]), the star metallicity vs. giant planets occurrence correlation, the existence of the groups of hot and warm Jupiters separated by a gap in the semi-major axis distribution, the radial distribution of gas giants (such as the possible presence of a turnover at the ice line, the location in the disc where the temperature is low enough to allow water to condense, [Fernandes et al.(2019)]), the eccentricity distribution of the gas giants, the fact that we observe many more stars with a single transiting-planet than with multiple transiting-planets around them (called the Kepler dichotomy, e.g. [Lissauer et al.(2011)]), the period ratios distribution of neighbouring planets in multi-planetary systems (e.g. [Fabrycky et al.(2014)]), the mass-radius relationship, the fact that Kepler planets orbiting the same star appear to be quite homogeneous in terms of their radii [Weiss et al.(2018)] (the so-called *peas in a pod* interpretation) as well as in their masses [Millholland et al.(2017)]. For a review of these key observations, see e.g. [Winn and Fabrycky(2015)]. Ultimately, any formation model must account for all these features to be considered successful.

Currently, the exoplanet population is dominated by Kepler’s transit detections, making the planetary physical radii and orbital periods the better constrained parameters of the sample. Concerning the first aspect, an important question is whether Kepler’s planets are mainly rocky (like the Earth) or if they host low-density atmospheres which enlarge their observed size (like Neptune). Although the terms Super-Earths and Mini-Neptunes have been used interchangeably, the aforementioned Fulton gap in the radius distribution does actually suggest a separation between planets with a radius less than $\simeq 1.8R_{\oplus}$ and larger than this value (see Figure 1.6), and much work has been done recently to understand how photoevaporation sculpts the physical radii of these planets (see [Fulton et al.(2017), Owen and Wu(2017), Fulton and Petigura(2018), Jin and Mordasini(2018), Ehrenreich et al.(2015)]).

In this thesis, we wish to address the complementary problem of understanding the key physical and dynamical processes that shape the observed orbital distribution of planetary systems. Since in the following we will be concerned mainly with dynamical aspects, we will use the term Super-Earth to broadly describe planets with a mass between 1 and ~ 20 Earth masses or a radius between 1 and ~ 4 Earth radii, which have been so-far discovered with an orbital period typically shorter than ~ 100 days. It is generally expected that such planets form (mostly) within the lifetime of the protoplanetary disc of gas and therefore they should undergo radial migration towards the central star, as a result of the planet-disc interactions described in the previous section (see also [Ogihara et al.(2015), Izidoro et al.(2017)]). Migration brings the Super-Earths to the inner edge of the disc, where inward migration stops [Masset et al.(2006)]. By this process, the Super-Earths are captured into mutual mean motion resonances, where

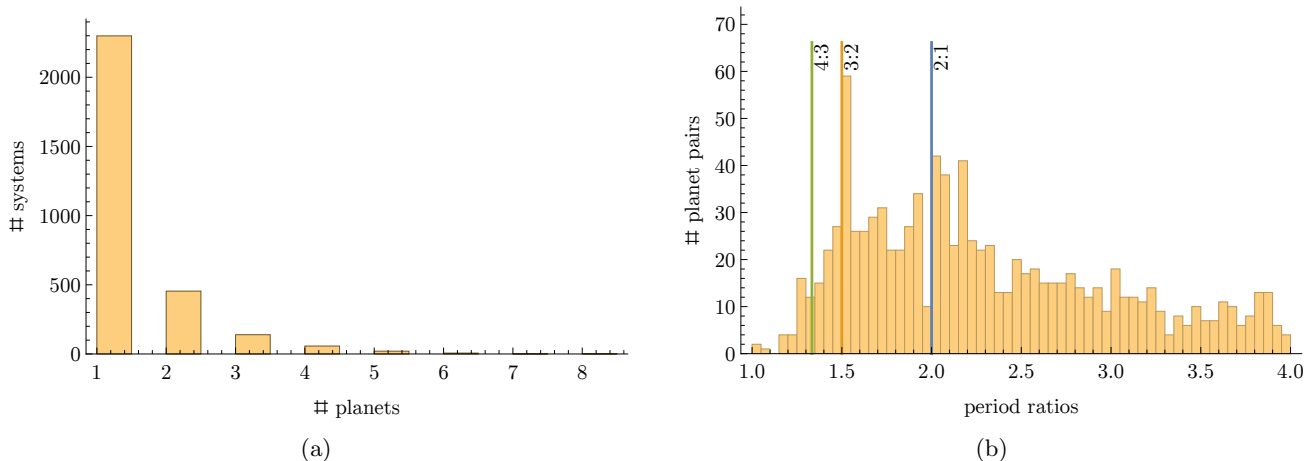


Figure 1.7: The observed orbital architecture of exoplanetary systems. The left panel shows the distribution of the number of planets in the same system. The large number of systems with only one observed planet (the *singles*) compared with the smaller number of systems with multiple observed planets (the *multis*) is noticeable, and for the Kepler sample has been called the Kepler dichotomy (see main text). In any case, observations of planet-hosting stars reveal that multi-planetary systems are not rare, hosting over 1600 confirmed planets. The period ratio distribution of neighbouring planets in the same system is shown in the right panel. One can observe an overall broad distribution as well as a number of peaks slightly wide of resonant ratios, especially the 2:1 and 3:2 commensurabilities. Data was obtained from the Nasa Exoplanet Archive <https://exoplanetarchive.ipac.caltech.edu/>.

the ratios of orbital periods are equal to the ratios of (low) integer numbers such as $k:k-1$ for first order resonances; in this configuration, the planets efficiently exchange orbital angular momentum in such a way that prevents their orbits from approaching further. This is observed in all numerical simulations of migrating planets in their protoplanetary disc (e.g. [Terquem and Papaloizou(2007), Cresswell and Nelson(2008), Morbidelli et al.(2008)], the aforementioned [Ogihara et al.(2015), Izidoro et al.(2017)], and more recently [Izidoro et al.(2019)]). Although details of disc-driven migration remain an active topic of research, it is clear that such a process should play some role in the dynamical history of planetary systems. For example, it is not easy to envision a formation narrative which does not require convergent migration for systems such as Trappist-1, a star famously hosting seven planets with period ratios very close to small integer ratios ([Gillon et al.(2016), Gillon et al.(2017)]), and evidence suggesting that the planets around Trappist-1 truly reside in a resonant configuration comes from the observed libration of the three-body Laplace angles [Luger et al.(2017)]. Moreover, [Gillon et al.(2017)] performed N -body integrations with the orbital fits as initial conditions and these went unstable over timescales 10,000 times shorter than the estimated age of the system; in contrast, [Tamayo et al.(2017)] remarked that if an initial condition which results from capture into resonance through migration is chosen, then the system is stable over timescales two orders of magnitude longer than the ones found in [Gillon et al.(2017)]. They also note that the addition of tidal eccentricity damping should help maintain the evolution stable over the system's age. Other good examples of systems in resonant chains are the four sub-Neptune planets of Kepler-223 [Mills et al.(2016)], the now-classic example of Laplace-like resonance in GJ-876 [Rivera et al.(2010), Batygin et al.(2015)] and Kepler-60 [Goździewski et al.(2016)]. These long resonant chains are extremely unlikely to have formed by pure chance, and therefore these systems are considered proof that convergent migration occurred, leading to resonant trapping.

Nevertheless, although resonant capture is typical of migration simulations and some resonant systems exist, the observed orbital configurations seem at first at odds with this statement (Figure 1.7 panel (b)): the period ratio distribution is relatively flat, with only a few peaks just to the right (*wide*) of the exact commensurabilities (mainly the 2:1 and 3:2 period ratios). Note however that analytical models of resonance do predict that a pair of planets in a first order mean motion resonance need not satisfy the exact resonance condition $a_1/a_2 = ((k-1)/k)^{2/3}$ (where a_1 and a_2 are the semi-major axes of the inner and outer planet, respectively, and k is a positive integer), but they can reside wide of resonance while the resonant angles are still librating. This divergence of the resonant equilibrium configurations happens at vanishingly low eccentricities and is linked to a fast precession of the perihelia, which is well understood analytically, as we will see in the next chapters. Therefore, many authors have pondered on the possibility that the observed peaks just wide of the exact $k : k - 1$ period ratios might actually con-

tain resonant systems [Papaloizou and Terquem(2010), Lithwick and Wu(2012), Batygin and Morbidelli(2013)b, Delisle and Laskar(2014)]; we will revisit this issue, looking specifically at three-planet systems. Then, we must still face the fact that the overall distribution still shows that most systems show little preference for near-integer period ratios, and their orbital separations are usually much wider than those characterising planets in resonant chains (Figure 1.7). However, [Izidoro et al.(2017)] showed that this observation is not inconsistent with the migration/resonant trapping paradigm. In fact, simulations show that, after the removal of the disc of gas, the resonant planetary systems often become unstable. Moreover, [Izidoro et al.(2017)] pointed out that the Kepler dichotomy can also be explained by these instabilities, by arguing that a significant fraction of observed single-planet systems are the remnants of systems that suffered instabilities and therefore an increase in mutual inclination among the planets, so that the other inclined planets cannot be detected by transit. Concerning the rates of these instabilities, [Izidoro et al.(2017)] showed that the Kepler observations are very well reproduced if the fraction of the resonant systems that eventually become unstable is $\sim 90\%$, with the remaining stable systems representing observed systems such as Trappist-1, Kepler-223, etc. These high rates of post-disc phase instabilities are actually recovered in some simulations in [Izidoro et al.(2019)], especially the ones where the formed systems are more massive and more compact. They therefore conclude that the final number of planets in the chain, the compactness of the system and the planets' masses are crucial parameters that differentiate between systems that remain stable after disc removal (for total integration times of 50 – 300 My) and system that suffer dynamical instabilities (collisions or ejections). In this context, [Matsumoto et al.(2012)] studied numerically the stability of resonant multi-planetary systems for high-integer first-order mean motion resonances. They built the desired resonant configuration by simulating the type-I migration phase in a protoplanetary disc of gas; then they slowly depleted the disc. They observed that there is a critical number of planets above which the resonant systems go naturally unstable, with a crossing time comparable to that of non-resonant systems, and studied how this number changes with the planetary masses and the compactness of the chain. They thus demonstrated that, given the planetary masses and the compactness of the chain, there is a limit number of planets that can form a stable resonant chain or, equivalently, that given the number of planets and the compactness of the chain, there is a limit mass for stability. The reason of the instability observed in [Matsumoto et al.(2012)] and [Izidoro et al.(2017), Izidoro et al.(2019)], however, was not discussed and remains elusive.

In this context, the main subject of this thesis is the dynamical evolution of resonant Super-Earth/Mini-Neptune systems after the dissipation of the disc of gas, to understand how it can shape their current observed orbital distribution. In particular, we want to address the problem of the structure of first order mean motion resonant chains and their stability in terms of planetary mass for a fixed number of planets and a fixed compactness of the chain. A useful simplification will be to assume that the planets in the same system are coplanar and of equal mass. These assumptions make it easier to state the results and work analytically, but should not be considered as too restrictive. Indeed, as we saw in the previous section the effect of the disc is to damp the mutual inclinations, and the planets in the observed resonant chains (which in this framework would represent the original configurations at the very end of the disc phase that actually remained stable) are nearly coplanar. Moreover, planets orbiting the same star appear to be quite homogeneous in terms of their radii [Weiss et al.(2018)] and their masses [Millholland et al.(2017)].

The remaining chapters of this thesis are organised as follows. In Chapter 2, I recall the basic tools of Hamiltonian dynamics which will be used extensively throughout the thesis. I give a standard textbook introduction of the main concepts, focusing on those tools, techniques and simple models that are useful to guide our understanding of the dynamical phenomena that we are interested in. Most importantly, I introduce in a self-contained way the two-body- and planetary problems, and I recall the main tools of perturbation theory and the adiabatic invariant. In Chapter 3 I use these tools to describe the structure of first order mean motion resonances and the evolution in resonance. This allows us to understand the process of capture into resonance via slow, convergent type-I migration of a pair of planets in a protoplanetary disc by calculating the location of the stable equilibrium point in the purely resonant approximation. In Chapter 4, I extend the resonant model to three planets, and show how it can be used in a statistical way to determine whether an observed system of planets with period ratios near exact commensurability actually carries a trace of a present or past resonant dynamical history. In Chapter 5, I address the main problem of the dynamical stability of chains of planets deeply in resonance, depending on the planetary mass. I start with the problem of two equal-mass planets in mean motion resonance, where dynamical close encounters are found to be the cause of instability. In the case of three or more planets, we observe a new dynamical phenomenon which excites the system and anticipates the instability, with a dependence on the number of planets and the compactness of the chain which agrees qualitatively with [Matsumoto et al.(2012)]. Finally, in Chapter 6, we investigate the applicability of dynamical instabilities to the problem of the pollution of the atmospheres of White Dwarfs. *White Dwarfs* are the remnants of main sequence stars with relatively

low masses, \lesssim a few M_{\odot} (the solar mass). During the course of their lives, such stars lose mass until their deaths, leaving behind a core with $M_* \sim M_{\odot}$ and a radius comparable to that of the Earth. A significant fraction of White Dwarf’s atmospheres are observed to be polluted with heavy metals with rates of at least 30% [Zuckerman et al.(2003), Koester et al.(2014)]. These elements should rapidly sink to the core leaving behind only Hydrogen and Helium [Fontaine and Michaud(1979), Vauclair and Fontaine(1979)]. This is usually seen as evidence of infalling planetesimals, which are driven close enough to the White Dwarf to be tidally disrupted and thus continuously replenish the atmospheres with heavy elements [Debes and Sigurdsson(2002), Jura(2003)]. Since White Dwarfs are relatively old objects, planetesimal formation is unlikely to be an active process around these stars, so the presence of a large population of planetesimals must be explained in some other way. Assuming that these stars hosted compact resonant chains during their main sequence stage, it is conceivable that, as the stellar mass decreases, the mutual planetary perturbations become stronger and the chain may be broken (enacting in nature the numerical experiments outlined in Chapter 5), so that a phase of planetary collisions may trigger the formation of planetesimals as collisional debris. Notice that compact but non-resonant systems of Super-Earths can also become unstable because their orbital separation in terms of mutual Hill radii decreases as the mass of the star decays. Anyway, the main focus of this chapter is not the origin of the instability but the fate of the debris, since the process responsible to drive these planetesimals so close to the White Dwarf should also be investigated. We show that the extreme secular excitation of the eccentricity of planetesimals residing in mean motion resonance with a slightly eccentric outer perturber can be an efficient mechanism to significantly reduce the periastron distance $a(1 - e)$ of the planetesimals, and drive them sufficiently close to the White Dwarf to undergo tidal disruption. We also include the effects of General Relativity, which can be important at such small distances from the central star, and estimate the lowest planetary perturber’s mass which ensures the efficiency of this dynamical mechanism.

A few appendices accompany the main text of the thesis. In Appendix A, I derive in a self-contained way an integrable approximation for the purely resonant interactions of two planets orbiting in the same plane, valid at first order in the eccentricities (this reduction is based on [Batygin and Morbidelli(2013)a, Batygin(2015)], see also references therein). In Appendix B, I detail a rescaling of the Hamiltonian for three planets in first order mean motion resonance that is used implicitly in Chapter 4. In Appendix C I report some code snippets, written for the algebraic manipulator Mathematica, that can be used to implement the Lie series approach of perturbation theory, which is used extensively in Chapter 5. In Appendix D, I include the full code that is used to produce the figures of Chapter 6; this chapter is based on [Pichierri et al.(2017)], and the code was added as supplementary online material for that paper at the time of publication. Finally, in Appendix E, I include a list of symbols that are used consistently throughout the thesis, to help the reader in getting familiar with the notations.

Chapter 2

Hamiltonian mechanics and the planetary problem

In this section I introduce the tools of the Hamiltonian formalism that will be used throughout the thesis. For a more in-depth discussion of this topic, I refer to [Arnold(1978), Morbidelli(2002)]. I then introduce the basic concepts and equations of Celestial Mechanics, which will be used extensively in the thesis. This is done in the setting of the Hamiltonian formalism since it is better suited for the tools of perturbation theory, a sketch of which is presented in the last section of this Chapter.

2.1 Hamiltonian systems

In its most abstract form, a *Hamiltonian system* is given by a differential manifold \mathcal{F} of dimension $2n$ with coordinates $\mathbf{x} = (\mathbf{p}, \mathbf{q}) = (p_1, \dots, p_n, q_1, \dots, q_n)$ and a real function

$$\begin{aligned} \mathcal{H} : \mathcal{F} \times \mathcal{I} &\rightarrow \mathbb{R} \\ (\mathbf{x}, t) &\mapsto \mathcal{H}(\mathbf{x}, t) \end{aligned} \tag{2.1}$$

called the *Hamiltonian* (which is assumed regular enough – we may actually consider here Hamiltonians that are analytic in all of their variables), such that the evolution of the system is governed by *Hamilton's equations*

$$\begin{cases} \dot{\mathbf{p}} = -\frac{\partial \mathcal{H}}{\partial \mathbf{q}}(\mathbf{p}, \mathbf{q}, t), \\ \dot{\mathbf{q}} = +\frac{\partial \mathcal{H}}{\partial \mathbf{p}}(\mathbf{p}, \mathbf{q}, t), \end{cases} \tag{2.2}$$

where we use the notation $\dot{\mathbf{p}} = \frac{d\mathbf{p}}{dt}$, $\dot{\mathbf{q}} = \frac{d\mathbf{q}}{dt}$. $\mathcal{I} \subseteq \mathbb{R}$ is an interval and $t \in \mathcal{I}$ represents time, with $0 \in \mathcal{I}$ without loss of generality. \mathcal{F} is called the *phase space*; typical examples are $\mathcal{F} = \mathbb{R}^{2n}$ or $\mathcal{F} = \mathbb{R}^n \times \mathbb{T}^n$, where \mathbb{T}^n is the n -th dimensional torus. The positive integer n is the number of degrees of freedom (d.o.f.'s) of the system. The state of the dynamical system is described by the canonical coordinates (\mathbf{p}, \mathbf{q}) which are called respectively *momenta* and *positions*. Hamilton's equations (2.2) are first order ordinary differential equations and are written here in vectorial form. They state that the evolution of p_i is obtained from the partial derivative of the Hamiltonian with respect to q_i , and vice versa. p_i and q_i are then called conjugated variables. Hamilton's equations can be made more compact introducing the so-called *symplectic matrix*

$$J = \begin{bmatrix} \mathbf{0} & -\mathbb{I}_n \\ \mathbb{I}_n & \mathbf{0} \end{bmatrix}, \quad J^2 = -\mathbb{I}_{2n}, \tag{2.3}$$

where \mathbb{I}_n is the $n \times n$ identity matrix and $\mathbf{0}$ is the null matrix; Equations (2.2) can then be written concisely as

$$\dot{\mathbf{x}} = J\nabla\mathcal{H} = \mathbf{X}_{\mathcal{H}}, \tag{2.4}$$

where ∇ is the gradient with respect to $\mathbf{x} = (\mathbf{p}, \mathbf{q})$. We call the right-hand side the *Hamiltonian field* $\mathbf{X}_{\mathcal{H}}$ generated by \mathcal{H} . Hamilton's equations take then the usual form of a dynamical system $\dot{\mathbf{x}} = \mathbf{X}$, and the general theory of ordinary differential equations applies. Then, for a given initial condition $\mathbf{x}(t=0) = \mathbf{x}_0 = (\mathbf{p}_0, \mathbf{q}_0)$,

equations (2.2) may admit a solution $\mathbf{x}(t; \mathbf{x}_0) = (\mathbf{p}(t; \mathbf{x}_0), \mathbf{q}(t; \mathbf{x}_0))$ over a time interval $\mathcal{I}_{\mathbf{x}_0} \subseteq \mathcal{I}$, and one may write $\mathbf{x}(t; \mathbf{x}_0) = \phi_{\mathcal{H}}^t(\mathbf{x}_0)$. The function

$$\begin{aligned} \phi_{\mathcal{H}} : \mathcal{F} \times \mathcal{I}_{\mathbf{x}} &\rightarrow \mathcal{F} \\ (\mathbf{x}, t) &\mapsto \phi_{\mathcal{H}}^t(\mathbf{x}), \end{aligned} \tag{2.5}$$

which associates to each point \mathbf{x} and each point in time t the state of the canonical variables after an evolution of time t with initial datum \mathbf{x} , is called the *canonical flow* generated by \mathcal{H} (or Hamiltonian flow), and represents the evolution of the system. The subset $\Omega_{\mathbf{x}} = \bigcup_{t \in \mathcal{I}_{\mathbf{x}}} \phi_{\mathcal{H}}^t(\mathbf{x})$ is called an *orbit* of the system.

An important property of Hamiltonian flow is that it preserves the volume on the phase space. Indeed, recall that for a dynamical system $\dot{\mathbf{x}} = \mathbf{X}(\mathbf{x})$ the evolution of a set of initial conditions with volume δV follows the equations

$$\frac{1}{\delta V} \frac{d\delta V}{dt} = \operatorname{div} \mathbf{X}, \tag{2.6}$$

where $\operatorname{div} \mathbf{X}$ is the divergence of \mathbf{X} . For a Hamiltonian vector field as one can easily see $\operatorname{div} \mathbf{X}_{\mathcal{H}} = 0$ from Hamilton's equation, so the volume is preserved under Hamiltonian flow. This is called Liouville's Theorem.

2.1.1 Link with Lagrangian formalism

Usually, a Hamiltonian system represents some specific mechanical or dynamical system. In this sense, the Hamiltonian one is an equivalent reformulation of the Newtonian or Lagrangian formalisms. For a given classical mechanical system with Lagrangian $\mathcal{L}(\mathbf{q}, \dot{\mathbf{q}}, t)$ which is function of the generalised coordinates and velocities $\mathbf{q}, \dot{\mathbf{q}}$ and time, one can construct an equivalent Hamiltonian system. The canonical variables are given by $p_i := \frac{\partial \mathcal{L}}{\partial \dot{q}_i} = p_i(\mathbf{q}, \dot{\mathbf{q}}, t)$ and q_i , which shows again why p_i is considered conjugated to q_i and vice versa. The positions q_i are thus also called *coordinates*, and the equations that define the momenta p_i can be inverted if

$$\det \left(\frac{\partial^2 \mathcal{L}}{\partial q_i \partial q_j} \right)_{i,j} \neq 0, \tag{2.7}$$

to obtain $\dot{q}_i = \dot{q}_i(\mathbf{p}, \mathbf{q}, t)$. The Hamiltonian is then given by the so-called Legendre transform of the Lagrangian¹:

$$\mathcal{H}(\mathbf{p}, \mathbf{q}, t) := [\mathbf{p} \cdot \dot{\mathbf{q}} - \mathcal{L}(\mathbf{q}, \dot{\mathbf{q}}, t)]_{\dot{\mathbf{q}} = \dot{\mathbf{q}}(\mathbf{p}, \mathbf{q}, t)}. \tag{2.8}$$

Hamilton's equations (2.2) follow from

$$\begin{aligned} d\mathcal{H} &= \dot{\mathbf{q}} \cdot d\mathbf{p} + \mathbf{p} \cdot d\dot{\mathbf{q}} - \frac{\partial \mathcal{L}}{\partial \mathbf{q}} \cdot d\mathbf{q} - \cancel{\frac{\partial \mathcal{L}}{\partial \dot{\mathbf{q}}} \cdot d\dot{\mathbf{q}}} - \frac{\partial \mathcal{L}}{\partial t} dt = \dot{\mathbf{q}} \cdot d\mathbf{q} - \dot{\mathbf{p}} \cdot d\mathbf{q} - \frac{\partial \mathcal{L}}{\partial t} dt, \\ d\mathcal{H} &= \frac{\partial \mathcal{H}}{\partial \mathbf{p}} \cdot d\mathbf{p} + \frac{\partial \mathcal{H}}{\partial \mathbf{q}} \cdot d\mathbf{q} + \frac{\partial \mathcal{H}}{\partial t} dt, \end{aligned} \tag{2.9}$$

where we used Lagrange's equations, $\frac{\partial \mathcal{L}}{\partial \mathbf{q}} = \frac{d}{dt} \frac{\partial \mathcal{L}}{\partial \dot{\mathbf{q}}} \equiv \dot{\mathbf{p}}$ in the first line, and Hamilton's equations emerge by comparing coefficients. We also note that by the same token $\frac{\partial \mathcal{L}}{\partial t} = 0$ if and only if $\frac{\partial \mathcal{H}}{\partial t} = 0$, which is the case for autonomous systems. If this is the case, and if $\mathcal{L}(\mathbf{q}, \dot{\mathbf{q}}) = T(\mathbf{q}, \dot{\mathbf{q}}) - V(\mathbf{q})$ with T and V the kinetic and potential energies, then $\mathcal{H} = T + V$ is the mechanical energy of the system. This follows from the fact that for autonomous systems $T = T_2$ is a homogeneous function of degree two, and using Euler's theorem on homogeneous functions²

$$\mathbf{p} \cdot \dot{\mathbf{q}} = \frac{\partial T_2}{\partial \dot{\mathbf{q}}} \cdot \dot{\mathbf{q}} = 2T \Rightarrow \mathcal{H} = 2T - T + V = T + V. \tag{2.10}$$

There are many advantages of the Hamiltonian formalism over the Newtonian and Lagrangian ones. For one, the equations (2.2) are already first order rather than second order ordinary differential equations. This does not necessarily make it easier to solve the equation, but, as it will be clear below, the Hamiltonian framework is much

¹We use the notation $\mathbf{a} \cdot \mathbf{b} = \sum_{i=1}^n a_i b_i$ for the dot product.

²The theorem states: let the continuously differentiable function $f : \mathbb{R}^n \rightarrow \mathbb{R}$ be homogeneous of degree k : $f(t\mathbf{x}) = t^k f(\mathbf{x})$. Then

$$\mathbf{x} \cdot \nabla f(\mathbf{x}) = k f(\mathbf{x}).$$

better suited for perturbation theory. The reason is that if one limits oneself to a class of transformation of variables that preserve the Hamiltonian equations (called *canonical transformations*), one can simply work on one object, the Hamiltonian function, rather than on the equations of motion. Another advantage is that the classical Theorem of Noether, which allows one to reduce the number of d.o.f.'s and possibly yield to an explicit solution of the equations of motion, takes a much simpler and manifest formulation. That is, if a Hamiltonian does not depend on a variable, say q_i , then its conjugated variable is a first integral, since $\dot{p}_i = -\frac{\partial \mathcal{H}}{\partial q_i} = 0$ and $p_i(t) = p_i(0)$. The remaining $2(n-1)$ equations now only contain $p_i(0)$ as a constant, that is a parameter, and we have therefore reduced the number of d.o.f.'s by one (i.e. the number of variables by two). In view of this, in studies of Hamiltonian dynamics, one often looks for a canonical change of coordinates that makes the Hamiltonian independent of some of the new variables. Therefore, the knowledge of canonical transformations is crucial to work in the Hamiltonian formalism.

2.1.2 Dynamical variables

2.1.2.1 Autonomous vs. Non-autonomous systems

As usual in dynamical systems, it is valuable to examine not only how the variables \mathbf{x} themselves evolve, but how functions of the dynamical variables change under the canonical flow generated by \mathcal{H} . One can start with the evolution of \mathcal{H} itself, and we obtain

$$\dot{\mathcal{H}} = \frac{d\mathcal{H}}{dt} = \frac{\partial \mathcal{H}}{\partial \mathbf{p}} \frac{\partial \mathbf{p}}{\partial t} + \frac{\partial \mathcal{H}}{\partial \mathbf{q}} \frac{\partial \mathbf{q}}{\partial t} + \frac{\partial \mathcal{H}}{\partial t} = \frac{\partial \mathcal{H}}{\partial t}, \quad (2.11)$$

where the last equation follows from Hamilton's equations (2.2). A natural distinction then emerges, between those systems where \mathcal{H} does not depend explicitly on the time t (which we called *autonomous*), in which case $\frac{\partial \mathcal{H}}{\partial t} = 0$ and \mathcal{H} is a constant of motion (also called first integral), and those where \mathcal{H} depends on the time t (called *non-autonomous*). A non-autonomous system $\mathcal{H}_{\text{non-aut}}(\mathbf{p}, \mathbf{q}, t)$ can always be over-extended to an autonomous one by introducing a new pair of canonical variables (p_t, q_t) , a new Hamiltonian $\mathcal{H}_{\text{aut}}(\mathbf{p}, p_t, \mathbf{q}, q_t) = \mathcal{H}_{\text{non-aut}}(\mathbf{p}, \mathbf{q}, q_t) + p_t$, and imposing as initial datum $q_t(0) = 0$. Then one sees immediately that the two Hamiltonian systems have the same evolution with $q_t = t$. Therefore, from now on we may just as well only consider autonomous systems.

2.1.2.2 Lie derivatives, Lie series and Poisson brackets

In this subsection we introduce the key concepts of Lie derivatives and Lie series which are used extensively in perturbation theory, and the Hamiltonian equivalent of the Lie derivative: the Poisson brackets.

A real function f over the phase space:

$$\begin{aligned} f : \mathcal{F} &\rightarrow \mathbb{R} \\ \mathbf{x} &\mapsto f(\mathbf{x}) \end{aligned} \quad (2.12)$$

is called a *dynamical variable*. For example, the Hamiltonian \mathcal{H} is a dynamical variable. For a flow $\phi_{\mathbf{X}}$ generated by the field $\mathbf{X} = (X_1, \dots, X_N)$ (Hamiltonian or not), one can introduce:

$$\begin{aligned} (\phi_{\mathbf{X}} f) &:= (f \circ \phi_{\mathbf{X}}) : \mathcal{F} \times \mathcal{I} \rightarrow \mathbb{R} \\ (\phi_{\mathbf{X}} f) &: (\mathbf{x}, t) \mapsto f(\phi_{\mathbf{X}}^t(\mathbf{x})), \end{aligned} \quad (2.13)$$

that is the *evolution of f under the flow $\phi_{\mathbf{X}}$* . We are again interested in how $\phi_{\mathbf{X}} f$ evolves with time. The change \dot{f} of this function is given by the *Lie derivative* operator $L_{\mathbf{X}}$ applied to f , which is a new function on \mathcal{F} :

$$L_{\mathbf{X}} f \equiv \left. \frac{d}{dt} (\phi_{\mathbf{X}} f) \right|_{t=0} : \mathcal{F} \rightarrow \mathbb{R}, \quad (2.14)$$

and in coordinates takes the form

$$L_{\mathbf{X}} f(\mathbf{x}) = \sum_{i=1}^N \frac{\partial f}{\partial x_i}(\mathbf{x}) X_i(\mathbf{x}). \quad (2.15)$$

This follows from the fact that $\dot{\mathbf{x}} = \mathbf{X}$ and the chain rule, so that

$$\frac{d(\phi_{\mathbf{X}} f)}{dt} := \frac{d}{dt} (f \circ \phi_{\mathbf{X}}) = \sum_{i=1}^N \frac{\partial f}{\partial x_i}(\phi_{\mathbf{X}}) \dot{x}_i \equiv \sum_{i=1}^N \frac{\partial f}{\partial x_i}(\phi_{\mathbf{X}}) X_i(\phi_{\mathbf{X}}) \equiv \left(\sum_{i=1}^N \frac{\partial f}{\partial x_i} X_i \right) \circ \phi_{\mathbf{X}}, \quad (2.16)$$

and the fact that $\phi_{\mathbf{X}}^0$ is the identity over \mathcal{F} . Notice that $L_{\mathbf{X}}$ is a linear operator, and that $\frac{d(\phi_{\mathbf{X}}f)}{dt}$ is given by $L_{\mathbf{X}}f$ (again, a new dynamical variable) composed with $\phi_{\mathbf{X}}$. Taking now higher order derivatives with respect to t , one clearly sees that $\frac{d^2}{dt^2}(\phi_{\mathbf{X}}f) = \frac{d}{dt}\left(\frac{d}{dt}(\phi_{\mathbf{X}}f)\right)$ will itself be a dynamical variable (which we can call $L_{\mathbf{X}}^2f$) composed with $\phi_{\mathbf{X}}$, etc. We get a recursive definition for the powers of the Lie derivatives:

$$L_{\mathbf{X}}^0f := f, L_{\mathbf{X}}^1f := L_{\mathbf{X}}f = \left.\frac{d}{dt}(\phi_{\mathbf{X}}f)\right|_{t=0}, L_{\mathbf{X}}^i f := L_{\mathbf{X}}(L_{\mathbf{X}}^{i-1}f); \quad (2.17)$$

this way one gets the following Taylor series for $\phi_{\mathbf{X}}f(\mathbf{x}, t)$ with respect to t around $t = 0$:

$$\phi_{\mathbf{X}}f(\mathbf{x}, t) = \sum_{i=0}^{\infty} \frac{t^i}{i!} (L_{\mathbf{X}}^i f)(\mathbf{x}). \quad (2.18)$$

This gives the evolution of f under the flow $\phi_{\mathbf{X}}$, and is called the *Lie series* of f under the flow. The Lie series operator is then

$$\exp(tL_{\mathbf{X}}) := \sum_{i=0}^{\infty} \frac{t^i}{i!} L_{\mathbf{X}}^i. \quad (2.19)$$

The Lie derivatives emerge in a similar manner in the Hamiltonian setting, where $N = 2n$ and for two dynamical variables f, g one defines the *Poisson bracket*

$$\begin{aligned} \{f, g\} &= (\nabla f)^\top J (\nabla g) = \sum_{i,j=1}^n J_{i,j} \frac{\partial f}{\partial x_i} \frac{\partial g}{\partial x_j} \\ &= \frac{\partial f}{\partial \mathbf{q}} \cdot \frac{\partial g}{\partial \mathbf{p}} - \frac{\partial f}{\partial \mathbf{p}} \cdot \frac{\partial g}{\partial \mathbf{q}}. \end{aligned} \quad (2.20)$$

Indeed, given a Hamiltonian \mathcal{H} , with corresponding Hamiltonian field $\mathbf{X}_{\mathcal{H}}$ and flow $\phi_{\mathbf{X}_{\mathcal{H}}} = \phi_{\mathcal{H}}$, since $J\nabla\mathcal{H} = \mathbf{X}_{\mathcal{H}} = \dot{\mathbf{x}}$ one has $\{f, \mathcal{H}\} = \nabla f \cdot \mathbf{X}_{\mathcal{H}}$, and we can immediately write the Lie derivative $L_{\mathbf{X}_{\mathcal{H}}} =: L_{\mathcal{H}}$ in the form

$$\{f, \mathcal{H}\} \equiv L_{\mathcal{H}}f = \left.\frac{d}{dt}(\phi_{\mathcal{H}}f)\right|_{t=0} : \mathcal{F} \rightarrow \mathbb{R}; \quad (2.21)$$

the Lie series $\exp(tL_{\mathcal{H}})f$ of f then also rewrites

$$\exp(tL_{\mathcal{H}})f = f + t\{f, \mathcal{H}\} + \frac{t^2}{2}\{\{f, \mathcal{H}\}, \mathcal{H}\} + \dots \quad (2.22)$$

The Poisson bracket operator $\{\bullet, \bullet\}$ has many interesting algebraic properties given in most textbooks. For example, it is linear: $\{\alpha f, \beta g\} = \alpha\beta\{f, g\}$ for $\alpha, \beta \in \mathbb{R}$ and $\{f_1 + f_2, g\} = \{f_1, g\} + \{f_2, g\}$, and it is antisymmetric: $\{f, g\} = -\{g, f\}$, so that $\{f, f\} = 0$.

The evolution of any dynamical variable f under the Hamiltonian flow $\phi_{\mathcal{H}}$ is given by the Poisson bracket of f against \mathcal{H} :

$$\dot{f} = \{f, \mathcal{H}\}; \quad (2.23)$$

the condition that f be a first integral for the dynamics of \mathcal{H} is that $\{f, \mathcal{H}\} = 0$. Considering the canonical coordinates \mathbf{x} themselves as dynamical variables, one gets the so-called *fundamental Poisson brackets*

$$\{x_i, x_j\} = J_{i,j}, \quad (2.24)$$

that is,

$$\{p_i, p_j\} = 0, \quad \{q_i, q_j\} = 0, \quad \{p_i, q_j\} = -\delta_{i,j}, \quad (2.25)$$

where $\delta_{i,j}$ is the Kronecker delta, $\delta_{i,j} = 1$ if $i = j$ and $\delta_{i,j} = 0$ otherwise. Then, the Poisson brackets are at the very core of Hamiltonian dynamics: one immediately realises that Hamilton's equations can be rewritten as

$$\begin{cases} \dot{\mathbf{p}} = \{\mathbf{p}, \mathcal{H}\}, \\ \dot{\mathbf{q}} = \{\mathbf{q}, \mathcal{H}\}, \end{cases} \quad \text{i.e. } \dot{\mathbf{x}} = \{\mathbf{x}, \mathcal{H}\}. \quad (2.26)$$

We finally remark that for $f = f(\mathbf{x}, t)$, $\dot{f} = \{f, \mathcal{H}\} + \frac{\partial f}{\partial t}$.

2.1.3 Canonical transformations

2.1.3.1 Definition and Criteria

We look for transformations $\mathbf{x} = \mathbf{x}(\mathbf{x}')$, that is $\{\mathbf{p} = \mathbf{p}(\mathbf{p}', \mathbf{q}'), \mathbf{q} = \mathbf{q}(\mathbf{p}', \mathbf{q}')\}$, from the old variables $\mathbf{x} = (\mathbf{p}, \mathbf{q})$ to new variables $\mathbf{x}'(\mathbf{p}', \mathbf{q}')$ which preserve the Hamiltonian structure in the following strict sense: For any Hamiltonian $\mathcal{H}(\mathbf{p}, \mathbf{q})$, its Hamilton equations are equivalent to the Hamilton's equations for $\mathcal{H}'(\mathbf{p}', \mathbf{q}') := \mathcal{H}(\mathbf{p} = \mathbf{p}(\mathbf{p}', \mathbf{q}'), \mathbf{q} = \mathbf{q}(\mathbf{p}', \mathbf{q}'))$. Such a transformation is said to be *canonical*. There are many useful criteria for canonicity. Here we recall only a few.

The first one comes straight from the definition: denoting with $D = \frac{\partial \mathbf{x}}{\partial \mathbf{x}'}$ the Jacobian of the transformation, using Hamilton's equations a necessary (but *a posteriori* also sufficient) condition is that

$$D^\top J D = J, \text{ i.e. } D^{-1} J (D^{-1})^\top = J; \quad (2.27)$$

that is, that the Jacobian D is a symplectic matrix. Using (2.20) this is rewritten in terms of the Poisson brackets as

$$\{x'_i(x), x'_j(x)\} = J_{i,j}, \quad (2.28)$$

and since in the original variables $\{x_i, x_j\} = J_{i,j}$ as well, a necessary and sufficient criterion for canonicity can be stated as the fact that the transformation preserves the fundamental Poisson brackets. The conservation of the (fundamental) Poisson brackets is probably the most useful criterion of canonicity as it can easily be implemented (moreover, it can be proven that a transformation conserves the fundamental Poisson brackets if and only if it conserves the Poisson bracket between any two dynamical variables).

Another useful sufficient (but not necessary) criterion that is used in the literature makes use of a *generating function* $S(\mathbf{p}', \mathbf{q})$. One can show that the transformation given implicitly by

$$\begin{cases} \mathbf{p} = \frac{\partial S}{\partial \mathbf{q}}(\mathbf{p}', \mathbf{q}) \\ \mathbf{q}' = \frac{\partial S}{\partial \mathbf{p}'}(\mathbf{p}', \mathbf{q}) \end{cases} \quad (2.29)$$

is canonical.

A final, extremely useful sufficient (but not necessary) criterion makes use of a *generating Hamiltonian* χ and its flow ϕ_χ^t . One can show that the Hamiltonian flow induces a family of canonical transformations parametrised by the time t , which we can also write as a Lie series

$$\mathbf{x} = \exp(tL_\chi)\mathbf{x}' = \mathbf{x}' + tL_\chi\mathbf{x}' + \dots \quad (2.30)$$

This class of transformations is very useful in perturbation theory, and they are also so-called *close-to-the-identity transformation*, see the next subsection.

2.1.3.2 Examples of canonical transformations

The set of all canonical transformation is only a subgroup of all possible transformations. There are nonetheless some non-trivial canonical transformations that are very useful and will be used later on. Here we only mention a few.

Extended (linear) point transformations. A given (invertible) transformation on the coordinates $\mathbf{q} = \mathbf{q}(\mathbf{q}')$ (a so-called *point transformation* of the type used in the Lagrangian formalism) can be canonically extended using the generating function $S(\mathbf{p}', \mathbf{q}) = \sum_i p'_i q'_i|_{\mathbf{q}'=\mathbf{q}(\mathbf{q})}$. If the transformation on the coordinates is linear, $\mathbf{q} = A\mathbf{q}'$ where A is a matrix, then the corresponding transformation on the momenta can be easily found: it is also linear, with matrix the transpose of the inverse of A , $\mathbf{p} = (A^{-1})^\top \mathbf{p}'$.

Canonical polar coordinates. Given a pair of Cartesian canonical variables $(p, q) \in \mathbb{R}^2$, one can introduce the new canonical variables (Σ, σ) via the transformation

$$(p = \sqrt{2\Sigma} \cos \sigma, q = \sqrt{2\Sigma} \sin \sigma), \text{ i.e. } \left(\Sigma = \frac{p^2 + q^2}{2}, \sigma = \text{atan2}(p, q) \right); \quad (2.31)$$

the canonicity is easily checked with the Poisson bracket criterion, which also shows that $\Sigma \in \mathbb{R}^+$ is the momentum and $\sigma \in \mathbb{T}$ the position.

Close-to-the-identity transformations. The generating function $S(\mathbf{p}', \mathbf{q}) = \mathbf{p}' \cdot \mathbf{q}$ generates the identity transformation. Using then a generating function $S_\epsilon(\mathbf{p}', \mathbf{q}) = \mathbf{p}' \cdot \mathbf{q} + \epsilon \tilde{S}(\mathbf{p}', \mathbf{q})$, we get the canonical transformation

$$\begin{cases} \mathbf{p} = \mathbf{p}' + \epsilon \frac{\partial \tilde{S}}{\partial \mathbf{q}}(\mathbf{p}', \mathbf{q}) \\ \mathbf{q}' = \mathbf{q} + \epsilon \frac{\partial \tilde{S}}{\partial \mathbf{p}'}(\mathbf{p}', \mathbf{q}), \end{cases} \quad (2.32)$$

which can be inverted as

$$\begin{cases} \mathbf{p} = \mathbf{p}' + \epsilon \frac{\partial \tilde{S}}{\partial \mathbf{q}'}(\mathbf{p}', \mathbf{q}') + \mathcal{O}(\epsilon^2) \\ \mathbf{q} = \mathbf{q}' - \epsilon \frac{\partial \tilde{S}}{\partial \mathbf{p}'}(\mathbf{p}', \mathbf{q}') + \mathcal{O}(\epsilon^2), \end{cases} \quad (2.33)$$

This type of transformations is called a close-to-the-identity transformation and are very useful in perturbation theory. We note that the canonical flow is a close-to-the-identity transformation.

Scaling transformations. We finally mention a set of transformations that are not canonical in the strict sense, but are very useful and will be used in the thesis. These are the scaling transformations

$$p_i = \alpha_i p'_i, \quad q_i = \beta_i q'_i, \quad \text{with } \alpha_i \beta_i \equiv \gamma. \quad (2.34)$$

Hamilton's equations are only conserved transforming the Hamiltonian as

$$\mathcal{H}'(\mathbf{p}', \mathbf{q}') = \frac{1}{\gamma} \mathcal{H}(\mathbf{p}(\mathbf{p}'), \mathbf{q}(\mathbf{q}')), \quad (2.35)$$

that is, also the Hamiltonian must be rescaled. The transformation is strictly canonical iff $\gamma = 1$. An application of this scheme is sometimes used to rescale e.g. the momenta by the mass m in a mechanical system. This shows that the Hamiltonian does not necessarily have to be the mechanical energy of the system.

Finally, it is sometimes useful to rescale the time t itself. Defining a new time by $t = \gamma t'$, the new Hamiltonian is $\mathcal{H}'(\mathbf{p}, \mathbf{q}) = \frac{1}{\gamma} \mathcal{H}(\mathbf{p}, \mathbf{q})$.

2.1.4 Integrable dynamics and action-angle variables

2.1.4.1 Liouville-Arnold-Jost Theorem

Among all dynamical systems, *integrable systems* (systems whose equations can be solved by solving definite integrals and inverse of functions) occupy a special place. Of course, most systems are not integrable, but most of the interesting ones, for example the planetary problem, are literally an ϵ away from integrability, where ϵ is a small parameter.

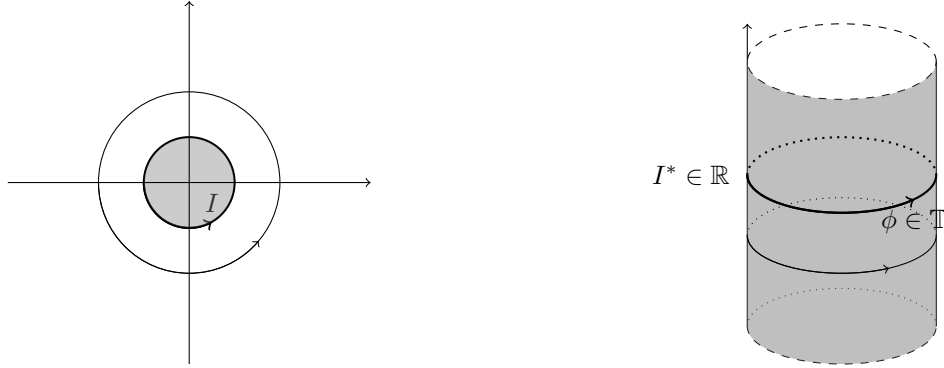
Concerning integrable systems, the first important result is that of Liouville, later improved by Arnold and Jost. One starts by defining an *involution system* as a set $\{\Phi_i\}_i$ of dynamical variables such that $\{\Phi_i, \Phi_j\} = 0$. Moreover, we recall that if we have a set $\{\Phi_i\}_i$ of first integrals for a Hamiltonian \mathcal{H} , $\{\Phi_i, \mathcal{H}\} = 0$ so that $\Phi_i(t) = \Phi_{i,0} = \text{const}$, then the Hamiltonian flow is confined to the sub-manifold $\mathcal{F}_\Phi = \bigcap_i \Phi_i^{-1}(\Phi_{i,0})$. Then one can prove the following

Theorem (Liouville-Arnold-Jost). Assume that a Hamiltonian system $\mathcal{H}(\mathbf{p}, \mathbf{q})$ with n d.o.f.'s admits n independent³ first integrals $\{\Phi_i\}_{i=1, \dots, n}$ in involution. Then:

1. The system is integrable by quadratures; more precisely, one can construct a generating function $S(\Phi, \mathbf{q})$ which generates a canonical transformation for which the new momenta are Φ and the transformed Hamiltonian only depends on Φ [Liouville(1855)].
2. Defining the invariant sub-manifold $\mathcal{F}_\Phi = \bigcap_{i=1}^n \Phi_i^{-1}(\Phi_{i,0})$, if \mathcal{F}_Φ is compact, then there exist canonical variables $(\mathbf{I}, \varphi) \in \mathbb{R}^n \times \mathbb{T}^n$ in a neighbourhood of \mathcal{F}_Φ such that the Hamiltonian \mathcal{H} depends only on the momenta, $\mathcal{H} = \mathcal{H}(\mathbf{I})$ [Arnold(1963), Jost(1968)].

In the conditions of the Liouville Theorem, one immediately realises from Hamilton's equations that the momenta are constant while the positions evolve linearly with time. The extension to Liouville's original statement that was

³Two dynamical variables are independent in a point if their gradients on that point are linearly independent. This is a local definition, but the variables themselves are defined locally.



(a) 1 d.o.f. system, $\mathcal{F} = \mathbb{R}^2$. The area enclosed by the energy contours (here depicted by circles for simplicity) defines the action I .

(b) In action-angle coordinates $(I, \phi) \in \mathbb{R} \times \mathbb{T}$, the action is constant, $I(t) = I^*$, and the angle moves with constant frequency.

Figure 2.1: Geometrical depiction of the construction of action-angle variables for a 1 d.o.f. system.

pointed out by Arnold and Jost is that if the invariant sub-manifold is compact, then it is diffeomorphic to a torus \mathbb{T}^n and one can construct the new momenta so that their conjugated positions are *angles*. The variables $(\mathbf{I}, \boldsymbol{\varphi})$ are then called *action-angle* variables for \mathcal{H} .

The action-angle variables carry an important geometrical property, which will be useful in Subsect. 2.3.2. The fact that $\{\Phi_i, \Phi_j\} = 0$ implies that the motion can be decomposed in the n independent Hamiltonian flows ϕ_{Φ_i} , $i = 1, \dots, n$, so that $\phi_{\mathcal{H}}^t = \phi_{\Phi_1}^t \circ \dots \circ \phi_{\Phi_n}^t$. The fact that \mathcal{F}_{Φ} is compact implies that the flows ϕ_{Φ_i} , and hence $\phi_{\mathcal{H}}$ can be decomposed in n independent periodic cycles, which we denote by γ_i , $i = 1, \dots, n$. Then, one can introduce the actions as

$$I_i = \frac{1}{2\pi} \oint_{\gamma_i} \mathbf{p} \cdot d\mathbf{q}. \quad (2.36)$$

Inverting the previous expression for \mathbf{p} to obtain $\mathbf{p} = \mathbf{p}(\mathbf{I}, \mathbf{q})$, one can define the generating function $S(\mathbf{I}, \mathbf{q}) = \int \mathbf{p}(\mathbf{I}, \mathbf{q}) \cdot d\mathbf{q}$. Finally (cfr. (2.29)), the angles are defined by

$$\phi_i = \frac{\partial S}{\partial I_i}(\mathbf{I}, \mathbf{q}); \quad (2.37)$$

one can prove that these are indeed angles, that is, they increase by 2π after a complete motion on the cycle γ_i [Arnold(1963)]. In the 1 d.o.f. case, one immediately recognises I as the area (rescaled by 2π) enclosed by the orbit, see Figure 2.1. This will be important in Subsect. 2.3.2.

2.1.4.2 Resonant and nonresonant motion

As we noticed above, under the conditions of the Liouville-Arnold-Jost Theorem the phase space \mathcal{F} is foliated by invariant tori $\mathcal{F}_{\mathbf{I}}$ parametrised by the actions \mathbf{I} , because the evolution of each initial datum is confined to a n dimensional torus \mathbb{T}^n . Writing explicitly the equations of motion and their solution,

$$\begin{cases} \dot{\mathbf{I}} = 0, \\ \dot{\boldsymbol{\varphi}} = \frac{\partial \mathcal{H}}{\partial \mathbf{I}}(\mathbf{I}), \end{cases} \Rightarrow \begin{cases} \mathbf{I}(t) = \mathbf{I}(0) = \mathbf{I}_0 = \text{const}, \\ \boldsymbol{\varphi}(t) = \frac{\partial \mathcal{H}}{\partial \mathbf{I}}(\mathbf{I}_0)t + \boldsymbol{\varphi}_0 =: \boldsymbol{\omega}(\mathbf{I}_0)t + \boldsymbol{\varphi}_0, \end{cases} \quad (2.38)$$

we see that the nature of the evolution on each torus depends on the frequencies

$$\boldsymbol{\omega}(\mathbf{I}) = \frac{\partial \mathcal{H}}{\partial \mathbf{I}}(\mathbf{I}). \quad (2.39)$$

In this context, one defines the *resonance condition*

$$\boldsymbol{\omega} \cdot \mathbf{k} = 0, \quad \mathbf{k} \in \mathbb{Z}^n : \quad (2.40)$$

we may say that, when it is satisfied, $\boldsymbol{\omega}$ is *\mathbf{k} -resonant*, or that \mathbf{k} is a *resonant n -tuple* for $\boldsymbol{\omega}$. There are three possibilities [Morbidegli(2002)]:

1. If $\nexists \mathbf{k} \in \mathbb{Z}^n \setminus \mathbf{0}$ which satisfies the resonance condition (2.40), the frequencies $\boldsymbol{\omega}$ are said to be *nonresonant*; the motion then densely covers the torus and is called *quasi-periodic*.
2. If $\exists \mathbf{k}^1, \dots, \mathbf{k}^{n-1} \in \mathbb{Z}^n \setminus \mathbf{0}$, $n - 1$ linearly independent, nonzero integer vectors which satisfy the resonance condition (2.40), the frequencies $\boldsymbol{\omega}$ are said to be *completely resonant*; one can express $n - 1$ angles as periodic functions of a unique angle and the motion on the torus is periodic.
3. If $\exists \mathbf{k}^1, \dots, \mathbf{k}^m \in \mathbb{Z}^n \setminus \mathbf{0}$, m linearly independent, non-zero integer vectors with $m < n - 1$ which satisfy the resonance condition (2.40), the frequencies $\boldsymbol{\omega}$ are said to be *resonant* (with *multiplicity* m); one can express m angles, say ϕ_1, \dots, ϕ_m , as periodic functions of the remaining $n - m$ angles $\phi_{m+1}, \dots, \phi_n$, and the projection of the motion on the $(n - m)$ -dimensional torus defined by $\phi_{m+1}, \dots, \phi_n$ is dense, while its projection on the m -dimensional torus defined by ϕ_1, \dots, ϕ_m is periodic.

The quantity⁴

$$\min_{1 \leq j \leq m} |\mathbf{k}^j|, \quad |\mathbf{k}^j| = |k_1^j| + \dots + |k_n^j|, \quad (2.41)$$

is called the *order of the resonance*⁵.

In most cases, Hamiltonian systems are however not integrable. Even when

$$\mathcal{H}(\mathbf{p}, \mathbf{q}, \epsilon) = \mathcal{H}_0(\mathbf{p}) + \epsilon \mathcal{H}_1(\mathbf{p}, \mathbf{q}), \quad \epsilon \ll 1, \quad (2.42)$$

which represents the most minute displacement from an integrable Hamiltonian $\mathcal{H}_0(\mathbf{p})$, if the perturbation is general enough the non integrability theorem of Poincaré ([Poincaré(1892)], Vol. I, chapter V) states that there exists no analytic first integral independent of \mathcal{H} . Thus, in order to extract interesting information on the dynamics even when a complete solution is beyond our grasp, one needs tools such as those offered by perturbation theory or the search for equilibrium points and the investigation of their stability, that we describe below.

2.1.5 Equilibrium points and linear stability

We recall that an *equilibrium point* of a dynamical system $\dot{\mathbf{x}} = \mathbf{X}(\mathbf{x})$ is a point \mathbf{x}_{eq} such that $\mathbf{X}(\mathbf{x}_{\text{eq}}) = \mathbf{0}$, so that the solutions with initial datum \mathbf{x}_{eq} are simply $\mathbf{x}(t) \equiv \mathbf{x}_{\text{eq}}$. From (2.4) and the fact that the symplectic matrix J is invertible we see that for a Hamiltonian system the equilibrium points are exactly the stationary points of the Hamiltonian: $\nabla \mathcal{H}(\mathbf{x}_{\text{eq}}) = \mathbf{0}$. As one does in dynamical systems, it is interesting to study the nature of the stability of an equilibrium point \mathbf{x}_{eq} , starting with the linear stability. To obtain the linearised system around \mathbf{x}_{eq} we introduce $\delta \mathbf{x}_{\text{eq}} = \mathbf{x} - \mathbf{x}_{\text{eq}}$ and we expand the Hamiltonian in Taylor series as

$$\mathcal{H} = \mathcal{H}(\mathbf{x}_{\text{eq}}) + \nabla \mathcal{H}(\mathbf{x}_{\text{eq}}) \cdot \delta \mathbf{x}_{\text{eq}} + \frac{1}{2} \delta \mathbf{x}_{\text{eq}}^\top \cdot \mathbb{H}(\mathcal{H}(\mathbf{x}_{\text{eq}})) \cdot \delta \mathbf{x}_{\text{eq}} + \mathcal{O}(\delta \mathbf{x}_{\text{eq}}^3), \quad (2.43)$$

where $\mathbb{H}(\mathcal{H}(\mathbf{x}_{\text{eq}})) =: C$ is the Hessian of \mathcal{H} with respect to the variables \mathbf{x} evaluated at \mathbf{x}_{eq} , and is a real symmetric matrix. Notice that $\nabla \mathcal{H}(\mathbf{x}_{\text{eq}}) \cdot \delta \mathbf{x}_{\text{eq}} = 0$ by definition of equilibrium point. Then the linearised Hamilton's equations read

$$\dot{\delta \mathbf{x}} = A \delta \mathbf{x}, \quad A = JC, \quad (2.44)$$

and appear as the typical linearised equations studied in dynamical systems. I follow below the arguments found in prof. A. Giorgilli's notes available online (http://www.mat.unimi.it/users/antonio/meccel/Meccel_A.pdf, see also [Wintner(1934), Williamson(1936)]).

The character of the linear stability of the equilibrium point are dictated by the eigenvalues of the matrix $A = JC$. One can prove the following properties

1. if λ is an eigenvalue of JC , its complex conjugate λ^* is also eigenvalue of JC ;
2. if λ is an eigenvalue of JC , $-\lambda$ is also eigenvalue of JC .

⁴We use the notation $|\mathbf{k}| := |k_1| + \dots + |k_n|$ for $\mathbf{k} \in \mathbb{Z}^n$.

⁵In Celestial Mechanics, the terminology "order of the resonance" has a different meaning, due to the specific case of d'Alembert rules of the series expansions of the perturbing Hamiltonian in powers of the eccentricity, as will be explained later.

The first property is general for any real matrix A since the characteristic polynomial has real coefficients. Moreover, it is well known that if λ is a complex eigenvalue with⁶ $\mathbf{w} = \Re\mathbf{w} + i\Im\mathbf{w}$ its eigenvector, then $\mathbf{w}^* = \Re\mathbf{w} - i\Im\mathbf{w}$ is an eigenvector corresponding to λ^* and the real vectors $\Re\mathbf{w}$, $\Im\mathbf{w}$ are linearly independent. The second property follows from the symplectic structure itself: $J^\top = J^{-1} = -J$, C is symmetric and $\det J = 1$ so

$$\begin{aligned}(JC - \lambda\mathbb{I})^\top &= ((JC)^\top - \lambda\mathbb{I}) = -(CJ + \lambda\mathbb{I}) = -JJ^{-1}(CJ + \lambda\mathbb{I}) \\ &= J(JCJ + \lambda\mathbb{I}J) = J(JC + \lambda\mathbb{I})J \Rightarrow \det(JC - \lambda\mathbb{I}) = \det(JC + \lambda\mathbb{I}).\end{aligned}$$

These two properties say that the eigenvalues of JC come always in pairs (purely real or imaginary eigenvalues) or in fours, and if there is any eigenvalue with non-vanishing real part there must be one with positive real part. This implies that in a Hamiltonian system the only stable points are *centres* (all purely imaginary eigenvalues $\pm i\omega$). Unstable points can be either *saddle points* (real eigenvalues $\pm\mu$) or a combination of a *stable sink* with an *unstable sink* (corresponding to a quadruple of eigenvalues with non vanishing real and imaginary part $\pm\mu \pm i\omega$).

2.1.5.1 Canonical diagonalisation around the equilibrium point

Let us assume without loss of generality that $\mathbf{x} = \mathbf{0}$ is an equilibrium point, and consider the linearised equations $\dot{\mathbf{x}} = JC\mathbf{x}$. Typically in the study of dynamical systems one wants to diagonalise the linear equations to disentangle the degrees of freedom and put the system in so-called normal form around the equilibrium point. We know that the real matrix JC can be diagonalised – that is, transformed under a linear transformation M into $M^{-1}(JC)M = \Lambda$ where $\Lambda = \text{diag}(\lambda_i)$ has the eigenvalues on the diagonal and zero everywhere else – if the eigenvalues have multiplicity 1. This is because if the eigenvalues are all distinct, the corresponding eigenvectors are linearly independent and the diagonalising matrix M can be constructed by placing the eigenvectors thought as column vectors one next to the other. Therefore, for simplicity we will assume that JC has distinct eigenvalues. In the case of Hamiltonian systems, we also must require that the linear transformation M be canonical, and we show below that this can be the case. Moreover, it is convenient to retain a real normal form even in the case of complex eigenvalues; this is because in the case of a centre this procedure yields a normal form that is equivalent to the simple model of uncoupled harmonic oscillators (see Subsect. 2.1.6.1). To this end, it is useful to recall that if $\lambda = \mu + i\omega$ is a complex eigenvalue with corresponding eigenvector $\mathbf{w} = \Re\mathbf{w} + i\Im\mathbf{w}$ (so that λ^* is also an eigenvalue with corresponding eigenvector $\mathbf{w}^* = \Re\mathbf{w} - i\Im\mathbf{w}$), one can choose to use the real, linearly independent vectors $\Re\mathbf{w}$, $\Im\mathbf{w}$ to construct the diagonalising matrix M . For example, in the simple case of a 2×2 real matrix with complex eigenvalues $\mu \pm i\omega$, placing the real and imaginary parts of the relative eigenvector one next to the other to construct $M = (\Re\mathbf{w} | \Im\mathbf{w})$ yields

$$M^{-1}(JC)M = \begin{pmatrix} \mu & \omega \\ -\omega & \mu \end{pmatrix}. \quad (2.45)$$

Let us now go through the procedure to diagonalise around the equilibrium point $\mathbf{x} = \mathbf{0}$ the linearised Hamiltonian equations $\dot{\mathbf{x}} = JC\mathbf{x}$, where as usual C the Hessian of the Hamiltonian evaluated at the equilibrium point. I consider here the cases of saddle points and centres (purely real or purely imaginary eigenvalues), which are the most interesting ones. We consider the matrix JC , its $2n$ eigenvalues which we assume all have multiplicity 1, and the corresponding eigenvectors \mathbf{w}_i . We can organise them as

$$\begin{array}{cccccccc} \lambda_1, & \dots, & \lambda_n, & -\lambda_1, & \dots, & -\lambda_n, & & \\ \mathbf{w}_1, & \dots, & \mathbf{w}_n, & \mathbf{w}_{n+1}, & \dots, & \mathbf{w}_{2n} & & \end{array} \quad (2.46)$$

since we saw that eigenvalues always come in pairs $(\lambda, -\lambda)$. We assume that the first $m < n$ pairs $(\lambda_i, -\lambda_i)_{i=1, \dots, m}$ are real eigenvalues (so the corresponding eigenvectors can be chosen to be real as well) and the remaining $n - m$ pairs $(\lambda_i, -\lambda_i)_{i=m+1, \dots, n}$ are purely imaginary. We start by noticing that for two distinct eigenvalues λ, λ' with corresponding eigenvectors \mathbf{w}, \mathbf{w}' , one has⁷

$$\mathbf{w}^\top J\mathbf{w}' = 0 \iff \lambda' \neq -\lambda. \quad (2.47)$$

Then, when $\lambda_i, i = 1, \dots, m$ is real we calculate $d_i = \mathbf{w}_i^\top J\mathbf{w}_{i+n} \neq 0$ which we can assume is positive (otherwise we exchange λ_i with $\lambda_{i+n} = -\lambda_i$). Instead, when $\lambda_i = i\omega_i, i = m + 1, \dots, n$ is purely imaginary, we calculate

⁶We indicate with $\Re z$ and $\Im z$ the real and imaginary part of the complex number z .

⁷To see this, a simple calculation shows that $(\lambda + \lambda')\mathbf{w}^\top J\mathbf{w}' = 0$. Now recall that all n eigenvalues are distinct, so for a fixed λ there is only another one which is equal to $-\lambda$. Therefore: (\Leftarrow) in all the other cases where $\lambda + \lambda' \neq 0$ we must have $\mathbf{w}^\top J\mathbf{w}' = 0$; and (\Rightarrow) in the single case where $\lambda + \lambda' = 0$, if it were still $\mathbf{w}^\top J\mathbf{w}' = 0$ then by the invertibility of J this would mean that \mathbf{w} must be zero, which is against the assumption that \mathbf{w} is an eigenvector for λ .

$0 \neq \mathbf{w}_i^\top J \mathbf{w}_{i+n} = \mathbf{w}_i^\top J \mathbf{w}_i^* = -2i \Re \mathbf{w}_i^\top J \Im \mathbf{w}_i$ and we put $d_i = \Re \mathbf{w}_i^\top J \Im \mathbf{w}_i \neq 0$, which is real and again we can assume is positive. We then introduce the (real) matrix made of the $2n$ column vectors

$$M = \left(\begin{array}{c|c|c|c|c|c|c|c|c|c} \frac{\mathbf{w}_{1+n}}{\sqrt{d_1}} & \dots & \frac{\mathbf{w}_{m+n}}{\sqrt{d_m}} & \frac{\Im \mathbf{w}_{m+1+n}}{\sqrt{d_{m+1}}} & \dots & \frac{\Im \mathbf{w}_{2n}}{\sqrt{d_n}} & \frac{\mathbf{w}_1}{\sqrt{d_1}} & \dots & \frac{\mathbf{w}_m}{\sqrt{d_m}} & \frac{\Re \mathbf{w}_{m+1}}{\sqrt{d_{m+1}}} & \dots & \frac{\Re \mathbf{w}_n}{\sqrt{d_n}} \end{array} \right) : \quad (2.48)$$

this follows the standard procedure of constructing the diagonalising matrix M by placing the eigenvectors next to one another, only we rescaled them by the factors $\sqrt{d_i}$ and ordered them to transform momenta and positions in order. One can see that because of these choices we have $M^\top J M = J$ so the matrix generates a canonical transformation $\mathbf{x} = M \mathbf{x}'$. This effectively diagonalises the system, as we describe below.

To see how the system is diagonalised, let us simplify matters and assume for simplicity that the system has one degree of freedom and the two eigenvalues $\lambda, \lambda' = -\lambda$ are real (saddle equilibrium point). Then the matrix M is simply constructed placing two eigenvectors \mathbf{w}, \mathbf{w}' next to the other and rescaling them by $\sqrt{d} = \sqrt{\mathbf{w}^\top J \mathbf{w}'}$ to ensure canonicity. Then, the matrix JC is transformed by M as $M^{-1}(JC)M = \text{diag}(-\lambda, \lambda)$ with the two eigenvalues on the diagonal, and the resulting Hamiltonian is simply $\mathcal{H}(p', q') = \lambda p' q'$. We note that although we had both eigenvalues $\pm\lambda$ with an apparent arbitrary choice for the sign, there is a specific sign of the λ that appears in the previous Hamiltonian, which is dictated by the choice that $d = \mathbf{w}^\top J \mathbf{w}'$ be a positive number. Instead, let us consider the case of a centre, again in the case of a one degree of freedom system for simplicity. In this case we have two purely imaginary eigenvalues $\lambda = i\omega, \lambda' = -\lambda = \lambda^* = -i\omega$, and the matrix M is such that

$$M^{-1}(JC)M = \begin{pmatrix} 0 & -\omega \\ \omega & 0 \end{pmatrix}, \quad (2.49)$$

so the resulting Hamiltonian takes the form $\mathcal{H}(p', q') = \frac{\omega}{2}(p'^2 + q'^2)$. This is indeed the well-known Hamiltonian of the harmonic oscillator (cfr. Equation (2.52)). Again, we note that although we had both eigenvalues $\pm\lambda = \pm i\omega$ with an apparent arbitrary choice for the sign of λ , there is a definite sign of the ω that appears in the previous Hamiltonian, which is dictated by the choice that $d = \Re \mathbf{w}^\top J \Im \mathbf{w}$ be a positive number. With this, we see that for a system with n d.o.f.'s, once the degrees of freedom have been split into independent saddles and centres using the matrix M , the resulting Hamiltonian will be a sum of independent ‘‘diagonalised’’ Hamiltonians of the forms $\mathcal{H}(p', q') = \lambda p' q', \mathcal{H}(p', q') = \frac{\omega}{2}(p'^2 + q'^2)$ obtained above.

We finally note that while a saddle equilibrium point is a saddle point as a stationary point of \mathcal{H} , the converse is not true: indeed, if

$$\mathcal{H}_0 = \frac{\omega_1}{2}(p_1^2 + q_1^2) + \frac{\omega_2}{2}(p_2^2 + q_2^2)$$

then the origin $\mathbf{x}_{\text{eq}} = \mathbf{0}$ is always a centre equilibrium point (JC has four purely imaginary eigenvalues $\pm i\omega_{1,2}$), but depending on the relative signs of ω_1 and ω_2 , \mathcal{H}_0 may have in $\mathbf{0}$ a maximum, a minimum (i.e. an extremum, when $\omega_1 \cdot \omega_2 > 0$, i.e. they have the same sign) or a saddle point (when $\omega_1 \cdot \omega_2 < 0$).

2.1.6 Basic examples of Hamiltonian systems

In this section I recall the elementary dynamics of the harmonic oscillator and of the pendulum, as they serve as a good introduction to the dynamical concepts and typical evolutions that are encountered in this thesis. I also include the Andoyer Hamiltonians which are useful in the study of resonances as they represent integrable approximations to resonant dynamics.

2.1.6.1 The harmonic oscillator

The kinetic and potential energies of the harmonic oscillator are $T(\dot{x}) = \frac{1}{2}m\dot{x}^2$ and $V(x) = \frac{1}{2}kx^2$, with x the cartesian coordinate. The canonical variables of the harmonic oscillator are then the position x and the conjugated momentum $y = m\dot{x}$, the physical linear momentum, so the phase space is \mathbb{R}^2 . The mechanical energy is

$$\mathcal{H}_{\text{osc}}(y, x) = \frac{1}{2m}y^2 + \frac{1}{2}kx^2, \quad k > 0. \quad (2.50)$$

One may rescale y introducing $y = mv$ and the Hamiltonian itself must be rescaled by m . Writing $\omega = \sqrt{k/m}$, which is a frequency, we get the ‘‘energy’’

$$\mathcal{H}_{\text{osc}}(v, x) = \frac{1}{2}v^2 + \frac{1}{2}\omega^2 x^2. \quad (2.51)$$

One can also introduce $v = \sqrt{\omega}p$ and $x = q/\sqrt{\omega}$ and we obtain

$$\mathcal{H}_{\text{osc}}(p, q) = \frac{\omega}{2}(p^2 + q^2). \quad (2.52)$$

This shows clearly that the origin $(p, q) = (0, 0)$ is a centre equilibrium point, shown in black in Figure 2.2 panel (a). Being a one d.o.f. system, the harmonic oscillator Hamiltonian is integrable. Indeed, one can introduce the canonical polar coordinates $p = \sqrt{2I} \cos \phi$, $q = \sqrt{2I} \sin \phi$, and we get

$$\mathcal{H}_{\text{osc}}(I, \phi) = \mathcal{H}_{\text{osc}}(I) = \omega I. \quad (2.53)$$

This shows that (I, ϕ) are global action-angle variables for the harmonic oscillator. The dynamics is simply $I(t) = \text{const}$ and $\phi(t) = \omega t + \phi_0$ with constant frequency ω .

2.1.6.2 The pendulum

The kinetic and potential energies of the pendulum are $T(\dot{\theta}) = \frac{1}{2}ml^2\dot{\theta}^2$ and $V(\theta) = -mgl \cos \theta$, with θ the angular coordinate. The canonical variables of the pendulum are then the angular position θ and the conjugated momentum $\tilde{\Theta} = ml^2\dot{\theta}$, the physical angular momentum, so the phase space is $\mathbb{R} \times \mathbb{T}$. The mechanical energy is

$$\mathcal{H}_{\text{pend}}(\tilde{\Theta}, \theta) = \frac{1}{2ml^2}\tilde{\Theta}^2 - mgl \cos \theta, \quad g, l > 0. \quad (2.54)$$

One may rescale $\tilde{\Theta}$ introducing $\Theta = ml^2\tilde{\Theta}$ and the Hamiltonian itself must be rescaled by ml^2 , yielding the ‘‘energy’’

$$\mathcal{H}_{\text{pend}}(\Theta, \theta) = \frac{1}{2}\Theta^2 - \frac{g}{l} \cos \theta. \quad (2.55)$$

Being a one d.o.f. system, the pendulum is integrable, and its general solution can be given in terms of elliptic integrals (see e.g. [Ferraz-Mello(2007)] appendix B). We can however gain a lot of information on the dynamics by looking at the level curves of the Hamiltonian, which are shown in Figure 2.2 panel (b). There is one stable equilibrium point at $(\Theta, \theta) = (0, 0)$ corresponding to the small angle/small amplitude regime. In this regime, $\cos \theta = 1 - \theta^2/2 + \mathcal{O}(\theta^4)$ so the Hamiltonian of the pendulum reduces to that of a harmonic oscillator with frequency $\omega = \sqrt{g/l}$. The level curves are topologically equivalent to circumferences, the orbits are periodic and undergo *librations*, i.e. the angle θ remains confined between $(-\theta_{\text{max}}, \theta_{\text{max}}) \bmod 2\pi$, with $\theta_{\text{max}} < \pi$. There is another equilibrium point at $(\Theta, \theta) = (0, \pm\pi)$, which is a saddle point, and is indicated in red in Figure 2.2(b). The two homoclinic orbits that asymptotically approach this point in the past or in the future are also shown in red, and are called *separatrices*. The period of the motion along these orbits is infinite, and they enclose the libration zone of the phase space, shown as the shaded area in Figure 2.2(b). Outside the separatrices the orbits undergo periodic *circulations*, i.e. the angle θ attains values in the whole \mathbb{T} . The highest/lowest points on the separatrices are at $(0, \pm 2\omega)$, giving a width of the libration region of 4ω .

While in the case of the harmonic oscillator we could introduce global action-angle variables, this is not the case for the pendulum because of the presence of the two separatrices which literally separate the phase space in two distinct regions of circulation and libration. One can still construct local action angle variables (which again take the geometrical definitions linked to the areas enclosed by the motion), but the presence of the separatrices having infinite period does not allow to pass with continuity from the cycles in the libration region to those in the circulation region. This topological change in the phase space is typical in the presence of resonances, and indeed the pendulum is extremely important as it is the most basic model for resonance [Henrard and Lemaitre(1983)]. The algebraic explanation of the impossibility of constructing global action angle variables in the presence of resonances will be given in Subsect. 2.3.1 (see also [Morbidelli(1995)]).

2.1.6.3 Andoyer Hamiltonians

As pointed out in [Henrard and Lemaitre(1983)], in the case of many resonance problems arising in Celestial Mechanics, the reduction of the Hamiltonian to that of a pendulum may not be appropriate. The reason is that when using a pair of canonical polar coordinates (Σ, σ) (for example, the modified Delaunay variables introduced in Subsect. 2.2.1) there is a singularity at the origin, while in fact the Hamiltonian is actually an analytic function of the corresponding cartesian coordinates $y = \sqrt{2\Sigma} \cos \sigma$, $x = \sqrt{2\Sigma} \sin \sigma$, so the singularity is only apparent (this

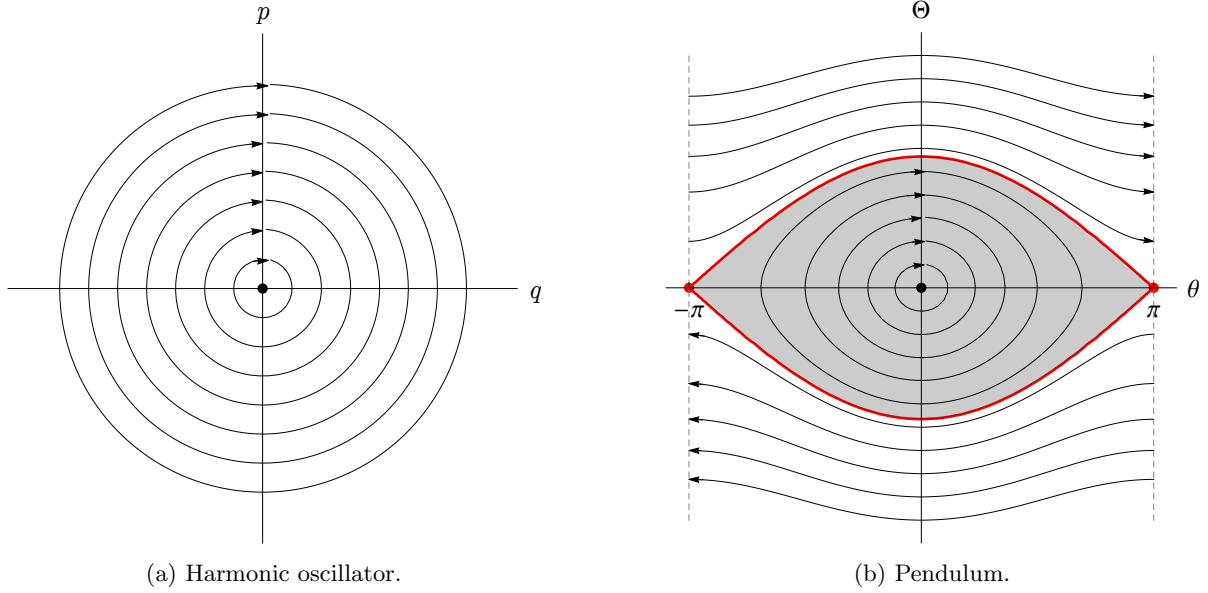


Figure 2.2: Phase diagrams for the harmonic oscillator and the pendulum. Equilibrium points are marked in black for centres and red for saddles.

property of the planetary Hamiltonian is usually expressed in terms of the d'Alembert characteristics, see Subsect. 2.2.2.1). A useful generalisation of the pendulum which takes this property into consideration is the class of Andoyer Hamiltonians

$$\mathcal{H}_{\text{And},k}(\Sigma, \sigma) = \delta\Sigma + \frac{\beta}{2}\Sigma^2 + c\sqrt{2\Sigma}^k \cos(k\sigma), \quad (2.56)$$

where δ , β , c are real constants, with $\beta \neq 0$ and $c \neq 0$. These are all one d.o.f. Hamiltonians and are therefore all integrable. Notice that the canonical polar coordinates (Σ, σ) are not action-angle coordinates for the Andoyer Hamiltonian (just as (Θ, θ) were not action-angle coordinates for the pendulum). The pendulum emerges from (2.56) using $k\sigma$ as an angle when one restricts oneself around a specific (finite) value $\bar{\Sigma}$ of the action, so that $\sqrt{2\Sigma} \simeq \sqrt{2\bar{\Sigma}}$; then, a simple translation $\Sigma = \Theta - \delta/\beta$ and renaming of the coefficients leads directly to the pendulum. As shown by [Henrard and Lemaître(1983)], the study of these Hamiltonians is extremely useful for understanding resonances and resonant capture, which we will detail in a later Subsect. 2.3.3 using the tools of adiabatic theory. For now, just as we did with the pendulum, we can concentrate only on the main qualitative aspects of the dynamics by looking at the phase diagrams in the cases $k = 1$ and $k = 2$, which are the ones that interest us the most. For a more in-depth description of this class of Hamiltonians, I refer to [Henrard and Lemaître(1983)] for the case $k = 1$ and to [Ferraz-Mello(2007)] Appendix C for the general case, from which I draw many of the ideas implemented below.

The level plots and therefore the dynamics obviously change with the parameters δ , β and c , whose specific values depend on the particular problem at hand. However, we can actually reduce the Hamiltonian so that it depends on a single parameter. First of all, we can assume without loss of generality that $\beta > 0$ and $c > 0$ (if this is not the case, we change t into $-t$ or σ into $\sigma + \pi/k$, respectively). Then, we rescale the action writing $\Sigma = \alpha\Sigma'$, and leaving σ unchanged; as we saw in Subsect. 2.1.3.2, the Hamiltonian is rescaled by α as well, and we get $\mathcal{H}'_{\text{And},k}(\Sigma', \sigma) = \delta\Sigma' + (\alpha\beta/2)\Sigma'^2 + \alpha^{k/2-1}c\sqrt{2\Sigma'}^k \cos\sigma$. By choosing $\alpha = (\beta/c)^{2/(k-4)}$ we get that the last two coefficients satisfy $\alpha\beta = \alpha^{k/2-1}c =: \tilde{c}$. Then, rescaling the time and dividing the Hamiltonian by \tilde{c} we get a new Hamiltonian

$$\tilde{\mathcal{H}}_{\text{And},k}(\Sigma', \sigma) = \tilde{\delta}\Sigma' + \frac{1}{2}\Sigma'^2 + \sqrt{2\Sigma'}^k \cos(k\sigma), \quad (2.57)$$

with $\tilde{\delta} = \delta/\tilde{c}$.

Consider the case $k = 1$ first. We start by finding the equilibrium points. Passing in canonical cartesian

coordinates ($X = \sqrt{2\Sigma'} \cos \sigma, Y = \sqrt{2\Sigma'} \sin \sigma$) we write the Hamiltonian as

$$\tilde{\mathcal{H}}_{\text{And},1}(X, Y) = \tilde{\delta} \frac{X^2 + Y^2}{2} + \frac{1}{2} \left(\frac{X^2 + Y^2}{2} \right)^2 + X, \quad (2.58)$$

whose equilibrium points can be found by taking the gradient with respect to (X, Y) and setting it equal to zero. One gets that all equilibria satisfy

$$Y = 0, \quad X^3 + 2\tilde{\delta}X + 2 = 0. \quad (2.59)$$

The first equation says that all equilibria correspond to values of $\sigma = 0, \pi$. By looking at the discriminant $\Delta = -32(\tilde{\delta}^3 + 27/8)$ of the second cubic equation, we see that it admits only one real solution X_1 if $\Delta < 0$ i.e. $\tilde{\delta} > -3/2$, one real solution X_1 and a double real solution $X_2 = X_3 > X_1$ if $\tilde{\delta} = -3/2$ and three distinct real solutions $X_1 < X_2 < X_3$ if $\tilde{\delta} < -3/2$ [Deck et al.(2013)]. Figure 2.3 shows these three possible situations. Stable equilibria are marked as black points and unstable ones in red. We see that X_1 is always a centre; when $\tilde{\delta} < -3/2$ then X_2 is also stable while X_3 is a saddle point; finally when $\tilde{\delta} = -3/2$ these two points bifurcate into a cusp. When this unstable point appears at $\tilde{\delta} = -3/2$, a separatrix is generated, indicated as a red contour line, and for $\tilde{\delta} < -3/2$ there are two separatrices emerging from X_3 which enclose a banana-shaped region in the phase space called the *resonant region*. The stable point X_1 enclosed by the resonant region is called the *resonant equilibrium point*. It is important to point out that resonances are usually associated to libration of the canonical angle, and in the case of the pendulum the two concepts are indeed equivalent. However, for Andoyer's Hamiltonian $\tilde{\mathcal{H}}_{\text{And},1}$ there is a difference between the resonant region and the region of libration of the angle σ . The presence of the separatrix (which is always a given in the pendulum) is a crucial topological condition for resonance [Delisle et al.(2012)]. Note also that the origin $X = Y = 0$ is never an equilibrium point so we never have to deal with the singularity when studying the stability of the equilibria.

We now consider the case $k = 2$. In order to have all equilibria on the same axis, we can use the angle $\theta = k\sigma = 2\sigma$, which introduces a k -folding [Ferraz-Mello(2007)], at the expense of losing the regularity at the origin. Rescaling the time by the same factor $k = 2$, and passing in "folded" cartesian coordinates ($\tilde{X} = \sqrt{2\Sigma'} \cos \theta, \tilde{Y} = \sqrt{2\Sigma'} \sin \theta$) the Hamiltonian becomes

$$\tilde{\mathcal{H}}_{\text{And},2}(\tilde{X}, \tilde{Y}) = \tilde{\delta} \frac{\tilde{X}^2 + \tilde{Y}^2}{2} + \frac{1}{2} \left(\frac{\tilde{X}^2 + \tilde{Y}^2}{2} \right)^2 + \left(2 \frac{\tilde{X}^2 + \tilde{Y}^2}{2} \right)^{1/2} \tilde{X}. \quad (2.60)$$

The equilibria can be found again taking the gradient with respect to (\tilde{X}, \tilde{Y}) and setting it equal to zero. One gets that all equilibria satisfy

$$\tilde{Y} = 0, \quad \tilde{X}^3 + 2\tilde{\delta}\tilde{X} + 4|\tilde{X}| = 0. \quad (2.61)$$

The first equation states that the equilibria always lie on the axis $\theta = 0, \pi$, i.e. on the two axes $\sigma = 0, \pi$ and $\sigma = \pm\pi/2$. The second equation is satisfied for any value of $\tilde{\delta}$ by $\tilde{X} = \tilde{X}_0 = 0$ so the origin is always an equilibrium point. Then one finds two other solutions $\tilde{X}_{\pm} = \pm\sqrt{2}\sqrt{-(\pm 2 + \tilde{\delta})}$: \tilde{X}_+ is real if $\tilde{\delta} < -2$, while \tilde{X}_- is real if $\tilde{\delta} < 2$. When $\tilde{\delta} = -2$, there is a bifurcation at $\tilde{X}_0 \equiv \tilde{X}_+$ and then the two equilibria separate for $\tilde{\delta} < -2$; when $\tilde{\delta} = 2$ there is a cusp at $\tilde{X}_0 \equiv \tilde{X}_-$ and then the two equilibria bifurcate for $-2 < \tilde{\delta} < 2$ (\tilde{X}_- and \tilde{X}_+ never appear to merge into a cusp because this would happen when $\tilde{\delta} = 0$, but for this value \tilde{X}_+ is not real). It is actually easier to grasp the stability properties and bifurcations of these equilibria by looking directly at the phase diagram. Indeed, now that the geometric properties of $\tilde{\mathcal{H}}_{\text{And},k}$ have been obtained using the "folded" variables (\tilde{X}, \tilde{Y}) , we go back to the original $\tilde{\mathcal{H}}_{\text{And},2}(\Sigma', \sigma)$ and introduce cartesian coordinates ($X = \sqrt{2\Sigma'} \cos \sigma, Y = \sqrt{2\Sigma'} \sin \sigma$), so that Andoyer's Hamiltonian writes

$$\tilde{\mathcal{H}}_{\text{And},2}(X, Y) = \tilde{\delta} \frac{X^2 + Y^2}{2} + \frac{1}{2} \left(\frac{X^2 + Y^2}{2} \right)^2 + (X^2 - Y^2), \quad (2.62)$$

and is now regular again at the origin; we can thus plot in Figure 2.4 the level curves of this Hamiltonian with the different possible cases depending on the value of $\tilde{\delta}$.

Figures 2.3 and 2.4 can be read left-to-right/top-to-bottom as $\tilde{\delta}$ goes from positive values to negative values and changes the shape of the Andoyer Hamiltonians. We will later use these models in Subsect. 2.3.3 to give a general description of capture into resonance as an application to the adiabatic principle.

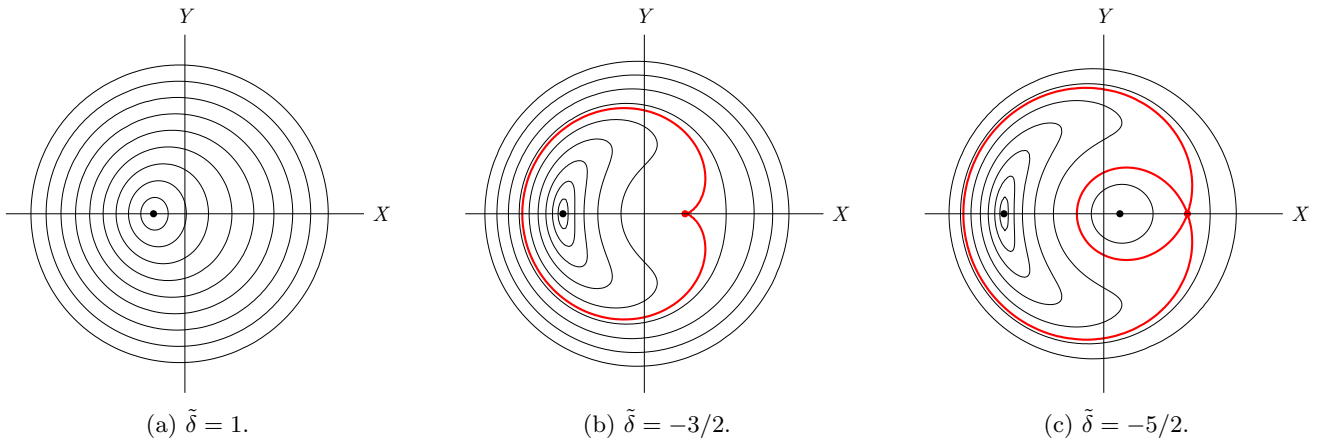


Figure 2.3: Phase diagrams for Andoyer Hamiltonian $\tilde{\mathcal{H}}_{\text{And},1}(X, Y)$ in canonical cartesian coordinates, for different values of $\tilde{\delta}$. Stable equilibrium points are marked in black, unstable points in red. The separatrices are also shown as red contour lines. The banana-shaped region enclosed by the separatrices is the resonant region, and it encloses a (stable) resonant equilibrium point.

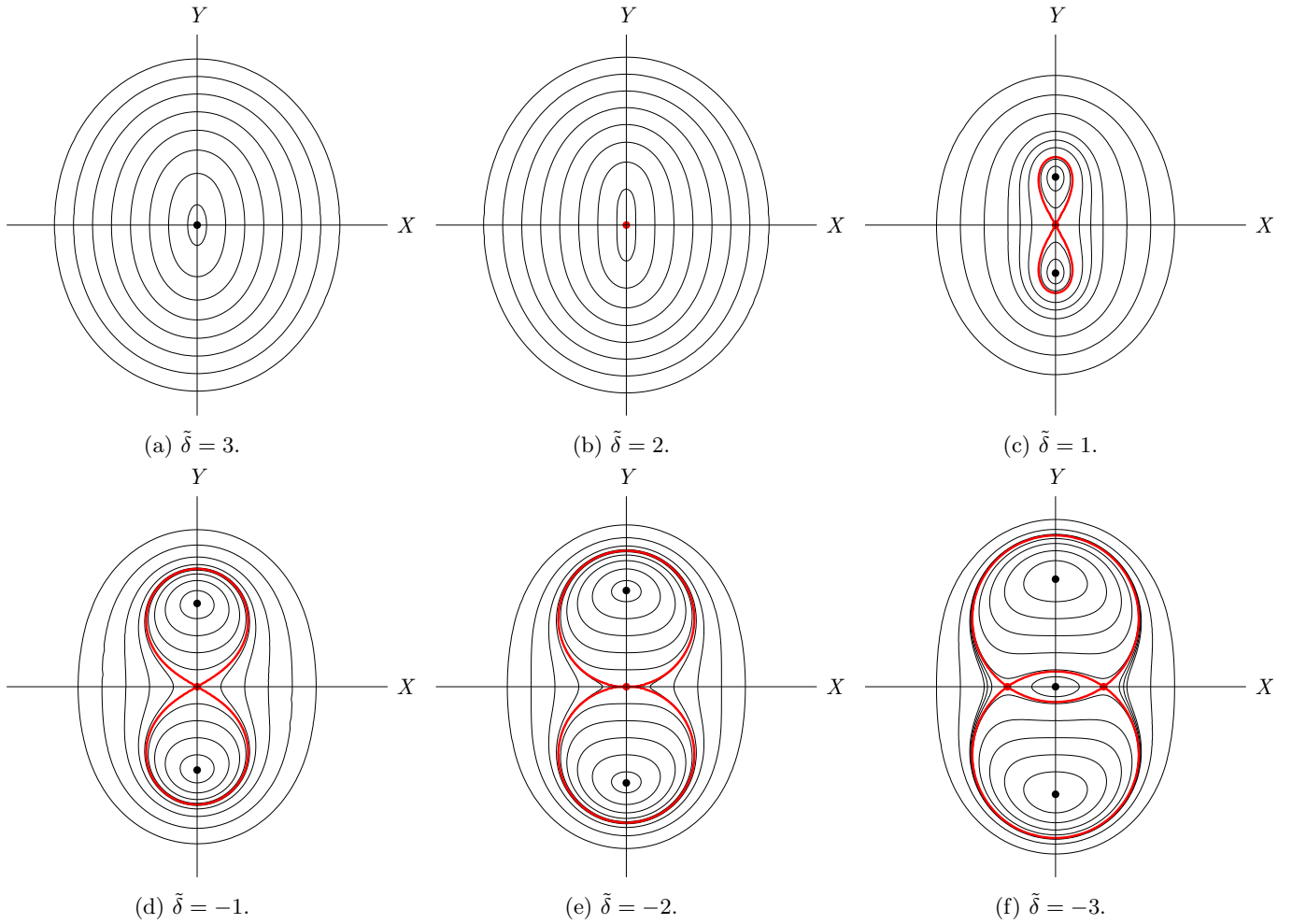


Figure 2.4: Phase diagrams for Andoyer Hamiltonian $\tilde{\mathcal{H}}_{\text{And},2}(X, Y)$ in canonical cartesian coordinates, for different values of $\tilde{\delta}$. Stable equilibrium points are marked in black, unstable points or bifurcations in red. The separatrices are also shown as red contour lines. In panels (c) to (f) the separatrices enclose the resonant lobes, the regions away from the origin which contain the (stable) resonant equilibrium points.

2.2 Planetary systems in Hamiltonian mechanics

In this section, we briefly review the main concepts of Celestial Mechanics, couched in the Hamiltonian formalism outlined above. We start with the case of two gravitationally interacting bodies, usually the star and a planet, which is known as the two-body problem. This problem is integrable and we briefly sketch its solution. This allows to introduce key concepts such as the orbital elements and the canonical action-angle Delaunay variables, which will be used extensively throughout the thesis. We then generalise to the case of N planets, which is not integrable when $N \geq 2$. This will prompt us to review the tools of perturbation theory in the next section. In this section I follow mainly the notes of prof. A. Giorgilli for his course on Celestial Mechanics (<http://www.mat.unimi.it/users/antonio/meccel/meccel.html>).

2.2.1 The two-body problem

The kinetic and potential energies of a system of two bodies of mass m_0, m_1 which interact with the gravitational attraction only are

$$\begin{aligned} T_{2BP}(\dot{\mathbf{u}}) &= \frac{1}{2}m_0\|\dot{\mathbf{u}}_0\|^2 + \frac{1}{2}m_1\|\dot{\mathbf{u}}_1\|^2, \\ V_{2BP}(\mathbf{u}) &= -\frac{\mathcal{G}m_0m_1}{\|\mathbf{u}_1 - \mathbf{u}_0\|}, \end{aligned} \tag{2.63}$$

with cartesian coordinates \mathbf{u}_i in an inertial frame. \mathcal{G} is the gravitational constant. The canonical variables are then the positions \mathbf{u}_i and the conjugated momenta $\tilde{\mathbf{u}}_i = m_i\dot{\mathbf{u}}_i$, the physical linear momenta, so the phase space is \mathbb{R}^{12} . The mechanical energy is

$$\mathcal{H}_{2BP}(\tilde{\mathbf{u}}, \mathbf{u}) = \frac{1}{2m_0}\|\tilde{\mathbf{u}}_0\|^2 + \frac{1}{2m_1}\|\tilde{\mathbf{u}}_1\|^2 - \frac{\mathcal{G}m_0m_1}{\|\mathbf{u}_1 - \mathbf{u}_0\|}. \tag{2.64}$$

Being a 6 d.o.f. system, we need additional first integrals independent of the energy and in involution to integrate the system, and it is well known that such integrals exist. Here we do not go through the detailed derivation, which can be found in most textbooks, but only describe the main points. The first step is to eliminate the barycentre $\mathbf{b} = \frac{m_0\mathbf{u}_0 + m_1\mathbf{u}_1}{m_0 + m_1}$ and to write the position vectors in terms of the mutual position \mathbf{r} . This can be achieved through the transformation

$$\begin{aligned} \tilde{\mathbf{b}} &= \tilde{\mathbf{u}}_0 + \tilde{\mathbf{u}}_1, & \mathbf{b} &= \frac{m_0\mathbf{u}_0 + m_1\mathbf{u}_1}{m_0 + m_1}, \\ \tilde{\mathbf{r}} &= \frac{-m_1\tilde{\mathbf{u}}_0 + m_0\tilde{\mathbf{u}}_1}{m_0 + m_1}, & \mathbf{r} &= \mathbf{u}_1 - \mathbf{u}_0. \end{aligned} \tag{2.65}$$

whose canonicity can be checked using the Poisson bracket criterion. Defining

$$\mu := \frac{m_0m_1}{m_0 + m_1} \tag{2.66}$$

called the reduced mass for the two masses m_0 and m_1 , we get that

$$\mathcal{H}_{2BP}(\tilde{\mathbf{b}}, \tilde{\mathbf{r}}, \mathbf{b}, \mathbf{r}) = \frac{1}{2(m_0 + m_1)}\|\tilde{\mathbf{b}}\|^2 + \frac{1}{2\mu}\|\tilde{\mathbf{r}}\|^2 - \frac{\mathcal{G}(m_0 + m_1)\mu}{\|\mathbf{r}\|} \tag{2.67}$$

splits into two independent bits. The first bit is $\mathcal{H}_{\mathbf{b}}(\tilde{\mathbf{b}}) = \frac{1}{2(m_0 + m_1)}\|\tilde{\mathbf{b}}\|^2$ and dictates the motion with constant velocity of the barycentre \mathbf{b} , which does not affect the mutual interaction between the two bodies, and can be safely dropped. This is tantamount to assuming that we used from the start inertial barycentric positions and velocities $\mathbf{x}, \dot{\mathbf{x}}$ such that $(m_0\mathbf{x}_0 + m_1\mathbf{x}_1)/(m_0 + m_1) = \mathbf{0}$. The second bit is the Keplerian Hamiltonian

$$\mathcal{H}_{\text{kepl}}(\tilde{\mathbf{r}}, \mathbf{r}) = \frac{1}{2\mu}\|\tilde{\mathbf{r}}\|^2 - \frac{k}{\|\mathbf{r}\|}, \quad k = \mathcal{G}(m_0 + m_1)\mu = \mathcal{G}m_0m_1. \tag{2.68}$$

Having done so, we have reduced the number of d.o.f.'s to 3 and to a problem which is equivalent to the classical central force problem of a mass $m = \mu$ feeling a central force coming from a point S . The solutions for the Keplerian problem were first found by Newton [Newton(1687)] and represent the main victory of his work since they proved

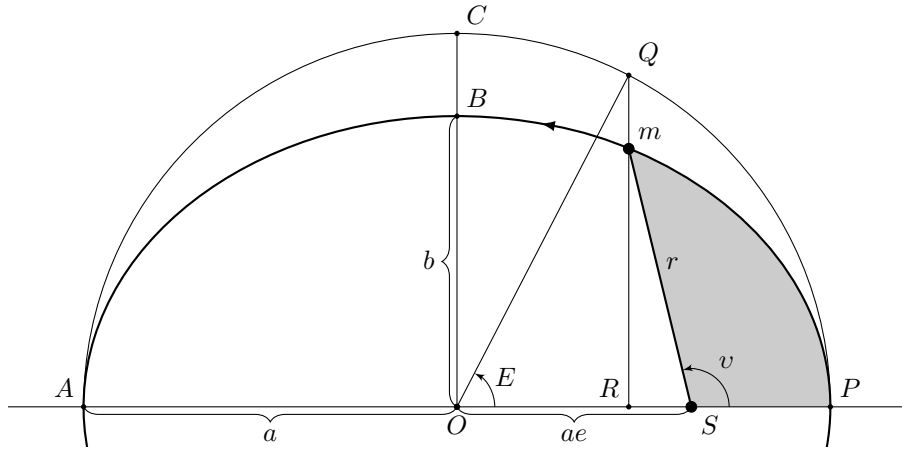


Figure 2.5: The orbital plane, where m is a planet orbiting a star S , and depiction of some of the orbital elements. r is the length of the radius vector from the star S to the planet m . The semi-major axis is a , the semi-minor axis is $b = \sqrt{a(1 - e^2)}$ where e is the eccentricity. The true (v) and eccentric (E) anomalies are the angles \widehat{PSm} and \widehat{POQ} . The mean anomaly (ℓ) is related to the $\text{Area}(\widehat{PmS})$.

Kepler's empirical laws on planetary motion. For the bound solutions, which are the ones we will be interested in throughout this thesis⁸, these are

1. The vector $\mathbf{r}(t)$ traces out an ellipse, with one of its focus in the origin S ;
2. The vector $\mathbf{r}(t)$ sweeps out equal areas in equal time intervals;
3. The orbital period squared is proportional to the semi-major axis of the ellipse cubed, the proportionality constant being⁹ $(2\pi)^2 / (\mathcal{G}(m_0 + m_1))$.

These laws lead directly to the solution of the Kepler problem (2.68), which we describe below using the usual terminology in the case when m_1 a planet, m_0 a star, and so $\mathbf{r} = \mathbf{u}_1 - \mathbf{u}_0$ is the planet's astrometric position.

By the first law, the motion of the planet is restricted to a plane, called the *orbital plane* shown in Figure 2.5, where absolute polar coordinates (r, θ) can be introduced. If we let θ_P denote the angle between the half-line $\{\theta = 0\}$ and the *direction of the pericentre* P , we can introduce the *true anomaly* $v := \theta - \theta_P$. Kepler's first law also states that the motion takes place on an ellipse. Therefore, the *radius-vector* $r = \|\mathbf{r}\|$ can be given as a function of the true anomaly v by

$$r = \frac{p}{1 + e \cos v}, \quad (2.69)$$

where p is the *parameter of the ellipse* and is related to the ellipse's *eccentricity* e and *semi-major axis* a and *semi-minor axis* b by

$$a = \frac{p}{1 - e^2}, \quad p = \frac{b^2}{a}. \quad (2.70)$$

The determination of the true anomaly $v(t)$ can be achieved with the introduction of two additional anomalies (angles). One first introduces the *eccentric anomaly* E , the angle \widehat{POQ} in Figure 2.5. Applying Pythagoras Theorem to the triangle \widehat{mSR} one easily obtains¹⁰

$$r = a(1 - e \cos E), \quad (2.71)$$

⁸In general, the solution is a conic section.

⁹Actually, in the planetary case when m_0 is the mass of the star, the dependence of this proportionality constant on m_1 represents a slight difference to Kepler's original statement, but this is a minute correction since $m_0 \gg m_1$.

¹⁰Use $|mS| = r$, $|mR| = b \sin E$ with $b^2 = a^2(1 - e^2)$, and $|RS| = |SO| - |RO| = a \cos E - ae$.

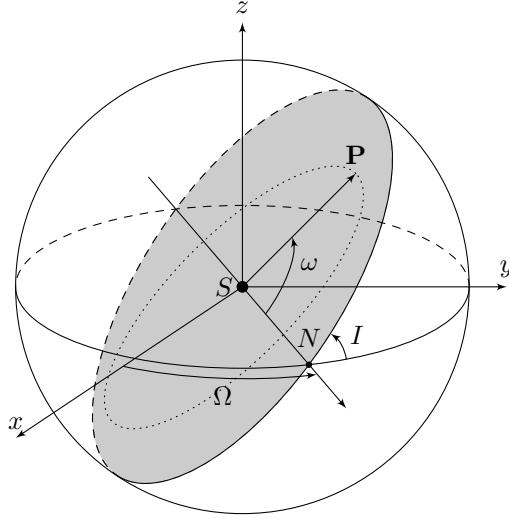


Figure 2.6: The orbital elements Ω , I and ω in the three-dimensional space. The orbital plane is highlighted.

so we need to find $E(t)$. To do this, one introduces the *mean anomaly* ℓ in order to make use of Kepler's second law of areas (in a way the mean anomaly *is* Kepler's second law). Introducing the *mean motion* $n = 2\pi/T$, T being the period of revolution (*orbital period* in the case of a planet), the mean anomaly is defined as

$$\ell := n(t - \tau), \quad (2.72)$$

where τ is the *instant of pericentre passage*. The relationship between E and ℓ is given by *Kepler's Equation*¹¹

$$E - e \sin E = \ell, \quad (2.73)$$

which was first obtained by Kepler in 1609 in Chapter LX of the *Astronomia Nova*. Finally, Kepler's Third Law states that

$$n = \sqrt{\mathcal{G}(m_0 + m_1)/a^3}, \quad (2.74)$$

and allows one to obtain the mean motion n given the semi-major axis a , which in turn yields the mean anomaly ℓ at time t . To obtain $E(t)$, one needs to invert Kepler's equation (2.73), and finally the solution $r(t)$ is given by (2.71). The motion of the planet on the orbital plane is therefore completely determined if the values of e , a and τ are known.

To describe the position of the planet in the three-dimensional space, consider an absolute (right-handed) cartesian coordinate system (x, y, z) with centre at the central star. This can be obtained with reference to the fixed stars. The (x, y) -plane will be called the *plane of reference*, the x -axis will be called the *reference direction*, or *origin of longitude*. If the orbital plane is inclined with respect to the plane of reference, the orbit will intersect

¹¹To derive Kepler's equation, notice that by Kepler's Second Law we have

$$\begin{aligned} \text{Area}(\widehat{PmS}) &= \left(\frac{t - \tau}{T}\right) \cdot \underbrace{\pi ab}_{\substack{\text{area} \\ \text{enclosed} \\ \text{by orbit}}} = \frac{1}{2} \left(\frac{2\pi(t - \tau)}{T}\right) ab \\ &= \frac{ab}{2} \ell, \end{aligned}$$

while

$$\begin{aligned} \text{Area}(\widehat{PmS}) &= \frac{b}{a} \text{Area}(\widehat{PSQ}) = \frac{b}{a} \left[\text{Area}(\widehat{POQ}) - \text{Area}(\widehat{SOQ}) \right] \\ &= \frac{b}{a} \left[\frac{a^2}{2} E - \frac{1}{2} |QR| \cdot |OS| \right] = \frac{b}{a} \left[\frac{a^2}{2} E - \frac{1}{2} a \sin E \cdot ea \right] \\ &= \frac{ab}{2} [E - e \sin E]. \end{aligned}$$

the latter at two points called *orbital nodes* (if not, the orbit has no nodes). The *ascending node* N is the one at which, as we follow its motion on the orbit, the planet cuts the plane of reference moving towards the positive direction of the z -axis, the other is the *descending node*. The orbital plane is then completely identified by two angles which we now describe. The first is the *longitude of the ascending node* Ω , which is the angle between the origin of longitude and the ascending node, measured on the reference plane. The second is the *inclination* I , which is the angle between the reference plane and the orbital plane, cfr. Figure 2.6. Finally, the orientation of the ellipse on the orbital plane described by the *argument of the pericentre* ω , which is the angle between the ascending node and the direction of the pericentre (so this plays the role of θ_P used earlier). Then in the three-dimensional space we can introduce the orthonormal vectors

$$\begin{aligned}\mathbf{P} &= \begin{pmatrix} \cos \Omega \cos \omega - \cos I \sin \Omega \sin \omega \\ \sin \Omega \cos \omega + \cos I \cos \Omega \sin \omega \\ \sin I \sin \omega \end{pmatrix}, \\ \mathbf{Q} &= \begin{pmatrix} -\cos \Omega \sin \omega - \cos I \sin \Omega \cos \omega \\ -\sin \Omega \sin \omega + \cos I \cos \Omega \cos \omega \\ \sin I \cos \omega \end{pmatrix}, \\ \mathbf{G} &= \begin{pmatrix} \sin I \sin \Omega \\ -\sin I \cos \Omega \\ \cos I \end{pmatrix},\end{aligned}\tag{2.75}$$

which form a right-handed coordinate basis system, where \mathbf{P} points in the direction of the pericentre and \mathbf{P} and \mathbf{Q} belong to the orbital plane. With simple algebraic calculations one finds that the position $\mathbf{r} = r(\mathbf{P} \cos v + \mathbf{Q} \sin v)$ and velocity $\dot{\mathbf{r}}$ are obtained as¹²

$$\begin{aligned}\mathbf{r} &= a(\cos E - e)\mathbf{P} + (a\sqrt{1 - e^2} \sin E)\mathbf{Q}, \\ \dot{\mathbf{r}} &= -\frac{na \sin E}{1 - e \cos E}\mathbf{P} + \frac{na\sqrt{1 - e^2} \cos E}{1 - e \cos E}\mathbf{Q},\end{aligned}\tag{2.76}$$

with $E = E(\ell)$ from Kepler's equation (2.73). As a result, we have a complete description of the planetary motion relative to the star in the three-dimensional space. All we need is a set of the so-called *orbital elements* of the planet $(a, e, \ell, \omega, \Omega, I)$: the first three are used to determine the position of the planet at any fixed time t on the orbital plane, the last three are needed to determine the orbital plane and the orientation of the ellipse in space. There are degeneracies in these definitions when the inclination and/or eccentricity are zero, in which case ω and/or ℓ are not well defined because the direction of the ascending node and/or the direction of the pericentre are not determined, respectively. To circumvent this, one introduces the *longitude of perihelion* $\varpi = \omega + \Omega$ and the *mean longitude* $\lambda = \ell + \varpi$: the first angle is well defined when $I = 0$, and the second one is well defined when $I = 0$ and/or $e = 0$. Clearly also the set of orbital elements $(a, e, I, \lambda, \varpi, \Omega)$ unequivocally defines \mathbf{P} , \mathbf{Q} and \mathbf{G} and therefore \mathbf{r} and $\dot{\mathbf{r}}$ via (2.76). Moreover, if $I = 0$ (planar case), the vectors \mathbf{P} , \mathbf{Q} and \mathbf{G} depend on ϖ only:

$$\mathbf{P} = \begin{pmatrix} \cos \varpi \\ \sin \varpi \\ 0 \end{pmatrix}, \quad \mathbf{Q} = \begin{pmatrix} -\sin \varpi \\ \cos \varpi \\ 0 \end{pmatrix}, \quad \mathbf{G} = \begin{pmatrix} 0 \\ 0 \\ 1 \end{pmatrix};\tag{2.77}$$

similarly, when $e = 0$ (circular case), the expressions in (2.76) depend on $\ell + \omega$ only.

Coming back at the Hamiltonian formulation of the problem, the orbital elements do not form a canonical set, so we cannot use them directly in a canonical sense. However, since the problem is integrable, one could think of

¹² To see this, write $\mathbf{r} = X\mathbf{P} + Y\mathbf{Q}$, $\dot{\mathbf{r}} = \dot{X}\mathbf{P} + \dot{Y}\mathbf{Q}$ on the orbital plane. The first equation reads

$$\begin{aligned}X &= a(\cos E - e), \\ Y &= (a\sqrt{1 - e^2} \sin E),\end{aligned}$$

which is obtained easily applying geometric considerations to Figure 2.5. Then, we derive with respect to time and obtain

$$\begin{aligned}\dot{X} &= -a\dot{E} \sin E, \\ \dot{Y} &= a\dot{E} \sqrt{1 - e^2} \cos E;\end{aligned}$$

to obtain \dot{E} we use Kepler's equation (2.73) together with the fact that $\dot{\ell} = n$ which yields $\dot{E} = n/(1 - e \cos E)$, or, using also the equation for the ellipse (2.71), $\dot{E} = n(a/r)$.

applying the Liouville-Arnold-Jost theorem and obtain canonical action-angle variables. Indeed, since the Kepler problem is a central force problem, the angular momentum vector, which in coordinates (2.65) takes the form

$$\mathcal{L} = \mathbf{r} \times \tilde{\mathbf{r}} = \mu \mathbf{r} \times \dot{\mathbf{r}}, \quad (2.78)$$

is conserved, yielding three constants of motion (one for each component). In the Keplerian case, when the central force is proportional to the inverse of the distance squared, there is an additional vector that is conserved, the Laplace-Runge-Lenz vector, which in coordinates (2.65) takes the form

$$\mathbf{A} = \tilde{\mathbf{r}} \times \mathcal{L} - \mu k \frac{\mathbf{r}}{\|\mathbf{r}\|}, \quad k = \mathcal{G}m_0m_1. \quad (2.79)$$

With the Hamiltonian this gives a total of seven first integrals, from which one can obtain three independent first integrals in involution and apply the Arnold-Jost procedure. Referring to [Morbidelli(2002)] for the details, this leads to the so-called *Delaunay variables* [Delaunay(1867)], which are action-angle variables for the Kepler problem and are strictly linked to the orbital elements:

$$\begin{aligned} L &= \mu \sqrt{\mathcal{G}(m_0 + m_1)a}, & \ell &= n(t - \tau), \\ G &= L \sqrt{1 - e^2}, & g &= \omega \\ \Theta &= G \cos I, & \theta &= \Omega. \end{aligned} \quad (2.80)$$

L is the norm of the angular momentum if the orbit were circular, G is the norm of the angular momentum and Θ is the norm of its projection on the z axis. The Hamiltonian in these variables takes the simple form

$$\mathcal{H}_{2\text{BP}}(L) = -\mathcal{G}^2 \frac{\mu^3 (m_0 + m_1)^2}{2L^2}, \quad (2.81)$$

and is evidently highly degenerate since it does not depend on the momenta G and Θ , which encapsulate the inclination and eccentricity of the orbit. These variables are not well defined when the inclination and/or the eccentricity vanish, in which case to avoid the apparent singularity the *modified Delaunay variables* are used, defined as

$$\begin{aligned} \Lambda &= L = \mu \sqrt{\mathcal{G}(m_0 + m_1)a}, & \lambda &= \ell + g + \theta = \ell + \varpi, \\ \Gamma &= L - G = L(1 - \sqrt{1 - e^2}), & \gamma &= -g - \theta = -\varpi, \\ Z &= G - \Theta = 2G \sin^2 \frac{I}{2}, & \zeta &= -\theta = -\Omega. \end{aligned} \quad (2.82)$$

Now λ is always well defined, while γ (resp., ζ) is not defined only when the conjugate action Γ (resp., Z) vanishes. Therefore, (Γ, γ) and (Z, ζ) are canonical polar coordinate variables, from which cartesian variables

$$\begin{aligned} \xi_1 &= \sqrt{2\Gamma} \cos \gamma, & \eta_1 &= \sqrt{2\Gamma} \sin \gamma, \\ \xi_2 &= \sqrt{2Z} \cos \zeta, & \eta_2 &= \sqrt{2Z} \sin \zeta \end{aligned} \quad (2.83)$$

can be constructed, called *Poincaré variables* [Poincaré & Fichot(1905)].

We note that in the change of coordinates (2.65) no mass is actually privileged, only the barycentre is: once the solution for $\mathbf{r}(t)$ is known the motions of the two bodies are recovered by

$$\begin{aligned} \mathbf{u}_0 &= \mathbf{b} - \frac{m_1}{m_0 + m_1} \mathbf{r}, \\ \mathbf{u}_1 &= \mathbf{b} + \frac{m_0}{m_0 + m_1} \mathbf{r}. \end{aligned}$$

So, defining $\mathbf{r} = \mathbf{u}_1 - \mathbf{u}_0$ so that \mathbf{u}_1 is referred to \mathbf{u}_0 is purely a choice. However, in Celestial Mechanics it is typical to refer the position of orbiting bodies to that of the star, so m_0 would be the stellar mass. In this case, $\mathbf{r} = \mathbf{u}_1 - \mathbf{u}_0$ is called the astrometric position (or heliocentric in the case of the Sun). We now notice that, since $\tilde{\mathbf{u}}_i = m_i \dot{\mathbf{u}}_i$,

$$\tilde{\mathbf{r}} \equiv \frac{m_0 m_1}{m_0 + m_1} (\dot{\mathbf{u}}_1 - \dot{\mathbf{u}}_0) =: \mu (\dot{\mathbf{u}}_1 - \dot{\mathbf{u}}_0) = \mu \dot{\mathbf{r}}, \quad (2.84)$$

so $\tilde{\mathbf{r}}$ is a constant away from the astrometric velocity $\dot{\mathbf{r}}$. We can rescale $\tilde{\mathbf{r}}$ by μ introducing $\tilde{\mathbf{r}} = \mu \dot{\mathbf{r}}$, and the Hamiltonian must be rescaled as well:

$$\mathcal{H}_{\text{kepl}}(\dot{\mathbf{r}}, \mathbf{r}) = \frac{1}{2} \|\dot{\mathbf{r}}\|^2 - \frac{\mathcal{G}(m_0 + m_1)}{\|\mathbf{r}\|}. \quad (2.85)$$

Notice that with this rescaling the momenta in the Delaunay sets are also rescaled by μ . This shows that in the case of the two-body problem astrometric position and velocity can be used as canonical variables, from which the orbital elements can be defined inverting (2.76). This is not true in the case of multiple planets, as we will see.

This reduced Hamiltonian is also useful in the case of a particle of negligible mass, $m_1 = 0$, and therefore in the treatment of the *restricted problem*, where a massless particle feels the gravitational attraction of a main central body (e.g. the star) and of N planets on given orbits around the central body (if only one perturbing planet is considered, this is the *restricted three-body problem*). If the planets have masses m_i and heliocentric position vectors \mathbf{r}_i , the Hamiltonian of the restricted problem is [Morbidelli(2002)]

$$\mathcal{H}_{\text{RP}}(\dot{\mathbf{r}}, \mathbf{r}; \mathbf{r}_i) = \frac{1}{2} \|\dot{\mathbf{r}}\|^2 - \frac{\mathcal{G}m_0}{\|\mathbf{r}\|} - \sum_{i=1}^N \mathcal{G}m_i \left(\frac{1}{\|\mathbf{r} - \mathbf{r}_i\|} - \frac{\mathbf{r} \cdot \mathbf{r}_i}{\|\mathbf{r}_i\|^3} \right). \quad (2.86)$$

If the masses of the planets are small compared to that of the star and the distances $\|\mathbf{r} - \mathbf{r}_i\|$, $\|\mathbf{r}_i\|$ are not small, the Hamiltonian (2.86) appears as the rescaled Keplerian Hamiltonian (2.85) with $m_1 = 0$ plus some perturbation terms, whose sizes are of the order of the planets' masses relative to that of the central body m_0 . In the restricted problem, one assumes that the orbits of the planets $\mathbf{r}_i(t)$ are known (the Hamiltonian \mathcal{H}_{RP} is therefore non-autonomous, cfr. Subsect. 2.1.2.1). The equations that govern the planetary motion are described in the next subsection.

2.2.2 The planetary problem

The kinetic and potential energies of a system of $N + 1$ bodies of mass m_i , $i = 0, \dots, N$, which interact with the gravitational attraction only are

$$\begin{aligned} T_{\text{PP}}(\dot{\mathbf{u}}) &= \sum_{i=0}^N \frac{1}{2} m_i \|\dot{\mathbf{u}}\|^2, \\ V_{\text{PP}}(\mathbf{u}) &= - \sum_{0 \leq i < j \leq N} \frac{\mathcal{G}m_i m_j}{\|\mathbf{u}_i - \mathbf{u}_j\|}, \end{aligned} \quad (2.87)$$

with cartesian coordinates \mathbf{u}_i in an inertial frame. We remark right away that in the planetary problem, m_0 plays the role of the stellar mass, and the other N bodies are the planets. The canonical variables are then the positions \mathbf{u}_i and the conjugated momenta $\tilde{\mathbf{u}}_i = m_i \dot{\mathbf{u}}_i$, the physical linear momenta, so the phase space is $\mathbb{R}^{2 \times 3(N+1)}$. The mechanical energy is

$$\mathcal{H}_{\text{PP}}(\tilde{\mathbf{u}}, \mathbf{u}) = \sum_{i=0}^N \frac{1}{2m_i} \|\tilde{\mathbf{u}}\|^2 - \sum_{0 \leq i < j \leq N} \frac{\mathcal{G}m_i m_j}{\|\mathbf{u}_i - \mathbf{u}_j\|}. \quad (2.88)$$

This is a $3(N + 1)$ d.o.f. system, which in general apart from the Hamiltonian only possesses as first integrals the components of the total linear momentum

$$\mathbf{P} = \sum_{i=0}^N \tilde{\mathbf{u}}_i \quad (2.89)$$

and of the angular momentum

$$\mathcal{L} = \sum_{i=0}^N \mathbf{u}_i \times \tilde{\mathbf{u}}_i, \quad (2.90)$$

so it is not integrable as pointed out by Poincaré. We can however use the total linear momentum to eliminate the barycentre, which will allow us to write the Hamiltonian as an integrable part (the star-planet interactions) plus a small correction (the planet-planet interactions). This step is similar to the one performed for the case of

one planet, except that now one cannot use astrometric positions *and* astrometric momenta since the resulting transformation would not be canonical (e.g. [Laskar(1990)]). One can use instead the astrometric positions and (a multiple of the) barycentric momenta in the following canonical transformation

$$\begin{aligned}\mathbf{p}_0 &= \sum_{i=0}^N \tilde{\mathbf{u}}_i, & \mathbf{r}_0 &= \mathbf{u}_0, \\ \mathbf{p}_i &= \tilde{\mathbf{u}}_i, & \mathbf{r}_i &= \mathbf{u}_i - \mathbf{u}_0, \quad i = 1, \dots, N.\end{aligned}\tag{2.91}$$

These mixed variables are sometimes called *canonical astrometric* (but again, the momenta are *not* the astrometric momenta). Simple algebraic manipulations show that the Hamiltonian becomes

$$\begin{aligned}\mathcal{H}_{\text{PP}}(\mathbf{p}, \mathbf{r}) &= \frac{\|\mathbf{p}_0\|^2}{2m_0} - \sum_{i=1}^N \frac{\mathbf{p}_0 \cdot \mathbf{p}_i}{m_0} \\ &+ \sum_{i=1}^N \frac{\|\mathbf{p}_i\|^2}{2\mu_i} + \sum_{1 \leq i < j \leq N} \frac{\mathbf{p}_i \cdot \mathbf{p}_j}{m_0} \\ &- \sum_{i=1}^N \frac{\mathcal{G}(m_0 + m_i)\mu_i}{\|\mathbf{r}_i\|} - \sum_{1 \leq i < j \leq N} \frac{\mathcal{G}m_i m_j}{\|\mathbf{r}_i - \mathbf{r}_j\|},\end{aligned}\tag{2.92}$$

where

$$\mu_i := \frac{m_i m_0}{m_0 + m_i}, \quad i = 1, \dots, N\tag{2.93}$$

is the reduced mass of each planet. The Hamiltonian (2.92) does not depend on \mathbf{r}_0 so \mathbf{p}_0 is a constant of motion, which we knew already since it is the total linear momentum \mathbf{P} . We can set $\mathbf{p}_0 = \mathbf{0}$ without loss of generality and drop the first line in (2.92) when considering the equations for $(\mathbf{p}_i, \mathbf{r}_i)$ for $i > 1, \dots, N$. Note also that with this choice the total angular momentum \mathcal{L} in these variables takes the form

$$\mathcal{L} = \sum_{i=1}^N \mathbf{r}_i \times \mathbf{p}_i.\tag{2.94}$$

Now the Hamiltonian rewrites

$$\mathcal{H}_{\text{PP}}(\mathbf{p}, \mathbf{r}) = \underbrace{\sum_{i=1}^N \left(\frac{\|\mathbf{p}_i\|^2}{2\mu_i} - \frac{\mathcal{G}(m_0 + m_i)\mu_i}{\|\mathbf{r}_i\|} \right)}_{\mathcal{H}_{\text{kepl}}} + \underbrace{\sum_{1 \leq i < j \leq N} \left(\frac{\mathbf{p}_i \cdot \mathbf{p}_j}{m_0} - \frac{\mathcal{G}m_i m_j}{\|\mathbf{r}_i - \mathbf{r}_j\|} \right)}_{\mathcal{H}_{\text{pert}}},\tag{2.95}$$

which shows that \mathcal{H}_{PP} can be seen as a sum $\mathcal{H}_{\text{kepl}}$ of N Keplerian Hamiltonians (2.68), one for each planet, plus some perturbation terms whose size relative to the Keplerian Hamiltonians is proportional to the mass of the planets relative to that of the star.

We should remark that from (2.95) we get Hamilton's equation $\dot{\mathbf{r}}_i = \mathbf{p}_i/\mu_i + \sum_{j \neq i} \mathbf{p}_j/m_0$, which shows that, unlike in the case of one planet (Equation (2.68)), the momenta \mathbf{p}_i conjugated to the astrometric positions \mathbf{r}_i are not proportional to $\dot{\mathbf{r}}_i$.¹³ Nonetheless, the functional form of the addends in $\mathcal{H}_{\text{kepl}}$ in (2.95) is the same as that of (2.68), regardless of the physical meaning of the canonical momenta. It is important to keep this in mind when introducing the orbital elements for multiple planets [Laskar(1990)]. One can still apply the relationships (2.76) which uniquely define the orbital elements of a planet for given position and velocity vectors, using \mathbf{r}_i and $\mathbf{v}_i = \mathbf{p}_i/\mu_i = m\dot{\mathbf{u}}_i/\mu_i$ instead of \mathbf{r}_i and $\dot{\mathbf{r}}_i$. The resulting elements $(a_i, e_i, I_i, \ell_i, \omega_i, \Omega_i)$ are called *formal osculating elements*. These are different from the osculating elements that are used by astronomers, which are defined from (2.76) using astrometric positions and astrometric velocities: the osculating elements define an ellipse that is tangent to the motion of the planet, so that if the perturbation $\mathcal{H}_{\text{pert}}$ suddenly vanished, the planet would follow

¹³This follows from the fact that the kinetic energy in the canonical astrometric variables (2.91) has non-diagonal terms, see (2.92). Another possibility would have been to use the Jacobi coordinates instead (e.g. [Laskar(1990)]), which have the advantage of retaining the kinetic energy in its diagonal form so the conjugated momenta are proportional to the velocities. However, the expression of the potential energy is in turn more cumbersome, as one must make use of a series expansion in the planetary masses which is not needed when using the canonical astrometric coordinates (2.91).

a Keplerian motion described by these orbital elements; instead, the formal osculating elements define an ellipse that cuts transversally the motion of the body (for this reason, astronomers have not made frequent use of these variables).

With this clarification, we can proceed to define the Delaunay variables for the N -planets problem. Indeed, since $\mathcal{H}_{\text{kepl}}$ is integrable, we can introduce its action-angle variables, and since $\mathcal{H}_{\text{kepl}}$ is the sum of the independent Hamiltonians (2.68) for each planet, these are simply the Delaunay variables (2.80) for each planet, namely

$$\begin{aligned} L_i &= \mu_i \sqrt{\mathcal{G}(m_0 + m_i)a_i}, & \ell_i &= n_i(t - \tau_i), \\ G_i &= L_i \sqrt{1 - e_i^2}, & g_i &= \omega_i \\ \Theta_i &= G_i \cos I_i, & \theta_i &= \Omega_i. \end{aligned} \quad (2.96)$$

for $i = 1, \dots, N$. The Keplerian Hamiltonian in these variables takes the simple form

$$\mathcal{H}_{\text{kepl}} = -\mathcal{G}^2 \sum_{i=1}^N \frac{\mu_i^3 (m_0 + m_i)^2}{2L_i^2}. \quad (2.97)$$

As in the case of a single planet, to avoid apparent singularities we can introduce the modified Delaunay variables

$$\begin{aligned} \Lambda_i &= L_i = \mu_i \sqrt{\mathcal{G}(m_0 + m_i)a_i}, & \lambda_i &= \ell_i + g_i + \theta_i = \ell_i + \varpi_i, \\ \Gamma_i &= L_i - G_i = L_i(1 - \sqrt{1 - e_i^2}), & \gamma_i &= -g_i - \theta_i = -\varpi_i, \\ Z_i &= G_i - \Theta_i = 2G_i \sin^2 \frac{I_i}{2}, & \zeta_i &= -\theta_i = -\Omega_i. \end{aligned} \quad (2.98)$$

and the cartesian Poincaré variables

$$\begin{aligned} \xi_i &= \sqrt{2\Gamma_i} \cos \gamma_i, & \eta_i &= \sqrt{2\Gamma_i} \sin \gamma_i, \\ \xi_{i+N} &= \sqrt{2Z_i} \cos \zeta_i, & \eta_{i+N} &= \sqrt{2Z_i} \sin \zeta_i. \end{aligned} \quad (2.99)$$

In terms of these variables, the perturbation $\mathcal{H}_{\text{pert}}$ takes the form of a Fourier series

$$\mathcal{H}_{\text{pert}}(\mathbf{\Lambda}, \mathbf{\Gamma}, \mathbf{Z}, \boldsymbol{\lambda}, \boldsymbol{\gamma}, \boldsymbol{\zeta}) = \sum_{\alpha, \beta \in \mathbb{N}_0^N} \sum_{\mathbf{k}, \mathbf{m}, \mathbf{s} \in \mathbb{Z}^N} c_{\alpha, \beta, \mathbf{k}, \mathbf{m}, \mathbf{s}}(\mathbf{\Lambda}) \Gamma^{\alpha/2} \mathbf{Z}^{\beta/2} \exp[i(\mathbf{k} \cdot \boldsymbol{\lambda} + \mathbf{m} \cdot \boldsymbol{\gamma} + \mathbf{s} \cdot \boldsymbol{\zeta})], \quad (2.100a)$$

$$\mathcal{H}_{\text{pert}}(\mathbf{\Lambda}, \boldsymbol{\xi}, \boldsymbol{\lambda}, \boldsymbol{\eta}) = \sum_{\alpha, \beta \in \mathbb{N}_0^N} \sum_{\mathbf{k} \in \mathbb{Z}^N} c_{\alpha, \beta, \mathbf{k}}(\mathbf{\Lambda}) \boldsymbol{\xi}^\alpha \boldsymbol{\eta}^\beta \exp[i\mathbf{k} \cdot \boldsymbol{\lambda}]. \quad (2.100b)$$

There is no simple expression of the perturbation in terms of these variables. Nonetheless it possesses some important analytical properties which are used extensively throughout this thesis and are briefly described below.

2.2.2.1 The perturbing Hamiltonian for the planetary problem

The development of the perturbing function $\mathcal{H}_{\text{pert}}$ has been a topic of vast research and I do not intend to cover all of its aspects, but I will concentrate on two main points that are of interest for us.

The first point is that there are rules that allow us to exclude certain Fourier terms in the expansions (2.100). These are called *d'Alembert rules*, and they follow directly from the analytical properties of the Hamiltonian and the geometrical definitions of the angles of the set of orbital elements. I will state them for the case of the perturbing function written in modified Delaunay elements, Equation (2.100a), since we will mainly use these in the following chapters:

1. The coefficients $c_{\alpha, \beta, \mathbf{k}, \mathbf{m}, \mathbf{s}}(\mathbf{\Lambda})$ are real and satisfy $c_{\alpha, \beta, \mathbf{k}, \mathbf{m}, \mathbf{s}}(\mathbf{\Lambda}) = c_{\alpha, \beta, -\mathbf{k}, -\mathbf{m}, -\mathbf{s}}(\mathbf{\Lambda})$, so there are only cosine terms ($\mathcal{H}_{\text{pert}}$ is invariant under simultaneous change of sign of all angles $\boldsymbol{\lambda}, \boldsymbol{\gamma}, \boldsymbol{\zeta}$);
2. $\sum_{i=1}^N (k_i - m_i - s_i) = 0$ ($\mathcal{H}_{\text{pert}}$ is invariant under an arbitrary rotation around the z axis, i.e. the origin of longitudes x is arbitrary) ;
3. The sum $\beta_1 + \dots + \beta_n$ is even ($\mathcal{H}_{\text{pert}}$ is invariant under simultaneous change of sign of all inclinations $I_i \rightarrow -I_i$);

4. $\left\{ \begin{array}{l} |m_j| \leq \alpha_j \text{ and they have the same parity, i.e. } m_j = -\alpha_j, -\alpha_j + 2, \dots, \alpha_j - 2, \alpha_j, \\ |s_j| \leq \beta_j \text{ and they have the same parity, i.e. } s_j = -\beta_j, -\beta_j + 2, \dots, \beta_j - 2, \beta_j \end{array} \right\}$ (in $\mathcal{H}_{\text{pert}}$ the singularity at $\Gamma_i = 0/Z_i = 0$ is apparent).

I refer to [Morbidelli(2002)] §1.9.3 for a more detailed proof.

The second point is a more practical one: how do we compute the coefficients $c_{\alpha,\beta,\mathbf{k},\mathbf{m},\mathbf{s}}$ in (2.100a) to actually make use of this Hamiltonian? To do this end, we notice that the perturbing Hamiltonian $\mathcal{H}_{\text{pert}}$ is a sum of interaction terms $\mathcal{H}_{\text{pert},i,j}$ with $i \neq j$, one for each planet-planet pair, so we can limit ourselves to investigate a single $\mathcal{H}_{\text{pert},i,j}$. Using as a temporary notation unprimed quantities for the inner planet and primed quantities for the outer planet in the selected pair, the planet-planet interaction term is a sum of two contributions

$$\mathcal{H}_{\text{pert},i,j} = \underbrace{-\mathcal{G} \frac{mm'}{\Delta}}_{\text{direct part } V_1} + \underbrace{\frac{\mathbf{p} \cdot \mathbf{p}'}{m_0}}_{\text{indirect part } T_1}, \quad \Delta := \|\mathbf{r} - \mathbf{r}'\| : \quad (2.101)$$

the direct part describes the pure planet-planet gravitational attraction, while the indirect term comes from the fact that we are not using a barycentric coordinate system.

For the direct part of the disturbing function, we introduce $\mathcal{R}_D = a'/\Delta$ and write

$$\text{direct part } V_1 = -\mathcal{G} \frac{mm'}{a'} \underbrace{\frac{a'}{\Delta}}_{\mathcal{R}_D} = -\frac{\mathcal{G}^2 (M_* + m') \mu'^2 mm'}{\Lambda^2} \mathcal{R}_D \simeq -\frac{\mathcal{G}^2 M_* mm'^3}{\Lambda'^2} \mathcal{R}_D :$$

the expansion of the function \mathcal{R}_D is the subject of many published works and can be found in [Murray & Dermott(1999)] (see also [Laskar(1985), Ellis and Murray(2000)]). The functional form of the typical term in \mathcal{R}_D is

$$b(\alpha) e^\alpha e'^{\alpha'} s^\beta s'^{\beta'} \cos(\phi), \quad s = \sin \frac{I}{2}, \quad s' = \sin \frac{I'}{2},$$

where $\alpha = a/a' < 1$, and $b(\alpha)$ is given in terms of the Laplace coefficients which depend weakly on α – in many problems, one actually considers $b(\alpha)$ constant.

The indirect part is easier to expand (see [Laskar and Boué(2010)] §5). We write

$$\text{indirect part } T_1 := \frac{\mathbf{p} \cdot \mathbf{p}'}{m_0} = \frac{\mu\mu'}{m_0} \left(\frac{\mathbf{p}}{\mu} \cdot \frac{\mathbf{p}'}{\mu'} \right) = \frac{\mu\mu'}{m_0} \mathbf{v} \cdot \mathbf{v}' = \frac{\mu\mu'}{m_0} \mathcal{T}, \quad \mathcal{T} = \mathbf{v} \cdot \mathbf{v}', \quad (2.102)$$

where we recall that $\mathbf{v}_i = \mathbf{p}_i/\mu_i$ plays the role of a barycentric velocity ($\mathbf{v}_i = m_i \dot{\mathbf{u}}_i/\mu_i$ where $\dot{\mathbf{u}}_i$ is the velocity in the barycentric inertial frame). Since we linked these velocities to the formal osculating orbital elements via Equation (2.76) (cfr. the previous section), we can use the elementary equations for these quantities from the Keplerian problem. In particular, using the equation for the ellipse (2.71) (see also footnote 12), the velocities can be rewritten as

$$\mathbf{v} = \dot{X} \mathbf{P} + \dot{Y} \mathbf{Q} = -na \left(\frac{a}{r} \sin E \right) \mathbf{P} + na \sqrt{1 - e^2} \left(\frac{a}{r} \cos E \right) \mathbf{Q}. \quad (2.103)$$

Then, one uses the classical developments (e.g. [Brouwer & Clemence(1961)])

$$\begin{aligned} \frac{a}{r} \cos E &= \frac{2}{e} \sum_{k \geq 1} J_k(ke) \cos(k\ell), \\ \frac{a}{r} \sin E &= 2 \sum_{k \geq 1} J'_k(ke) \sin(k\ell), \end{aligned} \quad (2.104)$$

where $J_k(\bullet)$ are the Bessel functions and $J'_k(\bullet)$ their first derivatives. For example in the planar case (Equation (2.77)) one writes

$$\mathcal{T} = v_x v'_x + v_y v'_y, \quad (2.105)$$

and

$$\begin{aligned} v_x &= \dot{X} \cos \varpi - \dot{Y} \sin \varpi, \\ v_y &= \dot{X} \sin \varpi + \dot{Y} \cos \varpi, \end{aligned} \quad (2.106)$$

and similarly for primed quantities. The expansion for \mathcal{T} can now easily be obtained using an algebraic manipulator.

2.3 Elements of Hamiltonian perturbation theory

Following [Poincaré(1892)], the general problem of dynamics is the following: given a Liouville-Arnold-Jost integrable Hamiltonian $\mathcal{H}_0(\mathbf{p})$, consider a small perturbation of it

$$\mathcal{H}(\mathbf{p}, \mathbf{q}, \epsilon) = \mathcal{H}_0(\mathbf{p}) + \epsilon \mathcal{H}_1(\mathbf{p}, \mathbf{q}), \quad (2.107)$$

where $\epsilon \ll 1$ is a small parameter. Here we will assume that all functions are analytic in all of their variables. The naïve idea would be to find a canonical transformation for which the transformed Hamiltonian is equal to \mathcal{H}_0 : then the system in the new variables would be integrable and the evolution of the old variables would be easily obtained from the latter and the change of variables. The non integrability theorem of Poincaré ([Poincaré(1892)]) however states that this hope is vain: If the perturbation \mathcal{H}_1 is general enough (as in the case of the planetary problem) there exist no analytic first integrals independent of \mathcal{H} , and the system is not integrable.

Nonetheless, one might hope to find a series of canonical transformations which push the perturbation to a higher order¹⁴ in the perturbative parameter ϵ . Then, the perturbation would become smaller, possibly negligible at least on short timescales, and an approximate integrable solution may be found. This is the goal of perturbation theory. In this brief section I only present the main tools and ideas that interest us, following mostly [Morbidelli(2002)], to which I refer for a deeper discussion and some applications (see chapter 2). I start with the first order perturbation theory making use of the Lie series formalism and finally briefly mention how the adiabatic principle can be seen as an application of this theory. The principles outlined here will be used heavily throughout the thesis, especially in Chapter 5.

2.3.1 First order perturbation theory

The most frequently adopted approach is to make use of the canonical transformations given by the Lie series (2.30) generated by a (now unknown) generating Hamiltonian χ , which we rewrite here for readability:

$$\begin{aligned} \mathbf{x} = \exp(\epsilon L_\chi) \mathbf{x}' &= \mathbf{x}' + \epsilon L_\chi \mathbf{x}' + \frac{\epsilon^2}{2} L_\chi^2 \mathbf{x}' + \dots \\ &= \mathbf{x}' + \epsilon \{\mathbf{x}', \chi\} + \frac{\epsilon^2}{2} \{\{\mathbf{x}', \chi\}, \chi\} + \dots \end{aligned} \quad (2.108)$$

Such a transformation is well suited for perturbation theory since it is a near-the-identity transformation. We then need to know how the Hamiltonian $\mathcal{H}(\mathbf{p}, \mathbf{q}) = \mathcal{H}(\mathbf{x})$ transforms under this change of coordinates: the answer is given by

Gröbner's exchange theorem. Given a dynamical variable $f = f(\mathbf{x})$, if one applies the change of variables $\mathbf{x} = \exp(tL_{\mathbf{X}}) \mathbf{x}'$, the expression f' of the dynamical variable in the new coordinates \mathbf{x}' is simply

$$f'(\mathbf{x}') := f(\mathbf{x})|_{\mathbf{x}=\exp(tL_{\mathbf{X}})\mathbf{x}'} \equiv (\exp(tL_{\mathbf{X}})f)(\mathbf{x})|_{\mathbf{x}'}, \quad (2.109)$$

where the notation $(\exp(tL_{\mathbf{X}})f)(\mathbf{x})|_{\mathbf{x}'}$ means that we calculate $(\exp(tL_{\mathbf{X}})f)(\mathbf{x})$ and then we just rename the variables: $\mathbf{x} \rightarrow \mathbf{x}'$.

This is because $f(\exp(tL_{\mathbf{X}})\mathbf{x}')$ represents $\phi_{\mathbf{X}}^t f(\mathbf{x}')$, the evolution of f under the flow of \mathbf{X} at time t with initial datum \mathbf{x}' ; then, by (2.18), (2.19), this equals $(\exp(tL_{\mathbf{X}})f)(\mathbf{x}')$ obtained calculating $(\exp(tL_{\mathbf{X}})f)$ and simply evaluating at \mathbf{x}' . Notice that (2.109) states that the two series expansions in t around $t = 0$ coincide.

Since the Hamiltonian itself is a dynamical variable, we can apply Gröbner's theorem to it, and expanding to second order in ϵ we get

$$\begin{aligned} \mathcal{H}'(\mathbf{x}', \epsilon) &= \mathcal{H}_0|_{\mathbf{x}'} + \epsilon \{\mathcal{H}_0, \chi\}|_{\mathbf{x}'} + \frac{\epsilon^2}{2} \{\{\mathcal{H}_0, \chi\}, \chi\}|_{\mathbf{x}'} + \dots \\ &\quad + \epsilon \mathcal{H}_1|_{\mathbf{x}'} + \epsilon^2 \{\mathcal{H}_1, \chi\}|_{\mathbf{x}'} + \dots, \end{aligned} \quad (2.110)$$

where the dots indicate terms of order $\mathcal{O}(\epsilon^3)$. Again the notation $\bullet|_{\mathbf{x}'}$ means that we simply consider everything as function of \mathbf{x}' . This first $\mathcal{O}(\epsilon)$ step of the procedure is completed if one deals with the terms of $\mathcal{O}(\epsilon)$ in (2.110), that

¹⁴We do not elaborate here on the problem of the optimal order, which is beyond the scope of this thesis. The interested reader may consult e.g. [Morbidelli(2002)] chapter 2.4.

is, $\epsilon(\{\mathcal{H}_0, \chi\} + \mathcal{H}_1)$: we need to find χ so that this bit takes the easiest possible form. As we anticipated before and for a reason that will be clear later, one cannot in general eliminate this term completely, so the resulting equation that we are looking for is

$$\{\mathcal{H}_0, \chi\} + \mathcal{H}_1 = \mathcal{H}_1^{(1)}, \quad (2.111)$$

which is called the homological equation. To solve it, we write \mathcal{H}_1 and the (yet unknown) χ as a Fourier series in the angles \mathbf{q}' ,

$$\begin{aligned} \mathcal{H}_1(\mathbf{x}') &= \mathcal{H}_1(\mathbf{p}', \mathbf{q}') = \sum_{\mathbf{k} \in \mathbb{Z}^n} c_{\mathbf{k}}(\mathbf{p}') e^{i\mathbf{k} \cdot \mathbf{q}'}, \\ \chi(\mathbf{x}') &= \chi(\mathbf{p}', \mathbf{q}') = \sum_{\mathbf{k} \in \mathbb{Z}^n} d_{\mathbf{k}}(\mathbf{p}') e^{i\mathbf{k} \cdot \mathbf{q}'}, \end{aligned} \quad (2.112)$$

and we calculate $\{\mathcal{H}_0, \chi\}$ as a Fourier series as well,

$$\{\mathcal{H}_0, \chi\} = -i \sum_{\mathbf{k} \in \mathbb{Z}^n} d_{\mathbf{k}}(\mathbf{p}') \mathbf{k} \cdot \boldsymbol{\omega}(\mathbf{p}') e^{i\mathbf{k} \cdot \mathbf{q}'}, \quad \boldsymbol{\omega}(\mathbf{p}') = \frac{\partial \mathcal{H}_0}{\partial \mathbf{p}'}(\mathbf{p}'). \quad (2.113)$$

The expressions of the unknown functions χ and $\mathcal{H}_1^{(1)}$ are then obtained comparing Fourier coefficients, and the formal solution would be¹⁵

$$\chi(\mathbf{p}', \mathbf{q}') = \sum_{\mathbf{k} \in \mathbb{Z}^n} d_{\mathbf{k}}(\mathbf{p}') e^{i\mathbf{k} \cdot \mathbf{q}'}, \quad \text{with } d_0 = 0, \quad d_{\mathbf{k}}(\mathbf{p}') = -i \frac{c_{\mathbf{k}}(\mathbf{p}')}{\mathbf{k} \cdot \boldsymbol{\omega}(\mathbf{p}')} \text{ for } \mathbf{k} \neq \mathbf{0}, \quad (2.114a)$$

$$\mathcal{H}_1^{(1)}(\mathbf{p}') = c_0(\mathbf{p}'). \quad (2.114b)$$

Clearly, this formal solution makes no sense whenever $\mathbf{k} \neq \mathbf{0}$ and $\mathbf{k} \cdot \boldsymbol{\omega} = 0$, which we called the resonant condition, cfr. (2.40), because of the vanishing divisor in $d_{\mathbf{k}}$. Therefore, in the case of resonances, it is not possible to remove the corresponding harmonic from \mathcal{H}_1 : instead of being a function of the sole actions \mathbf{p}' , $\mathcal{H}_1^{(1)}$ will have to retain the term $c_{\mathbf{k}}(\mathbf{p}') e^{i\mathbf{k} \cdot \mathbf{q}'}$. Moreover, we immediately realise that for the scheme (2.110) to work, $\mathcal{H}_1^{(1)}$ will have to contain the corresponding Fourier term of \mathcal{H}_1 also when $\mathbf{k} \cdot \boldsymbol{\omega}$ is non vanishing but $\leq \epsilon$: this is because, if we try to eliminate this term with a function χ as defined above, we generate terms that are formally of order ϵ^2 but are in reality bigger than the original one, because the denominator of the coefficient $d_{\mathbf{k}}$ is smaller than ϵ . This is the well-known problem of the small divisors. One way to circumvent these difficulties is to demand that, in a fixed domain \mathcal{U} in the action space of interest for the problem at hand, $\mathbf{k} \cdot \boldsymbol{\omega} > \sqrt{\epsilon}$, in order to ensure that the terms that are formally of order ϵ^2 are really smaller than those of order ϵ (this definition is correct because the value of p at the apex of a separatrix of a pendulum is of order $\sqrt{\epsilon}$ and therefore the unperturbed frequency at that value of the action is of order $\sqrt{\epsilon}$). We therefore introduce the resonant set up to order K

$$\mathcal{M}_{\boldsymbol{\omega}}^{K, \epsilon}(\mathcal{U}) := \{\mathbf{k} \in \mathbb{Z}^n : |\mathbf{k}| = |k_1| + \dots + |k_n| < K \text{ and } |\mathbf{k} \cdot \boldsymbol{\omega}(\mathbf{p}')| \leq \sqrt{\epsilon} \text{ for some } \mathbf{p}' \in \mathcal{U}\} \subset \mathbb{Z}^n. \quad (2.115)$$

This set contains all $\mathbf{k} \in \mathbb{Z}^n$ of order $|\mathbf{k}| < K$ which would contribute zero or small divisors in the chosen domain \mathcal{U} . Then we split the perturbation \mathcal{H}_1 as

$$\begin{aligned} \mathcal{H}_1 &= \mathcal{H}_1^{\text{R}} + \mathcal{H}_1^{\text{NR}} + \mathcal{H}_1^{\geq K}, \quad \text{with} \\ \mathcal{H}_1^{\text{R}} &:= \sum_{\mathbf{k} \in \mathcal{M}_{\boldsymbol{\omega}}^{K, \epsilon}(\mathcal{U})} c_{\mathbf{k}}(\mathbf{p}') e^{i\mathbf{k} \cdot \mathbf{q}'} \quad (\text{resonant terms up to order } K), \\ \mathcal{H}_1^{\text{NR}} &:= \sum_{\mathbf{k} \notin \mathcal{M}_{\boldsymbol{\omega}}^{K, \epsilon}(\mathcal{U}), |\mathbf{k}| < K} c_{\mathbf{k}}(\mathbf{p}') e^{i\mathbf{k} \cdot \mathbf{q}'} \quad (\text{nonresonant terms up to order } K), \\ \mathcal{H}_1^{\geq K} &:= \sum_{|\mathbf{k}| \geq K} c_{\mathbf{k}}(\mathbf{p}') e^{i\mathbf{k} \cdot \mathbf{q}'}, \end{aligned} \quad (2.116)$$

and we choose the order K high enough so that $\mathcal{H}_1^{\geq K}$ is of order at least ϵ with respect to $\mathcal{H}_1^{\text{R}} + \mathcal{H}_1^{\text{NR}}$ (this is always possible due to the exponential decay of the Fourier coefficients). Then the terms of $\mathcal{O}(\epsilon)$ of \mathcal{H}' will only be

¹⁵Notice that $\mathbf{k} \cdot \boldsymbol{\omega} = 0$ when $\mathbf{k} = \mathbf{0}$ always.

$\epsilon (\mathcal{H}_1^R + \mathcal{H}_1^{NR} + \{\mathcal{H}_0, \chi\})$, and we can solve the resulting homological equation $\mathcal{H}_1^R + \mathcal{H}_1^{NR} + \{\mathcal{H}_0, \chi\} = \mathcal{H}_1^{(1)}$ setting

$$\begin{aligned} \chi(\mathbf{p}', \mathbf{q}') &= \sum_{\mathbf{k} \notin \mathcal{M}_{\omega}^{K, \epsilon}(\mathcal{U}), |\mathbf{k}| < K} -i \frac{c_{\mathbf{k}}(\mathbf{p}')}{\mathbf{k} \cdot \omega(\mathbf{p}')} \mathbf{e}^{i\mathbf{k} \cdot \mathbf{q}'}, \\ \mathcal{H}_1^{(1)}(\mathbf{p}', \mathbf{q}') &= \mathcal{H}_1^R. \end{aligned} \quad (2.117)$$

Now χ is well defined and well suited for the scheme (2.110) since there are no zero nor small divisors and the sum is finite. With this, the transformed Hamiltonian \mathcal{H}' reads

$$\mathcal{H}'(\mathbf{p}', \mathbf{q}', \epsilon) = \mathcal{H}_0(\mathbf{p}') + \epsilon \mathcal{H}_1^R(\mathbf{p}', \mathbf{q}') + \mathcal{O}(\epsilon^2), \quad (2.118)$$

where \mathcal{H}_1^R only contains harmonics of the form $\mathbf{k} \cdot \mathbf{q}'$ with $\mathbf{k} \in \mathcal{M}_{\omega}^{K, \epsilon}(\mathcal{U})$. This is called a resonant normal form.

To sum up, the takeaway is the following. If there are no resonances in the action domain \mathcal{U} of interest, $\mathcal{H}_1^{(1)}$ in the homological equation (2.111) can be chosen to depend only on the actions, and (2.114b) shows that it is simply the average over all the angles of the perturbation \mathcal{H}_1 (only truncated up to Fourier harmonics of order K). If there are resonances we have to keep some angles in $\mathcal{H}_1^{(1)}$, and the resulting $\mathcal{H}_1^{(1)}(\mathbf{p}', \mathbf{q}')$ is an average over only some combinations of the angles of \mathcal{H}_1 , namely the nonresonant combinations of the angles $\mathbf{k} \cdot \mathbf{q}'$ with $\mathbf{k} \notin \mathcal{M}_{\omega}^{K, \epsilon}(\mathcal{U})$: then, $\mathcal{H}_1^{(1)}(\mathbf{p}', \mathbf{q}')$ only contains the resonant combinations $\mathbf{k} \cdot \mathbf{q}'$ with $\mathbf{k} \in \mathcal{M}_{\omega}^{K, \epsilon}(\mathcal{U})$. Then, there are the higher order terms, among which those that have been generated via $\{\{\mathcal{H}_0, \chi\}, \chi\}$ and $\{\mathcal{H}_1, \chi\}$. Writing these out explicitly (for a concrete example, see §2.4.2 of [Morbidelli(2002)]), one realises that these terms contain new combinations of the angles \mathbf{q}' which were possibly not present in the original Hamiltonian. Therefore, the normalisation process actually generates new harmonics, but of higher order. For a theory to order $\mathcal{O}(\epsilon)$ these can be dropped: this is why in the jargon of Celestial Mechanics this procedure is called *averaging*. We will present in Chapter 3 an application of this scheme in the context of the planetary problem in the case of mean motion resonances between planets. Moreover, we will make heavy use of the Lie series approach and the fact that it generates new harmonic terms in Chapter 5.

2.3.2 An introduction to adiabatic theory

The main idea of adiabatic theory is that for “simple” integrable systems (e.g. the ones given in the examples of Section 2.1.6) where the Hamiltonian is subjected to slow variations of its parameters (e.g. a little devil pulling the string of the pendulum and changing its length, in the language of [Arnold(1978)]) the energy changes but the mean action (energy divided by frequency) stays relatively constant. In the following I only sketch the ideas of how one can apply perturbation theory to derive the conservation of the adiabatic invariant up to some order. I follow closely [Henrard(1993)], to which I refer for a more detailed and precise derivation.

Consider a Hamiltonian system \mathcal{H} for which the Liouville-Arnold-Jost theorem is applicable, and make it dependent on one parameter λ : $\mathcal{H}(p, q, \lambda)$, with $(p, q) \in D \subseteq \mathcal{F}$ an open domain in the phase space and $\lambda \in \mathcal{U} \subseteq \mathbb{R}$ an open interval. For any “frozen” (fixed) value of the parameter λ , we can construct action-angle variables (I, ϕ) ; this canonical transformation can be defined implicitly by a generating function $S = S(I, q, \lambda)$ (see [Henrard(1993)] for the details, and recall Subsect. 2.1.3.1) by

$$\begin{cases} p = \frac{\partial S}{\partial q}(I, q, \lambda), \\ \phi = \frac{\partial S}{\partial I}(I, q, \lambda). \end{cases} \quad (2.119)$$

By definition of angle-action variables the transformed Hamiltonian \mathcal{H}' does not depend on ϕ , $\mathcal{H}' = \mathcal{H}'(I, \lambda)$: I is a constant and ϕ is an angle which evolves linearly with time, so we can trace the trajectory of the “frozen” system, which one can call a “guiding trajectory”.

Now assume that λ changes over time. If λ changes slowly enough, across a given short period of time the evolution governed by $\mathcal{H}(p, q, \lambda)$ will not change considerably from that of the “frozen” guiding trajectory, but on the long term the guiding trajectory will change. Adiabatic theory tells us “how, on the long time scale, the guiding trajectory evolves by determining a function of the guiding trajectory and the parameter which stays approximatively constant” [Henrard(1993)]. We can formally write the fact that λ changes slowly over time by assuming that $\lambda = \epsilon t$, with $\epsilon \ll 1$ a small parameter. (Actually, this condition is equivalent to the condition

$(1/n!)|d^n\lambda/dt^n| \leq \epsilon^n$ uniformly: this means that as long as λ changes slowly, it actually does not matter how it changes, which is a powerful aspect of adiabatic theory.) So now we must consider $\mathcal{H} = \mathcal{H}(p, q, \epsilon t)$ which is not an autonomous system. To apply the techniques of perturbation theory outlined above, we can make it autonomous by overextending the phase space introducing λ as a coordinate and its conjugated momentum Λ (cfr. Subsect. 2.1.2.1). The extended autonomous Hamiltonian is $\mathcal{H}_e = \mathcal{H}(p, q, \lambda) + \epsilon\Lambda$. The canonical transformation (2.119) to pass to the action-angle variables (I, ϕ) also has to be extended to the variables (Λ, λ) which will be transformed into new variables (Λ', λ') , and in order to keep λ unchanged we use the new generating function $S_e = S(I, q, \lambda) + \lambda\Lambda'$. With this choice, the extended transformation to action-angle variables reads

$$\begin{cases} p = \frac{\partial S_e}{\partial q} = \frac{\partial S}{\partial q}, \\ \Lambda = \frac{\partial S_e}{\partial \lambda} = \Lambda' + \frac{\partial S}{\partial \lambda}, \\ \phi = \frac{\partial S_e}{\partial I} = \frac{\partial S}{\partial I}, \\ \lambda' = \frac{\partial S_e}{\partial \Lambda'} = \lambda, \end{cases} \quad (2.120)$$

that is, we get the old transformation for the pair (p, q) onto (I, ϕ) and a transformation which keeps $\lambda' = \lambda$ unchanged. The Hamiltonian now writes

$$\mathcal{H}''(I, \Lambda', \phi, \lambda) = \mathcal{H}'(I, \lambda) + \epsilon[\Lambda' + R(I, \phi, \lambda)]. \quad (2.121)$$

where $R = \partial S/\partial \lambda$. This Hamiltonian is now ready for perturbation theory, with integrable part $\mathcal{H}_0 = \mathcal{H}'$ and a perturbation $\mathcal{H}_1 = R$, where the small parameter ϵ is now the frequency of the evolution of λ over time. If we apply recursively the procedure n times to push the perturbation at some order $n+1$ in ϵ , the resulting Hamiltonian in the transformed ‘‘averaged’’ action-angle variables¹⁶ $(\bar{I}, \bar{\phi})$ takes the form

$$\bar{\mathcal{H}}(\bar{I}, \bar{\Lambda}, \bar{\phi}, \lambda) = \mathcal{H}'(\bar{I}, \lambda) + \epsilon\bar{\Lambda} + \sum_{j=1}^n \frac{\epsilon^j}{j!} \bar{\mathcal{H}}_j(\bar{I}, \lambda) + \epsilon^{n+1} \mathcal{H}_r; \quad (2.122)$$

the term $\sum_{j=1}^n \frac{\epsilon^j}{j!} \bar{\mathcal{H}}_j(\bar{I}, \lambda)$ encapsulates the fact that at each step we must keep the ϕ -independent terms of the perturbation, while the term $\epsilon^{n+1} \mathcal{H}_r$ is the $\bar{\phi}$ -dependent remainder of higher order in ϵ . This Hamiltonian gives for the ‘‘averaged’’ (mean) action \bar{I} the evolution equation

$$\left| \frac{d\bar{I}}{dt} \right| = \epsilon^{n+1} \left| \frac{\partial \mathcal{H}_r}{\partial \bar{\phi}} \right| \leq C_1^{(n)} \epsilon^{n+1}, \quad (2.123)$$

where $C_1^{(n)}$ is the supremum of $|\partial \mathcal{H}_r/\partial \bar{\phi}|$ over the domain of interest \bar{D} , the image of the initial domain D after all canonical transformations (this supremum depends on the order n of the perturbative procedure and may get large with n). From this, we get¹⁷

$$|\bar{I}(t) - \bar{I}(0)| \leq C_1^{(n)} \epsilon^{n+1} |t|, \quad (2.124)$$

as long as $(\bar{I}, \bar{\phi}, \lambda)$ remain in the domain $\bar{D} \times \mathcal{U}$. Assuming that $\lambda = \epsilon t$ does not leave the original domain \mathcal{U} , by (2.124) itself, we know that since $(\bar{I}(0), \bar{\phi}(0)) \in \bar{D}$, the condition that $(\bar{I}, \bar{\phi})$ remain in \bar{D} is satisfied over times $|t| < \epsilon^{-n}$. Therefore, over this length of time \bar{I} is approximatively conserved as indicated by (2.124).

Because of the geometrical definition of the action, this means that the (signed) area enclosed by the periodic orbit remains relatively constant along the evolution, whatever may the change in λ be, as long as it is slow compared to the evolution of the action-angle variables. For this reason \bar{I} is called the *adiabatic invariant*. Notice instead that the adiabatic principle does not hold when the orbit crosses a separatrix. This is because the system approaches an orbit of infinite period, so no matter how slow the change in λ is, it cannot be slower than the evolution of canonical variables themselves; this can also be seen as due to a boundary of the domain of definition of I and a loss of regularity of $\mathcal{H}(I)$ at that boundary. Therefore, the adiabatic invariant can indeed change due to separatrix crossing. After the orbit crosses a separatrix, its area jumps to become equal to that enclosed by the separatrix at the time of crossing, then the orbit typically goes into a region of growing area (if there are more than one region of increasing area, the jump into one or another is probabilistic and proportional to the ratio of the rates at which the areas increase), and then the area is preserved again. We apply these concepts in the next subsection, and make use of the adiabatic principle, implicitly or explicitly, throughout the remaining chapters of the thesis.

¹⁶The ‘‘averaged’’ variables actually depend on the order n of the perturbation procedure, so one should actually write $(\bar{I}^{(n)}, \bar{\phi}^{(n)})$.

¹⁷As usual in perturbation theory, this procedure can be extended up to an optimal order n that minimises $C_1^{(n)} \epsilon^{n+1}$.

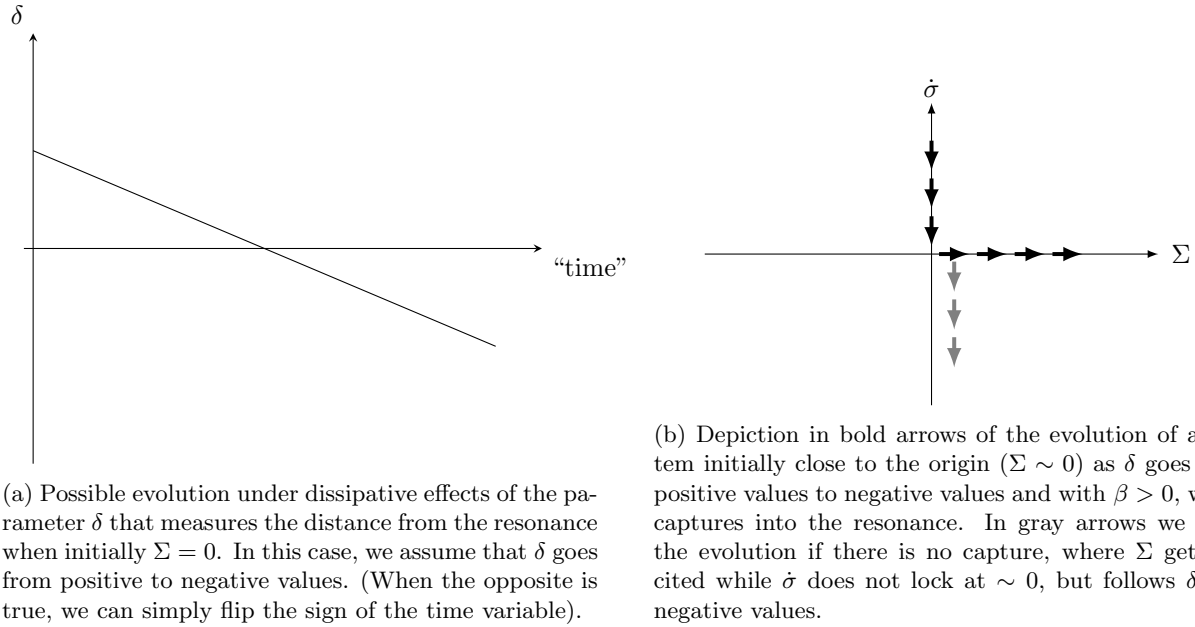


Figure 2.7: Depiction of the possibility of capture into a resonance.

2.3.3 Application of the adiabatic theory to resonant capture

The simplest model of a resonance with resonant angle σ and canonically conjugated action Σ makes use of an integrable Hamiltonian. The “first model for resonance” is the pendulum, which as we saw in Subsect. 2.1.6.3 is a local approximation for the dynamics. In the problems of Celestial Mechanics, a global integrable approximation for resonance usually takes the form of an Andoyer Hamiltonian, cfr. Equation (2.56), which I rewrite here for readability:

$$\mathcal{H}_{\text{And},k}(\Sigma, \sigma) = \delta\Sigma + \frac{\beta}{2}\Sigma^2 + c\sqrt{2\Sigma}^k \cos(k\sigma), \quad (2.125)$$

where δ , β , c are real numbers, with $\beta \neq 0$ and $c \neq 0$. The first two σ -independent addends are usually the larger contribution (which comes e.g. from the Keplerian Hamiltonian in a Celestial Mechanics resonance problem); it is expanded in power series in Σ as Σ is usually (at least initially) small. Notice that the last addend satisfies the d’Alembert rules in the canonical pair (Σ, σ) (this means that the singularity at the origin is only apparent and can be removed passing in canonical cartesian coordinates); this last term is usually smaller than the first (it comes e.g. from the perturbing Hamiltonian in Celestial Mechanics), which we can express by writing $c = \epsilon C$ where $\epsilon \ll |\beta|$ is a small parameter (e.g. the planet-to-star mass ratio).

As we saw in Subsect. 2.1.6.3, the system (2.125) is integrable, and we can draw phase diagrams such as the ones shown in Figures 2.3 and 2.4. There, we also recalled that resonances are not necessarily synonymous with libration and they are strictly linked to the presence of the separatrices, which enclose the resonant region(s) of the phase space. The emergence of the separatrices depends on the specific values of the parameters δ , β and c , and the fact that these coefficients are constants is true only in the conservative case. Whenever there are dissipative processes acting on the system (for example in the case of mean motion resonances it might be migration in protoplanetary disc, migration due to tides, ...) the coefficients will change, therefore the phase diagrams will change and the resulting dynamics will reflect these effects.

The general idea is the following. We consider a system which is initially close to an equilibrium point at (or near) the origin, so that $\Sigma \sim 0$, and whose dynamics is governed by (2.125) for some k . Over the evolution of δ , for $k = 1$ the dynamics around the equilibrium point is purely adiabatic, while for $k > 1$ the adiabatic principle breaks. As in Subsect. 2.1.6.3, we consider the cases $k = 1$ and $k = 2$ only, since they are enough to show when the adiabatic principle can be used and when it fails.

Consider the case $k = 1$ first, so the different phase diagrams for $\mathcal{H}_{\text{And},1}$ are the ones shown in Figure 2.3 (also reproduced in Figures 2.8 and 2.9 for readability, see below). Although the resonant region does not coincide with the libration region, at the resonant equilibrium point (the stable equilibrium point inside the resonant region)

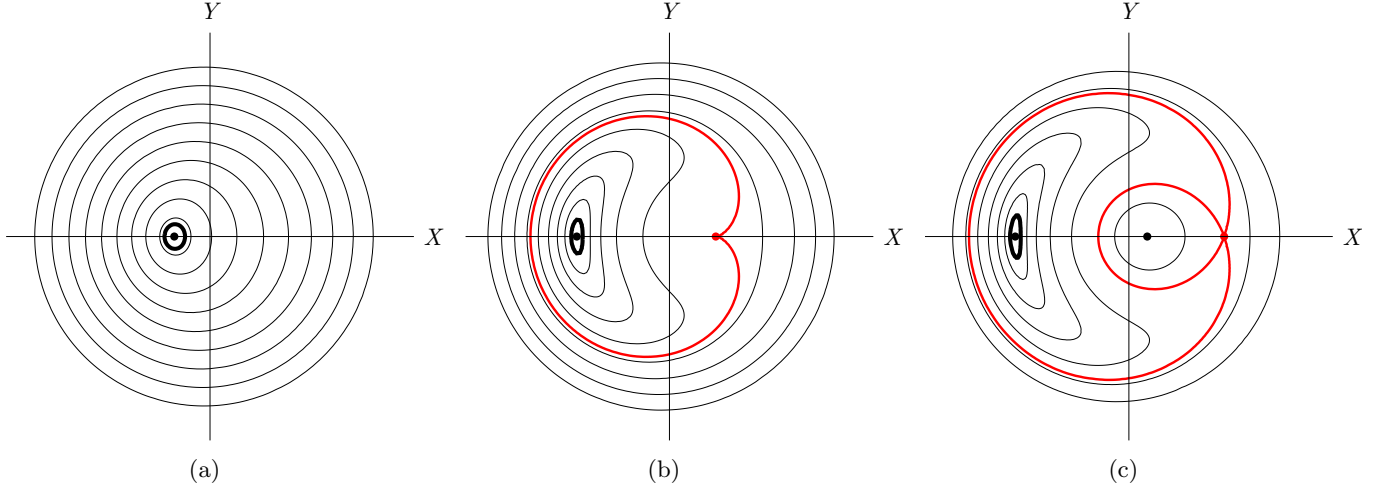


Figure 2.8: Depiction over the evolution of δ of the dynamics described in the text, in the case $k = 1$ and with $\delta\beta < 0$, so resonant capture is ensured by the adiabatic principle. The phase portraits are the same as in Figure 2.3, and the reference orbit is now marked with a thick black line. The system is initially close to the origin and with small amplitude of libration around the centre (panel (a)); it follows adiabatically the equilibrium point until the separatrix appears (panel (b)), so the orbit naturally ends up inside the resonant region (panel (c)). This situation corresponds to the black arrows in panel (b) of Figure 2.7.

the condition $\dot{\sigma} = 0$ must hold, so libration is a necessary condition for resonance at the equilibrium point. Since initially Σ is vanishingly small and the last term in (2.125) is small compared to the first two, we calculate

$$\dot{\sigma} \simeq \delta + \beta\Sigma \sim \delta \quad (2.126)$$

which shows that δ measures the initial distance from the resonance when the orbit is at (or close to) the origin. Therefore, for this orbit to cross and be captured in the resonance, δ must cross the value 0. Let us assume to fix ideas that δ changes from positive to negative, and write $\delta(t)$ as a function of some “time” t (Figure 2.7 panel (a)). Initially $\Sigma \sim 0$, so $\dot{\sigma} \sim \delta$ and therefore $\dot{\sigma}$ is initially positive and approaching 0. Then at one moment in “time”, $\dot{\sigma} \simeq \delta(t^*) = 0$: for there to be a capture, we need to keep $\dot{\sigma} \sim 0$ even for $t > t^*$ when actually $\delta(t) < 0$. Looking at equation (2.126), $\dot{\sigma} \simeq \delta + \beta\Sigma$, the only way for this to happen is if $\beta > 0$, so that the now negative term δ is cancelled by the positive term $\beta\Sigma$; in order for this to work though, Σ must keep increasing as δ keeps becoming more negative, and capture was successful. If the change in δ is much slower compared to the timescale of the evolution of the variables (Σ, σ) , this process is perfectly explained by adiabatic theory. If δ goes from positive to negative and $\beta > 0$, we are in the same situation studied in Subsect. 2.1.6.3 and we read the change in the phase diagrams in Figure 2.3 from left to right; the same sequence is reproduced in Figure 2.8 for readability, where we also mark the reference orbit as a thick curve. Assuming that we have a small amplitude of libration around the stable equilibrium point in panel (a), as δ decreases slowly we adiabatically follow the equilibrium as it shifts away from the origin, maintaining the same area enclosed by the orbit. Then, a bifurcation generates the separatrices (panels (b) and (c)) which enclose the centre equilibrium point followed by the orbit, which is the true condition for resonance. Therefore, for $k = 1$ when δ decreases slowly enough and β is positive, at small amplitude of libration around the equilibrium point resonant capture is guaranteed by adiabatic theory. Still in the case of decreasing δ , we saw at the beginning of Subsect. 2.1.6.3 that having instead $\beta < 0$ is equivalent to changing the sign of the time variable, and now the evolution is obtained reading Figure 2.3 right to left; this sequence is now reproduced in Figure 2.9 inverting the order of the panels (so Figure 2.9 can be read left to right like Figure 2.8), where again the reference orbit is marked as a thick curve. Initially we are still at small Σ , so now the evolution starts from the stable centre near the origin outside of the banana-shaped resonant region (panel (a) of Figure 2.9). As δ changes, the orbit is invested by the already present separatrix as it closes in towards the origin, and the adiabatic principle does not hold anymore (cfr. the last subsection). After the orbit crosses the separatrix, it typically goes into the region of growing area, that is into the the outer circulation zone in this case (panel (b)), and the orbit now encloses a bigger area than it did before, equal to the area enclosed by the separatrix at the moment of the crossing, and is then maintained adiabatically (Figure 2.9, panel (c)).

Consider now $k = 2$ so we refer to Figure 2.4, and again the case of δ going from positive to negative values to fix ideas. If $\beta > 0$ we can again read the panels of Figure 2.3 left-to-right/top-to-bottom to understand the

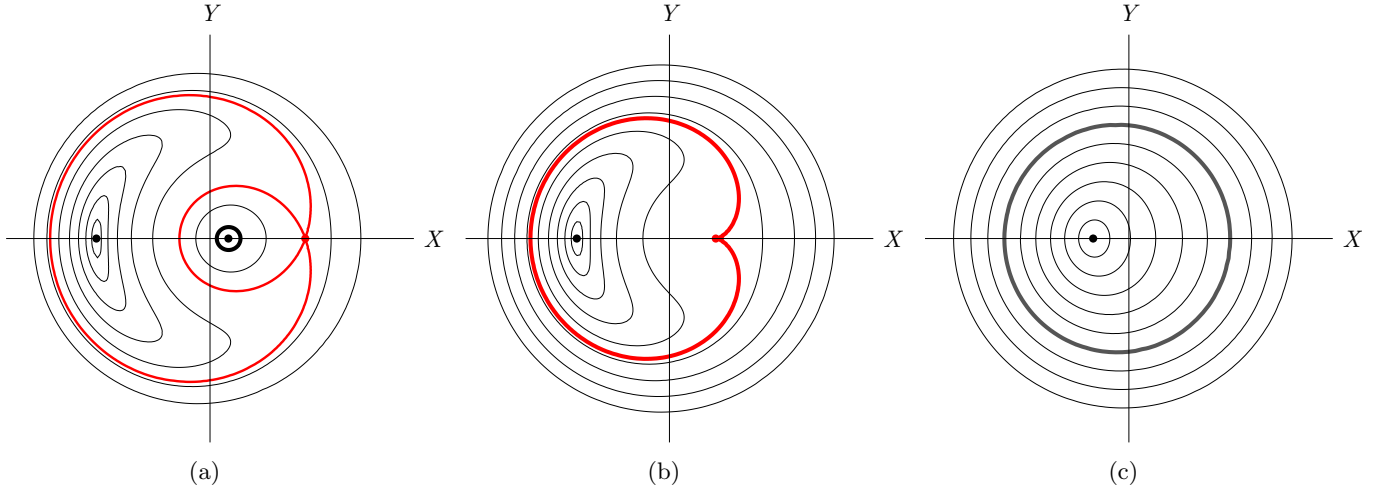


Figure 2.9: Same as Figure 2.8, but now $\dot{\delta}\beta > 0$ so the order of the phase diagrams over the evolution of δ is reversed respect to that of Figure 2.3. The orbit is again indicated by a thick line. At first, the system is near the centre close to the origin (panel (a)); then, as δ evolves, the orbit crosses the separatrix and its amplitude jumps non-adiabatically (panel (b), thick red line). This excited amplitude is then maintained adiabatically (panel (c), thick grey line). This situation corresponds to the grey arrows in panel (b) of Figure 2.7.

dynamics. We start again at vanishing Σ , that is at the centre equilibrium point at the origin in panel (a). As δ becomes smaller, there is a bifurcation (panel (b)) and a separatrix emerges from the origin itself. In this case, the adiabatic principle is not applicable anymore since the orbit crosses the separatrix. The system may enter one of the resonant lobes in panels (c), (d); then, after another bifurcation occurs (panel (e)), another stable centre appears at the origin enclosed by two new separatrices (panel (f)): if the orbit is still close enough to the separatrix, the adiabatic principle is again not applicable¹⁸ and the system may follow one of the resonant equilibria in the two resonant lobes, or end up in the inner circulation region. Therefore, for $k = 2$ when δ decreases slowly enough and β is positive, even at small amplitude of libration around the equilibrium point at the origin, resonant capture is a probabilistic phenomenon (the probability to fall into a region of expanding area or another is given by the ratio of the derivatives of the areas). In the case $\beta < 0$ (and still δ going from positive to negative) we again read the panels and the “time” in reverse order, starting as always from the equilibrium point at vanishing Σ , that is from the centre at the origin in panel (f). Now, as the value of δ changes the librating orbit is invested by the separatrices which are collapsing towards the origin (panel (e)), Σ gets excited and no capture is possible.

In both cases ($k = 1$ and $k = 2$), when $\delta(t)$ changes from negative to positive, the condition on the sign of β is flipped, as one can see by changing the sign to the time variable. Therefore, capture is only possible when $\dot{\delta}\beta < 0$.

The takeaway is the following. Resonant capture can occur only if $\dot{\delta}\beta < 0$. If the orbit is initially near $\Sigma = 0$, for $k = 1$ the capture in resonance is ensured by the adiabatic principle and for $k = 2$ (or larger) is probabilistic. The capture into resonance is followed by a monotonic increase of Σ over time. Instead, when $\dot{\delta}\beta > 0$, an orbit with initially $\Sigma \sim 0$ (whatever the k value) necessarily jumps across the resonance, with a consequent impulsive increase of Σ . The path taken by the evolution when capture is successful is shown in Figure 2.7 panel (b) in bold black arrows (for the case $\dot{\delta} < 0$ to fix ideas): $\dot{\sigma}$ initially follows the evolution of δ as long as $\Sigma \sim 0$, and when $\dot{\sigma}$ vanishes there is a capture in a resonance lobe which keeps $\dot{\sigma} = 0$ and forces Σ to increase as the resonant equilibrium gets farther and farther away from the origin. In grey arrows we show the case when there is no capture, so $\dot{\sigma}$ does not lock at ~ 0 and Σ gets a non-adiabatic kick due to the interaction with the separatrix; after the disappearance of the separatrix, the orbit maintains adiabatically its excited amplitude.

As a final remark, we should keep in mind that the Andoyer Hamiltonians (2.125) (or even the simpler pendulum model) represent only an integrable approximation to the real dynamics. In the real system (which is often non-integrable) the separatrices are replaced by chaotic bands. In this case, when an orbit meets the chaotic region around the separatrix, the probability to jump into a region or another is no longer simply proportional to the ratio of the derivatives of said areas. It depends also on the mixing properties of the chaotic zone [Henrard and Henrard(1991), Henrard and Morbidelli(1993)].

¹⁸This is typically the case when the second bifurcation occurs for a value of δ very close to that corresponding to the first bifurcation, as in the case of the 3:1 mean motion resonance and the secondary resonance studied in Chapter 5.

Chapter 3

Two planets – The structure of resonant pairs and capture into mean motion resonance

We begin in this chapter our investigation of planetary dynamics in mean motion resonance, focusing especially on Super-Earths/Mini-Neptunes. Recall from the Introduction, Subsections 1.2.2 and 1.2.3, that such planets are expected to form within the lifetime of their protoplanetary disc and interact gravitationally with it. A common outcome of planet-disc interactions is inward migration, which is halted at the inner edge of the disc. When multiple planets are embedded in the same disc, their slow convergent migration usually leads to the formation of a chain of mutual mean motion resonances. Due to this renewed interest in resonant captures, we revisit in this chapter the problem of capture in first order resonances of two equal-mass coplanar planets in convergent migration, using a semi-analytical approach and numerical simulations. In Section 3.1 we compute analytically the locus of equilibrium points of first-order resonances, where both the resonant and secular oscillations of the planetary orbits have a null amplitude. Our calculations are developed for unexpanded Hamiltonians, which allows to follow the dynamics up to arbitrarily large eccentricities (e.g. [Beaugé et al.(2006)], [Michtchenko et al.(2006)]). We compare the results with those obtained with first and second order expansions of the Hamiltonian in the eccentricity, showing qualitative and quantitative disagreements. The quantitative accuracy of our results is validated with simulations in which planets are forced to migrate towards each-other, without any eccentricity damping. These simulations have to follow the loci of the equilibrium points, and show perfect agreement with the unexpanded model. Moreover, we calculate the two frequencies of libration around the equilibrium points, therefore obtaining a complete understanding of the system; we again check the validity of the analytical calculations against numerical simulations in which the amplitudes of resonant and secular librations are slightly excited and the frequencies of oscillation of the semi major axis and the eccentricity are measured. In Section 3.2 we introduce the eccentricity damping exerted by the disc onto the planets. This leads to a final equilibrium configuration where convergent migration stops. The analytic calculation of the equilibrium eccentricities and semi major axes ratio is presented in Subsection 3.2.2. We check against numerical simulations the validity of these analytical predictions, showing excellent agreement. The content of this chapter has been published in [Pichierri et al.(2018)].

3.1 Structure of first-order mean motion resonances

Consider two planets of masses m_1 and m_2 orbiting the same star of mass M_* in a canonical heliocentric reference frame ([Poincaré(1892)], see also Subsect. 2.2.2), assuming coplanar orbits for simplicity. We introduce the Hamiltonian for the planar three-body problem $\mathcal{H} = \mathcal{H}_{\text{kepl}} + \mathcal{H}_{\text{pert}}$, in modified Delaunay variables $(\Lambda_i, \Gamma_i, \lambda_i, \gamma_i)$ (cfr. Equations (2.95) to (2.98)); the subscripts $i = 1, 2$ indicate the inner and outer planet respectively. We then impose a first order mean motion resonance between the two planets, that is we assume that the two mean motions $n_1 = \sqrt{\mathcal{G}(M_* + m_1)}/a_1^3$ and $n_2 = \sqrt{\mathcal{G}(M_* + m_2)}/a_2^3$ satisfy the resonance condition $kn_2 - (k-1)n_1 \sim 0$, where $k \in \mathbb{Z}$ is a positive integer, $k \geq 2$. In order to consider the resonant interactions only, we eliminate perturbatively the non-resonant angles: to first order in the planetary mass, this corresponds to averaging the Hamiltonian over the fast angles (cfr. Subsect. 2.3.1). In fact, since the Keplerian part $\mathcal{H}_{\text{kepl}}$ does not depend on the angles, only the perturbation Hamiltonian $\mathcal{H}_{\text{pert}}$ needs averaging. We note that we need to integrate $\mathcal{H}_{\text{pert}}$ e.g. with respect to

the angle λ_1 over the interval $[0, 2k\pi]$, corresponding to k revolutions of the inner planet around the star (which in turn by the resonance condition is equivalent to $(k - 1)$ revolutions of the outer planet), in order to fully recover the periodicity of the Hamiltonian. This leads to a new averaged perturbing Hamiltonian which we denote with \mathcal{H}_{res} :

$$\mathcal{H}_{\text{res}} := \langle \mathcal{H}_{\text{pert}} \rangle_{\lambda_1} = \frac{1}{2k\pi} \int_0^{2k\pi} \mathcal{H}_{\text{pert}} d\lambda_1; \quad (3.1)$$

the full averaged Hamiltonian is therefore

$$\bar{\mathcal{H}} = \mathcal{H}_{\text{kepl}} + \mathcal{H}_{\text{res}}, \quad (3.2)$$

where as usual (cfr. Equation (2.97))

$$\mathcal{H}_{\text{kepl}} = -\frac{\mathcal{G}^2(M_* + m_1)^2\mu_1^3}{2\Lambda_1^2} - \frac{\mathcal{G}^2(M_* + m_2)^2\mu_2^3}{2\Lambda_2^2}. \quad (3.3)$$

From an analytical perspective, we remark that only certain combinations of the angles will appear in the Fourier expansion of the averaged Hamiltonian $\bar{\mathcal{H}}$. Indeed, by the d'Alembert rules (cfr. Subsect. 2.2.2.1), after the averaging procedure, of all angles depending explicitly on λ_1 and λ_2 , only those of the form

$$j(k\lambda_2 - (k - 1)\lambda_1) + j_1\gamma_1 + j_2\gamma_2, \quad j, j_1, j_2 \in \mathbb{Z}^+, j_1 + j_2 = j, \quad (3.4)$$

will survive. With this in mind, in order to simplify the expression of the resonant harmonics appearing in the Hamiltonian \mathcal{H}_{res} one can introduce the following canonical action-angle variables ([Sessin and Ferraz-Mello(1984)]):

$$\begin{aligned} \Theta &= \Lambda_2/k, & \theta &= k\lambda_2 - (k - 1)\lambda_1, \\ \mathcal{K} &= \Lambda_1 + \frac{k - 1}{k}\Lambda_2, & \kappa &= \lambda_1. \end{aligned} \quad (3.5)$$

The newly defined angle κ does not appear explicitly in the Hamiltonian, making its conjugated action \mathcal{K} a constant of motion. The significance of the conservation of \mathcal{K} is already explained in [Michtchenko et al.(2008), Batygin and Morbidelli(2013)a]; in particular it yields the location of exact Keplerian resonance from the observed values of semi-major axes. As we will see, especially at low eccentricities the semi-major axes of the two planets deviate away from the nominal commensurability, by an amount which also depends on the planetary masses. Therefore the observed values of a_1 and a_2 do not alone reveal how close the planets are to resonance, nor they represent the nominal values \bar{a}_1 and \bar{a}_2 of the semi-major axes that satisfy the exact Keplerian resonant relationship $\bar{a}_1/\bar{a}_2 = ((k-1)/k)^{2/3}$. However by calculating from their observed values the value of the constant \mathcal{K} , and imposing in the formula

$$\frac{\mathcal{K}}{\Lambda_2} = \frac{\mu_1}{\mu_2} \sqrt{\frac{(M_* + m_1)a_1}{(M_* + m_2)a_2}} + \frac{k - 1}{k}, \quad (3.6)$$

the condition of exact resonance, $\alpha = a_1/a_2 = ((k - 1)/k)^{2/3}$, one can obtain \bar{a}_2 from $\bar{a}_2 = (\bar{\Lambda}_2/\mu_2)^2/(\mathcal{G}(M_* + m_2))$ and \bar{a}_1 from $\bar{a}_1 = ((k - 1)/k)^{2/3}\bar{a}_2$.

Considering now the remaining three pairs of canonical action-angle variables, a final canonical transformation is made¹:

$$\begin{aligned} \Psi_1 &= \Gamma_1 + \Gamma_2, & \psi_1 &= \theta + \gamma_1, \\ \Psi_2 &= -\Gamma_2, & \delta\gamma &= \gamma_1 - \gamma_2, \\ \Omega &= \Theta - \Gamma_1 - \Gamma_2, & \theta' &= \theta; \end{aligned} \quad (3.7)$$

Using again (3.4), it is trivial to see that in the Hamiltonian $\bar{\mathcal{H}}$ only angles of the form

$$j\psi_1 + j_2\delta\gamma, \quad j, j_2 \in \mathbb{Z}^+ \quad (3.8)$$

will appear, i.e. angles in which θ' does not enter explicitly, making Ω our second constant of motion and thus reducing to two the degrees of freedom of our system. Note that the two constants of motion Ω and \mathcal{K} are linked to the total angular momentum \mathcal{L} , which in these mixed variables (orbital elements derived from heliocentric positions and barycentric velocities) is given by

$$\mathcal{L} = m_1\sqrt{\mathcal{G}(M_* + m_1)a_1(1 - e_1^2)} + m_2\sqrt{\mathcal{G}(M_* + m_2)a_2(1 - e_2^2)}; \quad (3.9)$$

to first order in the masses, we have $\mathcal{K} + \Omega = \mathcal{L}$.

¹This transformation, as well as (3.5), is an example of the extended (linear) point transformations, cfr. Subsect. 2.1.3.2: the (linear) transformation on the angles is canonically extended to find the corresponding new momenta.

3.1.1 First and higher order expansions of the Hamiltonian in the eccentricities

An analytical treatment of first order resonances making use of an expansion of the Hamiltonian up to first order in the eccentricities was presented in [Batygin and Morbidelli(2013)a], yielding a qualitative description of the resonant dynamical evolution of two planets. Following this approach, the resonant Hamiltonian \mathcal{H}_{res} in modified Delaunay variables (2.98) takes the form

$$\mathcal{H}_{\text{res}} = -\frac{\mathcal{G}^2 M_* m_1 m_2^3}{\Lambda_2^2} \left(f_{\text{res}}^{(1)} \sqrt{\frac{2\Gamma_1}{\Lambda_1}} \cos(k\lambda_2 - (k-1)\lambda_1 + \gamma_1) + f_{\text{res}}^{(2)} \sqrt{\frac{2\Gamma_2}{\Lambda_2}} \cos(k\lambda_2 - (k-1)\lambda_1 + \gamma_2) \right), \quad (3.10)$$

where we used the approximation $\Gamma \simeq \Lambda e^2/2$, valid at small eccentricities. The coefficients $f_{\text{res}}^{(1)}$ and $f_{\text{res}}^{(2)}$ are typically of order unity and depend (weakly) on the semi-major axis ratio; it is straightforward to incorporate direct and indirect terms (cfr. Subsect. 2.2.2.1). Note that, since this is an expansion up to first order in e and the two terms in parenthesis are already of order $\sqrt{\Gamma} = \mathcal{O}(e)$, we can evaluate Λ on the nominal values of the semi-major axis, thus fixing them to $\bar{\Lambda}_1$ and $\bar{\Lambda}_2$. By doing so, the coefficients f_{res} can be truly considered constant; one may find in [Murray & Dermott(1999)] formulæ to obtain their numerical value in the case of different resonances. We notice that $f_{\text{res}}^{(1)} < 0$ and $f_{\text{res}}^{(2)} > 0$. After the change of variables (3.5) the resonant Hamiltonian \mathcal{H}_{res} takes the simple form

$$\mathcal{H}_{\text{res}} = -\alpha_1 \sqrt{2\Gamma_1} \cos(\theta + \gamma_1) - \alpha_2 \sqrt{2\Gamma_2} \cos(\theta + \gamma_2), \quad (3.11)$$

where

$$\alpha_i = \frac{\mathcal{G}^2 M_*^2 m_1 m_2^3}{(M_* + m_2) \Lambda_2^2} \times \frac{f_{\text{res}}^{(i)}}{\sqrt{\Lambda_i}}, \quad i = 1, 2, \quad \alpha_1 < 0, \quad \alpha_2 > 0, \quad (3.12)$$

are constants that describe the strength of the two harmonics. The full Hamiltonian still of course retains the form $\tilde{\mathcal{H}} = \mathcal{H}_{\text{kepl}} + \mathcal{H}_{\text{res}}$ as in (3.2). While this Hamiltonian contains at the moment two harmonics, it is actually integrable, since it is possible to carry out a series of canonical changes of variables, following e.g. the approach in [Sessin and Ferraz-Mello(1984)], which makes it dependent on only one harmonic and extracts another integral of motion. The resulting Hamiltonian $\tilde{\mathcal{H}}$ will therefore only depend on a pair of canonical variables $(\tilde{\Psi}_1, \tilde{\psi}_1)$, which up to a change of signs takes the form of an Andoyer Hamiltonian $\mathcal{H}_{\text{And},1}$, also called *second fundamental model for resonance*:

$$\tilde{\mathcal{H}} = \delta \tilde{\Psi}_1 - \frac{1}{2} \tilde{\Psi}_1^2 - \sqrt{2\tilde{\Psi}_1} \cos(\tilde{\psi}_1). \quad (3.13)$$

This is no surprise, since we know that this class of Hamiltonians is well suited to study resonance problems in Celestial Mechanics [Henrard and Lemaître(1983)]. This advantageous reduction is carried out in Appendix A (to which I refer for the definitions of the canonical variables $(\tilde{\Psi}_1, \tilde{\psi}_1)$ and of the proximity parameter $\tilde{\delta}$ – note in particular that $\tilde{\Psi}_1$ is proportional to the eccentricity squared), and can be used to obtain a general description of the dynamics (e.g. [Batygin and Morbidelli(2013)a, Batygin(2015)], [Ramos et al.(2017)]). However it is insufficient when one confronts even qualitatively the prediction of this theoretical model with results from numerical simulations, as we will see in the next subsection, where we compute the locus of equilibrium points (i.e. periodic orbits of the full problem) as a function of the system’s angular momentum.

Higher order expansions are possible. However the Hamiltonian can no longer be reduced to one depending on a single combination of angles, i.e. it will not be integrable. Moreover, while they represent a more faithful representation of the real dynamics, it is still not adequate enough for good quantitative accord with the results of numerical simulations, as we will see in the next section. Therefore we develop below the formalism for un-expanded Hamiltonians, using a semi-analytical approach (i.e. computing the integral (3.1) numerically), already employed e.g. in [Moons and Morbidelli(1993), Moons and Morbidelli(1995)], [Sidorenko(2006)] (as well as in [Pichierri et al.(2017)], on which Chapter 6 of this thesis is based) for the restricted problem and in [Beaugé et al.(2006)], [Michtchenko et al.(2006)] for the full three-body problem.

3.1.2 Equilibrium points of the averaged Hamiltonian

We now consider the averaged Hamiltonian $\bar{\mathcal{H}}(\Psi_1, \Psi_2, \psi_1, \delta\gamma; \Omega)$ as a system with two degrees of freedom with parametric dependence on the value of Ω , the action defined in (3.7) (note that the symbol Ω usually denotes the

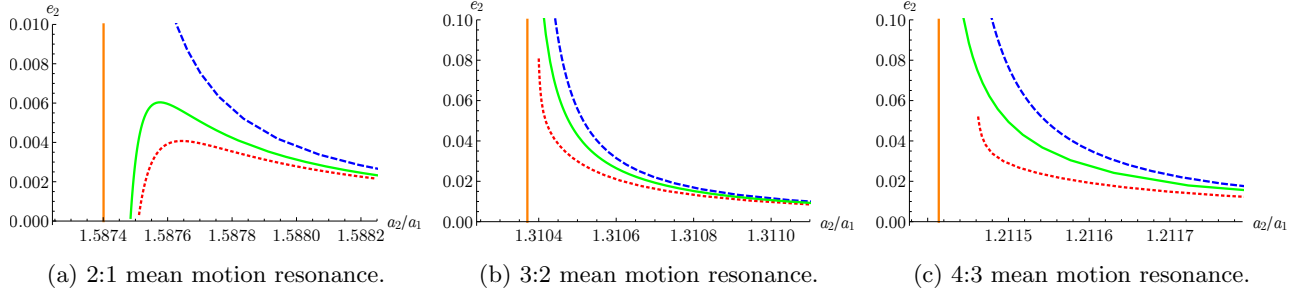


Figure 3.1: Equilibrium curves for three different first-order mean motion resonance, calculated using the first-order expansion (3.10) (dashed blue line), a second-order expansion (dotted red line) and the full averaged Hamiltonian (3.1) (continuous green line). Here we put $m_1 = m_2 = m = 10^{-5}M_*$. The equilibrium values for the angles are $\psi_{1,\text{eq}} = 0$ and $\delta\gamma_{\text{eq}} = \pi$. The orange vertical line indicates the location of exact Keplerian resonance, $a_2/a_1 = \bar{a}_2/\bar{a}_1 = (k/(k-1))^{2/3}$. Note the discrepancy between the equilibrium curves with and without the expansion of the resonant Hamiltonian, due to the presence of higher order harmonics which are not taken into account in the expanded Hamiltonians.

longitude of the node, which is not defined in this case given the planar nature of the problem), and look for its equilibrium points. The Hamiltonian also parametrically depends on \mathcal{K} , but as we have seen this variable encodes the location of exact resonance, for which $a_2/a_1 = \bar{a}_2/\bar{a}_1 = (k/(k-1))^{2/3} =: \bar{R}$, as well as the value of the planetary masses. Once we have fixed m_1, m_2 and k , we can choose units in which $\bar{a}_2 = 1$, so that \mathcal{K} obtains a natural value relative to the problem at hand.

Equilibrium points correspond to stationary solutions (cfr. Subsect. 2.1.5), and are therefore found by solving simultaneously in the variables $(\Psi_1, \Psi_2, \psi_1, \delta\gamma) = \mathbf{x}$ the set of equations

$$\frac{\partial \mathcal{H}}{\partial \Psi_1} = 0, \quad \frac{\partial \mathcal{H}}{\partial \Psi_2} = 0, \quad \frac{\partial \mathcal{H}}{\partial \psi_1} = 0, \quad \frac{\partial \mathcal{H}}{\partial \delta\gamma} = 0, \quad (3.14)$$

for different values of the constant of motion Ω . Because of the analytical properties of the Hamiltonian $\bar{\mathcal{H}}$, namely the fact that it contains only cosines of angles of the form (3.8), any combination of equilibrium values $\psi_{1,\text{eq}} = 0, \pi$ and $\delta\gamma_{\text{eq}} = 0, \pi$ will satisfy the last two equations in (3.14). Taking any of these possible combinations, we solve the first two equations in (3.14) for Ψ_1 and Ψ_2 , and we find two values $(\Psi_{1,\text{eq}}, \Psi_{2,\text{eq}})$. We then have to check that the point $\mathbf{x}_{\text{eq}} = (\Psi_{1,\text{eq}}, \Psi_{2,\text{eq}}, \psi_{1,\text{eq}}, \delta\gamma_{\text{eq}})$ is a *stable* equilibrium point for the Hamiltonian $\bar{\mathcal{H}}$. In principle, the last two equations in (3.14) could be satisfied for a combination of values of ψ_1 and $\delta\gamma$ different from $0, \pi$ (asymmetric equilibria), but this is the case only if all symmetric equilibria are unstable. This is because in the adiabatic limit in which one takes the second (slower) degree of freedom $(\Psi_2, \delta\gamma)$ as fixed, the Hamiltonian can be considered as describing an integrable one-degree-of-freedom system in the pair of (faster) variables (Ψ_1, ψ_1) , with slowly varying parameters corresponding to the slow degree of freedom. It is well known that, for a one-degree of freedom system and at the relatively low eccentricities that are obtained in the process of capturing into resonance, asymmetric equilibria are possible only if a bifurcation occurs which changes the nature of the symmetric equilibria (which always exist) from stable to unstable. Thus, if one finds a stable symmetric equilibrium the search for asymmetric stable equilibria can be avoided. The condition for stability of the equilibria is discussed in the next Section and is the usual criterion whereby one imposes that the eigenvalues of the matrix which describes the linear approximation of the system around the equilibrium be purely imaginary (see Subsection 2.1.5).

By changing the value of the constant Ω we obtain different equilibrium configurations, and once an equilibrium point in the canonical variables $(\Psi_1, \Psi_2, \psi_1, \delta\gamma)$ is obtained, we can easily work our way back through the canonical transformation and obtain the equilibrium values for the semi-major axes and eccentricities of the two planets, which we denote with $a_{1,\text{eq}}, a_{2,\text{eq}}, e_{1,\text{eq}}, e_{2,\text{eq}}$. This results in the stable equilibrium curves shown in Figures 3.1, 3.2, which are found for $\psi_{1,\text{eq}} = 0$ and $\delta\gamma_{\text{eq}} = \pi$.

We should immediately remark one property of these curves. As one can see from the first order expansion (3.10), the rates of precession of the perihelia are estimated by $\dot{\gamma} \propto 1/\sqrt{\Gamma} \sim 1/e$, which grows substantially as $e \rightarrow 0$. Therefore, in order to preserve the resonant condition $(\theta + \gamma) \sim 0$, it is necessary to have $\dot{\theta} = k\dot{\lambda}_2 - (k-1)\dot{\lambda}_1 \approx 0$, i.e. $a_2/a_1 \approx \bar{R} = (k/(k-1))^{2/3}$. Indeed, we see from Figures 3.1 that as the eccentricities vanish the equilibrium points deviate away from exact Keplerian commensurability, in a way that the semi-major axis ratio a_2/a_1 grows as $e \searrow 0$. This effect, as is shown in Figures 3.2, is more and more evident as the planetary mass increases, since

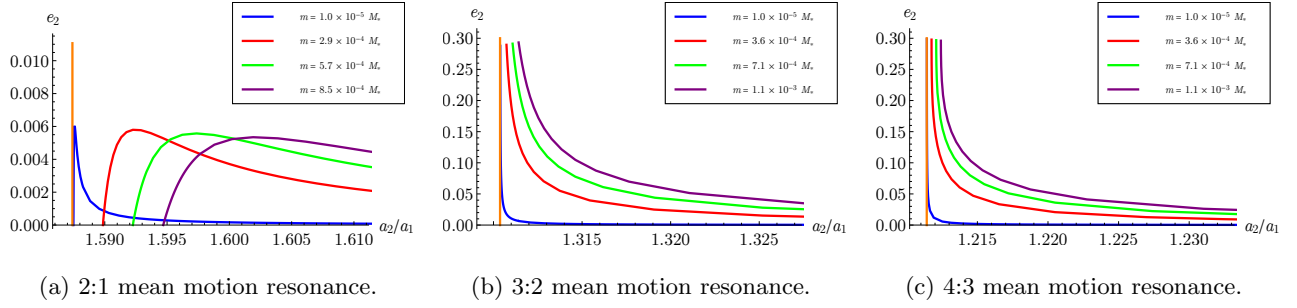


Figure 3.2: Equilibrium curves for the three different first-order mean motion resonance, calculated using the full averaged Hamiltonian (3.1), with different values for the planetary masses $m_1 = m_2 = m$. Here again we have fixed $\psi_{1,\text{eq}} = 0$ and $\delta\gamma_{\text{eq}} = \pi$. The orange vertical line indicates the location of exact Keplerian resonance, $a_2/a_1 = \bar{a}_2/\bar{a}_1 = (k/(k-1))^{2/3}$.

$\dot{\gamma} \propto m$. As a consequence, to sample these low-eccentricity equilibrium points with the correct value of Ω , it is necessary to plug into its analytical formula values of the semi-major axes such that $a_2/a_1 = \bar{R} + \delta(a_2/a_1)$.

We also point out the different equilibrium curves that one obtains using the expanded Hamiltonians and the non-expanded averaged Hamiltonian (Figure 3.1). The case of the 2:1 mean motion resonance is the most striking. Using a first order expansion, as the semi-major axis ratio approaches the exact Keplerian ratio one finds equilibrium points with increasing values of e_2 (and e_1). This is qualitatively different from the result obtained with higher order expansions and the averaged Hamiltonian: we see that e_2 reaches a maximum value and then starts approaching zero again (note that, although $e_2 \sim 0$, e_1 is large, so high order terms are important). This fact is known (e.g. [Beaugé et al.(2006)] and [Michtchenko et al.(2006)] using the numerical averaging of the Hamiltonian, [Hadjidemetriou(2002)] and [Antoniadou and Voyatzis(2014)] tracking periodic orbits). We further note that while the expansion to order 2 in the eccentricities captures this behaviour, it does not agree quantitatively with the averaged Hamiltonian. On the other hand, the analytical curve obtained with the full averaged Hamiltonian is in perfect agreement with a simulation in which two planets on initially circular orbits are subjected to convergent migration resulting in resonant capture (Figure 3.3). These simulations will be detailed in Section 3.2, but they are expected to track the locus of equilibrium points as the semi-major axis ratio a_2/a_1 decreases towards the Keplerian resonant ratio. Because here we apply no damping on the eccentricities, the latter are *a priori* free to grow towards unity. We observe that at the point in which e_2 vanishes, $\delta\varpi$ flips from π to 0, which is evident from Figure 3.3c. Indeed the equilibrium point on the $e_2 \cos(\delta\varpi)$ axis is initially on the negative side, and as the angular momentum decreases it moves to the positive axis. This transition from $\delta\varpi = \pi$ to 0 is smooth, and this is why the planets stay at the equilibrium point, without triggering secular oscillations.

We note that at higher values of e these equilibrium points found for $\delta\gamma = \pi$ (or $\delta\gamma = 0$ in the case of the 2:1 resonance) might be unstable, and stable asymmetric equilibrium points for different values of $\delta\gamma$ are possible (see for example [Beaugé et al.(2003)] and [Beaugé et al.(2006)], for a detailed study on the 2:1 mean motion resonance); in the case reported here, they are unstable for e_1 between about 0.28 and 0.35 corresponding to e_2 between about 0.08 and 0.11. We should also note that a similar behaviour of the equilibrium curves, where they reach a maximum value in e and then bend down to reach 0, is also present in the other resonances that we have considered, but that this happens at much higher values of e . In the case of the 3:2 and 4:3 resonances, it is e_1 that reaches a maximum value, of $e_1 \simeq 0.22$ and $e_1 \simeq 0.12$ respectively. However, these circumstances occur at high values of the eccentricities and are beyond the scope of this study.

3.1.3 Frequencies in the limit of small amplitude of libration

In this section we calculate the frequencies of the system around an equilibrium point for $\bar{\mathcal{H}}$ assuming small amplitude of libration by considering the linearised system near the equilibrium point. As we will see in the next section, we expect that in our numerical simulations the planets will be very close to the equilibrium in the variables (3.7), and will move from an equilibrium corresponding to some value of the constant of motion Ω to the next while preserving a small amplitude of libration. We then discuss how we can check numerically the validity of our calculations.

The procedure of calculating the frequencies is based on the general discussion of Subsect. 2.1.5. Near the

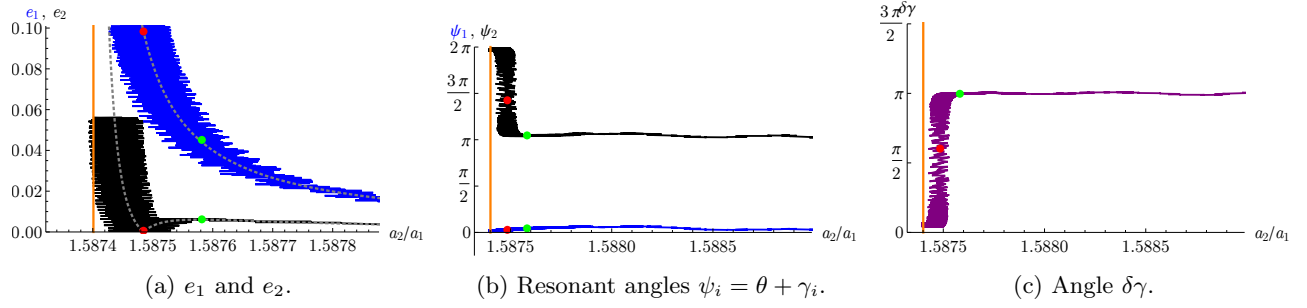


Figure 3.3: Result of a numerical simulation for two planets in the 2:1 mean motion resonance, with planetary masses $m_1 = m_2 = m = 10^{-5}M_*$. In panel (a) we show both eccentricities e_1 (in blue) and e_2 (in black); in panel (b) the resonant angles $\psi_1 = \theta + \gamma_1$ (in blue) and $\psi_2 = \theta + \gamma_2$ (in black); in panel (c) the angle $\delta\gamma$. In all panels the quantities are given in terms of the semi-major axes ratio a_2/a_1 , to easily compare the results with the panels in Figure 3.1a; in panel (a) we also superimpose the equilibrium curves, shown in dotted grey lines, for $\delta\gamma = \pi$ and $\delta\gamma = 0$. We again indicate in all plots the location of exact Keplerian resonance with an orange vertical line. The green points correspond to the equilibrium configuration of this system when $e_2 \simeq 0.006$ is maximal; the red points correspond to the equilibrium configuration of the system when e_2 has then reached the value 0. We observe that the evolution of the orbital parameters is very well described by our analytical curves; the large oscillations, visible especially in panel (a), are short-periodic, due mainly to the fast synodic angle $\lambda_1 - \lambda_2$, which is averaged out in the analytical model. We notice that when e_2 reaches 0 (red point) the value of $\delta\gamma$ is changing from π to 0. This happens without triggering large oscillations as the system is still smoothly following the curve of stable equilibrium points.

equilibrium point \mathbf{x}_{eq} the Hamiltonian $\bar{\mathcal{H}}(\Psi_1, \Psi_2, \psi_1, \delta\gamma) = \bar{\mathcal{H}}(\mathbf{x})$ can be approximated as

$$\bar{\mathcal{H}}(\mathbf{x}) = \bar{\mathcal{H}}(\mathbf{x}_{\text{eq}}) + \bar{\mathcal{H}}_{\text{lin}}(\mathbf{x}) + \bar{\mathcal{H}}_{\text{quad}}(\mathbf{x}) + \mathcal{O}(\mathbf{x}^3). \quad (3.15)$$

The linear part $\bar{\mathcal{H}}_{\text{lin}}(\mathbf{x}) \equiv 0$ by definition of equilibrium point, and the quadratic part is given by

$$\bar{\mathcal{H}}_{\text{quad}}(\mathbf{x}) = \frac{1}{2}(\mathbf{x} - \mathbf{x}_{\text{eq}})^T C (\mathbf{x} - \mathbf{x}_{\text{eq}}), \quad (3.16)$$

where $C := \mathbb{H}(\bar{\mathcal{H}}(\mathbf{x}_{\text{eq}}))$ is the Hessian of $\bar{\mathcal{H}}$ at the equilibrium point \mathbf{x}_{eq} . Dropping the unimportant constant term $\bar{\mathcal{H}}(\mathbf{x}_{\text{eq}})$ and ignoring the higher order terms, the linearised Hamiltonian system of equation then becomes

$$\frac{d}{dt}(\mathbf{x} - \mathbf{x}_{\text{eq}}) = J \nabla \bar{\mathcal{H}}_{\text{quad}} = J C (\mathbf{x} - \mathbf{x}_{\text{eq}}), \quad (3.17)$$

where $\nabla = \nabla_{\mathbf{x}}$, and J is the symplectic matrix

$$J = \begin{pmatrix} \mathbf{0} & -\mathbb{I} \\ \mathbb{I} & \mathbf{0} \end{pmatrix}. \quad (3.18)$$

The study of the stability of the equilibrium then reduces to writing the matrix $J C$ and finding its eigenvalues. Since we are dealing with a stable equilibrium point, we know from Subsect. 2.1.5 that the four eigenvalues will be purely imaginary and that they come in pairs, $(+i\omega_1, -i\omega_1)$ and $(+i\omega_2, -i\omega_2)$. These ω_1 and ω_2 are the two characteristic frequencies of the system at vanishing amplitude of libration around the equilibrium point: they are associated respectively with the (faster) libration of the resonant pair (Ψ_1, ψ_1) , and with the (slower) secular libration to which the pair of variables $(\Psi_2, \delta\gamma)$ is subjected. We expect that the frequency ω_1 will be much higher in absolute value than ω_2 , except at vanishing eccentricities, where the system exhibits a fast precession of the perihelia. As explained in Subsect. 2.1.5.1, there is a natural sign to the frequencies ω_l which is forced by the canonical diagonalisation procedure which yields the approximation $\mathcal{H} = \frac{\omega_1}{2}(p_1^2 + q_1^2) + \frac{\omega_2}{2}(p_2^2 + q_2^2)$ around the equilibrium point; we find that $\omega_l < 0$.

We check that our analytical calculations of the frequencies are correct as follows. We first take a system of two planets well in resonance, e.g. in the 3:2 mean motion resonance, $\lambda_1 \simeq \frac{3}{2}\lambda_2$, but not exactly on the equilibrium point. Here we take $m_1 = m_2 = 10^{-5}M_*$. We then observe the evolution of the orbital elements a and e , from which we obtain that of the four actions, and we record $\bar{\Psi}_1, \bar{\Psi}_2, \bar{\mathcal{K}}, \bar{\Omega}$ their mean values. Note that the mean values are needed

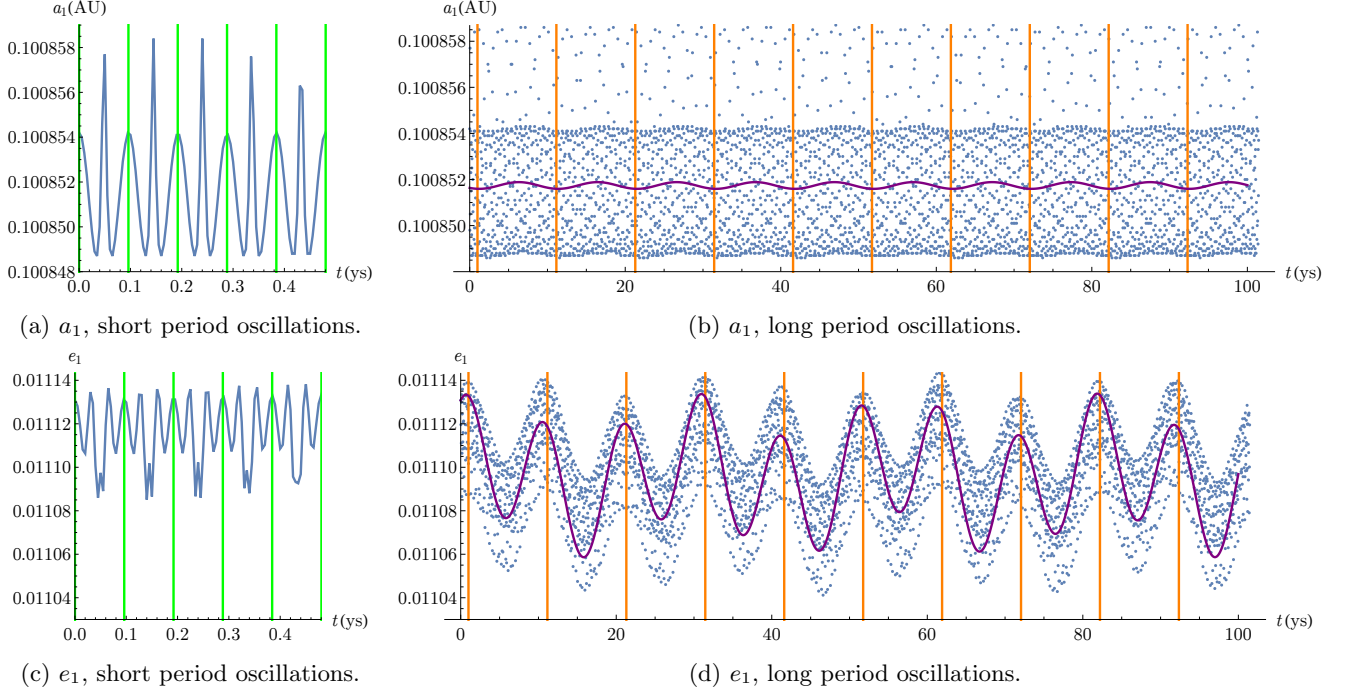


Figure 3.4: Evolution of a_1 and e_1 on different timescales for a system in the 3:2 mean motion resonance, after a forced small excitation of $R = a_2/a_1$. Here $m_1 = m_2 = 10^{-5}M_*$, $M_* = M_\odot$, in units where $\mathcal{G}M_* = (2\pi)^2$. We notice the fast evolution on the two left panels due to the synodic period $T_{\lambda_1 - \lambda_2} \simeq 0.096$ years (green vertical lines). On the right panels, we notice the oscillations with a longer period of $T_1 = 2\pi/|\omega_1| \simeq 10.5$ years (orange vertical lines), as predicted by the analytical calculation of ω_1 . The thick purple curve is the result of direct integration of the linearised equations of motion around the equilibrium point for the averaged Hamiltonian, equation (3.17); the initial conditions are the same as those for the numerical simulations. One sees that the analytical model follows very closely the averaged evolution obtained via 3-body numerical integration.

because the system is undergoing a fast evolution due to the non-resonant angles, which have been averaged out in our analytical model. In particular, e.g. in Figures 3.4a we notice the prominent effect of the harmonic relative to the circulating angle $\lambda_1 - \lambda_2$, with a frequency that can be calculated as $\omega_{\lambda_1 - \lambda_2} = (\dot{\lambda}_1 - \dot{\lambda}_2) = \frac{1}{3}\dot{\lambda}_1 = \frac{1}{3}2\pi/(a_1^{3/2}) \simeq 65.4$, for the actual value of $a_1 = 0.1008$ AU and assuming $\mathcal{G}M_* = (2\pi)^2$, that is a period $T_{\lambda_1 - \lambda_2} \simeq 0.096$ years for $M_* = M_\odot$. We then look at the two angles, checking that the resonant angle ψ_1 is librating (around 0) and noticing that $\delta\gamma$ librates (around π); we therefore fix $\bar{\psi}_1 = 0$ and $\delta\bar{\gamma} = \pi$. Using the values for $\bar{\mathcal{K}}$, $\bar{\Omega}$ and of the two angles $\bar{\psi}_1 = 0$, $\delta\bar{\gamma} = \pi$, we calculate analytically an equilibrium point \mathbf{x}_{eq} as explained above. This equilibrium point well represents the state of the system, with $\Psi_{1,\text{eq}}$ and $\Psi_{2,\text{eq}}$ differing from the observed mean values $\bar{\Psi}_1$, $\bar{\Psi}_2$ by less than 0.03%. For this equilibrium point we calculate the two frequencies $|\omega_1| \simeq 0.62$ and $|\omega_2| \simeq 0.23$, i.e. periods of $T_1 = 2\pi/|\omega_1| \simeq 10.5$ years and $T_2 = 2\pi/|\omega_2| \simeq 26.9$ years. In order to clearly see these two frequencies in a numerical simulation, we excite the system's initial condition in the semi-major axes ratio and in eccentricity respectively, thereby increasing the amplitude of librations relative to the resonant angle ψ_1 and the angle $\delta\gamma$. In practice, we first take the same initial conditions of the original unexcited system, and slightly excite the value of $R = a_2/a_1$, e.g. by forcibly change the initial value $a_2(0)$ of a_2 to $(1 + \epsilon)a_2(0)$, where ϵ is a small number. We plot the resulting evolution of the semi-major axis and eccentricity for the inner planet in Figure 3.4, where we see clearly an oscillation with period $T_1 \simeq 10.5$ years (panels (b), (d)). Similarly, we take again the same initial condition of the unexcited system and slightly excite the value of $e_2(0)$ to $(1 + \tilde{\epsilon})e_2(0)$, where $\tilde{\epsilon}$ is a small number. We plot the resulting evolution of the semi-major axis and eccentricity for the inner planet in Figure 3.5, where we now also see an oscillation with period $T_2 \simeq 26.9$ years on top of the one with period $T_1 \simeq 10.5$ years (panel (d)). In both Figures 3.4 and 3.5 we overplot the result of the analytical explicit integration of the linearised equations of motion (3.17) around the equilibrium point. These follow very closely the evolution of the 3-body integrations.

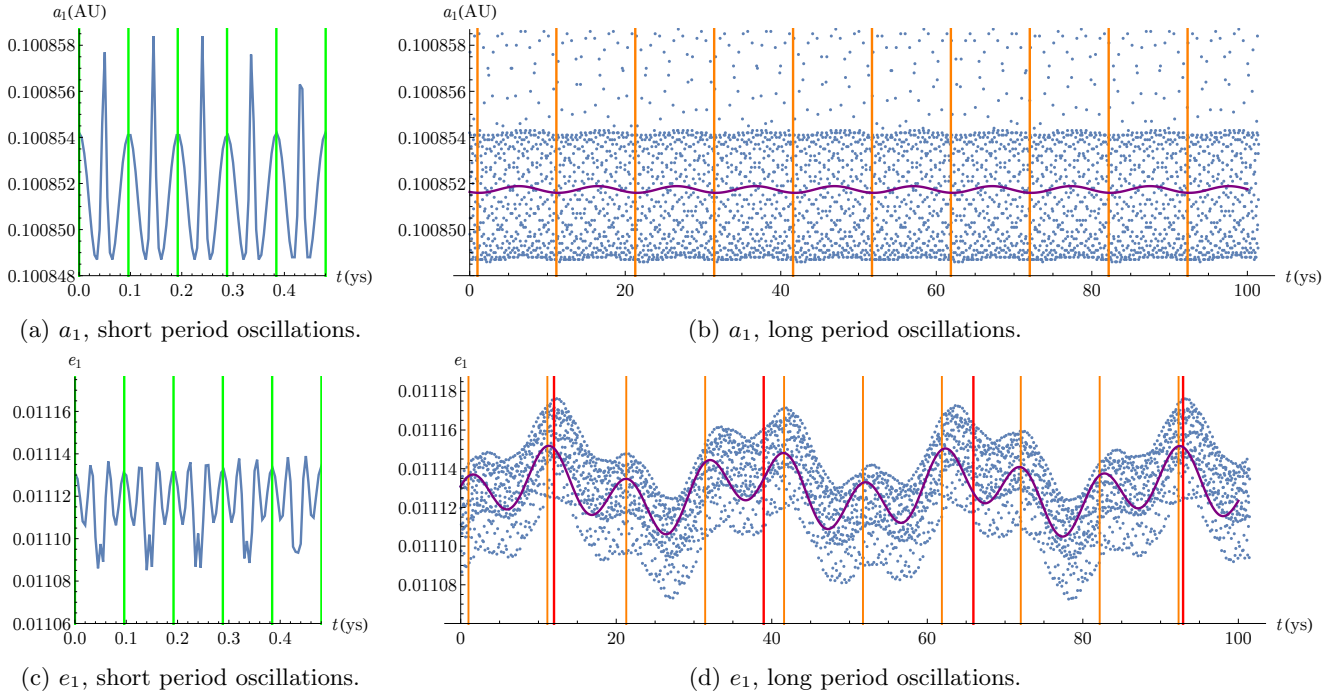


Figure 3.5: Evolution of a_1 and e_1 on different timescales for a system in the 3:2 mean motion resonance, after a forced small excitation of e_2 . Here $m_1 = m_2 = 10^{-5}M_*$, $M_* = M_\odot$, in units where $\mathcal{G}M_* = (2\pi)^2$, as in Figure 3.4. We notice again the fast evolution on the two left panels due to the synodic period $T_{\lambda_1-\lambda_2} \simeq 0.096$ years (green vertical line). On the right panels, we notice still the oscillations with a longer period of $T_1 = 2\pi/\omega_1 \simeq 10.5$ years (orange vertical lines); in addition, in panel (d) we notice how e_1 is now also effected by libration of $\delta\gamma$, with characteristic period of $T_2 = 2\pi/\omega_2 \simeq 26.9$ years (red vertical lines), as predicted by the analytical calculation of ω_2 . The thick purple curve is again the result of direct integration of equation (3.17), with the same initial conditions as the numerical simulations, showing again good fit.

3.2 Capture into resonance by type-I migration

With our resonant model at hand, we proceed in this section with the numerical and analytical treatment of resonant capture in a protoplanetary disc. This is an efficient method to obtain planets deeply in mutual mean motion resonance (e.g. [Matsumoto et al.(2012)], [Ramos et al.(2017)]). The first step is to consider the planet-disc interactions: we already discussed them in Subsect. 1.2.3 in the general context of planetary formation, and we give a more precise physical description below.

Because of its interactions with the disc, a planet feels a force and therefore an acceleration. This effect can be split into a component which causes the planet to migrate (generally inward), and a damping of the orbit's eccentricity and of the inclination with respect to the plane of the disc. [Cresswell and Nelson(2008)] give a recipe for these accelerations, see their formulæ (14-16)²:

$$\begin{aligned}
 [\text{acceleration due to migration}] &= \mathbf{a}_{\text{mig}} = -\frac{\mathbf{v}}{\tau_{\text{mig}}}, \\
 [\text{acceleration due to } e\text{-damping}] &= \mathbf{a}_e = -2\frac{(\mathbf{v} \cdot \mathbf{r})\mathbf{r}}{r^2\tau_e}, \\
 [\text{acceleration due to } I\text{-damping}] &= \mathbf{a}_I = -2\frac{v_z}{\tau_I}\hat{\mathbf{z}},
 \end{aligned} \tag{3.19}$$

where \mathbf{r} and \mathbf{v} are the heliocentric position and velocity vectors of the planet and $\hat{\mathbf{z}}$ is the unit vector in direction perpendicular to the disc. In the limit of small eccentricity and inclination, the timescales τ_{mig} , τ_e and τ_I are given

²We remark that formula (16) in [Cresswell and Nelson(2008)] contained a typo and the factor 2 was missing in the last equation, cfr. [Izidoro et al.(2019)] formula (A28).

by

$$\tau_{\text{mig}} \simeq 2 \frac{\tau_{\text{wave}}}{(2.7 + 1.1\alpha_{\Sigma})} h^{-2}, \quad (3.20a)$$

$$\tau_e \simeq \frac{\tau_{\text{wave}}}{0.780}, \quad (3.20b)$$

$$\tau_I \simeq \frac{\tau_{\text{wave}}}{0.544}, \quad (3.20c)$$

see [Cresswell and Nelson(2008)] formulæ (11-13); the timescale factor τ_{wave} is given by

$$\tau_{\text{wave}} = \frac{M_*}{m} \frac{M_*}{\Sigma a^2} \frac{h^4}{\sqrt{GM_*/a^3}}. \quad (3.21)$$

In these fomulæ, M_* is the mass of the star, m and a the mass and semi-major axis of the planet, $\Sigma = \Sigma(r) = \Sigma_0 r^{-\alpha_{\Sigma}}$ and $h = h(r) = H/r \propto (r/r_0)^{\beta_f}$ are the surface density and aspect ratio of the disc respectively and are evaluated at the position of the planet; α_{Σ} sets the surface density profile of the disc, β_f is flaring index (recall the general discussion on the disc structure in Subsect. 1.2.1).

In the following, we consider two equal-mass Super-Earth-type planets embedded in the same disc and under the influence of these dissipative forces in addition to their mutual gravitational interactions. We specialise for simplicity to the planar case where the mutual inclinations between the planets and with the disc vanishes, and we describe the process of capture into mean motion resonance by slow convergent migration.

3.2.1 Convergent inward migration in disc and resonant capture

Consider two planets of equal mass, $m_1 = m_2 = m$ (typically $m/M_* \simeq 10^{-5}$ in the case of Super-Earths), on coplanar orbits, embedded in a protoplanetary disc. We also write $\mu_1 = \mu_2 = \frac{M_* m}{M_* + m} =: \mu$ for the common reduced mass. To simulate the effect of the disc, we run numerical simulations consisting of the implementation of a symplectic 3-body integrator (`swift_symba`) to which the fictional analytical dissipative forces described above are added, following the [Cresswell and Nelson(2008)] prescriptions. We take as typical disc parameters $\beta_f = 0.25$ for the flaring index, $h|_{5.2\text{AU}} = 5\%$ for the scale-height, so that $z_{\text{scale}} = 0.05 \times (5.2 \text{ AU}/r_0)^{-\beta_f}$, and $\alpha_{\Sigma} = 1$ for the surface density profile of the disc. In what follows, we describe the effect of these forces in the context of capture in mean motion resonance, dropping for ease of reading the index $i = 1, 2$ to denote the planets' elements and parameters.

For each planet, the effect of the disc-planet interaction can be viewed as composed of two separate contributions, one operating on the eccentricity e and one operating on the semi-major axis a . Concerning the effect of the gas on the eccentricity e , our code implements a damping effect of the disc as

$$\dot{e}_{\text{damp}} := -\frac{e}{\tau_e}, \quad (3.22)$$

where τ_e is given, in the limit of vanishing eccentricities, by (3.20b). Secondly, the disc-planet interaction results in a torque, and therefore in an exchange of angular momentum \mathcal{L} . For a planet,

$$\mathcal{L} = m\sqrt{\mathcal{G}(M_* + m)a(1 - e^2)}. \quad (3.23)$$

The torque $T := \dot{\mathcal{L}}$ is taken here to be negative, so that the effect on the semi-major axis a is that of inward, type-I migration. It is modelled in our simulations as

$$\dot{\mathcal{L}}_{\text{mig}} = -\frac{\mathcal{L}}{\tau_{\text{mig}}}, \quad (3.24)$$

where τ_{mig} is given, again in the limit of vanishing eccentricities, by (3.20a), where we take $\alpha_{\Sigma} = 1$. To calculate the resulting effect on the semi-major axis a due to this planet-disc interaction, we take

$$\dot{\mathcal{L}} = \frac{d\mathcal{L}}{dt} = m\sqrt{\mathcal{G}(M_* + m)} \left(\frac{\dot{a}}{2\sqrt{a}} \sqrt{1 - e^2} - \frac{\sqrt{a}}{\sqrt{1 - e^2}} e\dot{e} \right), \quad (3.25)$$

and dividing by \sqrt{a} we obtain

$$\frac{\dot{a}}{a} = 2\frac{\dot{\mathcal{L}}}{\mathcal{L}} + \frac{2e\dot{e}}{1 - e^2} = -\frac{1}{\tau_a} - p\frac{e^2}{\tau_e}, \quad (3.26)$$

where $\tau_a = \tau_{\text{mig}}/2$ and $p \simeq 2$ for small e . Notice that for circular orbit the migration timescale τ_a is equal the one given in Equation (1.2). It is customary to introduce the quantity $K = \tau_a/\tau_e$ which we call K -factor (cfr. [Ramos et al.(2017)]). Notice that,

$$K = \frac{\tau_a}{\tau_e} \simeq \frac{0.780}{2.7 + 1.1} h^{-2} : \quad (3.27)$$

given that discs are very thin, e.g. here $h = \mathcal{O}(5 \times 10^{-2})$, we see that the K -factor is very large, of the order of at least $K = \mathcal{O}(10^2)$, meaning that the typical timescale of eccentricity damping is much shorter than that of migration. This allows us to assume that the planets approach the resonance on circular orbits, as any finite (but relatively small) initial eccentricity would be immediately damped by the disc.

In order to insure convergent migration and resonant capture, we need to stop the migration of the inner planet, since two equally massive planets would migrate inward at roughly the same rate and resonant capture would not occur (e.g. [Ramos et al.(2017)]). To do this, we simulate the effect of a disc edge, which corresponds to a sharp drop in Σ as r decreases. In this conditions, [Masset et al.(2006)] showed that a coorbital corotation torque is activated, which is positive and dominates the inward type-I torque, as we recalled in the Introduction, Subsect. 1.2.3. Thus inward migration stops at the inner edge of the disc. [Masset et al.(2006)] called this a *planet trap* and we follow this terminology here. For simplicity, the trap is modelled here by smoothly reversing the type-I torque. This is not what happens in reality. Modelling the real effects would require an appropriate implementation of the corotation torque, and that would depend on the Σ profile at the edge [Brasser et al.(2018), Izidoro et al.(2019)]. Our recipe, however, is effective to stop the inward migration of the innermost planet and to retain the second planet in resonance, that is to exhibit the same effects observed in hydrodynamical simulations ([Morbidelli et al.(2008)]). As we approach the disc edge d_{edge} (at 0.1 AU in our simulations) we implement the planetary trap by smoothly reversing the sign of the migration in order to stop the inner planet from migrating all the way into the star. This is achieved by dividing τ_a by a factor $\tau_{a,\text{red}}$ given by

$$\tau_{a,\text{red}} = \begin{cases} 1, & a \geq d_{\text{edge}}(1 + h_{\text{edge}}), \\ 5.5 \times \cos\left(\frac{((d_{\text{edge}} \times (1 + h_{\text{edge}}) - a)2\pi)}{4h_{\text{edge}} \times d_{\text{edge}}}\right) - 4.5, & d_{\text{edge}}(1 - h_{\text{edge}}) \leq a \leq d_{\text{edge}}(1 + h_{\text{edge}}), \\ -10, & 0 \leq a \leq d_{\text{edge}}(1 - h_{\text{edge}}), \end{cases} \quad (3.28)$$

where $h_{\text{edge}} = z_{\text{scale}}(d_{\text{edge}}/r_0)^{0.25}$ is the aspect ratio of the disc at the edge.

As initial conditions in our simulations we may assume circular orbits, $e_{1,\text{init}} = e_{2,\text{init}} = 0$, see above. Secondly, we choose the initial semi-major axes to be just outside a specific first order mean motion resonance, $a_{2,\text{init}} \gtrsim (k/(k-1))^{2/3} a_{1,\text{init}}$, $k = 2, 3, \dots$. The two planets will migrate inward at roughly the same rate (as they have the same mass) due to their interaction with the disc; the first planet will then reach the disc edge, where our imposed reversal of the sign of migration will cause it to stop migrating. The still migrating outer planet approaches the first planet and is then automatically locked in the desired mean motion resonance as a result of convergent type-I migration. The behaviour of the planets as they approach resonance can be understood using adiabatic theory, provided that the migration timescale is much longer than the resonant libration timescale (see Section 3.1.3 for the latter). When the planets are far from resonance, the damping effect of the disc ensures that their orbits are circular. But the circular orbit is also the limit of the curve of the resonant equilibria for large a_2/a_1 ratio (see Figures 3.1, 3.2). Thus, the planets are very close to the equilibrium in the variables (3.7) corresponding to their large a_2/a_1 ratio. If the evolution is adiabatic, the amplitude of libration around the equilibrium point (more precisely the value of the libration action) is preserved (cfr. Subsect. 2.3.2 and [Neishtadt(1999), Neishtadt et al.(2008), Henrard(1993)]). Given that initially this amplitude is close to zero, it will remain close to zero throughout the evolution. We can thus apply here the general discussion presented in Subsect. 2.3.3. Precisely, recall that, to first order in the eccentricities, the Hamiltonian may be cast in the form (3.13) – see Appendix A for a derivation and for the definition of the canonical variables $(\tilde{\Psi}_1, \psi_1)$ and of $\tilde{\delta}$, the proximity parameter to the desired $k : k - 1$ resonance. Note in particular that $\tilde{\Psi}_1$ is proportional to the eccentricity squared, while the parameter $\tilde{\delta}$ grows as the planets approach the resonance by convergent migration [Batygin(2015)]. Following the arguments of Subsect. 2.3.3, since the sign of the coefficient of $\tilde{\Psi}_1^2$ is negative, in the adiabatic limit resonant capture is guaranteed for small initial values of $\tilde{\Psi}_1$. Recall finally that $\tilde{\Psi}_1 \simeq 0$ is a condition naturally emerging in disc-planet interactions since $\tilde{\Psi}_1 \sim e^2$ and the eccentricities are initially small when the planets approach the resonance. This is shown in Figure 3.6, where a full numerical simulation (coloured dots) is superimposed to the level curves of the simple integrable Hamiltonian (3.13) at different moments in time during the capture into a 3:2 mean motion resonance.

In reality, the application of the adiabatic principle can be done only if the non-conservative forces change the parameters of the Hamiltonian, and not if they affect directly its variables. If there is no damping on the

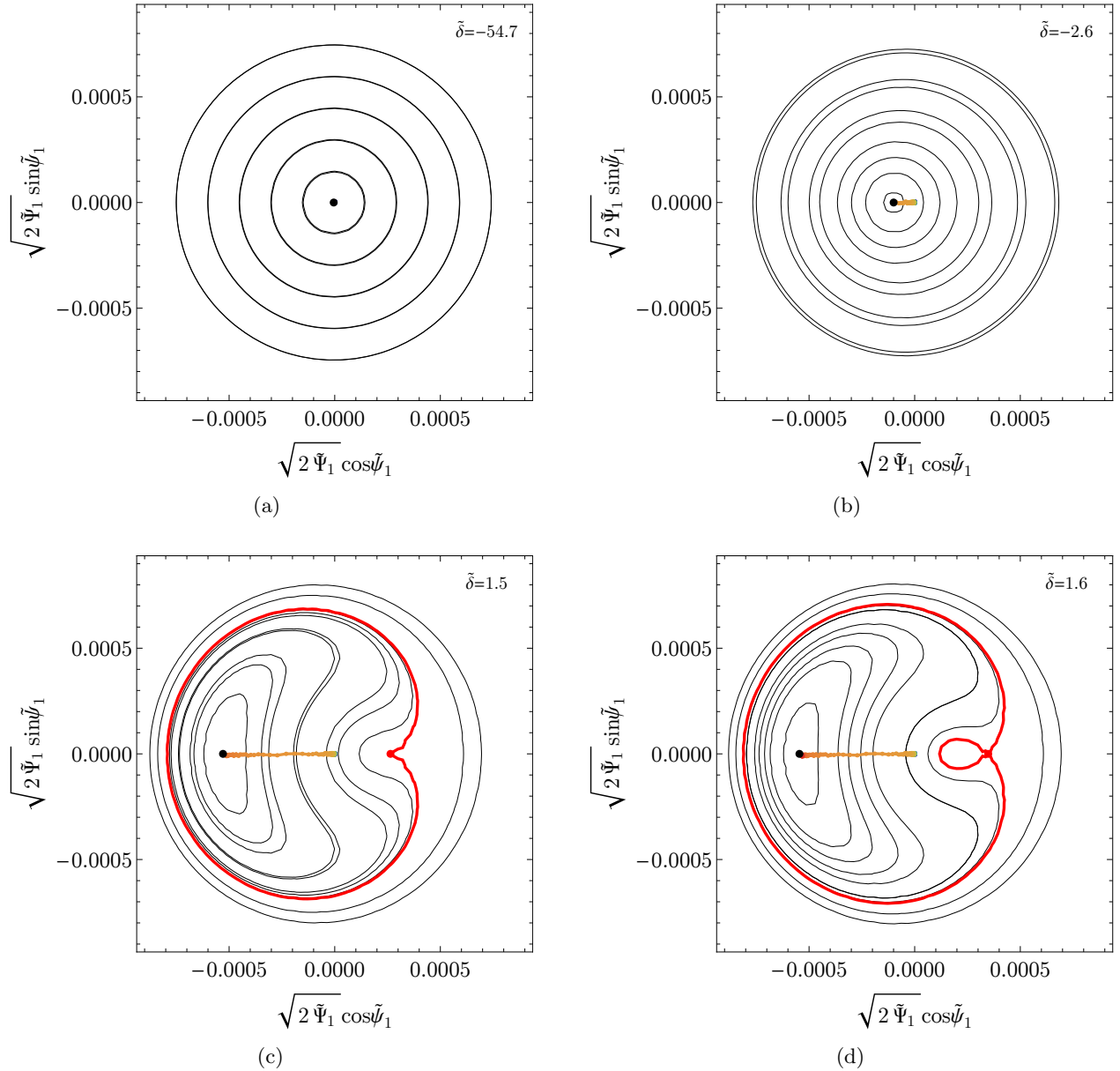


Figure 3.6: Evolution of two equal-mass planets into the 3:2 mean motion resonance. The contour lines are level curves for the integrable model for resonance (3.13) at different times, corresponding to different values for the parameter $\tilde{\delta}$ which encapsulates the proximity to the resonance (see Appendix A for more details). The red contour lines indicate the separatrices. The result of a numerical simulation including the dissipative forces due to the disc-planet interactions is shown as coloured dots. The dots show the numerical evolution up to the time at which the Hamiltonian model is plot in each panel. So, they are not expected to follow the level curves of the model. Instead, they show that the numerical solution always lays at the stable equilibrium point and follows its displacement towards larger values of $\tilde{\Psi}_1$, going from one panel to the next. The action $\tilde{\Psi}_1$ is proportional to e^2 and therefore its value in the numerical simulation is initially small since the gas damps the eccentricity on short timescales. Then, the dynamics follows very closely the general description of capture into resonance given in Subsect. 2.3.3.

eccentricities but only a drag on the semi major axes, [Deck and Batygin(2015)] show that, at low-order in e , the dissipation only acts on the otherwise constant of motion Ω (see (3.7)) and does not act on the dynamical variables $\Psi_1, \Psi_2, \psi_1, \delta\gamma$. In this case, the adiabatic principle can be used. Thus, as the planets approach each other, they have to follow the locus of equilibrium points computed in Section 3.1.2 and shown in Figures 3.1, 3.2. This is precisely what we observed in Figure 3.3 for the 2:1 resonance. Thus, as the planets approach each other, their eccentricities start to grow. As shown in Figure 3.3, if there were no eccentricity damping, at least one of the two

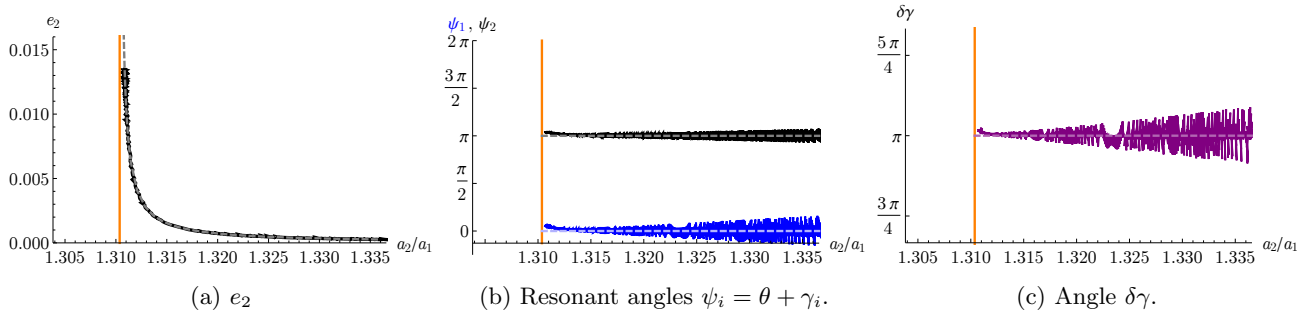


Figure 3.7: Typical evolution of a system during capture into 3:2 mean motion resonance, for two planets of equal mass $m_1 = m_2 = m = 10^{-5}M_*$. All quantities are given as a function of the semi-major axes ratio a_2/a_1 in order to compare with the analytical calculations carried out in Subsect. 3.1.2; to further aid the comparison, we superimposed to all plots the analytical values found using our averaged model with dashed lines. Notice that the initial configuration is at the far right of the plots and with vanishing eccentricity, so we are very close to the equilibrium point, i.e. in a configuration of small amplitude of libration; this property of the system is conserved during its evolution as explained in the text. In this simulation, both the migration and eccentricity damping effects of the disc on the planets are active, so that the system eventually reaches a final configuration of low-amplitude libration around an equilibrium point for some value of the angular momentum. This final configuration is stable. Notice that the amplitude of libration of ψ_1 , ψ_2 and $\delta\gamma$ shrinks as a_2/a_1 decreases. This is because initially the eccentricity is very small and therefore even a small oscillation around the equilibrium point can cause a large excursion in the angles.

planets' eccentricities would grow indefinitely. However, as discussed above, the disc exerts an eccentricity damping. This has two effects. On the one hand, it stops the eccentricity growth and keeps the planets at a fixed semi-major axes ratio. That is, the mutual planet configuration freezes out, as we show in Figure 3.7 for the 3:2 mean motion resonance. We discuss how to describe analytically this equilibrium configuration in the next subsection. On the other hand, it breaks the adiabatic approximation. The orbit either shrinks towards the equilibrium point, which becomes an attractor, or spiral away from the equilibrium, increasing the libration amplitude until it escapes from the resonance or reaches a limit cycle ([Goldreich and Schlichting(2014)]). The conditions for one or the other behaviour are quantified in [Delisle et al.(2015)] and [Deck and Batygin(2015)] as a function of planetary masses, damping forces, resonance index k . We come back to this in the next subsection, where we briefly discuss how, for the purposes of our work, we can ensure that the eventual instability would occur on very long timescales and by removing the gas early enough we can ignore this complication. Note moreover that more recently [Xu et al.(2018)] showed that these overstabilities and/or limit cycles are not observed in simulations where a more realistic e -damping is used instead of (3.20b), by including a dependence on e/h (cfr. also [Cresswell and Nelson(2008)] equation (11)). The idea is that at higher e , the e -damping becomes smaller, so the non-adiabatic push onto the actions (namely the semi-major axes) is less severe, and the system remains closer to the low-amplitude region around the stable resonant equilibrium point, at the price of reaching higher (average) eccentricities.

3.2.2 Planet-disc interactions and evolution in mean motion resonance

The value of the equilibrium eccentricity (and hence the semi-major axes ratio a_2/a_1) for two planets embedded in a protoplanetary disc in the phase of resonant orbital configuration has been computed in a number of works (e.g. [Papaloizou and Szuszkiewicz(2005), Crida et al.(2008), Goldreich and Schlichting(2014), Xu et al.(2018)]). We propose here a different formulation, consistent with the Hamiltonian resonant description provided in Section 3.1 and the adiabatic principle discussed in Subsect. 2.3.2. The formulation that we develop wants to describe not only the equilibrium state, but also the evolution of the planets towards the resonant equilibrium. In particular, a non trivial issue that we address is how the push from the outer planet trapped in resonance is partitioned between eccentricity excitation and migration of the inner planet, which cannot be captured in the simpler formulations (e.g. [Xu et al.(2018)]).

For simplicity, we first discuss the case in which the gas only interacts with the outer planet, and finally we add the condition that there is a planetary trap at the disc edge so that the inner planet stops migrating. The first assumption does not lead to any loss in generality, as the main idea will be to work in rescaled variables, putting $R = a_2/a_1$, and following the evolution of *this* quantity rather than each semi-major axis. The disc's

effects on a_1 and e_1 can be easily added into the equations for the total torque and work ((3.31) and (3.33) below), symmetrically with the terms acting on a_2 and e_2 , but they would just complicate the subsequent already long algebraic expressions, without changing the qualitative behaviour of the system. We will then compare the analytic results with the equilibrium values obtained in numerical simulations. To simplify the calculation we choose here units in which $m\sqrt{\mathcal{G}(M_* + m)} = 1$. We also assume small e to simplify the formulæ but the method is indeed general.

The idea is to start with two fundamental equations. The first states that the derivative of the angular momentum of the system is equal to the torque:

$$\frac{d\mathcal{L}}{dt} = \dot{\mathcal{L}} = T; \quad (3.29)$$

the second states that the derivative of the energy of the system is equal to the work

$$\frac{dE}{dt} = \dot{E} = W. \quad (3.30)$$

The total torque exerted on the planetary system from the gas is, from equation (3.24)

$$T = \dot{\mathcal{L}}_{\text{mig},2} = -\frac{\mathcal{L}_2}{\tau_{\text{mig},2}} = -\frac{\sqrt{a_2(1-e_2^2)}}{\tau_{\text{mig},2}}. \quad (3.31)$$

Using (3.26), the change in orbital energy is

$$\dot{E}_i = \frac{\dot{a}_i}{2a_i^2} = \frac{1}{a_i} \frac{\dot{a}_i}{2a_i} = \frac{1}{a_i} \left(-\frac{1}{\tau_{\text{mig},i}} - \frac{p}{2} \frac{e_i^2}{\tau_{e,i}} \right) \quad (3.32)$$

where $p \simeq 2$ for small e (we used Equations (3.31), (3.26) in the last equality). We then find that the total work is

$$W = \frac{1}{a_2} \left(-\frac{1}{\tau_{\text{mig},2}} - \frac{e_2^2}{\tau_{e,2}} \right), \quad (3.33)$$

We now pass in rescaled variables, and write $R = a_2/a_1$. Using the expression (3.33) for the work, (3.32) for \dot{E}_i and multiplying both sides by a_2 , equation (3.30) reads

$$R \frac{\dot{a}_1}{2a_1} + \frac{\dot{a}_2}{2a_2} = -\frac{1}{\tau_{\text{mig},2}} - \frac{e_2^2}{\tau_{e,2}}; \quad (3.34)$$

here, \dot{a}_1 is not the migration rate of planet 1 due to the planet-disc interaction, which we have assumed to be non-existent for simplicity, but the unknown migration rate due to the resonant interaction with the migrating planet 2. Using now

$$\frac{\dot{a}_2}{a_2} = \frac{\dot{R}}{R} + \frac{\dot{a}_1}{a_1} \quad (3.35)$$

this becomes

$$\frac{\dot{a}_1}{a_1} = \left[-\frac{2}{\tau_{\text{mig},2}} - \frac{2e_2^2}{\tau_{e,2}} - \frac{\dot{R}}{R} \right] / (R + 1). \quad (3.36)$$

Similarly, to rewrite equation (3.29) we write

$$\mathcal{L} = \sqrt{a_1} \left[\sqrt{1-e_1^2} + \sqrt{R} \sqrt{1-e_2^2} \right]; \quad (3.37)$$

then, ignoring in (3.25) the higher order terms in e and writing for each planet $\dot{\mathcal{L}}_i \simeq \frac{\dot{a}_i}{2\sqrt{a_i}} \sqrt{1-e_i^2} - \sqrt{a_i} e_i \dot{e}_i$, we use (3.31) and the relationship $\dot{a}_2/(2\sqrt{a_2}) = \dot{R}/(2\sqrt{R}) + \sqrt{R}\dot{a}_1/(2\sqrt{a_1})$ (cfr. (3.35)) to obtain

$$\dot{\mathcal{L}} \simeq \frac{\dot{a}_1}{2\sqrt{a_1}} \left[\sqrt{1-e_1^2} + \sqrt{R} \sqrt{1-e_2^2} \right] + \sqrt{a_1} \left[-e_1 \dot{e}_1 + \frac{\dot{R}}{2\sqrt{R}} \sqrt{1-e_2^2} - \sqrt{R} e_2 \dot{e}_2 \right] = -\frac{\sqrt{a_2(1-e_2^2)}}{\tau_{\text{mig},2}}. \quad (3.38)$$

Here, \dot{e}_1 is the evolution of the eccentricity of planet 1 due to the resonant interaction with the migrating planet 2, and \dot{e}_2 is the resultant evolution for planet 2 due to both the damping effect of the disc and the resonant interaction. Both \dot{e}_1 and \dot{e}_2 are unknown and determined below. Dividing last equation (3.38) by $\sqrt{a_1}$ and using (3.36) we get

$$\left[-\frac{1}{\tau_{\text{mig},2}} - \frac{e_2^2}{\tau_{e,2}} - \frac{\dot{R}}{2R} \right] \left[\sqrt{1-e_1^2} + \sqrt{R}\sqrt{1-e_2^2} \right] / (R+1) + \left[-e_1\dot{e}_1 + \frac{\dot{R}}{2\sqrt{R}}\sqrt{1-e_2^2} - \sqrt{R}e_2\dot{e}_2 \right] = -\frac{\sqrt{R}\sqrt{1-e_2^2}}{\tau_{\text{mig},2}}. \quad (3.39)$$

We now write $e_i = e_i(R)$ as given by the equilibrium curves shown in Figure 3.2, so that we can write an equation with R as the sole independent variable. Using then $\dot{e}_i = \frac{de_i}{dR}\dot{R}$ and grouping the terms in \dot{R} we get

$$\begin{aligned} & \left[-\left(\sqrt{1-e_1^2} + \sqrt{R}\sqrt{1-e_2^2} \right) / (2R(R+1)) - e_1 \frac{de_1}{dR} + \frac{\sqrt{1-e_2^2}}{2\sqrt{R}} - \sqrt{R}e_2 \frac{de_2}{dR} \right] \dot{R} \\ & = \left[\frac{1}{\tau_{\text{mig},2}} + \frac{e_2^2}{\tau_{e,2}} \right] \left[\sqrt{1-e_1^2} + \sqrt{R}\sqrt{1-e_2^2} \right] / (R+1) - \frac{\sqrt{R}\sqrt{1-e_2^2}}{\tau_{\text{mig},2}}; \end{aligned} \quad (3.40)$$

approximating each $1-e^2 \simeq 1$ for small e 's one can simplify this equation into

$$\left[\frac{1}{2\sqrt{R}} - e_1 \frac{de_1}{dR} - \sqrt{R}e_2 \frac{de_2}{dR} - \frac{1+\sqrt{R}}{2R(1+R)} \right] \dot{R} = \frac{(1-R^{3/2})}{\tau_{\text{mig},2}(1+R)} + \frac{e_2^2(1+\sqrt{R})}{\tau_{e,2}(1+R)}. \quad (3.41)$$

Such an equation gives the derivative of R as a function of R , whereas equation (3.36) gives the evolution of a_1 as a function of R . The evolution of e_1 and e_2 is obtained from that of R using the functions $e_1(R)$ and $e_2(R)$. Together these relationships describe the full evolution of the resonant system as it evolves under the torque and the damping caused by the disc before reaching an equilibrium. Eq. (3.41) is non-trivial and shows that the decrease of R is not simply due to the energy loss of the outer planet due to the interaction with the disc. It is reduced, because planet 1 is pushed inwards while the planets go deeper in resonance. If there is no damping ($\tau_{e,2} = \infty$) then no equilibrium is possible and R continues to decrease, the right hand side being negative, and the eccentricities keep following the curves in Figure 3.2. If instead $\tau_{e,2} \neq \infty$, the equilibrium point occurs when $\dot{R} = 0$, that is, putting the right hand side of e.g. the simplified equation (3.41) equal to 0, when

$$e_2^2 = \frac{(R^{3/2}-1)}{(1+R^{1/2})} \frac{\tau_{e,2}}{\tau_{\text{mig},2}} = \frac{(R^{3/2}-1)}{2(1+R^{1/2})} K_2^{-1}, \quad (3.42)$$

where $K_2 = \frac{\tau_{a,2}}{\tau_{e,2}}$ is the K -factor of the outer planet. The multiplicative factor multiplying K_2^{-1} can be further approximated by taking $R = \bar{R} = (k/(k-1))^{2/3}$. We stress that at equilibrium $\dot{R} = 0$ alone has $\dot{e}_1 = 0$, even if there is no direct damping on the eccentricity of planet 1.

In the case of a trap at the disc edge operating on the inner planet to stop the migration process, the requirement is that the torque on the inner planet adapts so that the total torque on the system is 0, whatever may be the additional effect of the disc on the inner planet. In this case, the first fundamental equation (3.29) rewrites

$$\frac{d\mathcal{L}}{dt} = \dot{\mathcal{L}} = 0 \quad \text{i.e.} \quad \dot{\mathcal{L}}_1 = -\dot{\mathcal{L}}_2. \quad (3.43)$$

This implies that the disc exerts a positive torque on the inner planet

$$\dot{\mathcal{L}}_1 = +\frac{\mathcal{L}_1}{\tau_{\text{mig},1}} \quad (3.44)$$

with $1/\tau_{\text{mig},1} \simeq \sqrt{R}/\tau_{\text{mig},2}$ (still approximating $1-e^2 \sim 1$). The total work on the system is instead not 0. Using the torque just computed for the inner planet and (3.26), it is easy to see that the work exerted by the disc on the inner planet is

$$W_1 = \frac{1}{a_2} \left[+\frac{R^{3/2}}{\tau_{\text{mig},2}} - \frac{Re_1^2}{\tau_{e,1}} \right], \quad (3.45)$$

where we also consider the eccentricity damping on the inner planet (on a timescale not necessarily equal to that of the second planet).³ This allows to rewrite equation (3.34) as

$$R \frac{\dot{a}_1}{2a_1^2} + \frac{\dot{a}_2}{2a_2^2} = \left[\frac{R^{3/2}}{\tau_{\text{mig},2}} - R \frac{e_1^2}{\tau_{e,1}} \right] + \left[\frac{-1}{\tau_{\text{mig},2}} - \frac{e_2^2}{\tau_{e,2}} \right], \quad (3.46)$$

and, using (3.35), the equivalent of (3.36) becomes:

$$\frac{\dot{a}_1}{a_1} = \left[-\frac{\dot{R}}{R} + \frac{2(R^{3/2} - 1)}{\tau_{\text{mig},2}} - \frac{2Re_1^2}{\tau_{e,1}} - \frac{2e_2^2}{\tau_{e,2}} \right] / (R + 1). \quad (3.47)$$

Then, redoing all the calculations as above from (3.38) to (3.41), but putting equal to 0 the right hand side of (3.38) (zero total torque) and using (3.47) instead of (3.36), the equivalent of equation (3.42) becomes

$$\frac{(R^{3/2} - 1)}{\tau_{\text{mig},2}} - \frac{Re_1^2}{\tau_{e,1}} - \frac{e_2^2}{\tau_{e,2}} = 0. \quad (3.48)$$

Notice that if this equation is satisfied, \dot{a}_1 in (3.47) vanishes when $\dot{R} = 0$, i.e. the system is at a complete equilibrium, unlike in the previous case where both planets were migrating in resonance, at constant R . Indeed, the equilibrium equation could also have been found by imposing directly $\dot{a}_1 = 0$ and $\dot{R} = 0$ in (3.47). Considering another limiting case as an example, if no damping is applied to planet 1, $\tau_{e,1} = \infty$, then the equilibrium in e_2 is

$$e_2^2 = (R^{3/2} - 1) \frac{\tau_{e,2}}{\tau_{\text{mig},2}} = \frac{(R^{3/2} - 1)}{2} K_2^{-1}; \quad (3.49)$$

e.g. for the 3:2 resonance the multiplicative coefficient, estimated again using $R = \bar{R}$, is about twice of the one in (3.42), meaning that the higher relative push between the two planets against one another, provided by the trap, has the effect of increasing the equilibrium eccentricity.

Analytical formulæ to calculate the equilibrium eccentricity during the capture in resonance and valid in the low-eccentricity regime have already been produced. E.g. [Ramos et al.(2017)] reproduce a formula which they derive from [Papaloizou and Szuszkiewicz(2005)]: taking these formulæ in the limiting case of $\tau_{e,1} = \infty$ and $\tau_{a,1} = \infty$, one obtains our formula (3.42). Another point of view was adopted in [Crida et al.(2008)], where the authors obtained the damping time $\tau_{e,1}$ needed to reach a given value of eccentricities at the equilibrium configuration. Their final formula (16) indeed leads to our formula (3.48) by using equation (3.44) and by again replacing $1 - e^2$ with 1, their η by \sqrt{R} and their ϵ by $1/R$ (note that their $-1/\tau_a$ is defined as \dot{a}/a , while in the present work the latter is expressed by $-1/\tau_a - 2e^2/\tau_e$). [Goldreich and Schlichting(2014)] derived a formula for the equilibrium eccentricity in the simplified case of the planar, circular, restricted three-body problem with a massless inner planet and using equations to first order in e_1 . They found that

$$e_{1,\text{eq}} = \sqrt{\frac{\tau_{e,1}}{k \tau_{\text{mig},\text{eff}}}}, \quad (3.50)$$

where $\tau_{\text{mig},\text{eff}}^{-1} = \tau_{\text{mig},2}^{-1} - \tau_{\text{mig},1}^{-1}$.

We now look at numerical simulations to confirm these analytical predictions. For formula (3.42), we consider the case of $\beta_f = 0$, β_f being the flaring index of the disc. This is because, even when the equilibrium described by (3.42) is reached, $\dot{R} = 0$ but the two planets keep migrating due to the torque on the outer one; now since $h(r) = z_{\text{scale}} r^{\beta_f}$ and the K -factor depends on h via (3.27), it is convenient to keep h a constant so that the equilibrium eccentricity attained by the system does not evolve as $r = a_2$ does. In this case, $K_2 \simeq 82.11$. We estimate with (3.42) the equilibrium eccentricity $e_{\text{eq},2} \simeq 0.0311$ for the 4:3 resonance, $e_{\text{eq},2} \simeq 0.0377$ for the 3:2 resonance, and $e_{\text{eq},2} \simeq 0.0519$ for the 2:1 resonance. We show in Figure 3.8 the result of numerical simulations with the described setup, showing good agreement with the predicted values. We note that the equilibrium found is always stable, because $\tau_{e,1} = \infty$ ([Lee and Peale(2002), Deck and Batygin(2015)]).

For formula (3.48), we can instead consider a flared disc, $\beta_f = 0.25$. To solve that equation, we first need to write $e_1 = e_1(e_2)$ from the equilibrium curves in Figure 3.2 for the different resonances, and then to calculate from (3.20b) and (3.20a) the values for $\tau_{e,1}$, $\tau_{a,2}$ and $\tau_{e,2}$. Notice that we do not need to calculate the value of each

³We stressed the plus sign in the first term in the right hand side of W_1 , in contrast with the negative sign of the corresponding term in W_2 , since the effect of the trap on the inner planet is that of outwards migration.

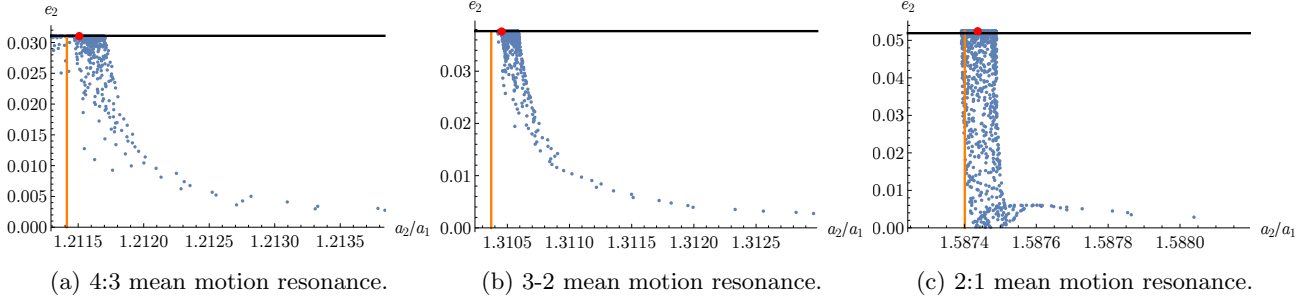


Figure 3.8: Confirmation of formula (3.42) for the equilibrium value of e_2 where $K_2 = \frac{\tau_{a,2}}{\tau_{e,2}} \simeq 82.11 \equiv \text{const}$ (in the case of a disc with flaring index $\beta_f = 0$), in the case of various first order mean motion resonances. We show as a function of the semi-major axes ratio $a_2/a_1 = R$ the evolution of e_2 in the numerical simulations under the conditions explained in the text. The red dot indicates the configuration of the system after the equilibrium is attained. We indicate with an horizontal line the predicted value for $e_{2,\text{eq}}$, showing good agreement. Notice that in the 2:1 mean motion resonance case, we see the same behaviour as shown in Figure 3.1a, associated to the smooth change of $\delta\gamma_{\text{eq}}$ from π to 0 as described in Section 3.1.2; the goodness of the prediction of $e_{2,\text{eq}}$ is unaffected.

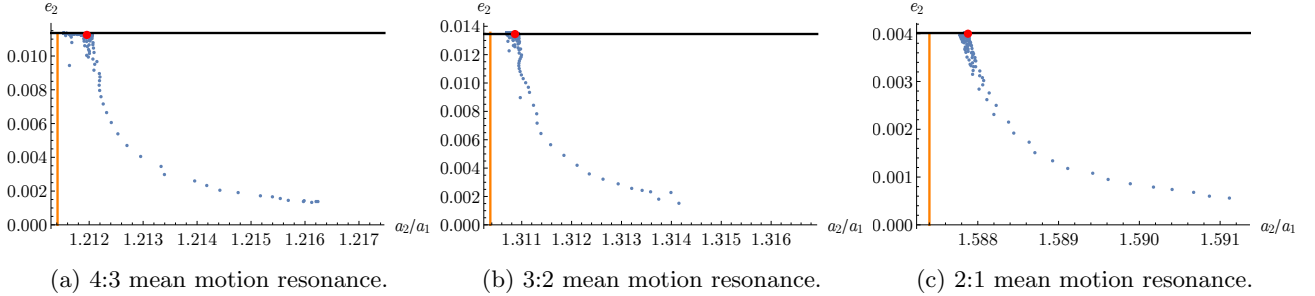


Figure 3.9: Confirmation of formula (3.48) for the equilibrium value of e_2 in the case of a disc with flaring index $\beta_f = 0.25$, for various first order mean motion resonances. We show as a function of the semi-major axes ratio $a_2/a_1 = R$ the evolution of e_2 in the numerical simulations under the conditions explained in the text. The red dot indicates the configuration of the system after the equilibria are reached. We indicate with an horizontal line the predicted value for $e_{2,\text{eq}}$, showing good agreement.

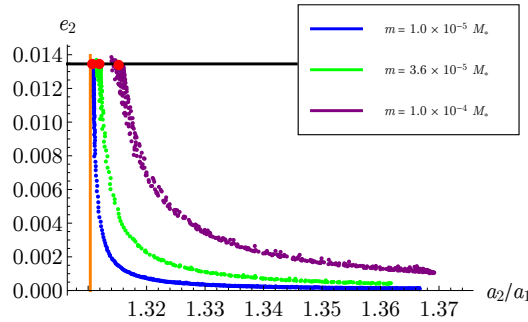


Figure 3.10: Evolution of e_2 during the capture in the 3:2 resonance for different planetary masses $m_1 = m_2 = m$. The vertical black line indicates the calculated value of $e_{2,\text{eq}}$ obtained with (3.42). The red dots represent the final configurations of the systems after the equilibria are reached, showing that the resulting equilibrium value of e_2 is independent of m , as predicted by the analytical formulæ.

$\tau_{\text{wave},1}$ and $\tau_{\text{wave},2}$ at the positions a_1, a_2 of the planets, since we can just factor out one of the semi-major axes and easily reduce this factor to a quantity depending only on R , which we again approximate with \bar{R} . However since the disc is flared, to obtain $\tau_{\text{mig},2}$ we need to calculate the value of $h = h(a_2)$ at the position of the outer planet, and we again write a_2 as a function of e_2 . We thereby estimate with (3.48) a value $e_{2,\text{eq}} \simeq 0.0114$ for the

4:3 resonance, $e_{2,\text{eq}} \simeq 0.0134$ for the 3:2 resonance and $e_{2,\text{eq}} \simeq 0.0040$ for the 2:1 resonance. We show in Figure 3.9 the result of numerical simulations with this setup, showing again good agreement with the analytical predictions. To use formula (3.50) from [Goldreich and Schlichting(2014)], we put $|\tau_{\text{mig},1}| = \tau_{\text{mig},2}/\sqrt{R}$ (cfr. equation (3.44)). We obtain in the cases discussed above $e_{1,\text{eq}} \simeq 0.019$ for the 4:3 resonance, $e_{1,\text{eq}} \simeq 0.022$ for the 3:2 resonance and $e_{1,\text{eq}} \simeq 0.024$ for the 2:1 resonance, the real values obtained from the numerical simulations being respectively $e_{1,\text{eq}} \simeq 0.011$, $e_{1,\text{eq}} \simeq 0.012$ and $e_{1,\text{eq}} \simeq 0.018$. This shows that using such an approximated formula one obtains the right order of magnitude but the accuracy may be off by a factor of 2.

We note that for the 2:1 resonance (Figure 3.9c), the case with $m_1 = m_2 = 10^{-5}M_*$ and $K \sim 100$ should lead to an instability of the equilibrium point. (see Fig. 3 of [Deck and Batygin(2015)]). We have checked that this is indeed the case. However the growth of the libration amplitudes manifests itself on a timescale τ_e (see Eq. (29) in [Goldreich and Schlichting(2014)]), which is very long given the low surface density of the disc that we assume to ensure a slow evolution. We stop the simulation before the instability produces any noticeable effect. This is appropriate for the purposes of our study in the next chapters, specifically Chapter 5, where we study the stability of resonant chains as a function of planetary mass in absence of dissipation.

We conclude this section by noticing that in both equations (3.42) and (3.48) the coefficient in τ_{wave} which depends on the planetary mass m and of the gas surface density Σ is eliminable (formula (3.48) in principle depends on the planet mass-ratio, here fixed to 1), meaning that the final configuration does not depend on these quantities. This is confirmed by our simulations, as shown in Figure 3.10. The fact that the final configuration does not depend on the disc surface density means also that we can, for the purposes of our study, let Σ be small so to ensure a slow enough change in angular momentum and invoke the adiabatic approach mentioned at the beginning of Section 3.1.2, without affecting the final resonant configuration reached by the system.

Chapter 4

Three-planet systems and the near-resonant population

Numerical simulations show that compact chains of mean motion resonances are a common outcome of slow, convergent orbital transport of planets within protoplanetary discs, which is also a well understood process from the analytical point of view, as we discussed in the previous chapter. Although details of disc-driven migration remain an active topic of research, it is clear that such a process should play some role in the dynamical history of planetary systems. We already mentioned in Section 1.3 that Trappist-1, Kepler-223, GJ-876 and Kepler-60 are known examples of resonant systems, whose configurations are unlikely to have formed by pure chance. However, one of the most notable aspects of the Kepler data is that the distribution of the period ratios of neighbouring planets in multi-planets systems shows two seemingly conflicting features: on the one hand, it appears relatively broad and smooth, without any single, unmistakably emerging feature; on the other hand, a slight preference for near-resonant configurations is evident upon close examination. In fact, it is often pointed out that there is a lack of planet pairs in correspondence with period ratios very close to low-integer ratios, and a definite excess just wide of these values, especially the 2:1 and 3:2, see Figure 1.7.

Whereas the broad distribution of period ratios can be explained if most resonant chains become unstable after the dissipation of the disc [Izidoro et al.(2017), Izidoro et al.(2019)], the overabundance of systems just wide of exact 2:1 and 3:2 resonant ratios requires a more subtle explanation based on resonant dynamics. This chapter revisits the divergent migration of resonant planets under dissipative forces such as tidal dissipation, and focuses on three-planet systems where each planet pair is close to a first-order mean motion resonance. The content of this chapter has been published in [Pichierri et al.(2019)].

4.1 The near-resonant population

As we saw in Section 3.1, analytical models of resonance do predict that a pair of planets in a first order mean motion resonance need not satisfy the exact resonance condition $a_1/a_2 = ((k-1)/k)^{2/3}$, but they can reside wide of resonance while the resonant angles are still librating. However some Kepler systems are so wide of resonance that, after the resonant configuration is attained and the disc of gas is dissipated, an auxiliary mechanism might need to be invoked which actively drives these planets farther away from the exact resonance. As we will see in Section 4.3, observations show that a significant fraction of nearly resonant systems have period ratios up to 50 times wider than the typical resonant width from the location of the resonance corresponding to a typical eccentricity of planets captured in resonance during migration in the disc (i.e., $e \sim 0.03 - 0.05$). These observations can potentially be interpreted as evidence for dissipative processes acting on the planetary systems after the disc phase.

[Papaloizou and Terquem(2010)] considered the specific case of the K-dwarf HD 40307, which hosts¹ three hot super-Earths/mini-Neptunes with both pairs wide of the 2:1 mean motion resonance, and planetary masses obtained with Radial Velocity methods. They showed that as tidal interaction between the planets and the star reduces the eccentricities, the system maintains the libration of the resonant angles even when the period ratios are considerably far away from exact commensurability. Subsequently, [Batygin and Morbidelli(2013)b], [Lithwick and Wu(2012)]

¹We note that since the publication of the aforementioned paper, more planets have been observed in the same system, including two confirmed planets HD 40307 f and HD 40307 g. For this reason, we will not consider this system in the current work, although we draw inspiration from the analysis of [Papaloizou and Terquem(2010)].

and [Delisle and Laskar(2014)] showed that two planets in mean motion resonance repel each other as energy is lost during tidal evolution. They thus proposed this as a viable mechanism to explain the observed distribution of period ratios in exoplanetary systems. We note that, for two planets, this repulsion can be easily understood if one considers that any process that dissipates the energy, $E \propto -m_1/a_1 - m_2/a_2$, and at the same time conserves angular momentum, $L \propto m_1\sqrt{a_1} + m_2\sqrt{a_2}$, should give rise to such an evolution. Indeed, this study applies to any dissipative evolution that maintains constant the angular momentum, not just tidal dissipation, and not just resonant coupling [Delisle et al.(2012)].

Thanks to these studies, the case of two planet systems is well understood. However, numerous systems of more than two planets are now known (Figure 1.7). Accordingly, in this chapter we aim to expand the study to detected extrasolar systems of three planets. More specifically, we envision the following scenario for the formation and evolution of these planetary systems. First, three planets are embedded in the protoplanetary disc in which they formed; they interact with the disc, which ultimately results in a resonant capture. Then, after the disc is slowly depleted, the dissipative effects mentioned above are introduced, leading to orbital divergence.

Naturally this is a simplified and idealised scenario. In reality, we still do not know with enough accuracy the final configuration obtained by multi-planetary systems migrating in a disc of gas. One approach towards a better approximation would be to perform full hydrodynamic simulations of planets immersed in their protoplanetary disc accounting for various disc parameters (such as disc surface density, turbulence, opacity, etc.). This approach would however be very expensive computationally. Moreover, to date we have virtually no direct observations of the specific physical processes acting during planet formation and evolution in the early epochs of the disc phase, so these simulations, no matter how exhaustive in terms of the implementation of the plausible physics, cannot yet be directly constrained by the available data. In any case, the fact that slow convergent orbital transport strongly favours resonant captured states is well supported both analytically and numerically, as well as by the specific observations of multi-planets resonant systems mentioned above.

We focus on slow convergent type-I migration in a disc of gas, and adopt simple synthetic analytical formulæ for the work and the torque generated by the disc on the planets ([Cresswell and Nelson(2006), Cresswell and Nelson(2008)], see also Section 3.2); the requirement that exact prescriptions for the interaction between the planets and the disc be implemented will be relaxed, invoking the aforementioned arguments favouring the plausibility of mean motion resonant capture. A similar reasoning can be applied for the post-disc phase. In order to simulate the dissipative forces that can act on a planetary system, we will implement tidal dissipation. Of course, the tidal parameters for these planets are not known (as we do not yet have a precise understanding of the interior structure of these bodies or the specific physical mechanisms that dominate the dissipation), which would pose additional questions concerning for example the timescales over which this type of dissipation takes place. However, the specific choice of tidal dissipation is only one possible example of a process such that $\dot{E} < 0$ and $\dot{L} = 0$. We conclude that our specific implementation of type-I migration and tidal dissipation after the disc removal is therefore not restrictive, which makes our results generalisable to any other equivalent processes. Recently, for example, [Millholland and Laughlin(2019)] showed that dissipation due to ‘obliquity tides’ can be a very efficient extra source of dissipation, which is generated when a large axial tilt is maintained by secular resonance-driven spin-orbit coupling.

In the light of these considerations, we investigate whether it is possible to reproduce the observed orbital configuration of real exoplanetary systems which reside close to resonance, assuming that planets are captured into resonance and undergo dissipative evolution after the disc phase. In other words we ask ourselves if the aforementioned physical processes are compatible with the distribution of near-resonant period ratios that emerges from available data.

4.1.1 Methods and physical setup

In order to answer this question, we examined the NASA Exoplanet Archive (<https://exoplanetarchive.ipac.caltech.edu>) and selected confirmed three-planet systems for which both planet pairs lie close to a first order mean motion resonance, in particular the 2:1 and 3:2 resonances, as these seem to be the most common in the Kepler data. Our aim is to analyse these systems’ orbital parameters and to evaluate quantitatively how close they are to a multi-resonant chain, which would be indicative of a dynamical history characterised by the physical processes described above.

Evidence suggesting that planets around Kepler-223 and Trappist-1 truly reside in a resonant configuration has recently been marshalled from the observed libration of the three-body Laplace angles [Mills et al.(2016), Luger et al.(2017)]. To this end, recall that if two neighbouring pairs of planets in a multi-planet systems are in the $k^{(1)}:(k^{(1)} - 1)$ and $k^{(2)}:(k^{(2)} - 1)$ resonances respectively (so that the resonant angles $k^{(1)}\lambda_2 - (k^{(1)} - 1)\lambda_1 - \varpi_2$ and $k^{(2)}\lambda_3 - (k^{(2)} - 1)\lambda_2 - \varpi_2$ are librating), then the Laplace angle $\varphi_L = (k^{(1)} - 1)\lambda_1 - (k^{(1)} + k^{(2)} - 1)\lambda_2 + k^{(2)}\lambda_3$

will be automatically librating as well. The advantage of examining this three-body angle over the two-body resonant angles is that the latter contain the longitudes of the pericenters ϖ , whose precession rates are poorly constrained by the data, while the former only includes the mean longitudes λ whose derivatives in time are directly deduced by the transit observations. However, solutions for which the resonant angles were originally in libration around a resonant equilibrium point can become circulating when the eccentricity of the equilibrium point becomes small enough under the effect of tidal damping [Delisle et al.(2015)], and, similarly, even a small distance from the equilibrium point could be responsible for breaking the libration of the three-body Laplace angle when the equilibrium eccentricity becomes small enough. Therefore, even if such circulations of the angles were observed, this would not necessarily be in disagreement with the envisioned scenario of resonant capture and subsequent dissipative evolution. In other words, the libration of the Laplace angle is a sufficient, but not necessary condition for past resonant capture in a chain of first-order resonances.

We therefore perform here a different analysis of the observed data, where we do not attempt to verify that a given system resides formally in resonance at the present day, but instead we evaluate the distance of a system from the considered resonance chain and the probability that this proximity is due to mere chance. In order to do this, we look for resonant solutions that provide the closest match to the observed planetary orbital configurations, that is the semi-major axis ratios. It is worth anticipating here the following important point. As it will be clear later (see Section 4.3.2), in the case of only two resonant planets residing wide of resonance it is always possible to find a resonant configuration which matches the observed data. This is because the eccentricities of these planets are at the present day not well constrained observationally, making the total orbital momentum of the system \mathcal{L} a free parameter: it is therefore always possible to find a value of \mathcal{L} that reproduces the observed a_2/a_1 with resonance-locked orbits. However, this is not the case for systems of three planets, since we still have \mathcal{L} as a single free parameter (whose value is linked to the initial captured state, not constrained observationally) but two observables, that is the two pairs' semi-major axis ratios.

As detailed below, we carried out our study of finding orbital configurations that match the observed data using both an analytical and a numerical approach. The semi-major axes of the planets may be inferred from the orbital periods once the stellar mass is known, however this quantity is not yet well constrained in all cases. Nonetheless, all we will be interested in are the semi-major axes ratios a_2/a_1 and a_3/a_2 , which can be obtained without any knowledge of the mass of the star directly from the period ratios and using Kepler's third law. This is tantamount to renormalising all separations by some arbitrary length, which does not affect the underlying physics since the dynamics only depends on the ratios of the semi-major axes and not on their individual values (only the timescale of the evolution does).

For the purposes of this study, we can limit ourselves to an analysis to first order in the planetary eccentricities. Indeed, the eccentricities that are expected for planets that have been captured into mean motion resonance by slow convergent migration in a disc are of order $\sqrt{\tau_e/\tau_a} \sim h$, where τ_a and τ_e are the timescales of migration and eccentricity damping respectively, and $h = H/r \sim 0.03 - 0.05$ is the aspect ratio of the disc, as we recalled in Subsect. 3.2.2. Since discs with high aspect ratios are not expected, the limit of small eccentricity is justified, and even more so in the phase of dissipative tidal evolution, which further damps the eccentricities. Moreover, given that these are transiting planets, and that during the disc phase any mutual inclination of the planets would be damped out, we assume coplanar orbits for simplicity. Another useful piece of information which is available to us are the radii of the planets. They could in principle be used to infer the planetary masses (e.g. [Wu and Lithwick(2013)]). However the radius-mass relationship in Kepler planets is marked by extreme scatter [Weiss et al.(2013)], and we therefore choose to keep the planetary masses as a free parameter. More specifically, we are only interested in the mass ratios m_1/m_2 and m_2/m_3 , since, as we will show, they are the only dynamically significant quantities that can affect the values of the semi-major axis ratios (see also Appendix B).

The remainder of this chapter is organised as follows. In Section 4.2 we obtain an analytical model for three planets in a chain of first order mean motion resonances, valid in the limit of small eccentricities. With this analytical model, we find the stable resonant configurations and map them in terms of the orbital elements. Finally we obtain an analytical confirmation of resonant repulsion for three-planets systems undergoing dissipation. In Section 4.3 we detail our study, employing both analytical and numerical methods. We select systems of three planets near mean motion resonances, focusing on the 2:1 and 3:2 resonances, and we analyse their orbital configuration using the available data in order to evaluate if they are consistent with the process of resonant capture and subsequent dissipative evolution. We present our results in Section 4.4 and we finally conclude by discussing their significance in Section 4.5.

4.2 Analytical model for three resonant planets

The Hamiltonian of two resonant planets in the limit of low eccentricities has been studied extensively in the literature (e.g. [Batygin and Morbidelli(2013)a, Batygin(2015)] and references therein, see also Appendix A). Collectively these studies have pointed out that even if both planets are massive and to first order in eccentricity it is possible to reduce the problem to an Hamiltonian that is analogous to the well-known Hamiltonian of the restricted, circular three-body problem of a massless particle in resonance with a massive unperturbed body. In particular, such a Hamiltonian is integrable and is equivalent to the so-called second fundamental model for resonance [Henrard and Lemaitre(1983)], also known as the Andoyer Hamiltonian $\mathcal{H}_{\text{And},1}$. This is, however, not the case for three planets. Nonetheless, it is useful to extend an analytical description of the resonant dynamics at low amplitude of libration of the resonant angles in the case of three planets orbiting a star. In this section, we introduce the Hamiltonian of the system, derive curves representing the loci of its stable equilibrium points, and show how these can provide a description of a system along the dissipative evolution. We will apply this model to real Kepler systems in Section 4.3.2.

Consider three planets of masses m_1 , m_2 and m_3 , orbiting around a star of mass M_* in a canonical heliocentric reference frame ([Poincaré(1892)], see also Subsect. 2.2.2). Indices 1, 2 and 3 will refer to the inner, middle and outer planet respectively. As usual, we consider the planetary Hamiltonian (2.95):

$$\mathcal{H} = \mathcal{H}_{\text{kepl}} + \mathcal{H}_{\text{pert}}, \quad (4.1)$$

where the Keplerian part is given by

$$\mathcal{H}_{\text{kepl}} = -\frac{\mathcal{G}M_*m_1}{2a_1} - \frac{\mathcal{G}M_*m_2}{2a_2} - \frac{\mathcal{G}M_*m_3}{2a_3}, \quad (4.2)$$

and describes the (integrable) motion of the three planets due to their interaction with the star, to which the small perturbation $\mathcal{H}_{\text{pert}}$ is added, which includes all the mutual interactions between the planets. We now assume that the inner pair of planets is close to a $k^{(1)}:(k^{(1)} - 1)$ mean motion resonance, and that the outer pair of planets is close to a $k^{(2)}:(k^{(2)} - 1)$ mean motion resonance, where $k^{(1)}$, $k^{(2)} > 1$ are two positive integers. In other words, we assume the resonance conditions $n_1/n_2 \simeq k^{(1)}/(k^{(1)} - 1)$, $n_2/n_3 \simeq k^{(2)}/(k^{(2)} - 1)$, where for each planet $n = \sqrt{\mathcal{G}(M_* + m)a^{-3}}$ is the mean motion. Since we are interested in the resonant interaction between the planets only, as we did in Section 3.1 we eliminate perturbatively the non-resonant angles to first order in the planetary masses, which is equivalent to averaging the Hamiltonian over the fast evolving angles so that only combinations of the resonant angles $k^{(1)}\lambda_2 - (k^{(1)} - 1)\lambda_1 - \varpi_1$, $k^{(1)}\lambda_2 - (k^{(1)} - 1)\lambda_1 - \varpi_2$, $k^{(2)}\lambda_3 - (k^{(2)} - 1)\lambda_2 - \varpi_2$, and $k^{(2)}\lambda_3 - (k^{(2)} - 1)\lambda_2 - \varpi_3$ remain in the Hamiltonian. As usual, λ is the mean longitude of a planet, and ϖ is its longitude of the periastron.

The resonant perturbing Hamiltonian expanded to first order in the eccentricities reads

$$\begin{aligned} \mathcal{H}_{\text{res}} = & -\frac{\mathcal{G}m_1m_2}{a_2} \left(f_{\text{res}}^{(1,1)} e_1 \cos(k^{(1)}\lambda_2 - (k^{(1)} - 1)\lambda_1 - \varpi_1) + \right. \\ & \left. + f_{\text{res}}^{(2,1)} e_2 \cos(k^{(1)}\lambda_2 - (k^{(1)} - 1)\lambda_1 - \varpi_2) \right) + \\ & -\frac{\mathcal{G}m_2m_3}{a_3} \left(f_{\text{res}}^{(1,2)} e_2 \cos(k^{(2)}\lambda_3 - (k^{(2)} - 1)\lambda_2 - \varpi_2) + \right. \\ & \left. + f_{\text{res}}^{(2,2)} e_3 \cos(k^{(2)}\lambda_3 - (k^{(2)} - 1)\lambda_2 - \varpi_3) \right), \end{aligned} \quad (4.3)$$

where the orbital elements are constructed from heliocentric positions and barycentric velocities ([Poincaré(1892)], see also Subsect. 2.2.2). This expression is the natural extension of Equation (3.10). As in Subsect. 3.1.1, the coefficients f_{res} are typically of order unity and depend (weakly) on the semi-major axis ratios; their expressions may be found in [Murray & Dermott(1999)]. We therefore write the Hamiltonian after the averaging procedure as

$$\bar{\mathcal{H}} = \mathcal{H}_{\text{kepl}} + \mathcal{H}_{\text{res}} + \mathcal{O}(e^2, I^2), \quad (4.4)$$

and then drop the higher order terms. We note that terms that describe the mutual influence of the innermost and outermost planet are not included in \mathcal{H}_{res} as this is a higher order effect. Note also that by dropping the higher order terms the problem is reduced to a planar one. In order to maintain the canonical nature of the equations of motion, we introduce for each planet the modified Delaunay action-angle variables $(\Lambda_i, \Gamma_i, \lambda_i, \gamma_i)$, Equation (2.98). In these variables, the Keplerian part $\mathcal{H}_{\text{kepl}}$ of the Hamiltonian (4.1) takes the form

$$\mathcal{H}_{\text{kepl}} = -\sum_{i=1}^3 \frac{\mathcal{G}^2(M_* + m_i)^2 \mu_i^3}{2\Lambda_i^2} \simeq -\sum_{i=1}^3 \frac{m_i^3}{2} \left(\frac{\mathcal{G}M_*}{\Lambda_i} \right)^2, \quad (4.5)$$

while the resonant Hamiltonian writes

$$\begin{aligned} \mathcal{H}_{\text{res}} = & -\frac{\mathcal{G}^2 M_* m_1 m_2^3}{\Lambda_2^2} \left(f_{\text{res}}^{(1,1)} \sqrt{\frac{2\Gamma_1}{\Lambda_1}} \cos(k^{(1)}\lambda_2 - (k^{(1)} - 1)\lambda_1 + \gamma_1) \right. \\ & \left. + f_{\text{res}}^{(2,1)} \sqrt{\frac{2\Gamma_2}{\Lambda_2}} \cos(k^{(1)}\lambda_2 - (k^{(1)} - 1)\lambda_1 + \gamma_2) \right) \\ & -\frac{\mathcal{G}^2 M_* m_2 m_3^3}{\Lambda_3^2} \left(f_{\text{res}}^{(1,2)} \sqrt{\frac{2\Gamma_2}{\Lambda_2}} \cos(k^{(2)}\lambda_3 - (k^{(2)} - 1)\lambda_2 + \gamma_2) \right. \\ & \left. + f_{\text{res}}^{(2,2)} \sqrt{\frac{2\Gamma_3}{\Lambda_3}} \cos(k^{(2)}\lambda_3 - (k^{(2)} - 1)\lambda_2 + \gamma_3) \right); \end{aligned} \quad (4.6)$$

we note that in going from (4.3) to (4.6) we have made use of the approximation $e \simeq \sqrt{2\Gamma/\Lambda}$, which holds at first order in e .

This Hamiltonian is clearly not integrable. However, one can perform a series of changes of variables that allow us to reduce by two the number of degrees of freedom. The first canonical transformation is

$$\begin{aligned} \Theta^{(1)} &= \frac{1}{k^{(1)}}\Lambda_2 + \frac{k^{(2)} - 1}{k^{(1)}k^{(2)}}\Lambda_3, & \theta^{(1)} &= k^{(1)}\lambda_2 - (k^{(1)} - 1)\lambda_1, \\ \Theta^{(2)} &= \frac{1}{k^{(2)}}\Lambda_3, & \theta^{(2)} &= k^{(2)}\lambda_3 - (k^{(2)} - 1)\lambda_2, \\ \mathcal{K} &= \Lambda_1 + \frac{k^{(1)} - 1}{k^{(1)}}\Lambda_2 + \frac{(k^{(1)} - 1)(k^{(2)} - 1)}{k^{(1)}k^{(2)}}\Lambda_3, & \kappa &= \lambda_1, \end{aligned} \quad (4.7)$$

which is analogous to (3.5) (a linear transformation on the angles canonically extended to find the corresponding momenta, cfr. Subsect. 2.1.3.2). Now, the new angle κ does not appear explicitly in the Hamiltonian, which makes \mathcal{K} a constant of motion. The significance of \mathcal{K} has already been discussed for two planets (e.g. [Michtchenko et al.(2008), Batygin and Morbidelli(2013)a]), see also Section 3.1), and it has to do with the location of exact resonance. As we have already mentioned, neighbouring planets can still be in resonance while their semi-major axis ratios do not satisfy exactly the resonant condition $a_i/a_{i+1} = ((k-1)/k)^{2/3}$, therefore the observed $a_{i,\text{obs}}$ do not alone reveal how close the planets are to resonance, nor do they represent the nominal \bar{a}_i that do satisfy it. However by calculating from $a_{i,\text{obs}}$ the value of the constant of motion \mathcal{K} , and imposing in the formula

$$\begin{aligned} \frac{\mathcal{K}}{\Lambda_3} &= \frac{\mu_1}{\mu_3} \sqrt{\frac{M_* + m_1}{M_* + m_3} \frac{a_1}{a_3}} + \frac{k^{(1)} - 1}{k^{(1)}} \frac{\mu_2}{\mu_3} \sqrt{\frac{M_* + m_2}{M_* + m_3} \frac{a_2}{a_3}} + \\ &+ \frac{(k^{(1)} - 1)(k^{(2)} - 1)}{k^{(1)}k^{(2)}}, \end{aligned} \quad (4.8)$$

the condition of exact resonance, $a_i/a_{i+1} = ((k-1)/k)^{2/3}$, for all pairs $i = 1, 2$, we derive the nominal value of $\bar{\Lambda}_3$. From this, one easily obtains \bar{a}_3 from $\bar{a}_3 = (\bar{\Lambda}_3/m_3)^2/(\mathcal{G}M_*)$, and then recursively $\bar{a}_2 = ((k^{(2)} - 1)/k^{(2)})^{2/3}\bar{a}_3$, and finally $\bar{a}_1 = ((k^{(1)} - 1)/k^{(1)})^{2/3}\bar{a}_2$.

Recall that even when they are in resonance, the planets' semi-major axes do not coincide exactly with their nominal resonant values at small values of the eccentricity, due to a fast precession of the periaapsis, as we saw in Subsect. 3.1.2. We can however already greatly simplify the calculations given that we will only consider deviations of the semi-major axis ratios from the nominal ones of no more than 5% (moreover, very small values of the eccentricities are observationally disfavoured for Kepler systems, [Hadden and Lithwick(2017)]). In this limit, we can expand the Keplerian part to second order in $\delta\Lambda_i = \Lambda_i - \bar{\Lambda}_i$, where $\bar{\Lambda}_i = \mu_1\sqrt{\mathcal{G}(M_* + m_i)\bar{a}_1}$ is the nominal resonant value of Λ_i , and write

$$\mathcal{H}_{\text{kepl}} = -\sum_{i=1}^3 \frac{\mathcal{G}^2(M_* + m_i)^2\mu_i^3}{2} \times \left(\frac{1}{\bar{\Lambda}_i^2} - 2\frac{1}{\bar{\Lambda}_i^3}\delta\Lambda_i + 3\frac{1}{\bar{\Lambda}_i^4}\delta\Lambda_i^2 + \mathcal{O}(\delta\Lambda_i^3) \right), \quad (4.9)$$

which, inserting the definition of $\delta\Lambda_i$ and dropping the unimportant constant term and the higher order terms, reduces to:

$$\mathcal{H}_{\text{kepl}} = \sum_{i=1}^3 \left(4\bar{n}_i\Lambda_i - \frac{3}{2}\bar{h}_i\Lambda_i^2 \right), \quad (4.10)$$

where $\bar{n}_i = \sqrt{\mathcal{G}(M_* + m_i)/\bar{a}^3}$ is the nominal mean motion and $\bar{h}_i = \bar{n}_i/\bar{\Lambda}_i = 1/(\mu_i \bar{a}_i^2)$ can be interpreted as the inverse of the moment of inertia of a circular orbit around the star. As we will see below, for the purposes of our study, considering the expanded Keplerian Hamiltonian up to order $\mathcal{O}(\delta\Lambda^2)$ does not introduce any significant inaccuracy in our calculations. Concerning the resonant Hamiltonian (4.6), we can evaluate it at the nominal values $\Lambda = \bar{\Lambda}$ as it is already of order $\mathcal{O}(e)$.

Finally, one last canonical change of variable is made:

$$\begin{aligned}
\Psi_1^{(1)} &= \Gamma_1 + \Gamma_2 + \Gamma_3 - \Theta^{(2)}, & \psi_1^{(1)} &= \theta^{(1)} + \gamma_1, \\
\Psi_1^{(2)} &= \Theta^{(2)}, & \psi_1^{(2)} &= \theta^{(2)} + \gamma_2, \\
\Psi_2^{(1)} &= -\Gamma_2 - \Gamma_3 + \Theta^{(2)}, & \delta\gamma^{(1)} &= \gamma_1 - \gamma_2, \\
\Psi_2^{(2)} &= -\Gamma_3, & \delta\gamma^{(2)} &= \gamma_2 - \gamma_3, \\
\Omega &= \Theta^{(1)} + \Theta^{(2)} - (\Gamma_1 + \Gamma_2 + \Gamma_3), & \theta' &= \theta^{(1)},
\end{aligned} \tag{4.11}$$

which is analogous to (3.7). Again, we see that the new angle θ' does not appear in the Hamiltonian, making Ω another constant of motion of the system (we note that here Ω does not denote the longitude of the node which does not appear in our model, since the problem is planar). We are therefore left with a four-degree-of-freedom Hamiltonian which depends parametrically on the constants of motion \mathcal{K} , Ω . We already mentioned the meaning of \mathcal{K} ; for Ω , one can easily show that $\mathcal{K} + \Omega = (\Lambda_1 - \Gamma_1) + (\Lambda_2 - \Gamma_2) + (\Lambda_3 - \Gamma_3) \equiv \mathcal{L}$, the total angular momentum of the system, which is to be expected knowing that it is a conserved quantity.

4.2.1 Resonant equilibrium points

Let us briefly summarise our work so far. We have obtained a 4-degrees-of-freedom Hamiltonian $\bar{\mathcal{H}}$ which is a function of the actions $(\Psi_1^{(1)}, \Psi_1^{(2)}, \Psi_2^{(1)}, \Psi_2^{(2)})$ and the angles $(\psi_1^{(1)}, \psi_1^{(2)}, \delta\gamma^{(1)}, \delta\gamma^{(2)})$, and depends parametrically on the values of \mathcal{K} and Ω (which are linked to the orbital elements as expressed in (2.98), (4.7) and (4.11)); the Hamiltonian in these variables reads

$$\begin{aligned}
\bar{\mathcal{H}} &= \mathcal{H}_{\text{kepl}} + \mathcal{H}_{\text{res}}, \\
\mathcal{H}_{\text{kepl}} &= \mathcal{H}_{\text{kepl}}(\Psi_1^{(1)}, \Psi_1^{(2)}; \mathcal{K}, \Omega), \\
\mathcal{H}_{\text{res}} &= \mathcal{H}_{\text{res}}(\Psi_1^{(1)}, \Psi_1^{(2)}, \Psi_2^{(1)}, \Psi_2^{(2)}, \psi_1^{(1)}, \psi_1^{(2)}, \delta\gamma^{(1)}, \delta\gamma^{(2)}; \mathcal{K}, \Omega),
\end{aligned} \tag{4.12}$$

where the explicit dependence of each term can be obtained by direct substitution. We now consider the stable equilibria of this system, following the same procedure as in Subsect. 3.1.2. We look for equilibrium points of this Hamiltonian by simultaneously solving the set of equations

$$\begin{aligned}
\frac{\partial \bar{\mathcal{H}}}{\partial \Psi_1^{(1)}} = 0, \quad \frac{\partial \bar{\mathcal{H}}}{\partial \Psi_1^{(2)}} = 0, \quad \frac{\partial \bar{\mathcal{H}}}{\partial \Psi_2^{(1)}} = 0, \quad \frac{\partial \bar{\mathcal{H}}}{\partial \Psi_2^{(2)}} = 0, \\
\frac{\partial \bar{\mathcal{H}}}{\partial \psi_1^{(1)}} = 0, \quad \frac{\partial \bar{\mathcal{H}}}{\partial \psi_1^{(2)}} = 0, \quad \frac{\partial \bar{\mathcal{H}}}{\partial \delta\gamma^{(1)}} = 0, \quad \frac{\partial \bar{\mathcal{H}}}{\partial \delta\gamma^{(2)}} = 0.
\end{aligned} \tag{4.13}$$

We note that by the functional form of the Hamiltonian, any combination of values in $\{0, \pi\}$ for the angles immediately satisfies the last line. These are known as the symmetric equilibria. Asymmetric equilibria are possible (e.g. [Beaugé et al.(2006)]), but they do not play a role at the low eccentricities at which we are limiting ourselves here.

Plugging in specific values for the angles in $\{0, \pi\}$ reduces the problem of solving the four equations that appear in the first line to find the stable equilibria of the system. Like in the case of two planets, Subsect. 3.1.2, we note that although the Hamiltonian depends on both Ω and \mathcal{K} , the latter assumes a natural value for any specific problem at hand (that is, any values of m_1, m_2, m_3 and of $k^{(1)}, k^{(2)}$) by rescaling the units so that for example $\bar{a}_1 = 1$. To trace out the loci of the resonant equilibria, we then simply change the value of Ω (which corresponds to changing the angular momentum \mathcal{L} , at constant \mathcal{K}) and solve equations (4.13) to find $(\Psi_{1,\text{eq}}^{(1)}, \Psi_{1,\text{eq}}^{(2)}, \Psi_{2,\text{eq}}^{(1)}, \Psi_{2,\text{eq}}^{(2)})$, which are then translated into orbital elements working backwards through the canonical transformations.

We show in Figure 4.1 one example of equilibrium curves for three equal-mass planets down to eccentricities of order 10^{-3} , where we also show that the expanded Keplerian Hamiltonian provides an accurate description of the system. These curves are then matched against the result of full N -body numerical simulations of a system

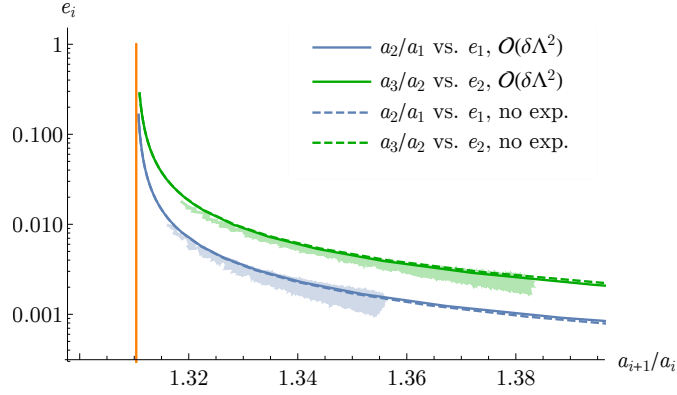


Figure 4.1: Equilibrium curves showing the loci of the stable resonant equilibrium points calculated as explained in the text, in the case of a 3:2 – 3:2 mean motion resonance chain, with $m_1 = m_2 = m_3 = 10^{-4}M_*$. The full curves are calculated using the expanded Keplerian Hamiltonian (4.10), while the dashed curves are calculated using the unexpanded Keplerian Hamiltonian (4.5), showing very little difference down to very small eccentricities and for reasonable values of the nearly exactly resonant semi-major axis ratio. The location of the nominal resonant semi-major axis ratio $(3/2)^{2/3}$ is shown by a vertical orange line. We also superimpose the numerically computed evolution of a three-planet system deep in the 3:2 mean motion resonance (for both pairs) and undergoing dissipative evolution depicted with transparent lines: the system follows the locations of the equilibrium points, which are close to the curves calculated analytically.

with the same physical parameters which starts deep in resonance and evolves dissipatively so to slowly follow the resonant equilibrium points (transparent lines).² These N -body integrations with the addition of dissipative effects will be detailed below in Section 4.3.3.

4.2.2 Resonant repulsion for three-planets systems

The equilibrium curves in the a_{i+1}/a_i vs e_i plane deviate to large semi major axis ratios with decreasing eccentricity. For systems of two planets, it is well known that for first order resonances the resonant equilibria always reside wide of the exact resonant ratio of the semi-major axes. That is, because the resonant condition requires $k\dot{\lambda}_2 - (k-1)\dot{\lambda}_1 - \dot{\varpi}_{1,2} \simeq 0$ and since the perihelion precession is always retrograde, $\dot{\varpi}_{1,2} < 0$, one necessarily has $k\dot{\lambda}_2 - (k-1)\dot{\lambda}_1 < 0$, that is $a_2/a_1 > (k/(k-1))^{2/3}$, as discussed in Chapter 3. More concretely, at low enough eccentricities and at semi-major axis ratios close to the nominal ones, one finds directly using the resonant Hamiltonian expanded to first order in e that $\dot{\varpi}_1 = \alpha f_{\text{res}}^{(1)} n_1 (m_2/M_*) e_1^{-1}$, $\dot{\varpi}_2 = -f_{\text{res}}^{(2)} n_2 (m_1/M_*) e_2^{-1}$ with $f_{\text{res}}^{(1)} < 0$, $f_{\text{res}}^{(2)} > 0$: this means that the lower are the eccentricities, the wider are the equilibria from the exact commensurability. At higher eccentricities the secular terms, of $\mathcal{O}(e^2)$, become more important, and they give a positive contribution (that is constant in e) in $\dot{\varpi}$; however, one still finds $\dot{\varpi}_{1,2} < 0$ at higher eccentricities as well (e.g. [Pichierri et al.(2018)], see also Subsect. 3.1.2).

For systems with three planets, since we used a first order expansion in e in the analytical model and therefore we are not including the mutual interaction between the inner planet and the outer planet, the perihelion precession will still be retrograde and it will remain true that for each pair of planets the resonant equilibria lie wide of the exact nominal resonance, and that, in the limit of small enough eccentricities, the separations grow with diminishing eccentricities. This is indeed what we see in Figure 4.1, where the analytically computed resonant equilibria agree very well with our numerical simulations.³

Consider now a resonant three-planet system that is close to some resonant equilibrium point and is subjected to (tidal) dissipation. Assuming that the dissipative evolution is slow compared to that of the resonant variables, which has a characteristic timescale given by the libration period at vanishing amplitude of libration, the system will remain bound to the equilibrium curves. Since the eccentricities are damped by the dissipation, we conclude that the semi-major axes are expected to diverge. We also conclude that systems of three planets that are close to

²We note that even away from nominal resonance all four resonant angles can continue to librate when the system is sufficiently close to the resonant equilibrium point, unlike what has been erroneously stated in Section 4 of [Batygin and Morbidelli(2013)b].

³At higher eccentricities the main term which might shift the equilibria in a_2/a_1 , a_3/a_2 to the left of exact resonance is the second order (secular) term which describes the interaction between the inner planet and outer planet; however, we checked that adding this term to the Hamiltonian, even at high eccentricities and for a very massive outer planet the picture does not change.

a given first-order mean motion resonance but for which one or both pairs is narrow of the resonance can only be explained by a resonant configuration if the amplitude of libration around the resonant equilibrium point is large, and temporarily takes the planets to period ratios that are lower than the exact resonant period ratios.

We finally note here a property of these curves that will be used later. The Hamiltonian (4.12) can be rescaled by a parameter which encapsulates all of the information regarding how the dynamics scales with mass ratios and physical sizes of the orbits. This is analogous to the rescaling found in [Batygin and Morbidelli(2013)a] for the two-planets case (see also Appendix B), and only works when using an expanded Hamiltonian and for semi-major axes close to the nominal resonant ones, which are our working assumptions anyway. Therefore, after rescaling all planetary masses by a certain factor \tilde{m} , the corresponding loci of the resonant equilibria are also simply rescaled, and can be immediately calculated. More specifically, one can easily see that for given semi-major axis ratios, the values of the eccentricities that correspond to the resonant equilibrium point are just rescaled by \tilde{m} , since the eccentricities and the planetary masses appear as a product in the perturbing Hamiltonian. This can be easily understood using the previous formula $\tilde{\omega} \propto (m_{\text{pl}}/M_*)e^{-1}$, and noticing that fixing the semi-major axis ratio ultimately fixes $\tilde{\omega}$ by the resonance condition; therefore, rescaling the planetary masses, at fixed $\tilde{\omega}_1 = \tilde{\omega}_2 = \tilde{\omega}_3$ (i.e. at constant semi-major axis ratios), the eccentricities are simply rescaled by the same factor. This also implies that for a given equilibrium configuration characterised by a semi-major axis ratio $a_{2,\text{eq}}/a_{1,\text{eq}}$, the corresponding equilibrium of the ratio $a_{3,\text{eq}}/a_{2,\text{eq}}$ will be independent of \tilde{m} , that is independent of the absolute value of the planetary masses. Only the ratios m_1/m_2 and m_2/m_3 are significant, meaning that if one changes one of these ratios, the equilibrium in $a_{3,\text{eq}}/a_{2,\text{eq}}$ corresponding to the same $a_{2,\text{eq}}/a_{1,\text{eq}}$ will change (see Appendix B for an explicit presentation of this rescaling procedure).

4.3 A scenario for dissipative evolution of three-planet systems

In this section, we select near-resonant systems of 3 planets from the NASA Exoplanet Archive catalogue, and discuss whether or not their observed orbital configuration is compatible with the dynamical evolution driven by the following physical processes. Resonant capture for three planets is analogous to that of two planets, described in the previous chapter. The planets can be captured in sequence: first the second planet goes in resonance with the first one when the latter is trapped at the inner edge of the disc; then the third planet goes in resonance with the second, once the migration of the latter is stopped (or slowed down) by the resonant interaction with the first planet. The disc is then slowly depleted and the planets maintain their configuration. Following the depletion of the gas, dissipation is introduced which removes orbital energy at constant angular momentum; this is done here implementing tidal dissipation but again the method is general. During this phase of dissipative evolution, the planets will follow again the equilibrium curves of the resonant Hamiltonian for changing Ω , this time decreasing their eccentricities and hence increasing the semi major axis ratios a_{i+1}/a_i for each planet-planet pair. We note that Ω changes because \mathcal{K} changes (since do the semi-major axes as a consequence of the dissipation of energy) and \mathcal{L} has to stay constant for this kind of dissipation.

4.3.1 Choice of systems

Recall that the only orbital parameters that are well constrained by transit data are the orbital periods, which allow us to obtain the semi-major axis ratios even without knowing the mass of the star. The orbital periods listed in the NASA Exoplanet Archive catalogue are, for the cases considered below, obtained by phase-folding the observed signal. Since we will be considering short-period planets this is equivalent to obtaining the mean orbital period, so that we can directly compare the corresponding observed semi-major axis ratios with the ones coming from our averaged model of resonance.⁴ The masses of the planets could be obtained starting from the estimates for the planetary radii, and making use of a scaling relation such as the one found in [Wu and Lithwick(2013)], $m_{\text{pl}} = 3M_{\oplus}(R_{\text{pl}}/R_{\oplus})$, where m_{pl} , R_{pl} are the mass and radius of the exoplanet, and R_{\oplus} , M_{\oplus} those of the Earth. However this is only a statistical law and the uncertainties on the mean densities usually preclude accurate estimates for the masses, which are indeed not yet known. We will therefore use the masses as free parameters of our study. In fact, as we already saw, the only significant quantities for our study are the mass ratios between the planets; this follows from the discussion at the end of Section 4.2.2. In practice, we will choose a total planetary mass $m_{\text{tot}} = m_1 + m_2 + m_3$ by using for each system the mean planetary radius $(R_1 + R_2 + R_3)/3$, the aforementioned scaling relationship from [Wu and Lithwick(2013)] to obtain an average planetary mass $m_{\text{pl,avg}}$,

⁴We should remark however that even the periods are not known with arbitrary precision, meaning that there might be small discrepancies in the values that are used in different works. In this work, we will use the ones listed in the NASA Exoplanet Archive catalogue without considering error bars. This is enough for the scope of our analysis.

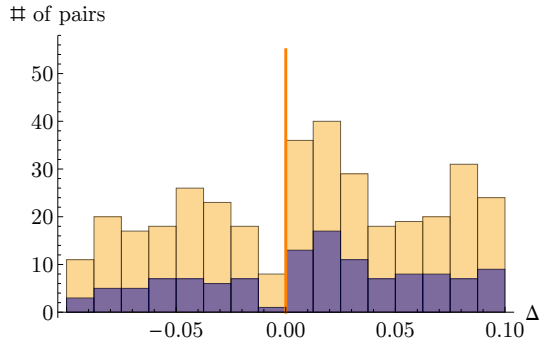


Figure 4.2: Distribution of the (signed) normalised distance from first order mean motion resonances $\Delta = \frac{k-1}{k} \frac{P_2}{P_1} - 1$ with $k = 2, 3$ in all exoplanetary systems (yellow) and for three-planet systems (purple). We note a clear peak to the right of the value $\Delta = 0$ (corresponding to the exact nominal resonance, indicated by a vertical orange line), which is most prominent for $0 < \Delta \lesssim 0.05$. Out of the 358 pairs plotted here, there are 123 total pairs in this configuration. For the three-planets systems only, 48 pairs have $0 < \Delta \lesssim 0.05$, out of the 121 shown in the purple histogram.

and setting $m_{\text{tot}} = 3m_{\text{pl,avg}}$. Again, this is simply a choice that we are forced to make in order to run N -body simulations, but it does not in any way change our result, which is therefore not sensitive to the uncertainties on the radii (or to the lack of their knowledge, as will be the case for YZ Ceti). Note however that since individual Kepler systems seem to show a homogeneity in planetary radii and masses [Weiss et al.(2018), Millholland et al.(2017)], this choice likely constitutes a good approximation to the real architecture of these systems.

Given a pair of neighbouring planets with periods P_1 and P_2 respectively, which are close to a given first order resonance, $P_1/P_2 \simeq (k-1)/k$, one can define (see for example [Lithwick et al.(2012), Hadden and Lithwick(2014)])

$$\Delta_{k/(k-1)} = \Delta := \frac{k-1}{k} \frac{P_2}{P_1} - 1, \quad (4.14)$$

called the *normalised distance from (exact) resonance*. When $\Delta > 0$ the planets reside *wide* of the $k : k-1$ resonance, while when $\Delta < 0$ the planets are *narrow* of the resonance.

We will be selecting planetary systems of three planets with both pairs close to some first order mean motion resonance such that $|\Delta| \lesssim 0.05$ holds for both pairs, with $k = 2, 3$ as they appear to be the most common resonances. We recall that the normalised width of a resonance, calculated when the separatrix enclosing the resonant island first appears, is of order $\sim 4(m/M_*)^{2/3}(k-1)^{1/3}$ ([Deck et al.(2013), Batygin(2015)]), and the average planetary mass for Kepler systems is of order $m \sim 3 \times 10^{-5} M_*$. This gives a typical resonance width of order $\Delta \sim$ a few 10^{-3} in normalised units, meaning that in selecting systems with $0 < \Delta \lesssim 0.05$ we are generously including planetary pairs with separation 50 – 100 times larger than the typical resonant width. Moreover, the available data shows that for systems close to mean motion resonance, the distribution of Δ favours values between 0 and $\lesssim 0.05$ ([Hadden and Lithwick(2017)], see also Figure 4.2). Additionally, we will require that $\Delta > 0$, which is justified by our results in the previous section.

Of all three-planet systems, only 8 satisfy $|\Delta| < 0.05$ for both pairs, that is, appear to be close to a multi-resonant chain (they are Kepler-31, Kepler-53, Kepler-114, Kepler-207, Kepler-289, Kepler-305, Kepler-326, YZ Ceti). The architecture of these systems is shown in Figure 4.3; of these, only 3 satisfy $\Delta > 0$ for both pairs. These are Kepler-31, Kepler-305 and YZ Ceti. For these systems, we consider whether or not their observed orbital configuration can be consistent with the scenario envisioned above.

4.3.2 Analytical maps

With our analytical model of resonance from Section 4.2, we can construct analytical maps of resonant equilibrium points for different resonant chains and different planetary mass ratios. For the purposes of the current study, we proceed as follows. For an arbitrary system, we assume to have observations for the orbital period ratios and obtain the values of $k^{(1)}$ and $k^{(2)}$. We then pick both mass ratios m_2/m_1 and m_3/m_2 and construct the equilibrium curves as explained in Section 4.2.1 (in practice, we work with the aforementioned Hamiltonian rescaled by the common planetary mass factor \tilde{m} , see Appendix B). Then, we find the resonant equilibrium point (i.e. the

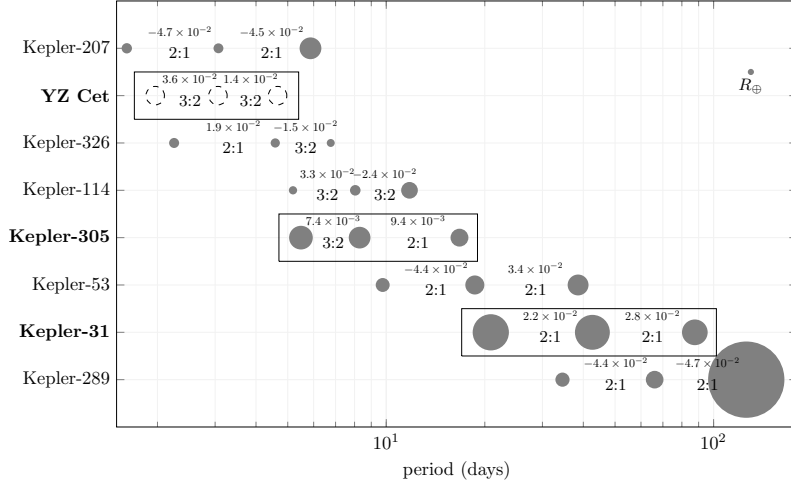


Figure 4.3: Orrery of the three-planets systems sufficiently close to first order mean motion resonances $k:k-1$ with $k = 2, 3$, with a normalised distance to resonance $|\Delta| < 0.05$ for both pairs. For each system, we place a circle in correspondence of the period of each planet, and indicate between pairs of planets the first order mean motion resonance in which they are envisioned to reside (below) and the normalised distance to that resonance Δ (above); the sign of Δ indicates if the pair of planets are narrow ($\Delta < 0$) or wide ($\Delta > 0$) of the resonance. For our analysis, we will only consider systems for which $\Delta > 0$ for both pairs (the systems enclosed by a box). The size of the circle is an indication of the estimated radius of the planet (the small dot in the top right corner demonstrates the size of Earth). For YZ Ceti this information is not available, but this does not pose a problem for our study.

value of \mathcal{L}) that corresponds to a value of a_3/a_1 equal to the observed semi-major axis ratio, and therefore put $(a_3/a_1)|_{\text{eq}} \equiv (a_3/a_1)|_{\text{obs}}$. The determined value of \mathcal{L} fixes the eccentricities of all three planets, since they are all linked by the equilibrium curves.

Recall that we only have one free parameter to select the chosen equilibrium configuration: the angular momentum; however, we have two observables that we want to match, which are both semi-major axis ratios a_2/a_1 and a_3/a_2 . This is unlike the case of only two resonant planets, where one has one free parameter (again the angular momentum \mathcal{L}) and only one observable (the single a_2/a_1 ratio): in this case, it would always be possible to find a suiting value of \mathcal{L} which gives a resonant equilibrium configuration such that the semi-major axis ratio is equal to the observed one (provided that the latter is wide of the nominal value $(k/(k-1))^{2/3}$). In the case of three planets, choosing \mathcal{L} such that $(a_3/a_1)|_{\text{eq}} \equiv (a_3/a_1)|_{\text{obs}}$ automatically fixes the equilibrium values of both semi-major axis ratios a_2/a_1 and a_3/a_2 . Considering for example the corresponding equilibrium $(a_3/a_2)|_{\text{eq}}$, we obtain the weighted difference

$$\bar{\delta}(a_3/a_2) := \frac{((a_3/a_2)|_{\text{eq}} - (a_3/a_2)|_{\text{obs}})}{(a_3/a_2)|_{\text{obs}}} \quad (4.15)$$

between $(a_3/a_2)|_{\text{eq}}$ and the observed value $(a_3/a_2)|_{\text{obs}}$. The same can be done for a_2/a_1 , which gives a similar (absolute) result, $|\bar{\delta}(a_2/a_1)| \simeq |\bar{\delta}(a_3/a_2)|$. Maintaining this procedure, we loop over different planetary mass ratios.

We applied this procedure to the three systems selected above, starting with Kepler-305, which resides close to a 3:2 – 2:1 mean motion resonance chain. First of all, to better represent what these analytical maps intend to show, we draw in Figure 4.4 equilibrium curves (equivalent to those shown in Figure 4.1) which describe the locations of the resonant equilibria for this resonant chain and for one specific choice of mass ratios $m_1/m_2 = m_2/m_3 = 1$. The observed values of the semi-major axis ratios are indicated by dashed vertical lines; then, we indicate with a red dot the location of the specific equilibrium point that is selected when we impose $(a_3/a_1)|_{\text{eq}} \equiv (a_3/a_1)|_{\text{obs}}$; finally, we obtain $\bar{\delta}(a_3/a_2)$ as defined in (4.15) (and similarly for $\bar{\delta}(a_2/a_1)$). As explained above, imposing $(a_3/a_1)|_{\text{eq}} \equiv (a_3/a_1)|_{\text{obs}}$ automatically fixes all equilibrium eccentricities $e_{1,\text{eq}}, e_{2,\text{eq}}, e_{3,\text{eq}}$, and we can store their maximum $\max\{e_{1,\text{eq}}, e_{2,\text{eq}}, e_{3,\text{eq}}\}$ to better describe the orbital configuration at the selected equilibrium point. We choose to consider the quantity $\max e_{\text{eq}}$ rescaled by a common planetary mass factor \tilde{m} in order to obtain results that are independent of the planet-to-star mass ratio, since again the latter quantity does not effect equilibrium semi-major axis ratio configurations, and therefore does not affect $\bar{\delta}(a_3/a_2)$. Panels (a) and (b) in Figure 4.5 are the result of

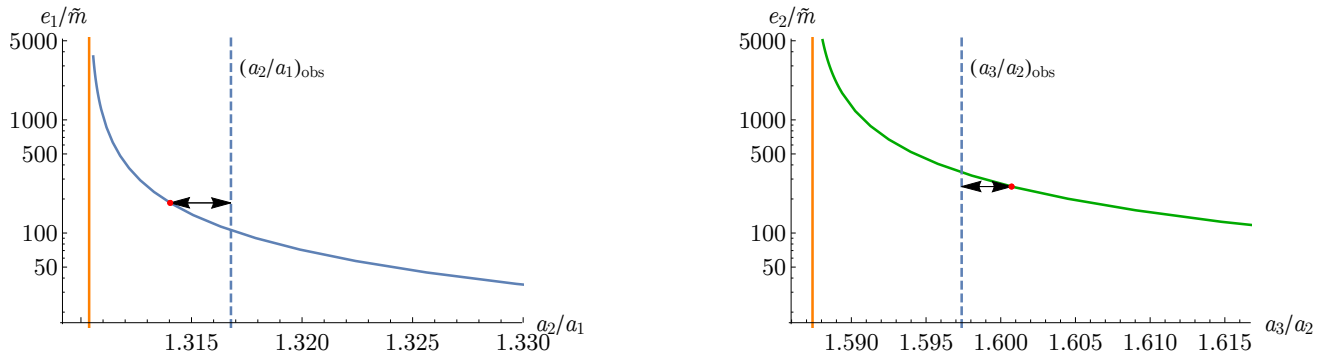


Figure 4.4: Locations of the resonant equilibrium points in the a_{i+1}/a_i vs. e_i/\tilde{m} planes, $i = 1, 2$, for three equal-mass planets in a 3:2 – 2:1 mean motion resonance chain, close to which Kepler-305 resides. Orange vertical lines show the exact nominal commensurability, while dashed vertical lines show the observed a_2/a_1 and a_3/a_2 in the case of Kepler-305. As explained in the text, we select one equilibrium configuration (indicated by the red dot in both panels) by requiring that $(a_3/a_1)|_{\text{eq}} \equiv (a_3/a_1)|_{\text{obs}}$, which automatically fixes all orbital elements a_2/a_1 , a_3/a_2 , e_1 , e_2 and e_3 along the equilibrium curves. $\bar{\delta}$ is the relative distance between the dashed vertical line and the red dot in the a_{i+1}/a_i metric (indicated by the black arrows).

this procedure spanning different planetary mass ratios, showing maps of $\bar{\delta}(a_2/a_1)$ and $\max e/\tilde{m}$ using the observed semi-major axis ratios of Kepler-305 (the bottom panels (c) and (d) show the results of numerical simulations which will be detailed in Section 4.3.3, and are only intended to validate the analytical results). We show analogous results for the system YZ Cet, residing close to a 3:2 – 3:2 chain, in Figure 4.6, and for For Kepler-31, a chain (close to the) 2:1 – 2:1 mean motion resonances, in Figure 4.7. We remark that $\bar{\delta}(a_3/a_2)$ is very small for all planet mass ratios, of the order of the expected libration widths ($\mathcal{O}(10^{-3})$) as discussed before – with the exception of YZ Cet). This means that these systems can be very close to the exact resonance, provided that they have the appropriate eccentricities.

4.3.3 Numerical simulations

In order to check the validity of our analytical calculations, we turned to numerical simulations by performing the following study. We simulated the process of capture into a chain of first-order mean motion resonances by placing the planets relatively wide of the desired resonances, according to the specific values of $k^{(1)}$ and $k^{(2)}$ of each case, and simulating the effects of the protoplanetary discs by adding fictitious forces which mimic the interaction with the disc [Cresswell and Nelson(2006), Cresswell and Nelson(2008)] to the N -body integrator `swift-symba`. To ensure convergent migration for all planetary mass ratios, we stopped the migration of the inner planet by adding at the desired location a so-called planetary trap, which reproduces the effect of the inner edge of the disc and describes a disc cavity around a star [Masset et al.(2006)] (this step is equivalent to the numerical experiments presented in Section 3.2 for the case of two planets). As we mentioned above, the mass ratios m_1/m_2 and m_2/m_3 were kept as free parameters. Since again we are interested in mass ratios of order unity, in our simulations we limited ourselves to m_1/m_2 and m_2/m_3 between ~ 0.2 and ~ 5 , and repeated the same set of simulations.

Recall that the timescale for planetary migration depends on the mass of the planet, meaning that changing the mass ratios will change the relative speeds at which each planet’s semi-major axis decreases, which is practically inconvenient. Therefore, we used a fictitious τ_a which is kept equal for all planets and constant along the different simulations of resonant capture. This has the sole effect of making it easier to automate the simulations, and does not affect our results. We need only to make sure that at the end of the disc-migration phase the semi-major axis ratios are smaller than the observed ones, since the subsequent evolution dominated by tidal dissipation will only cause the semi-major axis ratios to expand. We note that this is always possible, since one can obtain different final eccentricities at the captured state by changing the ratio of the eccentricity damping τ_e and the migration rate τ_a , and thus obtain different corresponding equilibrium values of the semi-major axis ratios. The latter approach the exact commensurabilities as the eccentricities grow (Figure 4.1), and since for the systems that we are studying both pairs reside wide enough of the nominal resonance, the final eccentricities need not be too high, of order a few 10^{-2} for a typical planetary mass of order $10^{-5}M_*$. It does not matter how much smaller the semi-major axis ratios are at the end of the migration phase with respect to the observed ratios. A smaller post migration ratio will require a longer dissipative evolution of the system to reach the observed ratio, but the final results will be the

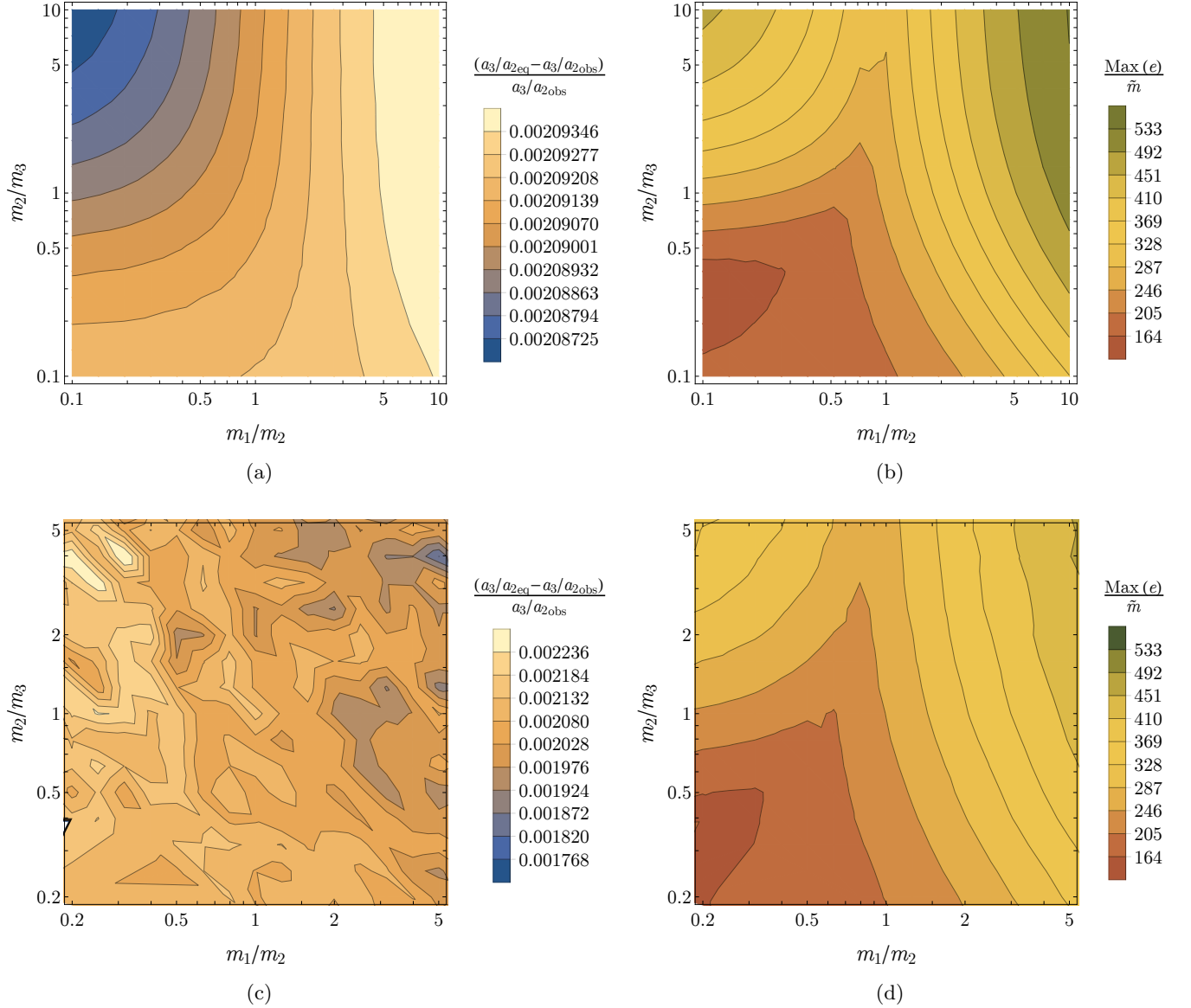


Figure 4.5: *Top row*: Analytical maps constructed for Kepler-305 as explained in Section 4.3.2. In panel (a) we plot the quantity $\bar{\delta}(a_3/a_2)$, which represents how close the system is now to some resonant equilibrium point, for different mass ratios m_1/m_2 and m_2/m_3 (each point in this plot is constructed by repeating the procedure described in Figure 4.4). We notice that $\bar{\delta}(a_3/a_2)$ changes very little with the mass ratios, and is of the order of ~ 0.002 . Comparing with Figure 4.8, we see that this can be the case by pure chance only in $\sim 15\%$ of randomly generated systems close to the 3:2 – 2:1 mean motion resonance chain. In panel (b) we show a map of the quantity $\max e_{\text{eq}}/\tilde{m}$ representing the equilibrium orbital configuration that is selected at each fixed value of m_1/m_2 and m_2/m_3 by imposing $(a_3/a_1)|_{\text{eq}} \equiv (a_3/a_1)|_{\text{obs}}$. *Bottom row*: Numerical maps constructed for Kepler-305 as explained in Section 4.3.3. We show numerical maps of $\bar{\delta}(a_3/a_2)$ in panel (c) and $\max e_{\text{eq}}/\tilde{m}$ in panel (d), analogous to the analytical plots above (over a slightly smaller range of mass ratios for simplicity), in order to validate the analytical calculations. While the agreement between panels (b) and (d) is very good, panel (c) is affected by large noise due to the fast oscillations in the numerical simulations, but the values encompassed by $\bar{\delta}(a_3/a_2)$ are consistent with the ones found in panel (a).

same.

After the desired resonant state is obtained, we slowly depleted the gas. Finally, we added the effects of tidal dissipation (following the prescription found in [Mardling and Lin(2002)]), using arbitrary quality factors for the planets but large enough to ensure that the dissipative evolution be slow compared to the resonant evolution of the

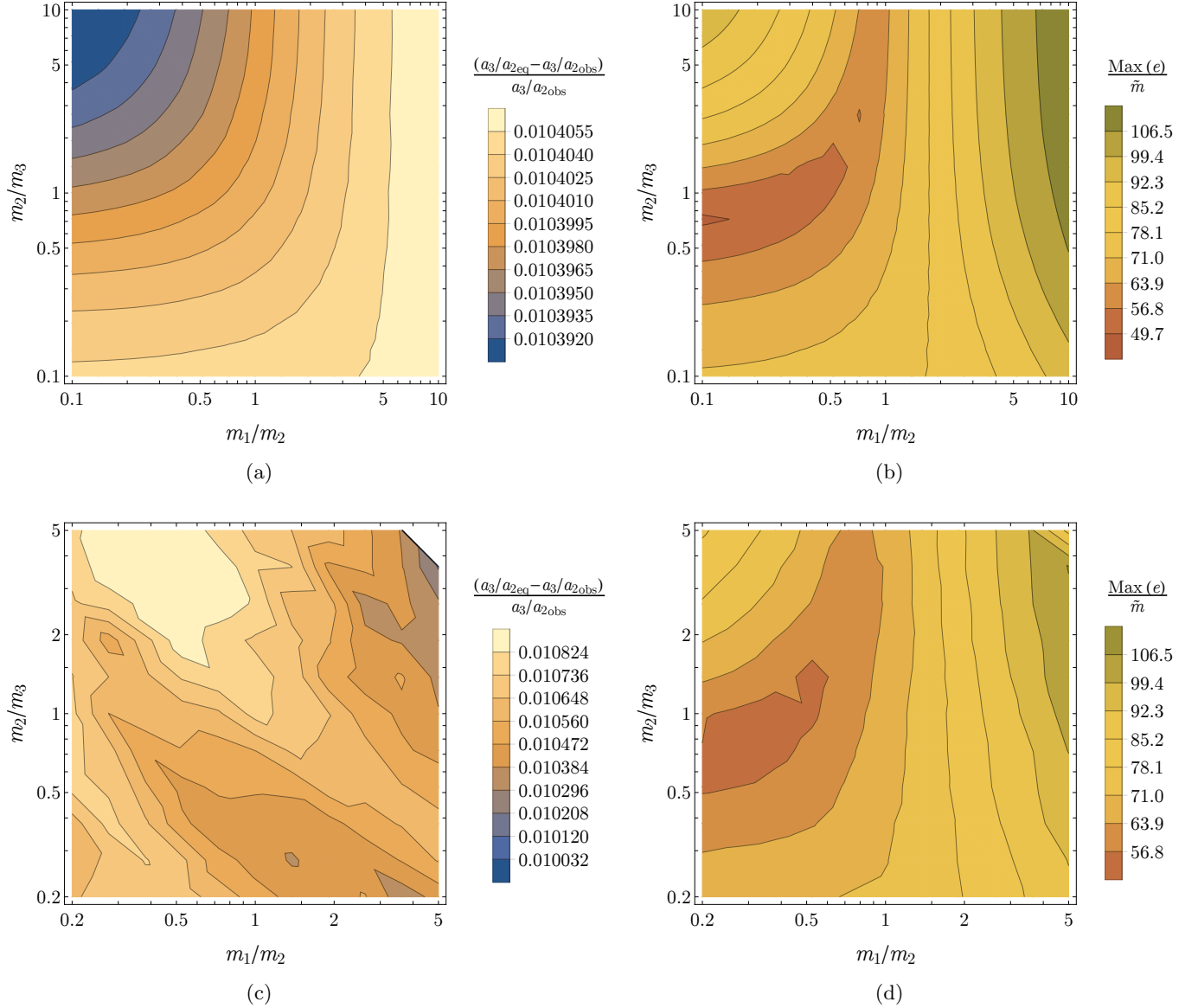


Figure 4.6: Same as in Figure 4.5, but for the system YZ Cet, residing close to a 3:2 – 3:2 chain. The value of $\bar{\delta}(a_3/a_2) \sim 0.01$ across all planetary mass ratios can be matched against the corresponding curve in Figure 4.8, where we find that $\sim 80\%$ of randomly generated systems lie this close to the 3:2 – 3:2 chain.

two planets’ pairs. This allows us to perform efficient integrations without breaking the adiabatic approximation which keeps the system close to the resonant equilibrium points. We note that we have little to no information on the internal structures of exoplanets, so we would not be able to confidently assign realistic eccentricity damping timescales anyway. Moreover, as we have already mentioned, tides are only one example of dissipation (that is, loss of orbital energy E) at constant angular momentum \mathcal{L} , so that these results are in fact generalisable to any dissipative process such that $\dot{E} < 0$ and $\dot{\mathcal{L}} = 0$. Therefore, a resonant system undergoing any such process is expected to follow the loci of the resonant equilibria, and the divergence of the semi-major axes is obtained as a general result. We now explain how we obtain maps similar to those drawn in the previous section from these numerical simulations.

Consider a choice of the mass ratios, and a simulation of the dissipative evolution of two pairs of resonant planets. The semi-major axis ratios a_3/a_1 and a_3/a_2 will increase in time. When, for two consecutive outputs of the simulation, the ratio a_3/a_1 crosses the observed one $(a_3/a_1)|_{\text{obs}}$, we store the corresponding value of a_3/a_2 from the simulation (an average of it at the two consecutive outputs). Since the system might be librating around the equilibrium points with some amplitude, and there are additional short period terms, this will happen many

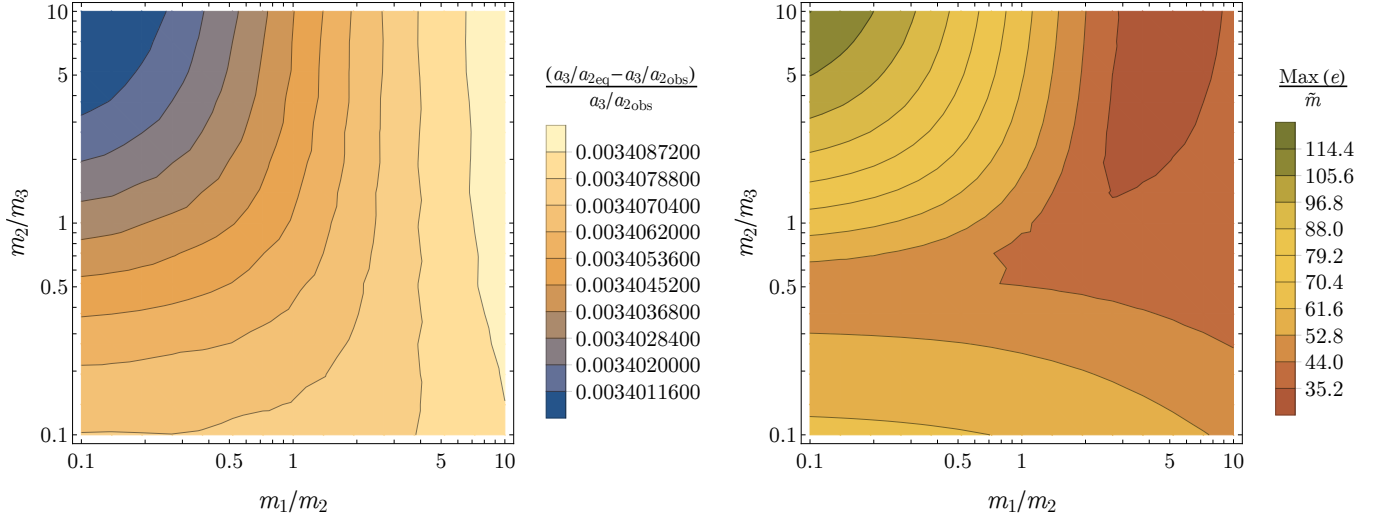


Figure 4.7: Same as in Figure 4.5, but for the system Kepler-31. Only analytical maps are shown in this case since in some simulations capture into resonance was unsuccessful due to overstability of the captured state for different planetary mass ratios. As explained in the text, this issue is model-dependent and is not within the scope of our analysis. Moreover, in the simulations where capture was successful, the results agree well with the analytical calculations, showing $\bar{\delta}(a_3/a_2) \sim 0.003$. Comparing with Figure 4.8 we see that there is a $\sim 20\%$ probability that Kepler-31 lies this close to the 2:1 – 2:1 chain by pure chance.

times for a single simulation, and we obtain a list of a_3/a_2 values. Then, we report the average of this list, and again compare this quantity with the observed $(a_3/a_2)|_{\text{obs}}$ (since they are obtained from the mean period extracted from the data) by computing the relative difference as in (4.15). We then loop over different choices of planetary mass ratios and obtain a map that can be compared with the analytical maps of the previous section. A similar procedure can be applied to a_2/a_1 (which gives again similar values to that of a_3/a_2 as we mentioned in Section 4.3.2), as well as the quantity $\max e/\tilde{m}$.

This analysis has been performed for the three selected systems. For Kepler-305 and YZ Cet, we show the resulting plots on the bottom panels (c) and (d) of Figures 4.5 and 4.6 respectively, and notice very good agreement with the analytical results. The noise that is observed in the panels (c) relative to the quantity $\bar{\delta}(a_3/a_2)$ is due to the fact that the numerically simulated systems are undergoing fast oscillation while they cross the observed value $(a_3/a_1)|_{\text{obs}}$, but the typical value of $\bar{\delta}(a_3/a_2)$ is similar to the one found analytically.

The case of Kepler-31, which resides close to a 2:1 – 2:1 mean motion resonant chain, is a bit different, since the 2:1 resonance capture might be only temporary if the librations around equilibrium are overstable [Goldreich and Schlichting(2014)]. This behaviour has been already investigated thoroughly in the case of two planets [Delisle et al.(2015), Deck and Batygin(2015)], however it has been shown to be dependent on the specific implementation of the disc-planet forces, and to disappear in some cases [Xu et al.(2018)], as we mentioned at the end of Subsections 3.2.1 and 3.2.2. In this thesis we do not intend to expand on these matters, since the formulas that mimic the planet-disc interactions represent only approximate implementations of the real forces that are felt by the planets from the disc, which themselves remain observationally unconstrained. We therefore take a practical approach, and note that in the numerical simulations where resonant capture was successful (typically for $m_1/m_2, m_2/m_3 \gtrsim 1$) the numerical results agree very well with the analytical ones; moreover we still observe that the theoretical value of $\bar{\delta}(a_3/a_2)$ varies extremely little with m_1/m_2 and m_2/m_3 (Figure 4.7), so the latter simulations can be considered as enough support for the analytical calculations.

4.4 Results

4.4.1 Probabilistic measure of a resonant configuration in Kepler-305, YZ Cet and Kepler-31

Using the maps of $\bar{\delta}(a_3/a_2)$ shown in Figures 4.5, 4.6 and 4.7 for the three selected systems Kepler-305, YZ Cet and Kepler-31, we draw the following conclusions. First of all, one might expect that the quantity $\bar{\delta}(a_3/a_2)$ should change with the different choices of mass ratios, thus allowing one to make a prediction on their (so far poorly known) values of m_1/m_2 and m_2/m_3 under the assumption that these systems are indeed in resonance and evolving dissipatively. Follow-up monitoring of these systems could then produce new observations from which to obtain the real masses of the planets, and so validate or disprove the hypothesis. However, in practice we find that these analytical maps show very little dependence on m_1/m_2 and m_2/m_3 spanning reasonable values. Note also that for all three systems $\bar{\delta}(a_3/a_2)$ is small, but never vanishing, which would represent an analytically computed equilibrium configuration such that $\delta(a_3/a_2) = 0$, that is, a resonant equilibrium point which satisfies $(a_3/a_2)|_{\text{eq}} = (a_3/a_2)|_{\text{obs}}$ and $(a_2/a_1)|_{\text{eq}} = (a_2/a_1)|_{\text{obs}}$. But even if this happened to be the case, the level curve $\bar{\delta}(a_3/a_2) = 0$ would still span a broad range of mass ratios: given moreover the uncertainty in the observed period ratios of exoplanetary systems, this would make any determination of m_2/m_1 or m_3/m_2 using this approach, in general, inconclusive.

Secondly, we note that we do obtain in all three cases small values for $\bar{\delta}(a_3/a_2)$, meaning that these systems are indeed close to some equilibrium point of the Hamiltonian (4.12) and therefore could potentially reside in a multi-resonant chain. However, these values by themselves do not contain any meaningful information. The quantity $\bar{\delta}(a_3/a_2)$ should indeed be calibrated if we intend to use it as a measure of the probability that the actual system (with its real unknown eccentricities) is in resonance, which in turn would yield a measure of how consistent the orbital architecture of such a system is with the envisioned scenario described above. To this end, for various resonant chains we randomly generate period ratios of fictional systems such that $0 < \Delta < 0.05$ for each pair, and extract the corresponding $\bar{\delta}(a_3/a_2)$ (calculated for the choice of mass ratios $m_1/m_2 = m_2/m_3 = 1$ for simplicity, since we saw above that the $\bar{\delta}(a_3/a_2)$ value depends extremely weakly on the mass ratios). From the cumulative distribution of $|\bar{\delta}(a_3/a_2)|$ that arises from this procedure we can obtain the probability that any given system has a given (small) $\bar{\delta}(a_3/a_2)$ purely by chance.

Since we are interested mainly in the 2:1 and 3:2 mean motion resonances, we show in Figure 4.8 these cumulative distributions for systems close to any possible combinations of these resonances. The results show that the proximity of YZ Cet to the 3:2 – 3:2 resonance is not statistically significant, since in $\sim 80\%$ of randomly generate systems close to the 3:2 – 3:2 chain we obtain an equivalent or smaller value of $\bar{\delta}(a_3/a_2)$. This result turns out to be confirmed by a more recent study on the RV data for YZ Cet, which seems to indicate that only in $\sim 20\%$ of the possible configurations does the system truly reside in resonance (Stephan Stock, private communication). Instead, Kepler-305 and Kepler-31 are likely to be in resonance at the 1σ level (i.e. the probability that their value of $\bar{\delta}(a_3/a_2)$ is smaller than the determined value by chance is less than 32%): for Kepler-305 there is a $\sim 15\%$ chance that this particular system lies this close to resonance by chance, while for Kepler-31 the probability is $\sim 20\%$.

We should remark that these specific values for the probabilities that each system is this close to exact resonance by chance depend on the choice $0 < \Delta < 0.05$ for both pairs of planets, which is used in generating the fictional systems. This value is however not arbitrary. For, it must be consistent with the choice made in Section 4.3.1, which produced only these three systems with both the inner and outer planet pair this close to first order mean motion resonance: there, the choice $|\Delta| < \max \Delta = 0.05$ was dictated by the observation of the location of the peak wide of nominal resonance ([Hadden and Lithwick(2017)] and our Figure 4.2), so restricting the interval in Δ values with smaller $\max \Delta$ might have resulted in excluding potential systems. On the other hand, increasing $\max \Delta$ in the generation of the fictional systems would have the only effect to decrease the calculated probabilities. Therefore, we conclude that our choice of $\max \Delta = 0.05$ is not arbitrary, and gives a reasonable upper bound to the probabilities that each system finds itself so close to exact resonance by pure chance.

For completeness, we report the observed variation of the three-body Laplace angle φ_L in these systems, since its libration can be in principle a sufficient condition to conclude that they are indeed resonant. For Kepler-305 we checked that the Laplace angle $\varphi_L = 2\lambda_1 - 4\lambda_2 + 2\lambda_3$ satisfies $\dot{\varphi}_L \simeq 0.5^\circ \text{ days}^{-1}$ given the observed transits periods; for Kepler-31, $\varphi_L = \lambda_1 - 3\lambda_2 + 2\lambda_3$ satisfies $\dot{\varphi}_L \simeq 0.1^\circ \text{ days}^{-1}$; finally for YZ Cet, $\varphi_L = 2\lambda_1 - 5\lambda_2 + 3\lambda_3$ satisfies $\dot{\varphi}_L \simeq 9.4^\circ \text{ days}^{-1}$. As we argued in Subsect. 4.1.1, in case of libration of the resonant angles around the equilibrium point (and hence libration of the Laplace angle) the average of the (a, e) oscillation falls on an equilibrium point, while in case of circulation, the average falls off the curve of equilibrium points. Consequently, the circulation of the Laplace angle implies that the distance of the system from the equilibrium point in a resonant diagram is larger than the distance of the equilibrium point itself from $e = 0$, and that $\bar{\delta}(a_3/a_2)$ cannot be zero. However, this does

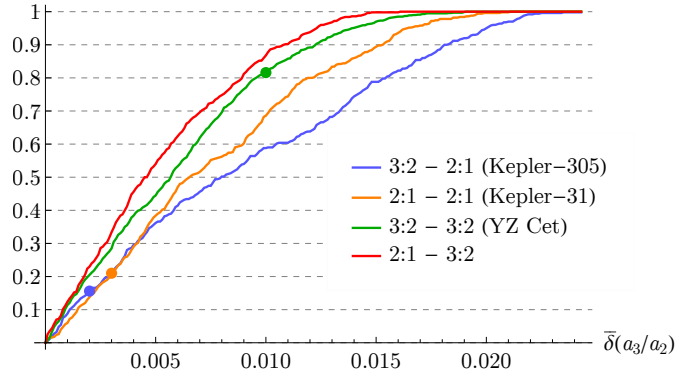


Figure 4.8: Cumulative distribution functions for $|\bar{\delta}(a_3/a_2)|$ for randomly generated systems close to chains of any possible combinations of the 2:1 and 3:2 mean motion resonances. We indicate the chains that represent selected systems from Figure 4.3; for each of them, a point indicates the observed $\bar{\delta}(a_3/a_2)$. From this, we obtain on the vertical axis the probability that these systems could have this value of $\bar{\delta}(a_3/a_2)$ by pure chance.

not mean that the system did not reach that point via divergent migration: being the (a, e) equilibrium so close to $e = 0$, even a minute perturbation can induce circulation of the Laplace angle. As we said in Subsect. 4.1.1, the libration of the Laplace angle is a sufficient but not necessary condition to conclude that a system’s dynamical history has been shaped by resonant capture and subsequent resonant repulsion driven by dissipation.

4.4.2 The 5:4 – 4:3 resonant chain on Kepler-60 and other near-resonant systems with $k > 3$

While in this work we have concentrated on the 2:1 and 3:2 mean motion commensurabilities, it is worthwhile to point out that more compact resonant chains are possible, and Kepler-60 represents a notable example. This system hosts three planets with mean observed periods of $\simeq 5.49$ days, $\simeq 8.29$ days and $\simeq 16.74$ days respectively. Their masses have been constrained via TTV to be $\simeq 4M_{\oplus}$ for all planets [Jontof-Hutter et al.(2016)]. The mean motions of the planets satisfy $4\dot{\lambda}_1 - 8\dot{\lambda}_2 + 4\dot{\lambda}_3 \simeq -0.02^\circ \text{ days}^{-1}$, hinting at a resonant configuration. Indeed, [Goździewski et al.(2016)] found that the TTV signal for these planets is consistent with a true three-body Laplace-like resonance as well as a chain of 5:4 – 4:3 two-body mean motion resonances. Using the system’s parameters we can find a resonant equilibrium configuration as in Subsec. 4.3.2, by imposing a_3/a_1 to be equal to the observed $(a_3/a_1)|_{\text{obs}}$. This gives $\bar{\delta}(a_3/a_2)$ of order 4×10^{-5} . Using an analogous argument to that of Figure 4.8, we find that there is only a 0.25% probability that Kepler-60 lies this close to a 5:4 – 4:3 resonant chain by pure chance. The eccentricities that we find at the selected resonant equilibrium point are of order $e_1 \simeq 0.02$, $e_2 \simeq 0.03$, $e_3 \simeq 0.01$ for the observed planetary masses. These numbers are quite close to the ones consistent for the two-body mean motion resonance chain solution found in [Goździewski et al.(2016)]. Note in passing that their solution is for non-vanishing libration amplitude of the four resonant angles (however their mean values are the same found here for a stable resonant equilibrium).

For completeness, we cite other near-resonant systems of three planets with $k > 3$ that are found in the catalogue. The only ones which satisfy our criterion $|\Delta| < 0.05$ for both pairs are K2-239 (close to a 3:2 – 4:3 chain), Kepler-289 (close to a 2:1 – 2:1 chain), Kepler-226 (close to a 4:3 – 3:2 chain) and Kepler-431 (close to a 5:4 – 4:3). Of these, only the latter two satisfy $\Delta > 0$ for both pairs.

4.5 Conclusions

In this chapter, we have generalised the formalism of dissipative divergence of resonant orbits to multi-resonant chains. The analytical study performed in Section 4.2 allows us to predict the orbital configurations of systems of planets deep in a chain of first order mean motion resonances, and therefore, even though at a lesser degree of precision, of systems that are in resonance with a finite amplitude of libration. Then, we showed in Section 4.2.2 that under the effect of slow dissipation a nearly-resonant system is expected to follow the loci of the equilibrium points of the resonant Hamiltonian (4.12) maintaining the amplitude of libration in an adiabatic manner. Therefore, if the orbital architecture of a system is found near one of these equilibrium points, it is strongly suggestive that the

envisioned scenario of slow convergent orbital migration leading to capture into resonance and subsequent orbital divergence due to dissipative evolution really occurred for the system. In the light of the results presented above, we can draw the following conclusions.

On the one hand, we must face the fact that the orbital architecture of a significant fraction of the systems of three planets is actually not consistent with these physical mechanisms. More precisely, the majority of the systems are not close to resonance, implying that either they never captured in resonance in the first place, or they escaped from resonance due to a violent instability [Izidoro et al.(2017)] losing any memory of their resonant dynamical past. To ponder these two possibilities, consider first of all that some form of orbital transport is expected to take place: for example, the majority of planets with $R_{\text{pl}} \gtrsim 1.6R_{\oplus}$ have H/He gaseous atmospheres that cannot be explained by production of volatiles after the formation of the planet [Rogers(2015)], implying that these planets formed while the protoplanetary disc was still present. The associated planet-disc interaction would then force the planets' orbital elements to change, in other words, force the planets to migrate. However, orbital migration may not be convergent [Migaszewski(2015), Migaszewski(2016)], that is, not leading to resonant capture. Moreover, some mechanisms have been proposed to inhibit the capture even in the case of convergent migration, such as turbulence in the disc or e -dependent migration rates. Nevertheless, these processes alone do not adequately explain the lack of resonance in the exoplanet sample (e.g. [Batygin and Adams(2017), Deck and Batygin(2015), Xu et al.(2018)]). For these reasons, it is more likely that capture into mean motion resonance is a common outcome of the early epochs of disc-planet interaction, but the subsequent evolution after the disc removal is subject to instabilities which break the compact configuration. This approach seems to be able to reproduce the observed distribution of period ratios if these instabilities are extremely common [Izidoro et al.(2017)]. In the next chapter, we investigate the dynamical mechanisms that may be responsible for ejecting the planets from resonance after the disc dissipation.

On the other hand, systems with orbital properties that are compatible with a (near) resonant state do exist in the exoplanet census. These include the already known examples mentioned above of Trappist-1, Kepler-223, GJ867 and Kepler-60, and, potentially, some of the systems analysed in this work. That is, while it is difficult to prove definitively that a given system is now in resonance in a formal sense (the resonant angles are in libration), in this work we have developed a method to quantitatively test the consistency of a given orbital architecture with a dynamical history characterised by resonant capture and subsequent dissipative evolution. This is achieved through the calculation of the quantity $\bar{\delta}(a_3/a_2)$ defined in (4.15), which is obtained directly from the observed semi-major axis ratios and, as we have shown, depends very weakly on the mass ratios between the planets, making the observational uncertainties on the latter quantities irrelevant. Then, using the approach illustrated in Figure 4.8, this 'indicator' can be turned into a quantitative probability that the system is related to the considered resonant chain. In this sense, we have found that there is a $\sim 15\%$, $\sim 20\%$ and $\sim 80\%$ probability that Kepler-305, Kepler-31 and YZ Cet respectively find themselves this close to resonance merely by chance. The probability that two systems out of three fall within the first quartile of the $\bar{\delta}(a_3/a_2)$ distribution and are therefore this close to a resonant equilibrium point just by chance is 14%. This suggests that at least some of them should have had a resonant dynamical history. Although the sample is clearly too small to make any meaningful inference, the probabilities of resonant association that we have found indicate that between 1/3 and 2/3 of the systems with $0 < \Delta < 0.05$ show memory of the processes of resonant capture; this is consistent with the histogram of Figure 4.2, where the peak wide of the resonance is about 2 times higher than the underlying random-like flat distribution.

The architecture of many planetary systems observed by transit is not well constrained by observations. Opportunities for more extensive characterisation will come from missions such as the Transiting Exoplanet Survey Satellite (TESS) or the PLAnetary Transits and Oscillations of stars (PLATO), which are designed to target bright stars to allow for follow-up via further ground-based and space-based observations (with methods such as radial velocity). This will allow for a better quantification of planetary masses, radii, ages of the systems and eccentricities. In the light of this augmented perception that we can expect to acquire, our study outlines the groundwork for further dynamical characterisation of the physical processes that shaped the present-day architectures of extrasolar planetary systems.

Chapter 5

The onset of instability in resonant chains

5.1 Introduction

One of the realisations of the last chapter is that the observed Super Earth systems show little preference for near-integer period ratios and their orbital separations are usually much wider than those characterising planets in resonant chains. This might seem in contradiction with the paradigm of migration and resonant trapping but, as we already mentioned, it is not necessarily the case. Indeed, [Izidoro et al.(2017)] showed that resonant planetary systems obtained from migration simulations often become unstable, and that the observations of the period ratio distribution are well reproduced if the fraction of the resonant systems that eventually become unstable exceeds 90%. In [Izidoro et al.(2017)], the rates of instability observed in their numerical $(N + 1)$ -body simulations was however “mysteriously” only about 50% - 60%. Instead, in the more recent study [Izidoro et al.(2019)], these needed higher rates of instability are recovered in some cases, and it is worth here discussing briefly why this is so, as it will help us to guide our argumentations below. The main difference between the two works is the implementation of pebble accretion in [Izidoro et al.(2019)], with the pebble accretion flux playing a crucial role in determining the final configuration at the end of the disc phase. In the previous work [Izidoro et al.(2017)], an initial population of 20 – 30 embryos of masses $0.6 - 4.5M_{\oplus}$ adding up to $\sim 60M_{\oplus}$ was used, which resulted in many collisions during the gas phase and a final configuration of a few planets with masses usually of order $10M_{\oplus}$. In [Izidoro et al.(2019)], implementing a low pebble mass-flux (Model III) yields again fewer, relatively low-mass planets, and in a not so compact configuration, which results in instability rates of $\sim 50\%$ after the disc is removed, consistent with the findings in [Izidoro et al.(2017)]. Instead, a higher efficiency of pebble accretion (Model I) yields the most compact planetary systems with the most populated and massive chains, which are then observed to reach instability rates of $\sim 95\%$. The main conclusion of [Izidoro et al.(2019)] is therefore that pebble accretion, migration (with formation of compact resonant chains) and subsequent dynamical instabilities can constitute a viable model to explain the properties of the observed Super-Earth population in terms of orbital configuration and mass distribution, *if* a dominant fraction of systems go unstable after the disc phase while only a few percent of resonant chains remain stable (such as Trappist-1, Kepler-223, etc).¹

In this chapter we focus on the dynamical mechanism leading to the instability of a mean motion resonance chain, even in absence of external perturbations². On this subject, an important numerical study was performed by [Matsumoto et al.(2012)]. There, the authors studied numerically the stability of resonant multi-planetary systems for high-integer first-order mean motion resonances. They built the desired resonant configuration by simulating the convergent type-I migration phase in a protoplanetary disc of gas; then they slowly depleted the disc. They observed that there is a critical number of planets N_{crit} above which the resonant systems go naturally unstable, with a crossing time comparable to that of non-resonant systems, and studied how this number changes with the planetary masses (m_{pl}/M_* , where M_* is the stellar mass) and compactness of the chain (index k of the $k : k - 1$

¹We should note however that in terms of composition, the findings of [Izidoro et al.(2019)] imply that Super Earths should be relatively ice-rich, which is not in accord with the observation that these planets are mostly rocky [Fulton et al.(2017), Owen and Wu(2017), Jin and Mordasini(2018)]. The problem of the composition of the exoplanet sample is indeed still an active topic of research.

²External perturbations have also been invoked to increase the fraction of unstable systems, such as the turbulence in the disc (which prevents capture in deep resonance, [Batygin and Adams(2017)]) or the scattering of left-over planetesimals from the planetary region [Chatterjee et al.(2016)].

resonance). More specifically, they demonstrated numerically that the critical number N_{crit} which guarantees stability decreases with increasing compactness of the chain (increasing k) and increasing planetary mass m_{pl} . The dynamical reason of the instability, however, was not discussed, nor the exact scaling law that links N_{crit} , m_{pl} and k .

The main goal of this chapter is to investigate both analytically and numerically the onset of instability in resonant chains, in order to explain the result of [Matsumoto et al.(2012)] and the large instability fraction of resonant chains observed in some of the [Izidoro et al.(2019)] simulations. More precisely we study the stability of resonant configurations like those presented in Section 3.2, with small amplitude of libration around a resonant equilibrium point. Because we intend to work analytically, and since the planetary Hamiltonian is not a continuous function of the number of planets N , it is convenient to rephrase the findings of [Matsumoto et al.(2012)] with the following equivalent statement: given the number N of planets and the compactness of the system (the resonant index k), there is a limit mass $(m_{\text{pl}}/M_*)_{\text{crit}}$ for stability, which decreases with increasing N and k . Thus, in this chapter we address the question of why resonant chains at an initial state of low amplitude of libration become unstable if the planets are too massive, for different values of N and k .

In order to fix ideas we consider in all cases systems of planets of the same mass, $m_i \equiv m_{\text{pl}}, \forall i = 1, \dots, N$. This is a useful simplification which allows one to grasp the main points having to work with only one parameter. We note also that individual Kepler systems seem to show a homogeneity in planetary masses [Weiss et al.(2018), Millholland et al.(2017)], so this simplification does not constitute a major inconvenience. Following the approach of [Matsumoto et al.(2012)], we will obtain resonant configurations numerically by implementing resonant capture in a protoplanetary disc as described in Section 3.2. However, unlike [Matsumoto et al.(2012)], we do not attempt resonant capture experiments with different masses. The reason is that for relatively large planetary masses, close to the instability limit, the capture itself can become quite chaotic and lead to large amplitudes of libration. Then, it becomes difficult to compare the long-term stability of these systems with large amplitude of libration with those with smaller masses that settle near the resonant equilibrium point. Instead, for a theoretical understanding of stability of a resonant chain as a function of planetary mass, it is preferable to capture all the planets in resonance at low libration amplitudes at small masses and then, after gas removal, slowly increase the planetary masses until an instability is achieved. This growth in mass should not be interpreted as a physical process. It is just a numerical artifice to explore resonant dynamics as a function of the planetary mass and achieve an analytic understanding of the instability process.

More precisely, we proceed as follows. In a first phase, the planets, of an equal, initially small mass, are put into some chosen chain of first order mean motion resonances via type-I migration in a protoplanetary disc. We implement a planetary trap at the inner edge in order to ensure convergent migration which is needed for the planets to capture. Then the disc is slowly dissipated away, leaving the system in a state of small libration around a resonant equilibrium point (cfr. Section 3.2). Then, in a second phase the mass of the planets is slowly increased in order to adiabatically maintain the small amplitude of libration around the resonant equilibrium point, until the onset of instability. We will also consider coplanar orbits for simplicity. Indeed, if the chains that we intend to study are the result of capture in mean motion resonances during the disc phase, any significant mutual inclinations would have been damped out by the disc. Moreover, the few confirmed truly resonant systems (such as Trappist-1 or Kepler-223) show very small mutual inclinations. This suggests that resonant chains form in a relatively planar orbital configuration.

We begin our investigation in Section 5.2 where we study the most simple case of $N = 2$ equal-mass planets in a first order mean motion resonance as a function of the planetary mass m_{pl} . We then proceed in Section 5.3, where we consider the first actual chain of $N = 3$ equal-mass planets. Here, we observe in our numerical simulations a novel phenomenon during the phase of (fictitious) mass increase, which anticipates and initiates the instability phase. To fix the ideas, we make use of the case $N = 3, k = 3$ as a specific instance of the problem, to better understand and describe this dynamical phenomenon. Finally, we proceed to generalise this result to more compact and/or populous resonant chains in Subsection 5.3.6 and Section 5.4, and set out the ground for future work.

5.2 2 Planets

We start our investigation of the stability of two equal-mass planets in a first order mean motion resonance with a set of numerical integrations. The results described in this section are extracted from the publication [Pichierri et al.(2018)]. We take the resonant equilibrium configurations obtained as described in Chapter 3, slowly

deplete the gas³, and then perform long-term integrations with the resulting orbital configuration as initial conditions, checking if the system exits the resonance, in which case the resonant configuration is deemed unstable; this analysis can then be performed for different masses $m_1 = m_2 = m_{\text{pl}}$. As explained above, unlike [Matsumoto et al.(2012)], we take a system of planets deep in resonance and slowly increase their masses until the system shows instability, so we can ensure that we are indeed probing the region of the phase space around the resonant equilibrium point. For, as long as the rate at which this increase is performed is small enough, the amplitude of libration around the equilibrium point will be an adiabatic constant and will be preserved (cfr. Subsection 2.3.2 on the adiabatic principle). For simplicity, we choose a linear law $m_{\text{pl}}(t) = m_{\text{pl}}(0) + \dot{M}t$, where \dot{M} is a constant (in practice, for the results shown below, we choose to increase the planetary mass so that it grows by 3 orders of magnitude in 5×10^4 years; changing m_{pl} slowly enough, we notice no apparent difference in the resulting evolution if one uses different laws or rates of change for $m_{\text{pl}}(t)$); in our code, we increase the planetary mass at each integration step. We stress once again that the increase in the planetary parameter is a purely numerical exercise: one should assign no physical meaning to it, and the fact of changing the value of m_{pl} is just a way to explore the stability of deeply resonant systems as a function of planetary masses starting from one system that is well in resonance.

Another advantage of operating this way is that we can follow analytically the evolution of the system as the mass increases, at least to a very good approximation. To this end, recall that in Chapter 3 we introduced the averaged Hamiltonian $\bar{\mathcal{H}} = \mathcal{H}_{\text{kepl}} + \mathcal{H}_{\text{res}}$ (Equation (3.2)) and the canonical variables $(\Psi_1, \Psi_2, \mathcal{K}, \Omega, \psi_1, \delta\gamma, \kappa, \theta')$ (Equations (3.5), (3.7)) which I rewrite here for readability:

$$\begin{aligned} \Psi_1 &= \Gamma_1 + \Gamma_2, & \psi_1 &= k\lambda_2 - (k-1)\lambda_1 + \gamma_1, \\ \Psi_2 &= -\Gamma_2, & \delta\gamma &= \gamma_1 - \gamma_2, \\ \mathcal{K} &= \Lambda_1 + \frac{k-1}{k}\Lambda_2, & \kappa &= \lambda_1, \\ \Omega &= \Lambda_2/k - \Gamma_1 - \Gamma_2, & \theta' &= k\lambda_2 - (k-1)\lambda_1. \end{aligned} \tag{5.1}$$

The angles κ and θ' do not enter explicitly in $\bar{\mathcal{H}}$ so \mathcal{K} and Ω are constants of motion for $\bar{\mathcal{H}}$; \mathcal{K} is fixed by the resonance and by the orbital separations of the planets, while Ω is linked to the angular momentum by $(m_{\text{pl}}/\mu)(\mathcal{K} + \Omega) = \mathcal{L}$, where $\mu = m_{\text{pl}}M_*/(m_{\text{pl}} + M_*)$ is the common reduced mass of the planets. Therefore, only the two canonical pairs $(\Psi_1, \Psi_2, \psi_1, \delta\gamma)$ evolve for $\bar{\mathcal{H}}$. Recall also that in Subsect. 3.1.2 we found the equilibrium points $(\Psi_{1,\text{eq}}, \Psi_{2,\text{eq}}, \psi_{1,\text{eq}}, \delta\gamma_{\text{eq}})$ for $\bar{\mathcal{H}}$.

As the planetary masses $m_1 = m_2 = m_{\text{pl}}$ increase, we look at the quantity

$$\mathcal{L}_{\text{spec}} := \frac{\mathcal{L}}{\mu} = \frac{m_{\text{pl}}}{\mu} \left(\sqrt{\mathcal{G}(m + M_*)a_1(1 - e_1^2)} + \sqrt{\mathcal{G}(m + M_*)a_2(1 - e_2^2)} \right), \tag{5.2}$$

which we (improperly) call *specific angular momentum*. This quantity is not exactly constant as the planetary mass increases, but its value changes very little up to high enough values of m_{pl}/M_* , cfr. Figure 5.1a. In the approximation $\mathcal{L}_{\text{spec}} = \text{const}$, we can follow analytically the evolution of a resonant system in which the planetary mass parameter m_{pl} is slowly changing. To do this, consider a resonant system in the vicinity of an equilibrium point $(\Psi'_{1,\text{eq}}, \Psi'_{2,\text{eq}}, \psi'_{1,\text{eq}}, \delta\gamma'_{\text{eq}})$ for some value m'_{pl} of m_{pl} and some values of the integrals of motion \mathcal{K}' and Ω' . Using $\mathcal{L} = (m_{\text{pl}}/\mu)(\mathcal{K} + \Omega)$, we have $\mathcal{L}_{\text{spec}} = (m_{\text{pl}}/\mu^2)(\mathcal{K} + \Omega)$. We can then obtain the values of these actions when we change m_{pl} to m''_{pl} , by setting

$$\mathcal{K}'' = \frac{m'_{\text{pl}}/(\mu')^2}{m''_{\text{pl}}/(\mu'')^2}\mathcal{K}', \quad \Omega'' = \frac{m'_{\text{pl}}/(\mu')^2}{m''_{\text{pl}}/(\mu'')^2}\Omega', \tag{5.3}$$

where μ' and μ'' are the reduced masses relative to the planetary masses m'_{pl} and m''_{pl} respectively. Finally we find the new equilibrium point $(\Psi''_{1,\text{eq}}, \Psi''_{2,\text{eq}}, \psi''_{1,\text{eq}}, \delta\gamma''_{\text{eq}})$ with the new planetary mass m''_{pl} and these two actions \mathcal{K}'' and Ω'' in the same manner as in Subsect. 3.1.2. We can then closely follow the evolution of the system as we show in Figure 5.1, where we have superimposed the results of a numerical simulation in the case of the 3:2 mean motion resonance and our analytical predictions. At the same time we plot the real evolution of $\mathcal{L}_{\text{spec}}$, against the fixed value used for the analytical calculations.

³That is, we have Σ decrease exponentially in Equation (3.21). This is done slowly enough and the system does not move considerably from the equilibrium configuration calculated in Chapter 3. We should only note that the damping in the eccentricities has the effect of changing the equilibrium values of the angles ψ_1 and $\delta\gamma$ from the ones which are found in the purely conservative planetary system

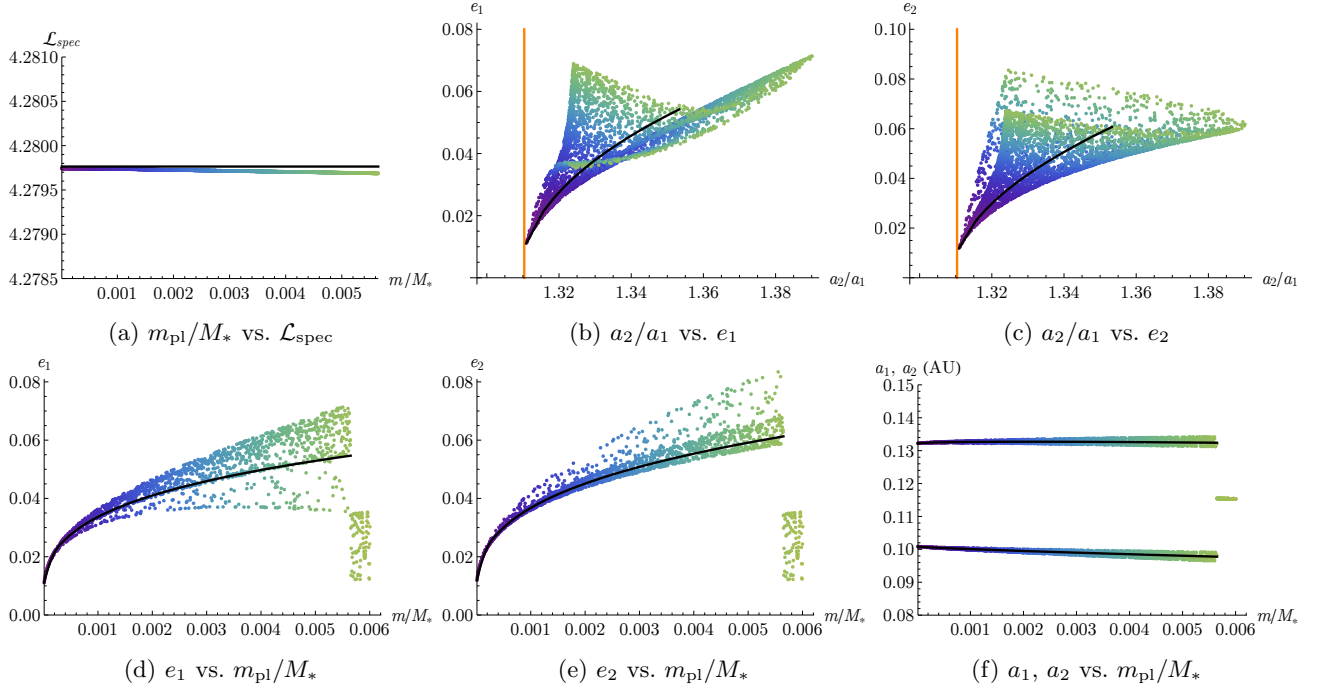


Figure 5.1: Evolution of a system deep in the 3:2 mean motion resonance as the planetary mass $m_1 = m_2 = m_{\text{pl}}$ increases. The initial configuration of the averaged system is $a_2/a_1 = 1.31093$, $e_1 = 0.01112$, $e_2 = 0.01195$ and $m_{\text{pl}}/M_* = 1 \times 10^{-5}$. The true evolution of $\mathcal{L}_{\text{spec}}$ along the simulation is plotted in panel (a) as a function of m_{pl}/M_* , see the coloured line (the colour-coding is reproduced only to indicate the value of m_{pl} in panels (b) and (c)). The black line represents the approximation $\mathcal{L}_{\text{spec}} = \text{const}$ used in the analytical calculations, showing relatively good agreement up to high values of m_{pl}/M_* . The plot of the analytic solution is interrupted at $m_{\text{pl}}/M_* \simeq 5.64 \times 10^{-3}$, at which point the system is observed to go unstable in the numerical simulations. In panels (b) and (c) we plot both eccentricities as a function of the semi-major axes ratio, as they evolve while m_{pl} increases. We colour-code the points based on the value of the planetary mass (with the same colours used in panel (a)). We superimpose, with a black line, the result of an analytical calculation aimed at reproducing the evolution of the system as explained in the text, assuming $\mathcal{L}_{\text{spec}} = \text{const}$. Note that the simulation follows closely the analytical prediction. The oscillations around the equilibrium points become larger and larger as m_{pl} increases, but they are short periodic ones, i.e. they are due to the evolution of the fast angles (the same as those shown in Figures 3.5c and 3.4c) which are averaged out in the analytical model and are not linked to a growth in the amplitude of resonant libration, which is conserved adiabatically until the system becomes unstable. Panels (d), (e) and (f) show the evolution of the eccentricities and semi major axes as functions of the planetary mass, with again a black line being the result of analytical calculations; since we imposed a linear increase of the mass with time, this can be seen as an evolution in time. Notice that in this case the outcome of the instability is a collision, as the two planets eventually merge.

At this point, a remark is in order. The eccentricity of the equilibrium configuration⁴ grows with the planetary masses, as shown in Figure 5.1, following roughly a line of constant specific angular momentum. Instead, the equilibrium eccentricity of planets captured in resonance by planet-disc interaction is independent of the planetary mass (see equation (3.48)). This means that capturing planets in the resonance with a mass m'_{pl} or capturing them with a smaller mass m''_{pl} , which is then grown to m'_{pl} after capture, leads to two different configurations. In other words, the two processes of a) first capturing the planets in mean motion resonance and then increasing their masses, and b) first increasing their masses and then putting them in resonance, do not commute. Nevertheless, by assuming different scale-heights of the disc when the planets are captured and then growing the planetary masses, we can explore numerically the full m_{pl}, e_2 parameter space characterising the resonant equilibrium (Figures 5.2

(see e.g. [Batygin and Morbidelli(2013)b] for a formula of this shift, linking $\psi_{1,\text{eq}}$, and $\delta\gamma_{\text{eq}}$ to τ_e). This means that when the latter admits stable symmetric equilibrium points, $\psi_{1,\text{eq}}, \delta\gamma_{\text{eq}} = 0, \pi$, the non-conservative system might seem to contradict this; however these are *not* asymmetric equilibrium points, as they are only due to the damping effect: when this is removed the system reaches the expected equilibrium values of the angles.

⁴We are of course referring to the eccentricity in the averaged system, in the full one e would oscillate due to the fast evolving angles.

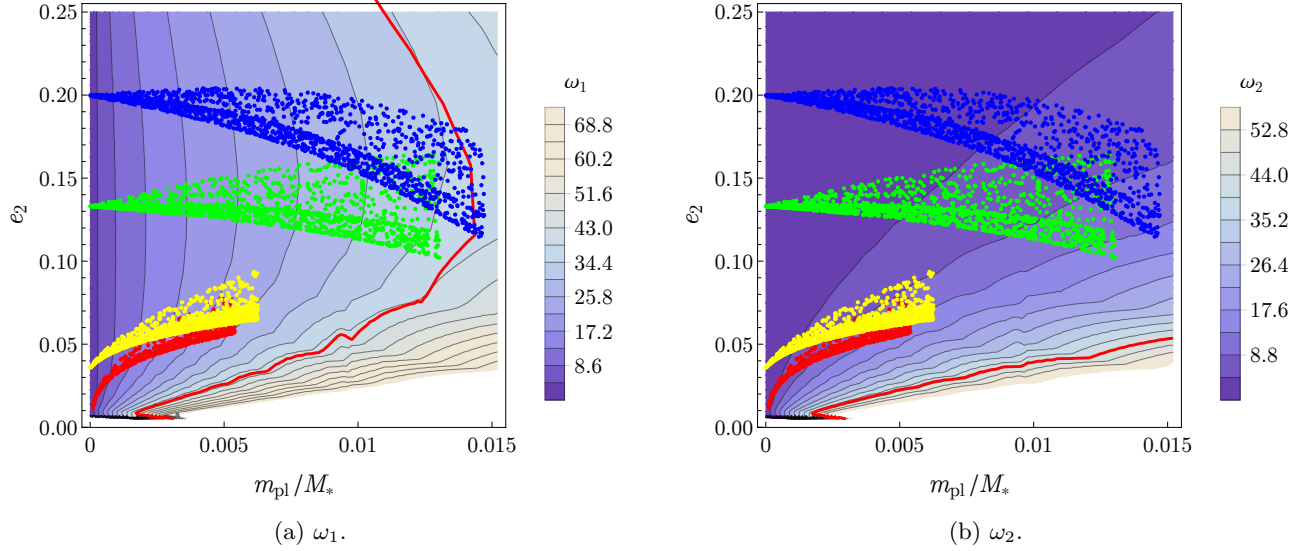


Figure 5.2: We show contour plots for the frequencies ω_1 , panel (a) and ω_2 , panel (b), as functions of the planetary mass m_{pl} and the eccentricity e_2 in the case of the 3:2 mean motion resonance. Lighter colours indicate a higher value of the frequencies. In both panels the red line corresponds to a 2:1 resonance between ω_l and the fast synodic frequency $\omega_{\lambda_1-\lambda_2}$, that is when $\omega_l = \omega_{\lambda_1-\lambda_2}/2$. As expected, the frequency ω_2 is smaller than ω_1 , except for extremely small values of e ; we can therefore concentrate on ω_1 , panel (a), when checking for the significance of secondary resonances in the system. The dots represent the result of the numerical simulations carried out as explained in the text. The simulations are interrupted when the system becomes unstable. We see that the simulations in red, yellow and green go unstable well before ω_l reaches any significant commensurability with $\omega_{\lambda_1-\lambda_2}$. The blue simulation becomes unstable when $\omega_1 \sim \omega_{\lambda_1-\lambda_2}/2$, but we checked that dynamics at the moment of the instability is qualitatively similar to that of the other three integrations, indicating that there is another mechanism that is causing the instability.

and 5.3). To make these figures, we take initial values of m_{pl} ranging from $10^{-5}M_*$ to $10^{-4}M_*$, and initial values of the eccentricities up to ~ 0.2 . Higher values of e are physically unrealistic as $e_{\text{eq},2} \propto h$ (cfr. equation (3.48)) and discs with high aspect ratios are not expected.

The coloured dots in Figure 5.2 and 5.3 show the evolution of e_2 as the planetary mass grows, starting from different initial values, for systems in the 3:2 mean motion resonance. We let the masses grow until an instability occurs. Denoting by m_{crit} the mass at which the discontinuity happens, we do a long-term simulation, over 3×10^7 revolutions of the inner planets, with a fixed mass $m_{\text{pl}} = 0.995 \times m_{\text{crit}}$ to check that the dynamics was still stable up to that point. Simulations with higher planetary masses go unstable immediately, after $\simeq 125$ revolutions of the inner planet. This is shown in Figure 5.4.

We test two possible origins of the instability of the system. The first one is that of a low-order secondary resonance between the frequency of libration of the resonant angles and that of the synodic angle $\lambda_1 - \lambda_2$, which has the most noticeable effect on the faster, short period dynamics of the system (cfr. Figures 3.4a, 3.5a). Note that as the planetary mass increases the frequency $\omega_{\lambda_1-\lambda_2}$ of $\lambda_1 - \lambda_2$ does not change considerably, as it is fixed by the resonance index k , the location of the planetary system and stellar mass; only the amplitude of oscillation of the orbital elements associated to this frequency grows with m_{pl} . This is visible already in Figure 5.1 and shown again in Figure 5.2. Instead, the frequency of libration around the equilibrium point increases with m_{pl} , so that for high enough planetary masses it can reach a $j : (j - 1)$ resonance with $\omega_{\lambda_1-\lambda_2}$, where $j \geq 2$ is an integer, and this might destabilise the system. To check this first hypothesis we build a map of the libration frequencies as a function of the planetary mass and the eccentricity. To do this, we first fix a planetary mass m_{pl} and obtain equilibrium points for different values of the constant of motion Ω , as detailed in Section 3.1.2, and for each point we calculate the frequencies of libration ω_1, ω_2 as explained in Section 3.1.3; finally we change the value of m_{pl} . When we do this, the value of \mathcal{K} is adjusted in order to keep fixed the location of the exact Keplerian resonance. For e.g. the 3:2 mean motion resonance, for each fixed value of m_{pl} , each equilibrium point is univocally characterised by the value of e_2 , so we can write $\omega_l(m_{\text{pl}}, e_2)$, $l = 1, 2$. We then compare it with the frequency $\omega_{\lambda_1-\lambda_2}$ of the synodic angle $\lambda_1 - \lambda_2$. We show in Figure 5.2 a contour plot of ω_1 and ω_2 as the background of the aforementioned

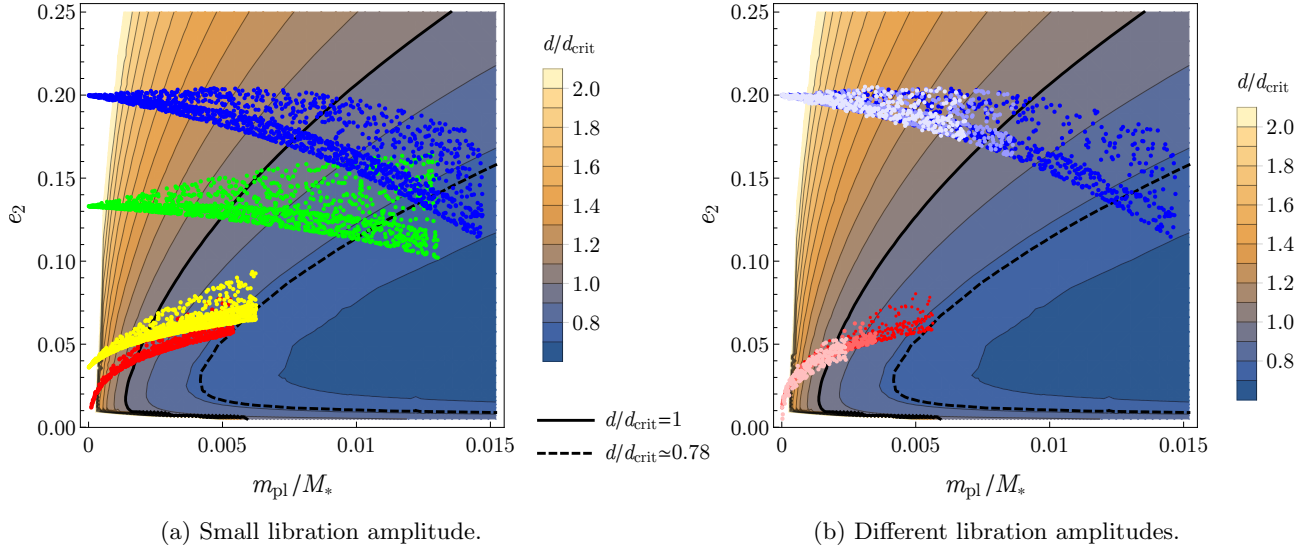


Figure 5.3: Contour plots of d/d_{crit} , where d is the minimal distance between the planets on their orbits around the star, and d_{crit} is the critical distance defined in (5.4) in terms of the mutual Hill radius. In both panels, lighter colours indicate higher values of d/d_{crit} , and the continuous black line indicates the level $d/d_{\text{crit}} = 1$. In panel (a) we superimpose the same numerical simulations as in Figure 5.2. We show that the systems cross this line undisturbed and reach configurations where $d/d_{\text{crit}} < 1$. We note however that the instability occurs roughly at the same level, indicated by a dashed black line, and corresponding to $d/d_{\text{crit}} \simeq 0.78$. In panel (b), we choose two simulations, but we also use initial conditions where we have excited the amplitude of libration of the resonant angles. In both cases, lighter colours represent increasingly excited amplitudes of libration. We see that with higher degrees of excitation the instabilities occur closer and closer to the usual condition $d = d_{\text{crit}}$. As the area enclosed by the libration around the equilibrium is an adiabatic constant with respect to the slowly changing parameter m_{pl} , as soon as the stable region becomes too small when increasing the planetary mass the system exits the resonance.

numerical simulations. Since $\omega_1 > \omega_2$, as we saw in Section 3.1.3, we can focus on secondary resonances between ω_1 and $\omega_{\lambda_1 - \lambda_2}$. We notice that the instabilities do not correspond to any specific commensurability between ω_1 and $\omega_{\lambda_1 - \lambda_2}$. We therefore conclude that these secondary resonances do not play a role in the dynamics of the system, at least at small libration amplitudes around the equilibrium point.

The second hypothesis for the onset of instability is inspired by the criterion of minimal distance between the planets, first proposed by [Gladman(1993)], then revised (see e.g. [Obertas et al.(2017), Petit et al.(2018)]). These studies show that two non-resonant planets go unstable when their orbital configuration is such that they come closer to each other than a critical distance

$$d_{\text{crit}} = 2\sqrt{3}r_{\text{H}}, \quad (5.4)$$

where

$$r_{\text{H}} = \left(\frac{m_1 + m_2}{3M_*} \right)^{1/3} \frac{a_1 + a_2}{2} \quad (5.5)$$

is the mutual Hill radius. Note that for non-resonant configurations, the closest distance of approach between the two planets coincides with the orbital distance, but for resonant ones this is not the case. Therefore, in this case we consider applying Gladman’s criterion not to the orbital distance, but to the actual closest approach of the two planets during the evolution in the resonant configuration. We can estimate this closest distance analytically as follows. As before we find for a fixed planetary mass and a fixed value of Ω an equilibrium point, which can again be identified in terms of the eccentricity. We then evaluate the real minimal distance d of the two planets in such orbital configuration, by sampling the distance between the planets at different values of λ_1 in $[0, 2k\pi]$, (recall that the full Hamiltonian is periodic in this angle with period $2k\pi$), and taking the minimum of these distances. We thus plot in the background of Figure 5.3 the value d/d_{crit} in the case of the 3:2 resonance, as a function again of m_{pl} and e_2 , where d_{crit} is given by (5.4). In Figure 5.3a we superimpose the same numerical simulations as in Figure 5.2. We observe that the planetary systems reach the critical distance d_{crit} (black continuous line) without displaying any

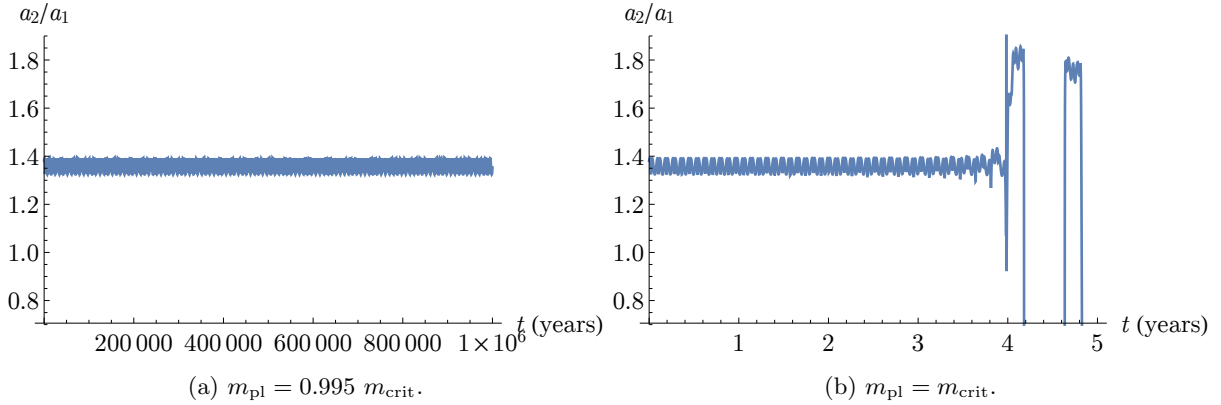


Figure 5.4: Two different evolutions of semi-major axis ratio a_2/a_1 for a system which starts in a 3:2 mean motion resonance, where the planetary masses $m_1 = m_2 = m_{\text{pl}}$ are kept constant. In panel (a) $m_{\text{pl}} = 0.995 m_{\text{crit}}$ and the system shows long-time stable quasi-periodic evolution; in panel (b), $m_{\text{pl}} = m_{\text{crit}}$ and the system immediately proves unstable (note that the timescales reported on the horizontal axes differ by 6 orders of magnitude).

instability. Therefore, we see that resonances are more stable against close encounters than non-resonant systems. It is well known that, given values of a_1, e_1, a_2, e_2 , a pair of resonant planets has a minimum approach distance which is larger than if the planets are not in resonance. Here we show, in our knowledge for the first time, that the centre of a resonance is more stable given an actual minimum approach distance (not an orbital distance), than a non-resonant configuration. In fact, we notice that the instability occurs when the planets reach an analytically estimated closest distance d such that $d/d_{\text{crit}} \simeq 0.78$, see the black dashed line. We should note however that as the planetary masses increase and the planets reach $d/d_{\text{crit}} \sim 1$, one is approaching a singularity (a collision) so that the remainder of the averaged Hamiltonian grows (e.g., [Pousse et al.(2017)]), meaning that the closest approach calculated along the trajectories of the averaged model might be incorrect. However we checked against the actual minimal approach distance that is obtained along a simulation and we saw that at $d/d_{\text{crit}} \simeq 1$ the analytically calculated distance is slightly bigger than the real one but correct within an error of $\sim 3\%$, and even closer to the instability, i.e. for $d < d_{\text{crit}}$ but $m_{\text{pl}} \lesssim m_{\text{crit}}$, it is again slightly bigger than the real minimal distance but correct within a $\sim 6\%$ error. The actual minimal distance at which planets in a 3:2 mean motion resonance go unstable is therefore $d/d_{\text{crit}} \simeq 0.74$; this is slightly smaller than the number obtained analytically and well smaller than 1. We repeated the analysis for the 4:3 resonance, and we find that the instability occurs when $d/d_{\text{crit}} \simeq 0.6$. We also run simulations where we took systems initially deep in resonance and slightly excited their amplitude of libration of the resonant angles, as we did in Section 3.1.3. With these systems, we repeat the numerical exercise of increasing the planetary mass, see the resulting evolutions for two of them in Figure 5.3b. We see that the instabilities occur now closer and closer to the usual criterion, where $d/d_{\text{crit}} = 1$. This indicates that as the mass increases the region of stability around the equilibrium point shrinks. We further test this explanation by taking a system that is deep in resonance, with low amplitude of libration of the resonant angles, and with a mass that is just below the critical mass m_{crit} . Recall that such a system was long-time stable. We then perturb the system to slightly excite the amplitude of libration, as explained before. We see that the system immediately goes unstable after ~ 150 revolutions of the inner planet, indicating that at values of $m_{\text{pl}} \sim m_{\text{crit}}$ the whole region of stability has shrunk to the equilibrium point itself. This behaviour is similar to what is shown in Figure 5.4. The sharp transition between stability and a short instability timescale should not surprise. In a planar model, the closest approach distance is achieved very early. This is true for both the stable and the unstable case. The difference is that in the first case the closest approach distance is large enough not to destabilise the orbit. The closest encounters can then repeat every few years, but the orbit remains stable forever. In the second case, instead, the first closest encounter makes the semi major axes of the planets jump out of resonance. The difference in the critical distance for instability between resonant configurations with low or large amplitudes of libration is probably due to the geometry of the trajectories of the encountering planets. At the exact equilibrium point, the trajectories approaching the close encounter mirror those leaving the encounter, so that the effects of the strong gravitational interaction are partially erased. In the large amplitude case, instead, the symmetry is broken and no compensations between the torques acting before and after the encounter is possible.

5.3 3 Planets

In this section we continue the investigation of the stability of equal-mass planets deep in resonance, expanding to the case of three planets. This work has not yet been published in a peer-reviewed publication, but it will be submitted soon. The first step is to perform numerical experiments similar to those presented in Chapter 3 and the previous section, to which we refer for a more detailed description of the numerical prescriptions used in this setup.

However, a main difference has to be discussed. In the previous section we could obtain any desired value of e_2 (equivalently, e_1) by playing on the value of the damping timescale τ_e . By setting a large value for τ_e , large planetary eccentricities could be obtained (cfr. Equation (3.48)). Here, because the planets capture in resonance in sequence (first planet 1 and 2, then planet 3) if τ_e is large, e_1 and e_2 can grow significantly before planet 3 enters in resonance. This can force large secular eccentricity oscillations of planet 3, which may preclude its resonant capture (see e.g. [Batygin(2015)] on criteria for resonant capture). We therefore use the following numerical recipe that allows us to capture all N planets at the desired resonance and at any reasonably eccentric configurations. We first capture all three planets at small eccentricities, that is with small τ_e . Then we slowly increase the value of τ_e while the planets are already locked in resonance: since the strength of the resonant interaction stays the same while $K = \tau_a/\tau_e$ decreases, Equation (3.48) shows that the planets will adjust to the change in τ_e by becoming more eccentric. By doing so adiabatically we obtain, at the fixed initial planetary mass, resonant chains with the same small amplitude of libration around the resonant equilibrium point with different equilibrium eccentricities. This method does not follow the real dynamical evolution of planetary systems, however we reiterate that the role of this first phase is simply to put the planets deeply into a desired resonant chain with a desired eccentricity (i.e. angular momentum) in order to subsequently study the stability of the obtained configuration as a function of the planetary mass. Similarly, we reiterate that the subsequent phase of slow increase in the planetary mass is a purely fictitious mechanism to numerically test the stability of such orbital configurations as a function of planetary masses. Notice also that the discouraged capture of planet 3 when planet 1 and 2 are too eccentric was not an issue in the three-planet simulations of Chapter 4, since in that case we were interested in capturing planets into low eccentricity configurations, of order $e \simeq H/r$.

5.3.1 Numerical stability maps for $N = 3$ and $k = 3$

We show in Figure 5.5a the result of the simulations of the second phase in our numerical experiments for the case $N = 3$ and the 3:2 – 3:2 resonant chain. On the horizontal axis we report the (increasing) planetary mass, while on the vertical axis we show the evolution of the eccentricity. The simulations are stopped when an instability occurs (a collision in all cases). This plot is to be compared with the similar Figures 5.2 and 5.3 for the case of $N = 2$ and the same resonance index $k = 3$, and uses the same scale on both axes to allow for an easier comparison. By comparing the two plots, there are two important observations to make. The first is that the instabilities occur at lower masses in the case $N = 3$ than in the case $N = 2$. This is in agreement with the results of [Matsumoto et al.(2012)]. This anticipated instability, in terms of planetary mass, is unlikely to be due to too-close encounters between pairs of planets as it was the case $N = 2$. This is because a resonant chain repeats the same orbital geometry between adjacent planets of a two-planet resonance of the same order. Thus, if the critical mass m_{crit} corresponding to the instability in the case $N = 3$ is smaller, the minimal approach distance between each pair of neighbouring planets is necessarily larger in terms of mutual Hill radii than that causing an instability for $N = 2$. There is no apparent reason for which the threshold distance for destabilising two-body encounters should significantly change with the number N of planets in the system. So, the instability is likely to have a different cause. Upon close examination of the $(N + 1)$ -body integrations shown in Figure 5.5a, one notices that a new phenomenon is evident which was not present in Figures 5.2 and 5.3. At some value of the planetary mass ($m_{\text{pl}}/M_* \simeq 1.28 \times 10^{-3}$, dashed vertical line in the figure) there is a sudden excitation of the amplitude of libration. For $m_{\text{pl}}/M_* < 1.28 \times 10^{-3}$, the amplitude of oscillation of the eccentricity grows linearly with the planets' mass due to the increasing amplitude of the fast-frequency term associated to $\lambda_1 - \lambda_2$, as in the two-planet case analysed before (here, the frequency $\lambda_2 - \lambda_3$ also plays a role). After the excitation at $m_{\text{pl}}/M_* \simeq 1.28 \times 10^{-3}$, the systems temporarily remain in resonance, albeit with an increased libration amplitude of the resonant angles; soon after, while the planetary mass is still increasing, the systems finally become unstable as the planets experience close encounters, eventually leading to collisions. This is observed in all simulations.

We have seen in Section 5.2 that the threshold distance for destabilising close encounters increases with the libration amplitude towards Gladman's criterion; moreover the minimal approach distance between two planets decreases with their amplitude of libration. So, our interpretation for the instability in the $N = 3$ case is the fol-

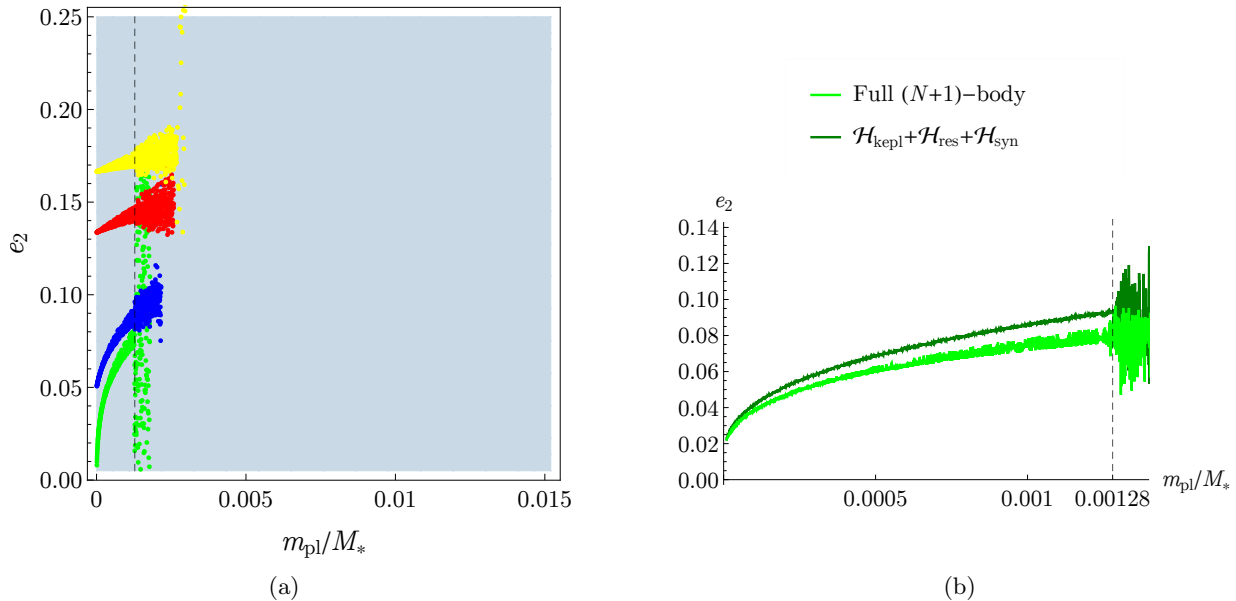


Figure 5.5: Numerical investigation of the stability of three planets deep in the 3:2 – 3:2 mean motion resonance chain, as a function of the planetary mass m_{pl} , equal for all planets. These $(N + 1)$ -body simulations (the coloured markers) are performed starting from low-mass planets ($m_{\text{pl}} = 10^{-5} M_*$) and slowly increasing the planetary mass until an instability occurs (a collision in all cases). In panel (a) we show a map similar to Figures 5.2 and 5.3 for two planets: the scales on the axes are kept the same on purpose to illustrate that three resonant planets go unstable at lower masses than two resonant planets, in accord with [Matsumoto et al.(2012)]. As explained in the main text, the anticipated instability is unlikely caused by close encounters as it was the case for the two-planet case. Indeed a new phenomenon appears which was not present in Figures 5.2, 5.3: the system experiences an excitation before going unstable. This excitation, starting at $m_{\text{pl}} \simeq 1.28 \times 10^{-3}$ (vertical dashed line) is more clearly visible in panel (b), where the result of one of these $(N + 1)$ -body simulation is shown in light green. In dark green we show the result of a Runge-Kutta-4 numerical integration of the simplified Hamiltonian equations where we only consider resonant and synodic interaction terms for each planet pair, up to order one in the eccentricities (cfr. Subsect. 5.3.3): we see that the phenomenon is well reproduced in this simplified system.

lowing: first some dynamical process excites the libration amplitude; then the planets become encounter-unstable because the threshold distance for instability exceeds the actual minimal distance of approach between planet pairs. Thus, below we will look for the dynamical mechanism increasing the libration amplitude. It should be noticed that if such mechanism exists, it would also preclude capture in the resonance at small libration amplitude for the corresponding planetary mass, which is what was observed by [Matsumoto et al.(2012)].

5.3.2 Numerical and analytical investigation of the phenomenon

In the previous subsection we have underlined the importance of the observed increase in the amplitude of libration around the equilibrium point in the $(N + 1)$ -body simulations, and its relevance for triggering the instability of resonant chains. In the following we aim at better understanding the dynamical origin of this growth of libration amplitude.

Our approach is to find a simplified N -planets Hamiltonian model which captures the main features of the dynamics that are observed in the $(N + 1)$ -body integrations. This is because the latter contain a virtually infinite number of harmonics, making it extremely hard to proceed analytically or to obtain any insights from the observed evolution. If we are able to see the same phenomenon in a simplified problem it will be easier to isolate its origin. Thus, in the following we start from a Hamiltonian planetary model that has only a minimal number of terms (harmonics) and we progressively add more terms until we observe in the integration of the considered Hamiltonian the same phenomenon that we have seen in the full numerical integration. The Hamiltonian models are integrated using a Runge-Kutta fourth-order method⁵ (RK4), where we slowly increase the mass of the planets

⁵We remark that since the integrator is not symplectic, we needed to decrease the time step down to $\sim 10^{-4}$ in units where $\bar{a}_1 \sim 0.1$,

at each integration time step in accordance with the $(N + 1)$ -body simulations in Subsection 5.3.1. Only when the numerical integrations show very good agreement with the full $(N + 1)$ -body integrations, will we consider the corresponding Hamiltonian as a good approximation to the full one and work directly with the former. Before we get into the technicalities of our investigation, we plan out our methodology below.

The first reasonable choice for the RK4 integrations is to consider the averaged equations of motion, expanded to some order in the eccentricity. This corresponds to dropping all non-resonant harmonics from the planetary Hamiltonian (2.95) and only keeping resonant harmonics up to some order in e , as we did in Sections 3.1 and 5.2. This approach is presented in Subsection 5.3.4. By doing so, one realises that these terms cannot alone be responsible for the increase in amplitude of libration observed in the $(N + 1)$ -body integrations. This is the first main result of this section: *the purely resonant system $\bar{\mathcal{H}} = \mathcal{H}_{\text{kepl}} + \mathcal{H}_{\text{res}}$ with initial conditions at vanishing amplitude around a resonant equilibrium point is Lyapunov stable for all planetary masses.*

The next step is therefore to include additional non-resonant terms, which were naturally present in the full Hamiltonian that governs the evolution of the $(N + 1)$ -body integrations. Maintaining for simplicity the expansion to first order in the eccentricity (which should be valid at least when all eccentricities are small enough), we then add synodic terms. In the case of three planets, these include the harmonics $\lambda_1 - \lambda_2$ and $\lambda_2 - \lambda_3$, which we add in an additional interaction Hamiltonian \mathcal{H}_{syn} . As we show in Section 5.3.5, the introduction of these terms is responsible for the same phenomenon observed in Figure 5.5a. This fact is anticipated in Figure 5.5b, where we plot with a darker colour the evolution of $\mathcal{H}_{\text{kepl}} + \mathcal{H}_{\text{res}} + \mathcal{H}_{\text{syn}} =: \mathcal{H}^*$ over one of the full $(N + 1)$ -body integration with the same initial conditions, and we see that there is good qualitative agreement between the two evolutions. We also investigate the possibility of adding only one of the two synodic terms, but show that both are needed to reproduce the phenomenon at similar planetary masses, which is a result that we will also explain analytically (cfr. Subsect. 5.3.5.2). In the light of this, we will use the evolution yielded by the simplified model $\mathcal{H}^* = \mathcal{H}_{\text{kepl}} + \mathcal{H}_{\text{res}} + \mathcal{H}_{\text{syn}}$ as a guide to understand the relevant dynamics contained in the full $(N + 1)$ -body integrations. At the same time, working with a controlled number of interaction terms allows us to proceed analytically (see Subsect. 5.3.5.1) and to understand what is the dynamical mechanism that gives rise to the increase in amplitude of libration around the resonant equilibrium point. Carrying out the calculation explicitly in the specific case of $N = 3$ planets and for the 3:2 – 3:2 chain, we show in Subsect. 5.3.5.2 that this is due to a set of secondary resonances between a fraction of the synodic frequency (which remains relatively constant with increasing m_{pl}) and specific combinations of the libration frequencies around the equilibrium point (which increase with m_{pl} , as we will show). Considering relevant canonical action-angle variables centred at the equilibrium, such secondary resonances have the effect of exciting the action to values farther and farther away from the origin. This is the second main result of this section: *the synodic contribution introduces terms of order $\mathcal{O}(m_{\text{pl}}^2)$ which include secondary resonances between a fraction the synodic frequency and the resonant libration frequencies, which are responsible for the excitation of the system and eventually for its instability.* In Subsect. 5.3.5.3 we build a model for the secondary resonance that is encountered in the specific case $N = 3$ and $k = 3$, but the method can be easily generalised to the other secondary resonances that can in principle be encountered. Finally, we proceed to generalise this result to more compact resonant chains in Subsection 5.3.6.

5.3.3 Rescaled Hamiltonian and new set of canonical variables

In order to make the calculations and algebraic expressions less cumbersome, we start by performing the following simplifications. These are clearly general and are carried out here for any number N of planets.

Firstly, since the instabilities for $N \geq 3$ planets occur at much lower values of m_{pl}/M_* than for 2 planets, we approximate the reduced mass $\mu = \frac{m_{\text{pl}}M_*}{M_* + m_{\text{pl}}} \sim m_{\text{pl}}$ and $M_* + m_{\text{pl}} \sim M_*$. Then, we recall that all the planets have the same mass m_{pl} , and we intend later on to make use of the tools of perturbation theory described in Subsection 2.3.1 to study the dynamics of the resonant chains. It is therefore convenient to write the Hamiltonian in the form similar to (2.107). The natural choice is to rescale all the actions (Λ, Γ) of the modified Delaunay variables by the planetary mass m_{pl} , which yields

$$\begin{aligned}\Lambda &= \sqrt{\mathcal{G}M_*a}, \\ \Gamma &= \Lambda(1 - \sqrt{1 - e^2}),\end{aligned}\tag{5.6}$$

$\mathcal{G}M_* = (2\pi)^2$ to obtain consistent results.

where for simplicity we have maintained the same notation as for the non-rescaled variables (notice also that we used a similar rescaling in Chapter 4, but in that case the planets had different masses and the spirit of the calculation was completely different: to avoid confusion we detail here the specific steps needed in this chapter). As pointed out in Subsect. 2.1.3.2, to maintain the canonicity of the Hamiltonian, \mathcal{H} itself must be rescaled by m_{pl} . With this choice the reduced N -planets Hamiltonian takes the form

$$\begin{aligned}\mathcal{H} &= \mathcal{H}_{\text{kepl}} + \mathcal{H}_{\text{pert}}, \\ \mathcal{H}_{\text{kepl}} &= - \sum_{i=1}^N \frac{\mathcal{G}^2 M_*^2}{2\Lambda_i^2},\end{aligned}\tag{5.7}$$

where $\mathcal{H}_{\text{kepl}}$ is independent of m_{pl} , and the perturbation is of order $\mathcal{O}(m_{\text{pl}})$: $\mathcal{H}_{\text{pert}} = m_{\text{pl}} \mathcal{H}_{\text{pert}}'$. We outlined in Subsec. 2.2.2.1 how one can obtain the expression of each term in $\mathcal{H}_{\text{pert}}$. For example, for a pair of neighbouring planets labelled by the indices i and $i+1$ which are near a $k^{(i)} : (k^{(i)} - 1)$ mean motion resonance, the perturbing resonant contribution to first order in the eccentricity takes the form

$$\begin{aligned}\mathcal{H}_{\text{res}}^{(i)} &= m_{\text{pl}} \left[\alpha_1^{(i)} e_i \cos \left(k^{(i)} \lambda_{i+1} - (k^{(i)} - i) \lambda_i + \gamma_i \right) \right. \\ &\quad \left. + \alpha_2^{(i)} e_{i+1} \cos \left(k^{(i)} \lambda_{i+1} - (k^{(i)} - i) \lambda_i + \gamma_{i+1} \right) \right], \quad i = 1, \dots, N-1,\end{aligned}\tag{5.8}$$

where the now rescaled coefficients α are

$$\alpha_j^{(i)} = - \frac{\mathcal{G}^2 M_*}{\bar{\Lambda}_{i+1}^2} f_{\text{res}}^{(j,i)}(\alpha_{\text{res}}^{(i)}); \tag{5.9}$$

here as usual $\alpha_{\text{res}}^{(i)} = \bar{a}_i / \bar{a}_{i+1} = ((k^{(i)} - 1) / k^{(i)})^{2/3}$ is the nominal semi-major axis ratio corresponding to the resonance location in the Keplerian approximation, so the Laplace coefficients are the same for each pair of planets in a resonant chain repeating the $k:k-1$ commensurability. Moreover, as in Subsection 3.1.1 and Section 4.2, we have evaluated the Λ_{i+1}^2 at denominator at its nominal Keplerian value $\bar{\Lambda}_{i+1}$, so the coefficients $\alpha_j^{(i)}$ are effectively constants for a given chain and a given nominal orbital separation. The other example of terms in the perturbing function $\mathcal{H}_{\text{pert}}$ that are of interest to us in this context are the synodic terms for each neighbouring planet pair, which at lowest order in the eccentricities take the form

$$\mathcal{H}_{\text{syn}}^{(i)} = c_i \cos(\lambda_i - \lambda_{i+1}) = m_{\text{pl}} C_i \cos(\lambda_i - \lambda_{i+1}), \tag{5.10}$$

where the coefficients C_i for the rescaled Hamiltonian are

$$C_i = - \frac{\mathcal{G}^2 M_*}{\bar{\Lambda}_{i+1}^2} \times \frac{1}{2} b_{1/2}^{(1)}(\alpha_{\text{res}}^{(i)}), \tag{5.11}$$

and have the same scaling in $\bar{\Lambda}_{i+1}$ as the coefficients in (5.9) but a different dependence on the Laplace coefficients $b_s^{(j)}$ (e.g. [Ellis and Murray(2000)]).

In the case of interest to us in this and in the subsequent section, namely that of N planets with neighbouring planets pair near a $k^{(i)} : (k^{(i)} - 1)$ mean motion resonance, it is also convenient to make use of slightly different canonical variables than (5.1) used in the previous one. The reason is that we also intend to work with the non-resonant synodic angles $\lambda_i - \lambda_{i+1}$, so it is preferable that one of them, say $\lambda_1 - \lambda_2$, be one of the canonical variables. The natural choice is to use as canonical positions the resonant angles $\psi_1^{(i)} = \theta^{(i)} + \gamma_i$ (where $\theta^{(i)} = k^{(i)} \lambda_{i+1} - (k^{(i)} - 1) \lambda_i$ is the longitude of conjunction for the i -th pair) and the apsidal differences $\delta\gamma_{i,i+1} = \gamma_i - \gamma_{i+1}$ for $i = 1, 2$, then define $\delta\lambda_{1,2} = \lambda_1 - \lambda_2$ and finally keep an angle which will not appear explicitly in the Hamiltonian, such as γ_N . These linear changes of variables for the positions are easily extended to a canonical transformation as explained in Subsection 2.1.3.2 (the transformation on the actions is linear, with matrix equal to the transpose of the inverse of the matrix defining the transformation on the angles). For example, in the case $N = 3$ we pass from the modified Delaunay variables $(\Lambda_1, \Lambda_2, \Lambda_3, \Gamma_1, \Gamma_2, \Gamma_3, \lambda_1, \lambda_2, \lambda_3, \gamma_1, \gamma_2, \gamma_3)$ to new action-angle variables

$(\Psi_1^{(1)}, \Psi_1^{(2)}, \Delta\gamma_{1,2}, \Delta\gamma_{2,3}, \Delta\lambda_{1,2}, \mathcal{L}, \psi_1^{(1)}, \psi_1^{(2)}, \delta\gamma_{1,2}, \delta\gamma_{2,3}, \delta\lambda_{1,2}, \gamma_3')$ defined by⁶

$$\begin{aligned}
\Psi_1^{(1)} &= \Lambda_1 + \Lambda_2 + \frac{k^{(2)} - 1}{k^{(2)}} \Lambda_3, & \psi_1^{(1)} &= k^{(1)} \lambda_2 - (k^{(1)} - 1) \lambda_1 + \gamma_1, \\
\Psi_1^{(2)} &= \frac{1}{k^{(2)}} \Lambda_3, & \psi_1^{(2)} &= k^{(2)} \lambda_3 - (k^{(2)} - 1) \lambda_2 + \gamma_2, \\
\Delta\gamma_{1,2} &= -(\Lambda_1 + \Lambda_2 + \frac{k^{(2)} - 1}{k^{(2)}} \Lambda_3) + \Gamma_1 & \delta\gamma_{1,2} &= \gamma_1 - \gamma_2, \\
&= -\Psi_1^{(1)} + \Gamma_1, & & \\
\Delta\gamma_{2,3} &= -(\Lambda_1 + \Lambda_2 + \Lambda_3) + \Gamma_1 + \Gamma_2 & \delta\gamma_{2,3} &= \gamma_2 - \gamma_3, \\
&= -(\Psi_1^{(1)} + \Psi_1^{(2)}) + \Gamma_1 + \Gamma_2, & & \\
\Delta\lambda_{1,2} &= k^{(1)} \Lambda_1 + (k^{(1)} - 1) \Lambda_2 + \frac{(k^{(1)} - 1)(k^{(2)} - 1)}{k^{(2)}} \Lambda_3 & \delta\lambda_{1,2} &= \lambda_1 - \lambda_2, \\
&= k^{(1)} \mathcal{K}, & & \\
\mathcal{L} &= (\Lambda_1 + \Lambda_2 + \Lambda_3) - (\Gamma_1 + \Gamma_2 + \Gamma_3) & \gamma_3' &= -\gamma_3. \\
&= (\Psi_1^{(1)} + \Psi_1^{(2)}) - (\Gamma_1 + \Gamma_2 + \Gamma_3), & &
\end{aligned} \tag{5.12}$$

This canonical change of variable has the advantage of being easily generalisable to any number N of planets and of having the specific angular momentum \mathcal{L} appearing as an explicit constant of motion, since its conjugated angle $\gamma_N' = -\gamma_N$ never appears explicitly in the transformed Hamiltonian. We remark that \mathcal{L} is now the specific angular momentum because the actions have been rescaled by the planetary mass; this also entails that when integrating the system (5.7) with increasing m_{pl} , \mathcal{L} will always remain constant. Moreover, the action $\Delta\lambda_{1,2}$ conjugated to the angle $\delta\lambda_{1,2}$ is simply a factor away from the previously used action \mathcal{K} (cfr. Equations (3.5), (4.7)), whose significance as a constant of motion in the averaged model (cfr. Equations (3.2), (4.4)) has already been described (cfr. Sections 3.1, 4.2).

We note that in these variables in the case of three resonant planets in a $k^{(1)} : (k^{(1)} - 1) - k^{(2)} : (k^{(2)} - 1)$ chain, the synodic harmonics for the two pairs of planets write

$$\begin{aligned}
\lambda_1 - \lambda_2 &= \delta\lambda_{1,2}, \\
\lambda_2 - \lambda_3 &= \frac{1}{k^{(2)}} ((k^{(1)} - 1) \delta\lambda_{1,2} + \psi_1^{(1)} - \psi_1^{(2)} - \delta\gamma_{1,2}).
\end{aligned} \tag{5.13}$$

Then, in the new variables the Keplerian Hamiltonian (5.7), the resonant contribution (5.8) and the synodic

⁶A note on notation can help clarify the meaning of the names of these variables. Reading the definitions for the angles, the upper indices (i) refer to which pair of planets is considered, so that $k^{(1)}$ is the index of the first order mean motion resonance for the inner pair and $\psi^{(1)}$ refers to a resonant angle for that pair. Similarly $\theta^{(i)} = k^{(i)} \lambda_{i+1} - (k^{(i)} - 1) \lambda_i$ is the longitude of conjunction of the i -th pair. The subscript 1 in $\psi_1^{(i)}$ signifies the fact that for each pair we choose to use the resonant angle which depends on the longitude of pericentre γ of the innermost planet of the pair, so $\psi_1^{(i)} = \theta^{(i)} + \gamma_i$, while the other resonant angle would then be $\psi_2^{(i)} = \theta^{(i)} + \gamma_{i+1}$ (and it does not appear since we also use $\gamma_i - \gamma_{i+1}$ as canonical angles). The conventions for the other angles are evident. For the actions, we simply use an uppercase first letter to indicate to which angle each action is conjugated, except for the last action since it is just the orbital angular momentum, which we always indicate with \mathcal{L} , and it is always a constant of motion.

contribution (5.10) for pairs of neighbouring planets write

$$\mathcal{H}_{\text{kepl}} = -\frac{\mathcal{G}^2 M_*^2}{2\left(-\Delta\lambda_{1,2} + k^{(1)}\Psi_1^{(1)} - k^{(2)}\Psi_1^{(2)} + \Psi_1^{(2)}\right)^2} - \frac{\mathcal{G}^2 M_*^2}{2\left(\Delta\lambda_{1,2} - k^{(1)}\Psi_1^{(1)} + \Psi_1^{(1)}\right)^2} - \frac{\mathcal{G}^2 M_*^2}{2\left(k^{(2)}\Psi_1^{(2)}\right)^2}, \quad (5.14a)$$

$$\begin{aligned} \mathcal{H}_{\text{res}} = m_{\text{pl}} & \left[\alpha_1^{(1)} \frac{\sqrt{\Delta\gamma_{1,2} + \Psi_1^{(1)}} \sqrt{2\Delta\lambda_{1,2} - \Delta\gamma_{1,2} - (2k^{(1)} - 1)\Psi_1^{(1)}}}{\Delta\lambda_{1,2} - (k^{(1)} - 1)\Psi_1^{(1)}} \cos\psi_1^{(1)} \right. \\ & + \alpha_2^{(1)} \frac{\sqrt{\Delta\gamma_{2,3} + \Psi_1^{(2)} - \Delta\gamma_{1,2}} \sqrt{\Delta\gamma_{1,2} - \Delta\gamma_{2,3} - 2\Delta\lambda_{1,2} + 2k^{(1)}\Psi_1^{(1)} - (2k^{(2)} - 1)\Psi_1^{(2)}}}{-\Delta\lambda_{1,2} + k^{(1)}\Psi_1^{(1)} - (k^{(2)} - 1)\Psi_1^{(2)}} \times \\ & \quad \times \cos(\psi_1^{(1)} - \delta\gamma_{1,2}) \\ & + \alpha_1^{(2)} \frac{\sqrt{\Delta\gamma_{2,3} + \Psi_1^{(2)} - \Delta\gamma_{1,2}} \sqrt{\Delta\gamma_{1,2} - \Delta\gamma_{2,3} - 2\Delta\lambda_{1,2} + 2k^{(1)}\Psi_1^{(1)} - (2k^{(2)} - 1)\Psi_1^{(2)}}}{-\Delta\lambda_{1,2} + k^{(1)}\Psi_1^{(1)} - (k^{(2)} - 1)\Psi_1^{(2)}} \times \\ & \quad \times \cos\psi_1^{(2)} \\ & \left. + \alpha_2^{(2)} \frac{\sqrt{-\mathcal{L} - \Delta\gamma_{2,3}} \sqrt{\mathcal{L} + \Delta\gamma_{2,3} + 2k^{(2)}\psi_1^{(2)}}}{k^{(2)}\psi_1^{(2)}} \cos(\psi_1^{(2)} - \delta\gamma_{2,3}) \right] \\ & = m_{\text{pl}} \mathcal{H}_{\text{res}}', \end{aligned} \quad (5.14b)$$

$$\begin{aligned} \mathcal{H}_{\text{syn}} & = m_{\text{pl}} \left[C_1 \cos(\delta\lambda_{1,2}) + C_2 \cos\left(\frac{1}{k^{(2)}}\left((k^{(1)} - 1)\delta\lambda_{1,2} + \psi_1^{(1)} - \psi_1^{(2)} - \delta\gamma_{1,2}\right)\right) \right] \\ & = m_{\text{pl}} \mathcal{H}_{\text{syn}}'. \end{aligned} \quad (5.14c)$$

$\mathcal{H}_{\text{kepl}}$ is independent of m_{pl} and depends on the variables $\Psi_1^{(1)}$, $\Psi_1^{(2)}$ and $\Delta\lambda_{1,2}$ only; one can introduce the frequencies (analogous to the mean motions n)

$$\begin{aligned} \eta_{\Psi_1^{(1)}} & := \frac{\partial\mathcal{H}}{\partial\Psi_1^{(1)}} = \frac{\mathcal{G}^2 k^{(1)} M_*^2}{\left(-\Delta\lambda_{1,2} + k^{(1)}\Psi_1^{(1)} - k^{(2)}\Psi_1^{(2)} + \Psi_1^{(2)}\right)^3} + \frac{\mathcal{G}^2(1 - k^{(1)})M_*^2}{\left(\Delta\lambda_{1,2} - k^{(1)}\Psi_1^{(1)} + \Psi_1^{(1)}\right)^3}, \\ \eta_{\Psi_1^{(2)}} & := \frac{\partial\mathcal{H}}{\partial\Psi_1^{(2)}} = \frac{\mathcal{G}^2(1 - k^{(2)})M_*^2}{\left(-\Delta\lambda_{1,2} + k^{(1)}\Psi_1^{(1)} - k^{(2)}\Psi_1^{(2)} + \Psi_1^{(2)}\right)^3} + \frac{\mathcal{G}^2 M_*^2}{k^{(2)2} \Psi_1^{(2)3}}, \\ \eta_{\Delta\lambda_{1,2}} & := \frac{\partial\mathcal{H}}{\Delta\lambda_{1,2}} = \frac{\mathcal{G}^2 M_*^2}{\left(\Delta\lambda_{1,2} - k^{(1)}\Psi_1^{(1)} + \Psi_1^{(1)}\right)^3} - \frac{\mathcal{G}^2 M_*^2}{\left(-\Delta\lambda_{1,2} + k^{(1)}\Psi_1^{(1)} - k^{(2)}\Psi_1^{(2)} + \Psi_1^{(2)}\right)^3}. \end{aligned} \quad (5.15)$$

In (5.14b), (5.14c) we use a prime ($'$) to indicate that the Hamiltonian term has been rescaled by m_{pl} itself, so, it is $\mathcal{O}(0)$ in m_{pl} , and the dependence on m_{pl} has been clearly expressed with a coefficient. In the following we will also use the notation $\mathbf{x} = (\Psi_1^{(1)}, \Psi_1^{(2)}, \Delta\gamma_{1,2}, \Delta\gamma_{2,3}, \Delta\lambda_{1,2}, \psi_1^{(1)}, \psi_1^{(2)}, \delta\gamma_{1,2}, \delta\gamma_{2,3}, \delta\lambda_{1,2})$ for the canonical variables that enter in \mathcal{H} ; we write for the actions $\mathbf{p} = (\Psi_1^{(1)}, \Psi_1^{(2)}, \Delta\gamma_{1,2}, \Delta\gamma_{2,3}, \Delta\lambda_{1,2})$ and for the angles $\mathbf{q} = (\psi_1^{(1)}, \psi_1^{(2)}, \delta\gamma_{1,2}, \delta\gamma_{2,3}, \delta\lambda_{1,2})$.

5.3.4 Purely resonant dynamics

The purely resonant dynamics is the one governed by the Hamiltonian averaged over the fast angle $\delta\lambda_{1,2}$, i.e. $\bar{\mathcal{H}} = \mathcal{H}_{\text{kepl}} + \mathcal{H}_{\text{res}}$. We are using the same averaging technique and notation as in Equations(3.2), 4.4, but the Hamiltonian is here rescaled by m_{pl} as explained in the previous section. $\bar{\mathcal{H}}$ is now rewritten in terms of the new canonical variables (5.12) (cfr. Equation (5.14)), and since the synodic terms have been removed by averaging, not only \mathcal{L} but also $\Delta\lambda_{1,2}$ is a constant of motion, so that only the ‘‘barred’’ variables $\bar{\mathbf{x}} = (\bar{\mathbf{p}}, \bar{\mathbf{q}}) = (\Psi_1^{(1)}, \Psi_1^{(2)}, \Delta\gamma_{1,2}, \Delta\gamma_{2,3}, \psi_1^{(1)}, \psi_1^{(2)}, \delta\gamma_{1,2}, \delta\gamma_{2,3})$ evolve.⁷ These barred variables $\bar{\mathbf{x}} = (\bar{\mathbf{p}}, \bar{\mathbf{q}})$ are simply a subset of

⁷From a technical point of view, these variables are only an approximation (up to order 0 in m_{pl}) to the actual canonical variables that eliminate the non-resonant contributions. These would be the primed variables introduced later on in (5.30).

the variables $\mathbf{x} = (\mathbf{p}, \mathbf{q})$ introduced above, and represent the purely resonant degrees of freedom (this notation is only introduced to separate these variables from the synodic canonical pair $(\Delta\lambda_{1,2}, \delta\lambda_{1,2})$; this will be a useful distinction later on).

We integrate this Hamiltonian with a RK4 integrator while slowly increasing the planetary mass at each time step as detailed above. We use again as an example the case of the 3:2 – 3:2 chain starting with an initial planetary mass $m_{\text{pl}}/M_* = 10^{-5}$ and we choose as initial condition that of Figure 5.5b. The resulting evolution is shown in dark green in Figure 5.6, panels (a) to (d). We observe that the four resonant degrees of freedom are never unstable even up to masses significantly higher than the critical mass $(m_{\text{pl}}/M_*)_{\text{crit}} \simeq 1.28 \times 10^{-3}$ which is found in the numerical $(N + 1)$ -body simulations with the same initial conditions (Figure 5.5b).

We can present an analytical explanation for this. In the same manner as in Subsect. 3.1.2 we find stable equilibrium points for $\bar{\mathcal{H}}(\bar{\mathbf{x}}; \mathcal{L}, \Delta\lambda_{1,2}, m_{\text{pl}})$ in the variables $\bar{\mathbf{x}}$, while keeping \mathcal{L} and $\Delta\lambda_{1,2}$ constants and for different values of m_{pl} , yielding $\bar{\mathbf{x}}_{\text{eq}}(m_{\text{pl}}) = \bar{\mathbf{x}}_{\text{eq}}(m_{\text{pl}}; \mathcal{L}, \Delta\lambda_{1,2})$. Recall that at these low eccentricities we are interested in symmetric linearly stable equilibria only, so the equilibrium values $\bar{\mathbf{q}}_{\text{eq}}$ of the angles are simply

$$\begin{aligned}\psi_{1,\text{eq}}^{(1)} &= 0, \\ \psi_{1,\text{eq}}^{(2)} &= 0, \\ \delta\gamma_{1,2,\text{eq}} &= \pi, \\ \delta\gamma_{2,3,\text{eq}} &= \pi,\end{aligned}\tag{5.16}$$

and we only need to solve for the equilibrium actions $\bar{\mathbf{p}}_{\text{eq}} = (\Psi_{1,\text{eq}}^{(1)}, \Psi_{2,\text{eq}}^{(1)}, \Delta\gamma_{1,2,\text{eq}}, \Delta\gamma_{2,3,\text{eq}})$. In Figure 5.6, panels (a) to (d), we superimposed the analytically calculated equilibrium points and the RK4 evolution, showing excellent agreement. Then, as explained in Subsect. 2.1.5.1, we diagonalise the system around the equilibrium point $\bar{\mathbf{x}}_{\text{eq}}$; since it is a stable equilibrium point, all eigenvalues are purely imaginary and the diagonalisation procedure yields a Hamiltonian of the form

$$\bar{\mathcal{H}}(\boldsymbol{\xi}, \boldsymbol{\eta}) = \sum_{l=1}^4 \frac{\omega_l}{2} (\xi_l^2 + \eta_l^2) + \mathcal{O}(\|\boldsymbol{\xi}, \boldsymbol{\eta}\|^3)\tag{5.17}$$

in cartesian coordinates $\bar{\mathbf{x}} = T(\boldsymbol{\xi}, \boldsymbol{\eta})$ with T a transformation matrix. Using canonical polar coordinates $(I_l, \phi_l)_{l=1,\dots,4}$ with $(\xi_l = \sqrt{2I_l} \cos \phi_l, \eta_l = \sqrt{2I_l} \sin \phi_l)$ (cfr. Subsect. 2.1.3.2) we get

$$\bar{\mathcal{H}} = \sum_{l=1}^4 \omega_l I_l + \mathcal{O}(\|\mathbf{I}^{3/2}\|),\tag{5.18}$$

which appears as the sum of four decoupled harmonic oscillators, Equation (2.53), plus higher order terms. The resulting four frequencies ω_l , $l = 1, \dots, 4$ are shown in Figure 5.6e as a function of the planetary mass m_{pl} , and we notice right away that they all have the same sign. This means that at vanishing amplitudes of libration the Hamiltonian has an extremum at the equilibrium point (a maximum) so that we can use the Hamiltonian itself as a Lyapunov function to deduce that the equilibrium point is Lyapunov stable for all planetary masses.

Since it will be useful later on, we also consider here how the libration frequencies grow with m_{pl} . This is shown in Figure 5.6 panels (e) and (f). We find numerically that $\omega_{1,2} \propto m_{\text{pl}}^{2/3}$ at low eccentricities ($e \simeq 0.01$) while $\omega_{1,2} \propto m_{\text{pl}}^{1/2}$ at higher eccentricities ($e \simeq 0.1$). Notice that for a pendulum-type Hamiltonian like

$$\mathcal{H}_{\text{pend}}(\Sigma, \sigma) = a\Sigma^2 - m_{\text{pl}}b \cos \sigma\tag{5.19}$$

the libration frequency would be $\propto m_{\text{pl}}^{1/2}$ (cfr. Subsect. 2.1.6), so it might be interesting to ponder analytically why at low eccentricities we get a different scaling. The reason is that with changing mass we also change the corresponding equilibrium point, which means that the parameters a and b in the pendulum-like Hamiltonian above also depend on m_{pl} , and the real scaling would therefore be $\sqrt{abm_{\text{pl}}}$. The way the equilibrium points adjust to changes in m_{pl} here is by following lines of constant specific angular momentum (cfr. Figure 5.1). Because of the curvature of the level curves of the specific angular momentum, the equilibrium points vary differently depending on the eccentricity, which is why we get different scalings.

We finally remark that [Batygin(2015)] estimates for two planets the (highest) libration frequency, at small amplitude of librations around the resonant equilibrium point and for a value of the angular momentum at which the separatrix first appears. He finds that this frequency scales with $((m_1 + m_2)/M_*)^{2/3}$: since the appearance of the separatrix happens at small eccentricities, this is consistent with our findings.

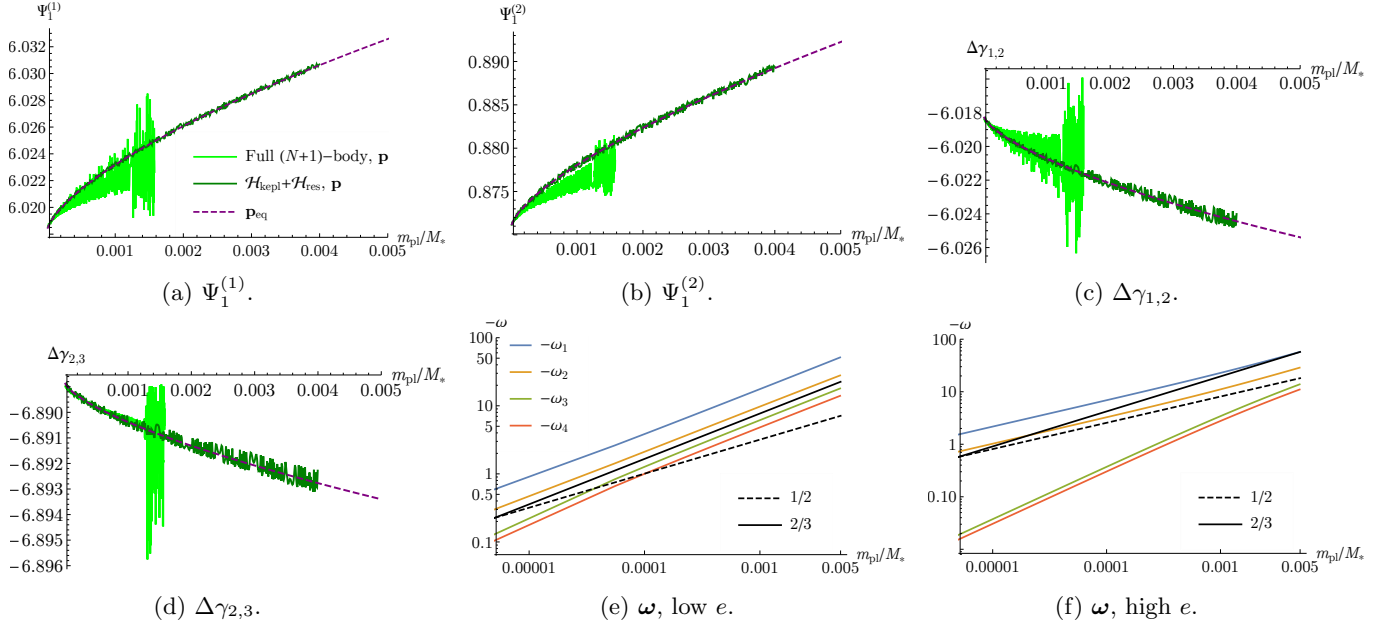


Figure 5.6: The purely resonant evolution governed by $\bar{\mathcal{H}}$ in the case of three planets in a 3:2 – 3:2 mean motion resonance chain, with the same initial conditions as in Figure 5.5b. We show in dark green in panels (a) to (d) the evolution of the actions $\bar{\mathbf{p}} = (\Psi_1^{(1)}, \Psi_2^{(1)}, \Delta\gamma_{1,2}, \Delta\gamma_{2,3})$ as the planetary mass m_{pl} is slowly increasing, and we match it to the calculated equilibria $\bar{\mathbf{p}}_{\text{eq}} = (\Psi_{1,\text{eq}}^{(1)}, \Psi_{2,\text{eq}}^{(1)}, \Delta\gamma_{1,2,\text{eq}}, \Delta\gamma_{2,3,\text{eq}})$ (purple dashed line); we also add the corresponding $(N + 1)$ -body integration with the same initial condition (light green). A legend for panels (a) to (d) is given in panel (a). We see that the system remains stable well after the value of $m_{\text{pl}} \simeq 1.28 \times 10^{-3}$ corresponding to the onset of excitation in Figure 5.5b. Panels (e) and (f) contain the analytical explanation of the observed stability: we plot with coloured lines all the frequencies of the four degrees of freedom and we notice that they have the same sign, therefore the Hamiltonian has a maximum at the equilibrium point and for low amplitude of librations the system remains Lyapunov-stable even if the frequencies grow in absolute value. In panel (e) we used the same eccentricities that correspond to the initial conditions of panels (a) to (d), $e \simeq 0.01$; in panel (f) we used higher initial eccentricities, $e \simeq 0.1$. We note that the scaling law for $\omega_l(m_{\text{pl}})$ changes depending on the eccentricity (see black solid and dashed lines).

5.3.5 The synodic contribution

In the previous subsection we have shown that the purely resonant system is Lyapunov-stable for all planetary masses. The next natural step is therefore to introduce non-resonant contribution of the disturbing function. To lowest order in e , we introduce the two synodic terms (5.10) for the inner and outer pairs, resulting in

$$\mathcal{H}_{\text{syn}} = m_{\text{pl}} [C_1 \cos(\lambda_1 - \lambda_2) + C_2 \cos(\lambda_2 - \lambda_3)] = m_{\text{pl}} \mathcal{H}_{\text{syn}}', \quad (5.20)$$

with coefficients given by (5.11). The full rescaled Hamiltonian written in the new variables (5.12) is now

$$\mathcal{H}^*(\mathbf{x}; \mathcal{L}, m_{\text{pl}}) = \mathcal{H}_{\text{kepl}} + \mathcal{H}_{\text{res}} + \mathcal{H}_{\text{syn}}; \quad (5.21)$$

we have stressed that it depends parametrically on the constant of motion \mathcal{L} and on the mass m_{pl} through $\mathcal{H}_{\text{res}} = m_{\text{pl}} \mathcal{H}_{\text{res}}'$ and $\mathcal{H}_{\text{syn}} = m_{\text{pl}} \mathcal{H}_{\text{syn}}'$.

We integrate this Hamiltonian for the 3:2 – 3:2 chain with the same RK4 scheme described before and the same initial conditions as in the previous section. This gives the evolution of the actions displayed in dark green in Figure 5.7, which is matched against the $(N + 1)$ -body integration with the same initial datum (lighter green) and the locations of the equilibria for $\bar{\mathcal{H}}$ calculated in the previous section for different planetary masses (purple dashed lines). The comparison for the eccentricity evolutions, instead of the canonical variables, has been already presented in Figure 5.5b. We notice two important aspects of these plots. The first is that, initially, for all variables the evolution described by \mathcal{H}^* follows on average that described by $\bar{\mathcal{H}}$. This can be easily understood realising that the difference between the two Hamiltonians is that \mathcal{H}^* contains fast, non-resonant angles, which, up to first order in the small parameter m_{pl} , have simply been averaged out in $\bar{\mathcal{H}}$; therefore, as long as the $\mathcal{O}(m_{\text{pl}}^2)$ contributions

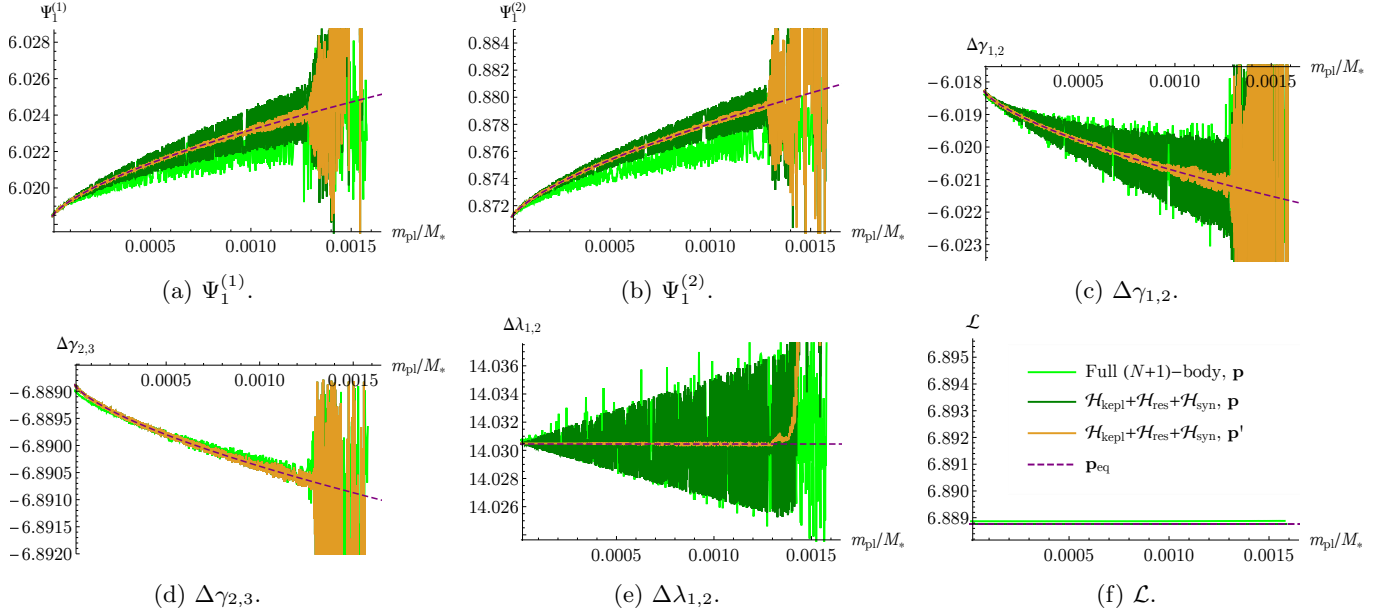


Figure 5.7: Panels (a) to (e) show in dark green the evolution of the actions $\mathbf{p} = (\Psi_1^{(1)}, \Psi_1^{(2)}, \Delta\gamma_{1,2}, \Delta\gamma_{2,3}, \Delta\lambda_{1,2})$ for the system $\mathcal{H}^* = \mathcal{H}_{\text{kepl}} + \mathcal{H}_{\text{res}} + \mathcal{H}_{\text{syn}}$ with the same initial condition as the $(N+1)$ -body integration of Figure 5.5b (the evolution of these variables in the $(N+1)$ -body integration is also shown here in light green for reference). The system follows on average the purple dashed lines, which correspond to the equilibria \mathbf{p}_{eq} for the system $\bar{\mathcal{H}} = \mathcal{H}_{\text{kepl}} + \mathcal{H}_{\text{res}}$. In orange we show the evolution of the averaged variables \mathbf{p}' calculated through analytical averaging of the fast synodic frequencies, Equation (5.31). Note that, for $m_{\text{pl}} < 1.28 \times 10^{-3}$, \mathbf{p}' has very little oscillation around the \mathbf{p}_{eq} curve, compared to the \mathbf{p} evolution. Instead, for $m_{\text{pl}} > 1.28 \times 10^{-3}$, the amplitude of oscillations of \mathbf{p}' and \mathbf{p} around \mathbf{p}_{eq} are almost the same. This reveals that, while the initial oscillation of \mathbf{p} is entirely due to the synodic terms and is effectively removed by passing to the \mathbf{p}' variables, it is then dominated by an increased amplitude of libration in the resonance. The evolution of the angular momentum \mathcal{L} is also shown in panel (f), and it is of course a conserved quantity; panel (f) also contains the legend for all panels in this figure.

are unimportant, the only difference between the two evolutions are the short-periodic, $\mathcal{O}(m_{\text{pl}})$ oscillations due to the $\delta\lambda_{1,2}$ synodic angle. We will actually study this effect analytically below. However, as soon as the $\mathcal{O}(m_{\text{pl}}^2)$ remainder introduces important contributions to the dynamics, as in the case of the emergence of a secondary resonance, the dynamics described by the averaged $\bar{\mathcal{H}}$ approximation is not valid anymore. This is indeed what we see in Figure 5.7, where a phenomenon similar to the one observed in the $(N+1)$ -body integrations appears, and at roughly the same value of $m_{\text{pl}}/M_* \simeq 1.28 \times 10^{-3}$, which was not found in $\bar{\mathcal{H}}$. Notice that such a secondary resonance cannot be caused by an interaction of the resonant degrees of freedom $\bar{\mathbf{x}}$ only, as we have shown that these are stable for all values of m_{pl} . Therefore, these secondary resonances must come from an interaction between some (combination) of the four resonant degrees of freedom and the synodic degree of freedom $(\Delta\lambda_{1,2}, \delta\lambda_{1,2})$. In the following, we use the analytical tools of the Lie series that we presented in Subsect. 2.3.1 in order to pinpoint the relevant secondary resonances that arise at order 2 in the planetary mass m_{pl} . We carry out the calculation for the case of three resonant planets in any resonant chain order to get the general picture, but we will focus on the case of $k^{(1)} = k^{(2)} = k$, and $k = 3$ when needed.

5.3.5.1 Eliminating the $\mathcal{O}(m_{\text{pl}})$ synodic term

The first step is to find a canonical transformation, that to first order in m_{pl} , eliminates the synodic contribution $m_{\text{pl}}\mathcal{H}_{\text{syn}}'$ from \mathcal{H}^* . This will introduce $\mathcal{O}(m_{\text{pl}}^2)$ terms that we want to calculate explicitly, since they contain harmonics mixing $\bar{\mathbf{q}}$ and $\delta\lambda_{1,2}$, potentially associated to secondary resonances.

As we explained in Subsect. 2.3.1, to eliminate $m_{\text{pl}}\mathcal{H}_{\text{syn}}'$ at $\mathcal{O}(m_{\text{pl}})$, we need to find a generating function χ_{syn} that solves the homological equation

$$\{\chi_{\text{syn}}, \mathcal{H}_{\text{kepl}}\} + \mathcal{H}_{\text{syn}} = 0. \quad (5.22)$$

Clearly χ_{syn} will be of order m_{pl} so we can write $\chi_{\text{syn}} = m_{\text{pl}}\chi_{\text{syn}}'$. From the expression for \mathcal{H}_{syn} , Equation (5.14c),

we see that χ_{syn} will have the form

$$\chi_{\text{syn}} = m_{\text{pl}} \left[\frac{C_1}{\eta_1} \sin(\delta\lambda_{12}) + \frac{C_2}{\eta_2} \sin \left(\frac{1}{k^{(2)}} ((k^{(1)} - 1)\delta\lambda_{12} + \psi_1^{(1)} - \psi_1^{(2)} - \delta\gamma_{1,2}) \right) \right], \quad (5.23)$$

where the divisors η_1 and η_2 are immediately found in terms of the frequencies (5.15) of the unperturbed Keplerian Hamiltonian and the combination of angles appearing in the harmonics in \mathcal{H}_{syn} , yielding

$$\begin{aligned} \eta_1 &= \eta_{\Delta\lambda_{1,2}}, \\ \eta_2 &= \frac{1}{k^{(2)}} \left((k^{(1)} - 1)\eta_{\Delta\lambda_{1,2}} + \eta_{\Psi_1^{(1)}} - \eta_{\Psi_1^{(2)}} \right). \end{aligned} \quad (5.24)$$

These divisors are not vanishing nor small, since clearly $\eta_1 = n_1 - n_2$, $\eta_2 = n_2 - n_3$ (remember that n_i is the mean motion frequency of planet i and that the harmonics in \mathcal{H}_{syn} in the modified Delaunay variables were simply $\lambda_1 - \lambda_2$ and $\lambda_2 - \lambda_3$) and the planets are evidently far from the 1:1 resonance. Therefore equation (5.22) can indeed be solved.

Having calculated χ_{syn} , we can then write out how the Hamiltonian \mathcal{H}^* transforms under the Lie series transformation generated by χ_{syn} . By (2.110), the new Hamiltonian \mathcal{H}' reads, up to $\mathcal{O}(m_{\text{pl}}^2)$,

$$\mathcal{H}' = \boxed{\mathcal{H}_{\text{kepl}}|_{\mathbf{x}'}} + m_{\text{pl}} \{ \mathcal{H}_{\text{kepl}}, \chi_{\text{syn}}' \}|_{\mathbf{x}'} + \frac{m_{\text{pl}}^2}{2} \{ \{ \mathcal{H}_{\text{kepl}}, \chi_{\text{syn}}' \}, \chi_{\text{syn}}' \}|_{\mathbf{x}'} + \dots \quad (5.25a)$$

$$\boxed{+ m_{\text{pl}} \mathcal{H}_{\text{res}}'|_{\mathbf{x}'}} \quad + m_{\text{pl}}^2 \{ \mathcal{H}_{\text{res}}', \chi_{\text{syn}}' \}|_{\mathbf{x}'} + \dots \quad (5.25b)$$

$$+ m_{\text{pl}} \mathcal{H}_{\text{syn}}'|_{\mathbf{x}'} \quad + m_{\text{pl}}^2 \{ \mathcal{H}_{\text{syn}}', \chi_{\text{syn}}' \}|_{\mathbf{x}'} + \dots \quad (5.25c)$$

where as in Subsect. 2.3.1 the notation $F|_{\mathbf{x}'}$ means that we take the function $F: \mathbf{x} = (\mathbf{p}, \mathbf{q}) \mapsto F(\mathbf{x}) = F(\mathbf{p}, \mathbf{q})$ and we simply rename the variables $\mathbf{x} \rightarrow \mathbf{x}'$. Here, \mathbf{x}' are the new variables, given by $\mathbf{x} = \exp(L_{\chi_{\text{syn}}})\mathbf{x}'$ (cfr. Equation (2.108)), as detailed below (Equations (5.30) and (5.31)). We note that the boxed terms are simply

$$[\mathcal{H}_0 + m_{\text{pl}} \mathcal{H}_{\text{res}}']|_{\mathbf{x}'} =: \bar{\mathcal{H}}|_{\mathbf{x}'}, \quad (5.26)$$

that is $\bar{\mathcal{H}}$ written in the new variables \mathbf{x}' via direct substitution. Recall that $\bar{\mathcal{H}}$ does not depend on $\delta\lambda_{1,2}$ and so $\Delta\lambda_{1,2}$ was a first integral; hence only the ‘‘averaged variables’’ $\bar{\mathbf{x}}' = (\Psi_1^{(1)'}, \Psi_1^{(2)'}, \Delta\gamma_{1,2}', \Delta\gamma_{2,3}', \psi_1^{(1)'}, \psi_1^{(2)'}, \delta\gamma_{1,2}', \delta\gamma_{2,3}')$ remain (as in Subsect. 5.3.4, we use a barred notation $\bar{\mathbf{x}}' = (\bar{\mathbf{p}}', \bar{\mathbf{q}}')$ for the purely resonant variables, the subset of $\bar{\mathbf{x}}'$ not including $(\Delta\lambda'_{1,2}, \delta\lambda'_{1,2})$). Concerning the remaining two $\mathcal{O}(m_{\text{pl}})$ terms in (5.25), these actually cancel out by construction, since χ_{syn} was chosen to satisfy (5.22). We can, therefore, write the transformed Hamiltonian as

$$\mathcal{H}' = \underbrace{\boxed{\mathcal{H}_{\text{kepl}}|_{\mathbf{x}'} + m_{\text{pl}} \mathcal{H}_{\text{res}}'|_{\mathbf{x}'}}}_{\bar{\mathcal{H}}|_{\mathbf{x}'}, \mathcal{O}(m_{\text{pl}})} + \mathcal{O}(m_{\text{pl}}^2): \quad (5.27)$$

this equation shows accurately that $\bar{\mathcal{H}}$ approximates \mathcal{H}' to first order in m_{pl} , and validates the fact that as m_{pl} increases the dynamics of the variables $\bar{\mathbf{p}}' = (\Psi_1^{(1)'}, \Psi_1^{(2)'}, \Delta\gamma_{1,2}', \Delta\gamma_{2,3}')$ closely follows the equilibrium points $\bar{\mathbf{p}}_{\text{eq}}$ calculated from $\bar{\mathcal{H}}$ in Subsection 5.3.4 (i.e. has oscillations around $\bar{\mathbf{p}}_{\text{eq}}$ of order $\mathcal{O}(m_{\text{pl}}^2)$, while the oscillations of $\bar{\mathbf{p}}$ are $\mathcal{O}(m_{\text{pl}})$) while $\Delta\lambda'_{1,2}$ undergoes oscillations of $\mathcal{O}(m_{\text{pl}}^2)$ around the initial value $\overline{\Delta\lambda_{1,2}}$ (again a conserved quantity in the purely averaged model $\bar{\mathcal{H}}$). This is what we observe in the numerical simulations, Figure 5.7. We can therefore simplify the calculation by writing

$$\chi_{\text{syn}}' = \underbrace{\chi_{\text{syn}}'(\bar{\mathbf{p}}' = \bar{\mathbf{p}}_{\text{eq}}; \mathcal{L}, \Delta\lambda'_{1,2} = \overline{\Delta\lambda_{1,2}})}_{\bar{\chi}'_{\text{syn}}} + \mathcal{O}(|(\bar{\mathbf{p}}' - \bar{\mathbf{p}}_{\text{eq}}, \Delta\lambda_{1,2}' - \overline{\Delta\lambda_{1,2}})|), \quad (5.28)$$

where we called $\bar{\chi}'_{\text{syn}}$ the first term of the last equation, and dropping the higher order terms, which correspond to small deviations from $\bar{\mathbf{p}}' = \bar{\mathbf{p}}_{\text{eq}}$ and from the initial value $\overline{\Delta\lambda_{1,2}}$ of $\Delta\lambda'_{1,2}$. With this approximation we can eliminate the term $m_{\text{pl}}^2 \{ \mathcal{H}_{\text{syn}}', \bar{\chi}'_{\text{syn}} \}$ in (5.25c) because now $\frac{\partial \mathcal{H}_{\text{syn}}'}{\partial \mathbf{p}} = \frac{\partial \bar{\chi}'_{\text{syn}}}{\partial \mathbf{p}} = 0$ so $\{ \mathcal{H}_{\text{syn}}', \bar{\chi}'_{\text{syn}} \} = \frac{\partial \mathcal{H}_{\text{syn}}'}{\partial \mathbf{q}} \frac{\partial \bar{\chi}'_{\text{syn}}}{\partial \mathbf{p}} - \frac{\partial \mathcal{H}_{\text{syn}}'}{\partial \mathbf{p}} \frac{\partial \bar{\chi}'_{\text{syn}}}{\partial \mathbf{q}} = 0$ (of course, by the same reasoning, also the higher order terms of the Lie series for $\exp(L_{\bar{\chi}'_{\text{syn}}})\mathcal{H}_{\text{syn}}$ cancel out). The resulting Hamiltonian becomes

$$\mathcal{H}' = \underbrace{\boxed{\mathcal{H}_{\text{kepl}}|_{\mathbf{x}'} + m_{\text{pl}} \mathcal{H}_{\text{res}}'|_{\mathbf{x}'}}}_{\bar{\mathcal{H}}|_{\mathbf{x}'}, \mathcal{O}(m_{\text{pl}})} + \underbrace{\left[\frac{m_{\text{pl}}^2}{2} \{ \{ \mathcal{H}_{\text{kepl}}, \bar{\chi}'_{\text{syn}} \}, \bar{\chi}'_{\text{syn}} \}|_{\mathbf{x}'} + m_{\text{pl}}^2 \{ \mathcal{H}_{\text{res}}', \bar{\chi}'_{\text{syn}} \}|_{\mathbf{x}'} \right]}_{\mathcal{O}(m_{\text{pl}}^2)} + \dots \quad (5.29)$$

We now explicit the transformation that to $\mathcal{O}(m_{\text{pl}})$ eliminates the fast synodic evolution in the numerical integrations. This is given by

$$\begin{aligned}\mathbf{p} &= \exp(L_{\bar{\chi}_{\text{syn}}})\mathbf{p}' = \mathbf{p}' + m_{\text{pl}}\{\mathbf{p}', \bar{\chi}'_{\text{syn}}\} + \mathcal{O}(m_{\text{pl}}^2) = \mathbf{p}' - m_{\text{pl}}\frac{\partial \bar{\chi}'_{\text{syn}}}{\partial \mathbf{q}'} + \mathcal{O}(m_{\text{pl}}^2), \\ \mathbf{q} &= \exp(L_{\bar{\chi}_{\text{syn}}})\mathbf{q}' = \mathbf{q}'.\end{aligned}\tag{5.30}$$

Notice that the angles remain unchanged since $\bar{\chi}_{\text{syn}}$ is independent of the actions, so $\frac{\partial \bar{\chi}'_{\text{syn}}}{\partial \mathbf{p}'} = 0$. The transformation for the actions reads, to first order in m_{pl} :

$$\begin{aligned}\Psi_1^{(1)} &= \Psi_1^{(1)'} - m_{\text{pl}}\frac{1}{k^{(2)}}\frac{C_2}{\bar{\eta}_2}\cos\left(\frac{1}{k^{(2)}}((k^{(1)} - 1)\delta\lambda_{1,2} + \psi_1^{(1)} - \psi_1^{(2)} - \delta\gamma_{1,2})\right), \\ \Psi_1^{(2)} &= \Psi_1^{(2)'} + m_{\text{pl}}\frac{1}{k^{(2)}}\frac{C_2}{\bar{\eta}_2}\cos\left(\frac{1}{k^{(2)}}((k^{(1)} - 1)\delta\lambda_{1,2} + \psi_1^{(1)} - \psi_1^{(2)} - \delta\gamma_{1,2})\right), \\ \Delta\gamma_{1,2} &= \Delta\gamma'_{1,2} + m_{\text{pl}}\frac{1}{k^{(2)}}\frac{C_2}{\bar{\eta}_2}\cos\left(\frac{1}{k^{(2)}}((k^{(1)} - 1)\delta\lambda_{1,2} + \psi_1^{(1)} - \psi_1^{(2)} - \delta\gamma_{1,2})\right), \\ \Delta\gamma_{2,3} &= \Delta\gamma'_{2,3}, \\ \Delta\lambda_{1,2} &= \Delta\lambda'_{1,2} - m_{\text{pl}}\left[\frac{C_1}{\bar{\eta}_1}\cos(\delta\lambda_{1,2}) + \frac{k^{(1)} - 1}{k^{(2)}}\frac{C_2}{\bar{\eta}_2}\cos\left(\frac{1}{k^{(2)}}((k^{(1)} - 1)\delta\lambda_{1,2} + \psi_1^{(1)} - \psi_1^{(2)} - \delta\gamma_{1,2})\right)\right],\end{aligned}\tag{5.31}$$

where $\bar{\eta}_1$ and $\bar{\eta}_2$ are the frequencies (5.24) evaluated at the reference values for the actions at each m_{pl} . We can invert these expressions to obtain \mathbf{p}' from (\mathbf{p}, \mathbf{q}) , and the evolution of \mathbf{p}' represents that of \mathbf{p} where to first order in m_{pl} the short periodic have been averaged out. The evolution of \mathbf{p}' is shown in orange in Figure 5.7 in our reference $N = 3, k = 3$ example, where we see that the averaged evolution follows closely the analytical calculation of the equilibrium points of \mathcal{H} for different planetary masses.

This is however only valid until a point in which the $\mathcal{O}(m_{\text{pl}}^2)$ contribution, which is still present in (5.29), has a non-negligible effect. Indeed, recall from Subsect. 2.3.1 that these terms are expected to contain higher-order harmonics which were not present in the original Hamiltonian $\mathcal{H}^* = \mathcal{H}_{\text{kepl}} + \mathcal{H}_{\text{res}} + \mathcal{H}_{\text{syn}}$: then, if these newly introduced $\mathcal{O}(m_{\text{pl}}^2)$ Hamiltonian terms contains angles which, for certain values of m_{pl} , have a vanishing or small enough frequency, they could not be eliminated by a further perturbative step because of the problem of small divisors, and may indeed change the dynamics considerably. We therefore proceed to analyse these terms below.

5.3.5.2 The $\mathcal{O}(m_{\text{pl}}^2)$ contribution

In this subsection, we look closely at the $\mathcal{O}(m_{\text{pl}}^2)$ terms in (5.29). We are specifically interested in the harmonics that they contain, to find explicitly which combinations of angles $\bar{\mathbf{q}}' = (\psi_1^{(1)'}, \psi_1^{(2)'}, \delta\gamma_{1,2}', \delta\gamma_{2,3}')$ and $\delta\lambda'_{1,2}$ can give rise to secondary resonances at values of the planetary masses close to those where the increase in amplitude of libration is observed in the numerical integrations. Since the synodic frequency of $\delta\lambda'_{1,2}$ is much higher than the libration frequencies characteristic of the angles $\bar{\mathbf{q}}'$, the most interesting harmonics are the ones where the lowest fraction of $\delta\lambda'_{1,2}$ appears next to a combinations of $\bar{\mathbf{q}}'$. This is because these are the harmonic terms that will be linked to the secondary resonances that appear at lowest resonant libration frequencies, that is, by Figure 5.6 panels (e) and (f), at lowest planetary mass. The following calculation is clearly general, but to simplify matters we will quickly specialise to the case of a chain of three planets with both pairs in the same resonance, $k^{(1)} = k^{(2)} = k$, as well as to the reference case $k = 3$ for which the numerical integrations in Figure 5.5 were performed.

We start with the main term $\{\{\mathcal{H}_{\text{kepl}}, \bar{\chi}'_{\text{syn}}\}, \bar{\chi}'_{\text{syn}}\}$ of order m_{pl}^2 in (5.29). Since $\mathcal{H}_{\text{kepl}}$ does not contain any angles, all secondary resonance contributions must come from combinations of the harmonics contained in $\bar{\chi}'_{\text{syn}}$. Recall that we defined $\bar{\chi}'_{\text{syn}}$ containing both synodic terms with harmonics $\lambda_1 - \lambda_2$ and $\lambda_2 - \lambda_3$, which we wrote in Equation (5.13) in terms of the new variables q . Therefore, the harmonics that are included in $\{\{\mathcal{H}_{\text{kepl}}, \bar{\chi}'_{\text{syn}}\}, \bar{\chi}'_{\text{syn}}\}$ are combinations of these synodic harmonics; more specifically, they come from the products of their cosines⁸.

⁸ This can be easily understood noting that if $\chi = \sin(q_1) + \sin(q_2)$ and f depends only on the actions p_i then

$$\{\{f, \chi\}, \chi\} = \frac{\partial^2 f}{\partial p_1^2} \cos^2 q_1 + 2\frac{\partial^2 f}{\partial p_1 \partial p_2} \cos q_1 \cos q_2 + \frac{\partial^2 f}{\partial p_2^2} \cos^2 q_2.$$

Using the standard trigonometric identity $\cos(a)\cos(b) = \frac{1}{2}(\cos(a-b) + \cos(a+b))$, the resulting harmonics are

$$\begin{aligned}
& 2\delta\lambda'_{1,2}, \\
& ((k^{(2)} + k^{(1)} - 1)\delta\lambda'_{1,2} + \psi_1^{(1)'} - \psi_1^{(2)'} - \delta\gamma'_{1,2})/k^{(2)}, \\
& ((k^{(2)} - k^{(1)} + 1)\delta\lambda'_{1,2} - \psi_1^{(1)'} + \psi_1^{(2)'} + \delta\gamma'_{1,2})/k^{(2)}, \\
& 2((k^{(1)} - 1)\delta\lambda'_{1,2} + \psi_1^{(1)'} - \psi_1^{(2)'} - \delta\gamma'_{1,2})/k^{(2)},
\end{aligned} \tag{5.32}$$

so the harmonic with the lowest fraction of $\delta\lambda'_{1,2}$ is $((k^{(2)} - k^{(1)} + 1)\delta\lambda'_{1,2} - \psi_1^{(1)'} + \psi_1^{(2)'} + \delta\gamma'_{1,2})/k^{(2)}$. Specialising now to the case of a chain with the same resonance index $k^{(1)} = k^{(2)} = k$, this simply gives

$$\frac{1}{k} \left(\delta\lambda'_{1,2} - \psi_1^{(1)'} + \psi_1^{(2)'} + \delta\gamma'_{1,2} \right). \tag{5.33}$$

With the aid of an algebraic manipulator one can compute the full expression of $\{\{\mathcal{H}_{\text{kepl}}, \bar{\chi}'_{\text{syn}}\}, \bar{\chi}'_{\text{syn}}\}$ and select the desired harmonic term (we used the software package Wolfram Mathematica, see Appendix C for useful codes in the Mathematica language), thus obtaining its coefficient (actually, one can see that this term emerges solely from the term $\propto \{1/\Lambda_2^2, \bar{\chi}'_{\text{syn}}\}, \bar{\chi}'_{\text{syn}}\}$). We avoid writing here the full expression, which is rather cumbersome, moreover as in (5.29) we evaluate it at the reference values of the actions so the term multiplying the cosine becomes a numerical coefficient, and we write this term as

$$\mathcal{H}_{\text{sec.res.kepl}} = \text{const} \times m_{\text{pl}}^2 \cos \left((\delta\lambda'_{1,2} - \psi_1^{(1)'} + \psi_1^{(2)'} + \delta\gamma'_{1,2})/k \right). \tag{5.34}$$

Since we want to compare the frequency of $\delta\lambda'_{1,2}/k$ to that of $(-\psi_1^{(1)'} + \psi_1^{(2)'} + \delta\gamma'_{1,2})/k$, we need to consider the resonant Hamiltonian $\bar{\mathcal{H}}$ in the \mathbf{x}' variables, expand the “barred” variables $\bar{\mathbf{x}}'$ around the equilibrium point characterised by the equilibrium actions $\bar{\mathbf{p}}_{\text{eq}}$ and the equilibrium angles $\bar{\mathbf{q}}_{\text{eq}}$ (Equation (5.16)) as in Subsect. 5.3.4, and then introduce the transformation $\bar{\mathbf{x}}' \rightarrow (I_l, \phi_l)_{l=1,\dots,4}$ to the action-angle variables $(\mathbf{I}, \boldsymbol{\phi})$, which transforms $\bar{\mathcal{H}}$ into the sum of decoupled harmonic oscillators plus higher order terms, Equation (5.18). It is also useful to translate the value of $\Delta\lambda'_{1,2}$ around its initial reference value $\overline{\Delta\lambda_{1,2}}$ introducing $\Delta\lambda'_{1,2} = \overline{\Delta\lambda_{1,2}} + \delta\Delta\lambda'_{1,2}$ which is clearly a canonical transformation. Therefore, we write $\mathcal{H}_{\text{sec.res.kepl}}$ in terms of the variables $(\mathbf{I}, \delta\Delta\lambda'_{1,2}, \boldsymbol{\phi}, \delta\lambda'_{1,2})$. The Hamiltonian $\mathcal{H}_{\text{sec.res.kepl}}$ will now contain harmonic terms of type

$$\left\{ \begin{array}{l} \sin \\ \cos \end{array} \right\} (\delta\lambda'_{1,2}/k + \mathbf{h} \cdot \boldsymbol{\phi}), \tag{5.35}$$

where $\mathbf{h} \cdot \boldsymbol{\phi}$ is an integer combination with coefficients $h_1, \dots, h_4 \in \mathbb{Z}$ of the angles ϕ_1, \dots, ϕ_4 , which we can calculate explicitly. Therefore, whenever $\frac{d}{dt}(\delta\lambda'_{1,2}/k) = -\frac{d}{dt}(\mathbf{h} \cdot \boldsymbol{\phi})$ a secondary resonance is crossed. We can rewrite this expression as $\delta\lambda'_{1,2}/k + \mathbf{h} \cdot \boldsymbol{\omega} = 0$. Since the Hamiltonian has d’Alembert characteristics in each pair (I_l, ϕ_l) , and the values of the actions \mathbf{I} are initially (that is, before their excitation) small, the strongest secondary resonances will come from lowest integer combinations $\mathbf{h} \cdot \boldsymbol{\phi}$, that is, where most h_l are zero. We also note that since $\delta\lambda'_{1,2} > 0$ and the frequencies ω_l are all negative, a secondary resonance term can only appear when $\mathbf{h} \cdot \boldsymbol{\omega} < 0$, which together with the requirement that $|\mathbf{h}|$ be small is tantamount to requiring that all non-zero integers h_l are positive. Since we calculated $\omega(m_{\text{pl}})$ in Subsect. 5.3.4, we can calculate for each \mathbf{h} the relative frequency $(\delta\lambda'_{1,2}/k + \mathbf{h} \cdot \boldsymbol{\omega})(m_{\text{pl}})$ as a function of m_{pl} , and check if any of these vanish, which corresponds to crossing a secondary resonance.

We carried out the calculation with the aid of the Mathematica software in the reference case $k = 3$ and $a_1 \simeq 0.1$, which corresponds to the evolution shown in Figure 5.5b (and also Figures 5.6 and 5.7). We found that $\mathcal{H}_{\text{sec.res.kepl}}$ contains, among many others, the following terms

$$1.24 \times m_{\text{pl}}^2 \sqrt{2I_1} \left\{ \begin{array}{l} \sin \\ \cos \end{array} \right\} (\delta\lambda'_{1,2}/3 + \phi_1 + \text{phase}), \tag{5.36a}$$

$$0.27 \times m_{\text{pl}}^2 (2I_2) \left\{ \begin{array}{l} \sin \\ \cos \end{array} \right\} (\delta\lambda'_{1,2}/3 + 2\phi_2 + \text{phase}), \tag{5.36b}$$

$$2.39 \times 10^{-3} \times m_{\text{pl}}^2 \sqrt{2I_1} \sqrt{2I_3} \left\{ \begin{array}{l} \sin \\ \cos \end{array} \right\} (\delta\lambda'_{1,2}/3 + \phi_1 + \phi_3 + \text{phase}), \tag{5.36c}$$

$$1.6 \times m_{\text{pl}}^2 \sqrt{2I_1} \sqrt{2I_4} \left\{ \begin{array}{l} \sin \\ \cos \end{array} \right\} (\delta\lambda'_{1,2}/3 + \phi_1 + \phi_4 + \text{phase}). \tag{5.36d}$$

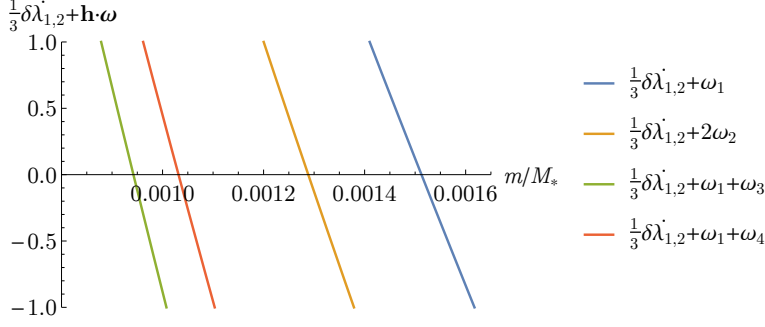


Figure 5.8: Frequencies of the angles $\delta\lambda'_{1,2}/3 + \mathbf{h} \cdot \boldsymbol{\phi}$ as a function of the planetary mass in the case of the 3:2 – 3:2 mean motion resonance chain with $a_1 \simeq 0.1$ (the situation depicted in Figure 5.5b). Notice that the synodic frequency $\delta\lambda'_{1,2}$ varies only slightly due to the change in the equilibrium point $\bar{\mathbf{x}}_{\text{eq}}$ for the averaged Hamiltonian $\bar{\mathcal{H}}$, which is followed by the full system \mathcal{H}' until the second order effects become significant (cfr. Equation (5.29)). The main change comes from the resonant frequencies $\boldsymbol{\omega}$, whose dependence on the planetary mass is depicted in Figure 5.6e. The result is that the frequencies $(\delta\lambda'_{1,2}/k + \mathbf{h} \cdot \boldsymbol{\omega})(m_{\text{pl}})$ vanish within a small range of values of the planetary mass m_{pl} , meaning that a capture into a secondary resonance becomes possible. By comparing with Figure 5.5b, we see that $\delta\lambda'_{1,2}/3 + 2\phi_2$ has vanishing frequency at the same value of $m_{\text{pl}} \simeq 1.28 \times 10^{-3}$ at which the excitation of the system occurs.

The nature of these harmonics is clearly general, while the numerical coefficients are specific to the reference case $k = 3$ and $a_1 \simeq 0.1$ mentioned above. We then calculated for each of the harmonics in (5.36) their frequency $(\delta\lambda'_{1,2}/k + \mathbf{h} \cdot \boldsymbol{\omega})(m_{\text{pl}})$ as a function of the mass. The results are presented in Figure 5.8.

We immediately remark that in the case of the harmonic $\delta\lambda'_{1,2}/3 + 2\phi_2$, the crossing of the secondary resonance happens precisely at the value of planetary mass $m_{\text{pl}}/M_* \simeq 1.28 \times 10^{-3}$ where the numerical integrations showed the increase in amplitude of libration, Figure 5.5. This is evidence that this phenomenon was indeed caused by the crossing of this secondary resonance.

Before we continue with an analytical description of the dynamics caused by this resonance, we should however go back and discuss a few technical details.

Firstly, if we had used in \mathcal{H}_{syn} only one synodic term, not all of the the harmonics in (5.32) would appear⁹. In particular, the harmonic $\delta\lambda'_{1,2}/3 + 2\phi_2$ would not appear, so that the observed dynamical effects linked to the crossing of secondary resonances at $m_{\text{pl}} \simeq 1.28 \times 10^{-3}$ are not expected. Indeed, we performed similar RK4 numerical integrations with only one of the synodic terms, $\lambda_1 - \lambda_2$ and separately $\lambda_2 - \lambda_3$, which are shown in Figure 5.9, and there is no effect at the right value of m_{pl} . Secondary resonances do occur, but at larger values of m_{pl} , given that the generated harmonics have a larger coefficient for $\delta\lambda'_{1,2}$.

Secondly, so far we have not considered the $\mathcal{O}(m_{\text{pl}}^2)$ term $\{\mathcal{H}'_{\text{res}}, \bar{\chi}'_{\text{syn}}\}$, which is also present in (5.29). However,

⁹To see this, as in footnote 8 we calculate for $\chi = \sin(q_1)$ and f which depends on the actions only,

$$\{\{f, \chi\}, \chi\} = \frac{\partial^2 f}{\partial p_1^2} \cos^2 q_1 = \frac{1}{2} \frac{\partial^2 f}{\partial p_1^2} (1 + \cos(2q_1)).$$

Clearly we do not obtain the needed $((k^{(2)} - k^{(1)} + 1)\delta\lambda'_{1,2} - \psi_1^{(1)'} + \psi_1^{(2)'} + \delta\gamma'_{1,2})/k^{(2)}$ in (5.32) neither when $q_1 = \lambda_1 - \lambda_2 = \delta\lambda_{1,2}$ nor when $q_1 = \lambda_2 - \lambda_3 = \frac{1}{k^{(2)}}((k^{(1)} - 1)\delta\lambda_{1,2} + \psi_1^{(1)} - \psi_1^{(2)} - \delta\gamma_{1,2})$.

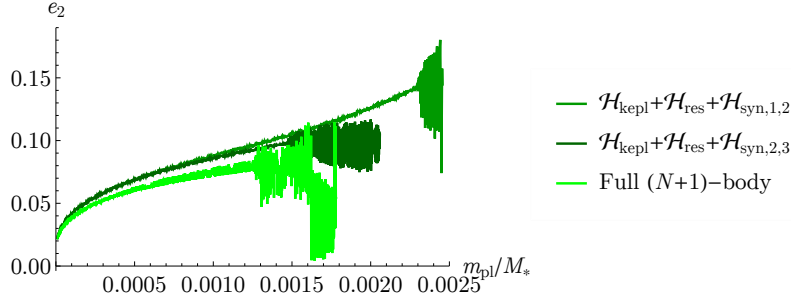


Figure 5.9: Comparison between the full $(N + 1)$ -body simulation from Figure 5.5b (lightest green) and two RK4 simulations with the same initial conditions where only one of the two synodic terms $\lambda_1 - \lambda_2$ and $\lambda_2 - \lambda_3$ appears (two darker shades of green). These two semi-synodic simulations initially appear identical, which is easily understood from the fact that they follow in average the evolution of $\bar{\mathcal{H}} = \mathcal{H}_{\text{kepl}} + \mathcal{H}_{\text{res}}$ which is the same for the two (cfr. Equation (5.27)). The important point is that in both cases, when only one synodic angle is considered, the system is not excited at value of $m_{\text{pl}} \simeq 1.28 \times 10^{-3}$, where it is excited in the $(N + 1)$ -body simulation as well as in the RK4 simulation which includes both synodic terms, see Figure 5.5b. This shows that both synodic terms must be included in order to have a good quantitative agreement with the $(N + 1)$ -body simulations.

with the same technique as above one can see that this term only yields harmonics of type

$$\begin{aligned}
& \delta\lambda'_{1,2} \pm \psi_1^{(1)'}, \\
& \delta\lambda'_{1,2} \pm \psi_1^{(2)'}, \\
& \pm \delta\lambda'_{1,2} - \psi_1^{(1)'} + \delta\gamma'_{1,2}, \\
& \left((k^{(1)} - 1)\delta\lambda'_{1,2} - (\pm k^{(2)} - 1)\psi_1^{(1)'} - \psi_1^{(2)'} + (\pm k^{(2)} - 1)\delta\gamma'_{1,2} \right) / k^{(2)}, \\
& \left((k^{(1)} - 1)\delta\lambda'_{1,2} + \psi_1^{(1)'} - (\pm k^{(2)} + 1)\psi_1^{(2)'} - \delta\gamma'_{1,2} \right) / k^{(2)}, \\
& \left((k^{(1)} - 1)\delta\lambda'_{1,2} + \psi_1^{(1)'} - (\pm k^{(2)} + 1)\psi_1^{(2)'} - \delta\gamma'_{1,2} \pm k^{(2)}\delta\gamma'_{2,3} \right) / k^{(2)}.
\end{aligned} \tag{5.37}$$

Whenever $k^{(1)} \geq 3$, as in our reference case $k^{(1)} = k^{(2)} = k = 3$, this does not contribute the needed harmonic (5.33) with $\delta\lambda_{1,2}$ appearing as a single $\delta\lambda_{1,2}/k$, it will only include multiples of $\delta\lambda_{1,2}/k$ and therefore to lowest order does not contribute to the secondary resonance harmonics in (5.36).

Finally, in (5.29) we used the simplification $\bar{\mathbf{p}}' = \bar{\mathbf{p}}_{\text{eq}}, \Delta\lambda_{1,2}' - \overline{\Delta\lambda_{1,2}}$ to define $\bar{\chi}'_{\text{syn}}$ (cfr. Equation (5.28)). However, the remaining terms of $\mathcal{O}(|(\bar{\mathbf{p}}' - \bar{\mathbf{p}}_{\text{eq}}, \Delta\lambda_{1,2}' - \overline{\Delta\lambda_{1,2}})|)$ do not contribute to the dynamics to lowest order. Indeed, concerning $m_{\text{pl}} \{\mathcal{H}_0, \chi\}_{|\mathbf{x}'}$, this term only contains the two separate synodic harmonics already contained in χ and therefore does not yield terms linked to secondary resonances. Finally, the remaining terms in $\frac{m_{\text{pl}}^2}{2} \{\{\mathcal{H}_{\text{kepl}}, \chi_{\text{syn}}'\}, \chi_{\text{syn}}'\}_{|\mathbf{x}'}$ will only yield higher order terms in the actions \mathbf{I} , so we can neglect them (recall that initially the values of the actions are small since we are close to the equilibrium point).

With these clarifications, we can proceed with the model of the secondary resonance linked to the angle $\delta\lambda'_{1,2}/3 + 2\phi_2$, which, as we discussed above, has vanishing frequency exactly at the value of m_{pl} when the increase in the amplitude of libration is observed in Figure 5.5b. This realisation is further supported by Figure 5.10. There, we plot the evolution of the actions I_l , $l = 1, \dots, 4$ along the simulation, with the planetary mass m_{pl} on the horizontal axis. We see that initially only one action is excited, namely I_2 , and after that the nonlinearities inherent in the system cause an exchange of energy between the degrees of freedom. This also suggests that the model that we are about to construct, which is valid only for small \mathbf{I} 's, breaks down whenever one of the actions is excited. This however presents no impediment in the description of the first phase, when the secondary resonance is encountered. One question that we wish to answer for example is whether or not there is or can be a capture in this secondary resonance or rather a jump across resonance. The integrable, low order model that we construct below can indeed answer this question.

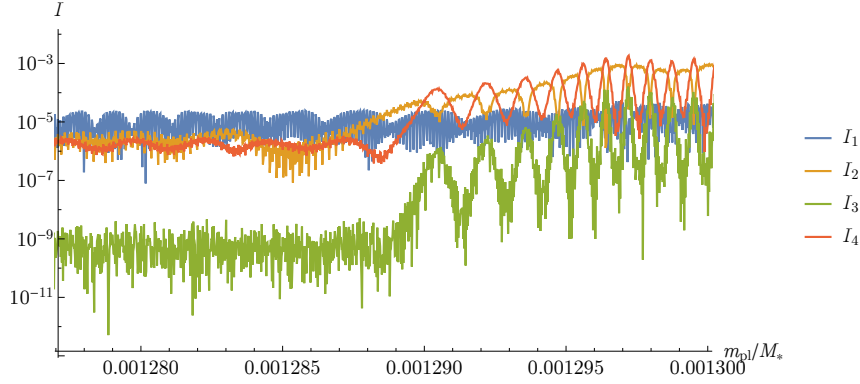


Figure 5.10: Evolution around $m_{\text{pl}} \simeq 1.28 \times 10^{-3}$ of the actions I_l , $l = 1, \dots, 4$ along the reference RK4 simulation shown in Figure 5.5b. We see that the actions are initially relatively constant, and the system is well approximated by a Hamiltonian of the form $\sum_{l=1}^4 \omega_l I_l$ (cfr. Equation (5.18)). Then, I_2 increases steadily, symptom of an interaction with a secondary resonance that involves $\Theta = I_2$ as a resonant action (cfr. Subsect. 2.3.3); this is confirmed by the canonical change of coordinates (5.38). Soon after I_2 is large enough, the degrees of freedom start interacting and exchanging energy, due to the non-linear effects

5.3.5.3 Model of the secondary resonance for $\delta\lambda'_{1,2}/3 + 2\phi_2$

In the following we detail how we can construct a model for the resonance associated with the angle $\delta\lambda'_{1,2}/3 + 2\phi_2$ since, as we saw before, it is the one that causes the observed increase in amplitude of libration. A similar approach can be implemented for the other resonances in (5.36).

We start by performing a canonical transformation which selects $\delta\lambda'_{1,2}/3 + 2\phi_2$ as an angle. Notice that, since ϕ_2 appears with a coefficient 2 and so $\sqrt{2I_2}$ appears as a power two in (5.36b), we have a secondary resonance of order 2; hence it is useful to define the resonant angle θ as $2\theta = \delta\lambda'_{1,2}/3 + 2\phi_2$ in order to maintain the d'Alembert characteristics so that the Hamiltonian will not be singular at the origin. The resulting transformation is

$$\begin{aligned}
\Theta &= I_2, & \theta &= \delta\lambda'_{1,2}/6 + \phi_2, \\
I_r^* &= I_r, \quad r = 1, 3, 4, & \phi_r^* &= \phi_r, \quad r = 1, 3, 4, \\
\delta\Delta\lambda_{1,2}^* &= \delta\Delta\lambda'_{1,2} - I_2/6 & \delta\lambda_{1,2}^* &= \delta\lambda'_{1,2},
\end{aligned} \tag{5.38}$$

whose canonicity follows immediately from the preservation of the Poisson brackets. We can already notice that $\Theta = I_2$ appears as the conjugated action to the angle θ associated to the secondary resonance: this explains why in Figure 5.10 it is I_2 which is initially excited. The other variables do not feel the resonance, except $\delta\Delta\lambda'_{1,2}$ which must change according to the change in I_2 in order to maintain $\delta\Delta\lambda_{1,2}^*$ constant; however since I_2 gets divided by 6 this change is minute, but nevertheless clearly visible in Figure 5.7e. The pair (Θ, θ) is the pair of resonant variables for this specific secondary resonance, while the others will have a faster evolution, which can be “averaged” away, in order to yield a 1-d.o.f. system that we write $\langle \mathcal{H}' \rangle_{(\phi^*, \delta\lambda_{1,2}^*)}(\Theta, \theta; \mathbf{I}^*, \delta\Delta\lambda_{1,2}^*)$. The notation $\langle \bullet \rangle_{(\phi^*, \delta\lambda_{1,2}^*)}$ means that we eliminated perturbatively to lowest order the non-secondary-resonant contributions from the angles $(\phi^*, \delta\lambda_{1,2}^*)$ (cfr. Equations (2.116) to (2.118)), and we stressed that the variables $(\mathbf{I}^*, \delta\Delta\lambda_{1,2}^*)$ will only play the role of parameters for $\langle \mathcal{H}' \rangle_{(\phi^*, \delta\lambda_{1,2}^*)}$. Ultimately, the functional form of $\langle \mathcal{H}' \rangle_{(\phi^*, \delta\lambda_{1,2}^*)}(\Theta, \theta)$ will be that of a Andoyer Hamiltonian $\mathcal{H}_{\text{And},2}$ (cfr. (2.56)), that is

$$\langle \mathcal{H}' \rangle_{(\phi^*, \delta\lambda_{1,2}^*)}(\Theta, \theta) = \delta\Theta + \frac{\beta}{2}\Theta^2 + \mathcal{O}(\Theta^3) + c\sqrt{2\Theta^2} \cos(2\theta); \tag{5.39}$$

the coefficient c will be of order m_{pl}^2 , while δ and β will be of order m_{pl} . Since the system is initially close to the resonant equilibrium point, Θ is small and we can drop the $\mathcal{O}(\Theta^3)$ terms. However, as we discussed in Subsect. 2.3.3, the parameter β (the second derivative at $\Theta = 0$) plays a crucial role in determining if there can be capture into the secondary resonance or not, so we must keep track of all $\mathcal{O}(\Theta^2)$ terms of the θ -independent part, the first two terms in (5.39). The main contribution to the θ -independent part comes from the $\bar{\mathcal{H}}$ term (the $\mathcal{O}(m_{\text{pl}})$ term in (5.29)), while $c\sqrt{2\Theta^2} \cos(2\theta)$ comes from (5.36b) and is $\mathcal{O}(m_{\text{pl}}^2)$. Concerning the first part deriving from $\bar{\mathcal{H}}$, we should stress that even if $\delta\Delta\lambda'_{1,2}$ appeared as a constant of motion when this Hamiltonian was treated alone, when

the $\mathcal{O}(m_{\text{pl}}^2)$ is taken into account the transformation (5.38) transforms $\delta\Delta\lambda'_{1,2}$ into $\delta\Delta\lambda_{1,2}^* + \Theta/6$, where $\delta\Delta\lambda_{1,2}^*$ is the new constant of motion. Therefore we must keep $\delta\Delta\lambda'_{1,2}$ as a variable in $\bar{\mathcal{H}}$ and apply (5.38) to it.

As explained in Subsect. 2.3.3, capture into resonance is possible only if $\dot{\delta}\beta < 0$. We already know from Figure 5.8 that, as the planetary mass increases, $\dot{\theta}$ goes from positive values to negative values, that is, that $\dot{\delta} < 0$. Following the reasoning of Subsect. 2.3.3, this means a capture into this secondary resonance is possible only if $\beta > 0$.

To obtain the sign of β in (5.39) we need to compute its value explicitly. We do this in steps as follows. First, we fix a value of m_{pl} right before the observed increase of amplitude of libration, $m_{\text{pl}}/M_* \simeq 1.28 \times 10^{-3}$, we calculate the equilibrium point $\bar{\mathbf{x}}_{\text{eq}} = \bar{\mathbf{x}}_{\text{eq}}(m_{\text{pl}})$ and we apply the canonical diagonalisation procedure as explained in Subsect. 5.3.4. This yields four pairs of cartesian canonical variables $(\boldsymbol{\xi}, \boldsymbol{\eta})$ which replace the $\bar{\mathbf{x}}$: $\bar{\mathbf{x}} = T(\boldsymbol{\xi}, \boldsymbol{\eta})$, with T the diagonalising matrix. Second, as in Subsect. 5.3.4, we introduce canonical polar coordinates $(I_l, \phi_l)_{l=1,\dots,4}$ by $(\xi_l = \sqrt{2I_l} \cos \phi_l, \eta_l = \sqrt{2I_l} \sin \phi_l)$. The Hamiltonian $\bar{\mathcal{H}}$ will then depend on the variables $(I_1, \dots, I_4, \delta\Delta\lambda'_{1,2}, \phi_1, \dots, \phi_4, \delta\lambda'_{1,2})$. Third, we write $\bar{\mathcal{H}}$ in the variables (5.38); $\bar{\mathcal{H}}$ contains a term in Θ^2 independent of the angles, but its coefficient is not β . To obtain the value of β we need to perform a fourth step, and calculate $\langle \bar{\mathcal{H}} \rangle_{(\boldsymbol{\phi}^*, \delta\lambda_{1,2}^*)}$, that is the perturbative elimination in $\bar{\mathcal{H}}$ of all the non-secondary-resonant contributions from the angles $(\boldsymbol{\phi}^*, \delta\lambda_{1,2}^*)$, up to order 2 in Θ . This is because, as detailed below, the elimination of these harmonics can generate terms in Θ^2 independent of the angles, that need to be added to the original term to obtain β . To this end, we take $\bar{\mathcal{H}}(I_1, \dots, I_4, \delta\Delta\lambda'_{1,2}, \phi_1, \dots, \phi_4, \delta\lambda'_{1,2})$ and expand it to order 2 with respect to the actions. Since these terms satisfy the d'Alembert characteristics in $(\mathbf{I}, \boldsymbol{\phi})$, we only obtain terms like

$$c_{\boldsymbol{\alpha}}(\delta\Delta\lambda'_{1,2}) \times \sqrt{2\mathbf{I}}^{\boldsymbol{\alpha}} \cos(\mathbf{m}\boldsymbol{\phi}), \quad m_j = -\alpha_j, -\alpha_j + 2, \dots, \alpha_j - 2, \alpha_j, \quad |\boldsymbol{\alpha}| = 1, 2, 3, 4, \quad (5.40)$$

where $\boldsymbol{\alpha} \in \mathbb{N}_0^4$, $|\boldsymbol{\alpha}| = \alpha_1 + \dots + \alpha_4$ is restricted to $|\boldsymbol{\alpha}|/2 \leq 2$, and $c_{\boldsymbol{\alpha}}(\delta\Delta\lambda'_{1,2})$ is a coefficient which depends on $\delta\Delta\lambda'_{1,2}$ only. These coefficients are expanded around $\delta\Delta\lambda'_{1,2} = 0$ to an optimal order which can be obtained in the following manner. Note that, from $\delta\Delta\lambda'_{1,2} = \delta\Delta\lambda_{1,2}^* + \Theta/6$ (Equation (5.38)) each term of order d in $\delta\Delta\lambda'_{1,2}$ contributes a term of order d in Θ , so for each term of order $|\boldsymbol{\alpha}|/2$ in \mathbf{I} we must obtain $c_{\boldsymbol{\alpha}}(\delta\Delta\lambda'_{1,2})$ only up to order $[2 - |\boldsymbol{\alpha}|/2]$ in $\delta\Delta\lambda'_{1,2}$ (where $[\bullet]$ is the floor function) to achieve the desired second order with respect to all the actions. We can then organise all terms with respect to the order of expansion in \mathbf{I} and $\delta\Delta\lambda'_{1,2}$, and write for each addend $\bar{\mathcal{H}}_{s/2}^j = \mathcal{O}(\mathbf{I}^{s/2}) \times \mathcal{O}(\delta\Delta\lambda'_{1,2}^j)$. To get a sense of what these terms look like, I write the terms only up to order $s = 2$ in $\sqrt{\mathbf{I}}$:

$$\begin{aligned} \bar{\mathcal{H}}_{1/2}^0 &\propto \sqrt{2I_l} \cos(\phi_l), & \bar{\mathcal{H}}_{1/2}^1 &\propto \delta\Delta\lambda'_{1,2} \sqrt{2I_l} \cos(\phi_l), \\ \bar{\mathcal{H}}_1^0 &\propto I_l, & \bar{\mathcal{H}}_1^1 &\propto \delta\Delta\lambda'_{1,2} \sqrt{2I_{l_1}} \sqrt{2I_{l_2}} \cos(\phi_{l_1} \pm \phi_{l_2}); \end{aligned} \quad (5.41)$$

the subsequent terms of higher order in $\sqrt{\mathbf{I}}$ follow this structure but the possible combinations of the angles get substantially more numerous and I avoid writing them all here in the interest of brevity. Among them, there are of course also the terms $\propto I_l^2$ appearing without angles, as well as the term $\propto \delta\Delta\lambda'_{1,2}{}^2$, which contribute directly to the Θ^2 term in (5.39). We note that the first terms $\bar{\mathcal{H}}_{1/2}^0 \propto \sqrt{2I_l} \cos(\phi_l)$ (corresponding to $|\boldsymbol{\alpha}| = 1$ and constant in $\delta\Delta\lambda'_{1,2}$) are actually zero by definition of equilibrium point calculated at the reference value $\delta\Delta\lambda'_{1,2} = 0$. Also, the coefficients in $\bar{\mathcal{H}}_1^0$ in front of the I_l 's are just the frequencies ω_l , since these are the ones calculated in (5.18). Therefore, in this case the role of the integrable part of the Hamiltonian (called \mathcal{H}_0 in Sect. 2.3) is naturally played by $\bar{\mathcal{H}}_1^0 = \sum_{l=1}^4 \omega_l I_l$.

To understand how the perturbative elimination of the non-resonant harmonics involving $(\boldsymbol{\phi}^*, \delta\lambda_{1,2}^*)$ can generate terms in Θ^2 independent of the angles, consider that if $f_n = \mathcal{O}(\mathbf{I}^n)$ and $\chi_m = \mathcal{O}(\mathbf{I}^m)$, then $\{f_n, \chi_m\} = \mathcal{O}(\mathbf{I}^{n+m-1})$, and so on for all the other terms of the Lie series: $\{\{f_n, \chi_m\}, \chi_m\} = \mathcal{O}(\mathbf{I}^{n+2m-2})$ etc. When we eliminate a $\bar{\mathcal{H}}_{n,\text{pert}}^j = \mathcal{O}(\mathbf{I}^n)$ term by solving the homological equation $\{\bar{\mathcal{H}}_1^0, \chi_m\} + \bar{\mathcal{H}}_{n,\text{pert}}^j = 0$, we must naturally use a $\chi_n = \mathcal{O}(\mathbf{I}^n)$. This introduces new terms $\{\{\bar{\mathcal{H}}_1^0, \chi_n\}, \chi_n\}$ and $\{\bar{\mathcal{H}}_{n,\text{pert}}^j, \chi_n\}$ which are $\mathcal{O}(\mathbf{I}^{2n-1})$ (given that $\bar{\mathcal{H}}_1^0$ is $\mathcal{O}(\mathbf{I})$). Thus, terms of order 2 can be generated for example if $n = 3/2$. We actually need to calculate explicitly only those terms that yield a Θ^2 independent of the angles, as the others would be eliminated further. Such terms derive from $\bar{\mathcal{H}}_{3/2}^0$ (which governs the non-linear interactions between the four resonant degrees of freedom around the equilibrium point, which Figure 5.10 proves to be strong) and $\bar{\mathcal{H}}_{1/2}^1$ (which describes the fact that the

equilibrium point $\bar{\mathbf{p}}_{\text{eq}}$ of $\bar{\mathcal{H}}$ shifts as $\delta\Delta\lambda'_{1,2}$ changes under the effects of the $O(m_{\text{pl}}^2)$ terms¹⁰.

We implemented this procedure with the aid of the algebraic manipulator Mathematica. In our reference case $k = 3$ and $a_1 \simeq 0.1$ at a mass $m_{\text{pl}}/M_* \simeq 1.28 \times 10^{-3}$ right before the development of the excitation of the resonant degrees of freedom (Figure 5.10) this yields

$$\langle \bar{\mathcal{H}} \rangle_{(\phi^*, \delta\lambda'_{1,2})}(\Theta) = \delta\Theta + \frac{\beta}{2}\Theta^2, \quad \delta \simeq 7.74 \times 10^{-3}, \quad \beta \simeq 101. \quad (5.44)$$

The fact that δ is positive and small is consistent with the fact that we put ourselves right before the development of the excitation (cfr. Figure 5.8). The fact that $\beta \sim 100$ is positive yields an analytical confirmation that there can be capture into this secondary resonance.

After we have obtained $\langle \bar{\mathcal{H}} \rangle_{(\phi^*, \delta\lambda'_{1,2})}$ (cfr. Equation (5.44)), we can easily complete the determination of the model (5.39) for this secondary resonance. To do this, with the help of the algebraic manipulator Mathematica we use the canonical transformation (5.38) applied to the term (5.36b) which contains the resonant harmonic 2θ , and we obtain

$$\langle \mathcal{H}' \rangle_{(\phi^*, \delta\lambda'_{1,2})}(\Theta, \theta) = \delta\Theta + \frac{\beta}{2}\Theta^2 + c\sqrt{2\Theta} \cos(2\theta + 2\pi/6), \quad \delta \simeq 7.74 \times 10^{-3}, \quad \beta \simeq 101, \quad c \simeq -7.8 \times 10^{-4}. \quad (5.45)$$

A phase is introduced which does not change the dynamics and could easily be eliminated by a simple translation. We can now compare the evolution predicted by this model to the RK4 integration of $\mathcal{H}^* = \mathcal{H}_{\text{kepl}} + \mathcal{H}_{\text{res}} + \mathcal{H}_{\text{syn}}$. The evolution of the action $\Theta = I_2$ is already shown in Figure 5.10. We plot in Figure 5.11 the evolution of the angle 2θ (which produces a numerical evolution that is graphically more legible than that of θ). One can see that the angle starts librating at the same value of m_{pl} where the conjugated action $\Theta = I_2$ starts increasing in Figure 5.10: this shows that there is a passage across the resonance. The situation is similar to the one described near the end of Subsect. 2.3.3, where the orbit finds itself close to the separatrix after the passage through the resonance, the adiabatic principle is not applicable and the orbit can end up in the inner circulation region (cfr. also Figure 2.4 panel (f)). In the spirit of Subsect. 2.3.3, to get a better sense of the dynamical interaction with this secondary resonance, we can fix different values for δ in (5.45) and look at the corresponding phase diagrams. Notice that changing δ essentially corresponds to changing m_{pl} ; we also checked that for different planetary masses near $m_{\text{pl}}/M_* \simeq 1.28 \times 10^{-3}$ the coefficients β and c do not change considerably, so we keep them fixed to obtain a qualitatively correct description of the dynamical portraits.

Figure 5.13 shows the level plots of the Hamiltonian (5.45), for different values of δ (i.e. of the frequency of $\delta\lambda'_{1,2}/3 + 2\phi_2$ at $\Theta = 0$), in the variables $(X = \sqrt{2\Theta} \cos(2\theta), Y = \sqrt{2\Theta} \sin(2\theta))$; we also overplot the evolution of $(\Theta, 2\theta)$ obtained from the RK4 simulation (a combination of Figures 5.10 and 5.11), truncated at the value of the planetary mass corresponding to the same δ used to plot the phase diagrams. Initially, there is only one stable centre at the origin (panel (a)) and the orbit circulates anti-clockwise around it with constant amplitude. Then, we see that a resonant island bifurcates from the origin in the bottom-right quadrant of the phase diagram (panel (b)), which is followed by the dynamical evolution. Almost immediately after, a second bifurcation occurs at roughly the same δ , so the inner circulation region starts to grow around the origin and catches up with the orbit (panels (c) and (d)). After crossing the inner separatrix, the dynamical evolution drops off the resonant island, falls inside the inner circulation region and the angle 2θ starts to circulate in clockwise fashion (panels (e) and (f)). This missed capture into resonance is one of the two probabilistic fates for a second order resonance when $\dot{\delta}\beta < 0$ and

¹⁰Precisely, starting from $\bar{\mathcal{H}}_{3/2}^0$, we look at the action of $\exp(L_{\chi_{3/2}})$ on each term $\bar{\mathcal{H}}_{s/2}^j$ in $\bar{\mathcal{H}}$, and we get that

$$\mathcal{O}(\mathbf{I}) \xrightarrow{\exp L_{\chi_{3/2}}} \underbrace{\mathbb{I}_d(\mathcal{O}(\mathbf{I}))}_{\mathcal{O}(\mathbf{I})} + \underbrace{\{\mathcal{O}(\mathbf{I}), \chi_{3/2}\}}_{\mathcal{O}(\mathbf{I}^{3/2})} + \frac{1}{2} \underbrace{\{\{\mathcal{O}(\mathbf{I}), \chi_{3/2}\}, \chi_{3/2}\}}_{\mathcal{O}(\mathbf{I}^2)} \quad (5.42)$$

is all we need to calculate from the $\mathcal{O}(\mathbf{I})$ terms, and that instead

$$\mathcal{O}(\mathbf{I}^{3/2}) \xrightarrow{\exp L_{\chi_{3/2}}} \underbrace{\mathbb{I}_d(\mathcal{O}(\mathbf{I}^{3/2}))}_{\mathcal{O}(\mathbf{I}^{3/2})} + \underbrace{\{\mathcal{O}(\mathbf{I}^{3/2}), \chi_{3/2}\}}_{\mathcal{O}(\mathbf{I}^2)} \quad (5.43)$$

is all we need to calculate from the $\mathcal{O}(\mathbf{I}^{3/2})$ terms, etc. The exact expression of this $\chi_{3/2}$ is obtained just as we did in Subsect. 5.3.5.1, only now we have a much higher number of terms in the perturbation part that we want to eliminate. Therefore, to perform this step it is advisable to make use of an algebraic manipulator (a simple Mathematica code which generates the needed χ given terms of the form $\bar{\mathcal{H}}_{s/2}^0$ is given in Appendix C). A similar reasoning applies to $\bar{\mathcal{H}}_{1/2}^1$, but since this term does not encapsulate a significant qualitative change to the dynamics, we checked that its final contribution is only a small quantitative deviation (of only a few percent) to the already present $\mathcal{O}(\mathbf{I}^2)$ terms.

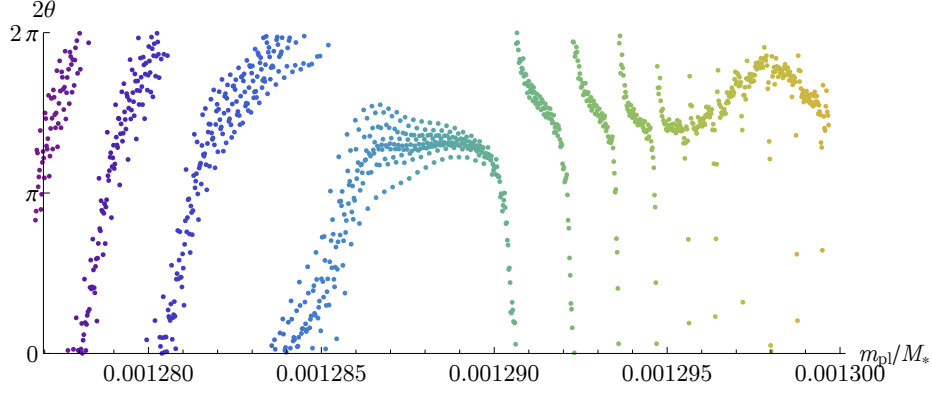


Figure 5.11: Evolution around $m_{\text{pl}} \simeq 1.28 \times 10^{-3}$ of the angle θ , the resonant angle for the secondary resonance encountered (we plot 2θ instead of θ , as explained in the main text), in panel (a). This figure should be compared to Figure 5.10: the action conjugated to θ is $\Theta = I_2$ (Equation (5.38)), and we see that when θ start librating I_2 increases, indicating that the system has captured into this secondary resonance. As in Figure 5.10, after the actions get excited the integrable approximation to the dynamics is not valid anymore. The colour of the dots in this figure only serve as a legend for the value of the planetary mass: we use the same colour-coding in Figure 5.13, where we take snapshots of the evolution of the pair (Θ, θ) at different values of m_{pl} .

when the two bifurcations occur at close values of δ , as discussed in Subsect. 2.3.3. However, in this specific case we checked that this evolution is actually the result of more complicated interactions among the resonant variables (I_l, ϕ_l) themselves, as well as another secondary resonance involving the variables (I_l, ϕ_l) and $(\delta\Delta\lambda'_{1,2}, \delta\lambda'_{1,2})$. First, from Figure 5.10, one can see that after the initial increase of I_2 , I_4 starts increasing also, after which there are wide oscillations of I_2 and I_4 in opposite phase. This is symptomatic of the effect of the term $\sqrt{I_2}I_4 \cos(\phi_2 - 2\phi_4)$, which is quasi-resonant because $\omega_2 \simeq 2\omega_4$ (Figure 5.6e). To prove this, we plot in Figure 5.12 the action $I_4 + 2I_2$, which is the constant of motion relative to this harmonic term: we see that the aforementioned oscillation undergone by I_2 and I_4 is completely eliminated. On the other hand, we see a much longer period large oscillation, which diverges towards the end of the integration. We interpret this as evidence of a transition of the system into the secondary resonance with argument $\delta\lambda'_{1,2}/3 + \phi_2 + 2\phi_4$ (which also has a small frequency, since $\delta\lambda'_{1,2}/3 + 2\phi_2$ and $-\phi_2 + 2\phi_4$ are both slow angles). The reason is that (up to a constant) $I_4 + 2I_2$ can also be seen as a conjugated action of $\delta\lambda'_{1,2}/3 + \phi_2 + 2\phi_4$ through the canonical change of variables

$$\begin{aligned}
 (I_4 + 2I_2)/4, & \quad \delta\lambda'_{1,2}/3 + \phi_2 + 2\phi_4, \\
 (I_4 - 2I_2)/4, & \quad -\delta\lambda'_{1,2}/3 - \phi_2 + 2\phi_4, \\
 \delta\Delta\lambda'_{1,2} - I_2/3, & \quad \delta\lambda'_{1,2}.
 \end{aligned} \tag{5.46}$$

We see that after the angle $\theta = \delta\lambda'_{1,2}/6 + \phi_2$ leaves the first resonance (at mass $m_{\text{pl}}/M_* \simeq 1.29 \times 10^{-3}$, see Figure 5.11) the action $2I_2 + I_4$ keeps growing, which indicates a transition to this new resonance involving $\delta\lambda'_{1,2}/3 + \phi_2 + 2\phi_4$.

This analysis shows that the evolution presented above is very rich, and does not allow any simple description of it. In any case, Figure 5.13 does not leave any doubt that the initial growth of I_2 is due to the interaction with the secondary resonance associated to the angle $\delta\lambda'_{1,2}/3 + 2\phi_2$, and that the simple model we have derived yields an effective understanding of the evolution, at least at a qualitative level.

The takeaway is the following. We showed that the numerical RK4 integration of the system $\mathcal{H}^* = \mathcal{H}_{\text{kepl}} + \mathcal{H}_{\text{res}} + \mathcal{H}_{\text{syn}}$ presents a similar phenomenon to the full $(N + 1)$ -body simulations where the resonant degrees of freedom get excited; we checked that the purely resonant system instead does not undergo the same evolution, and gave an analytical explanation to this fact. We then showed analytically that a set of secondary resonances are present in the \mathcal{H}^* system, which involve a fraction of the synodic frequency and combination of the resonant frequencies, and which appear at order two in the planetary mass. Then, we found the specific secondary resonance that is encountered in the RK4 integration of \mathcal{H}^* ; we built an integrable model for this resonance valid as long as the actions remain small, and confirmed analytically that there can be capture into this resonance. Finally, we verified that the numerical evolution we obtained in the RK4 integration corresponds to a temporary capture into the considered secondary resonance, followed by a rich and fascinating series of interactions with additional secondary resonances.

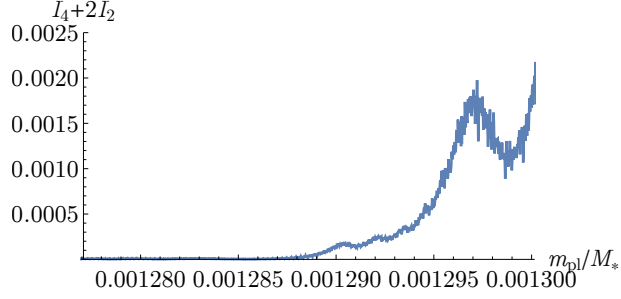


Figure 5.12: Evolution of the action $I_4 + 2I_2$, which is a constant of motion relative to the harmonic term $\phi_2 - 2\phi_4$, as well as the resonant action conjugated to the slow angle $\delta\lambda'_{1,2}/3 + \phi_2 + 2\phi_4$, cfr. Eq. (5.46).

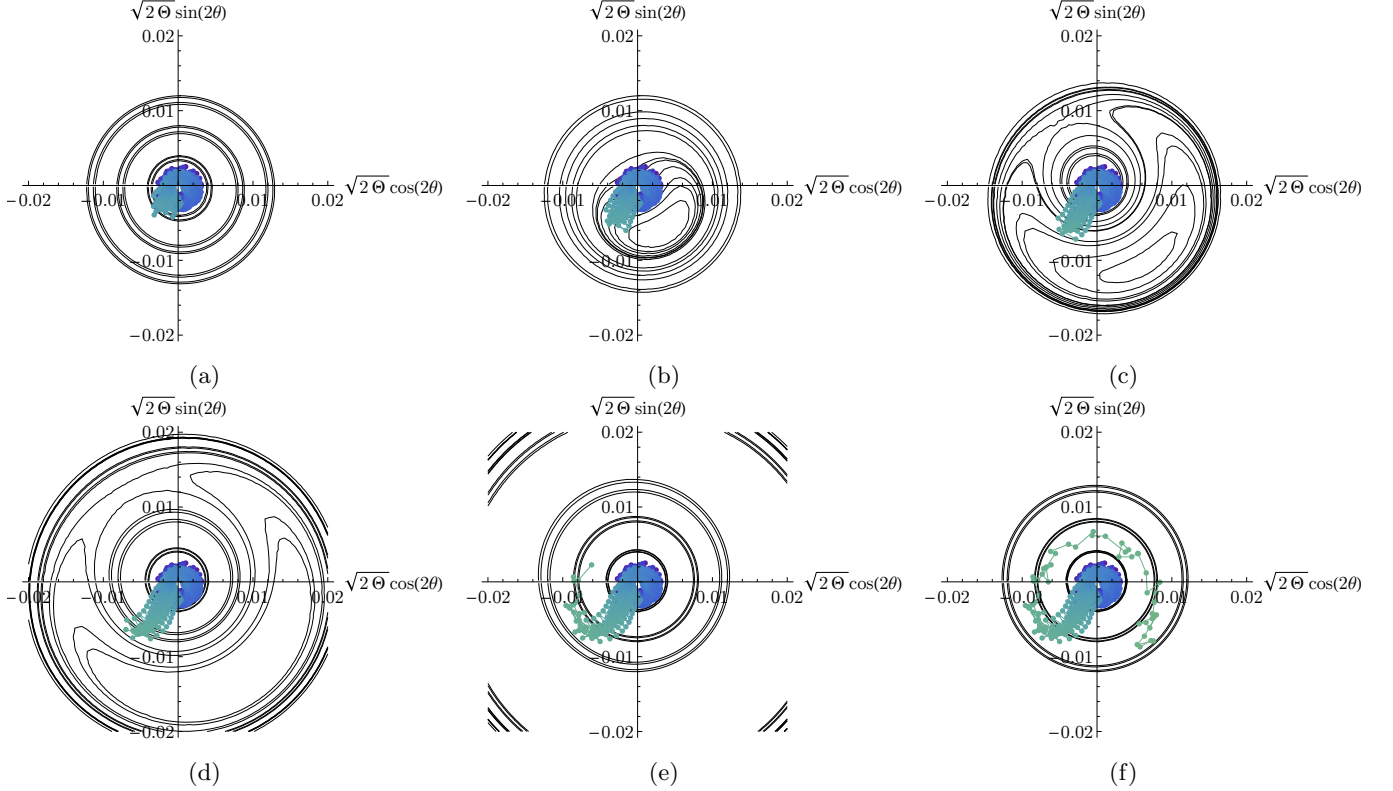


Figure 5.13: Contour plots of the Hamiltonian of the integrable model (5.45) for the secondary resonance involving $2\theta = \delta\lambda'_{1,2}/3 + 2\phi_2$ and $\Theta = I_2$, shown in panels (a) to (f) in canonical cartesian coordinates at different values of the parameter δ . The change in δ represents the change in the planetary mass m_{pl} implemented along the integration. The dots represent the evolution of the system along the RK4 simulation, and their colour indicate the value of m_{pl} using the same colour scheme as in Figure 5.11.

5.3.6 Dependence on k

In this subsection I present some preliminary results on the dependence on the mean motion resonant index k of the critical mass for the excitation of the system, described above for the specific case $k = 3$. We recall that [Matsumoto et al.(2012)] found that the critical planetary mass allowed for stability in resonant chains decreases with the compactness of the chain. Indeed in setup similar to that of Figure 5.5 but in the case of the 4:3 – 4:3 mean motion resonance chain, we find that the instability is triggered at $m_{\text{pl}} \sim 4 \times 10^{-4} M_*$, which is smaller than the critical value for the $k = 3$ chain.

The reduced value of the critical mass m_{pl} for more compact chains can be explained by the mechanism of capture into secondary resonances between a fraction of the synodic frequency and a combination of the resonant libration frequencies discussed throughout this chapter, which causes the excitation of the amplitude of libration

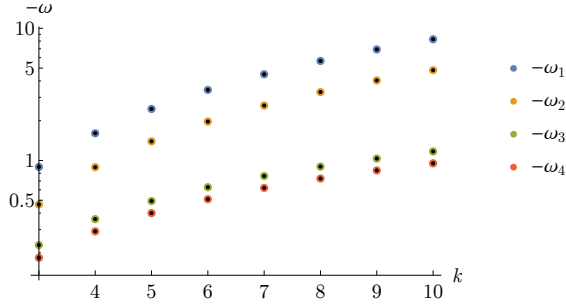


Figure 5.14: Dependence of the resonant libration frequencies ω_l , $l = 1, \dots, 4$ on the index k of the resonance in a three-planet $k : (k - 1)$ mean motion resonance chain, for a given fixed mass of the planets. In colour we plot the calculated frequencies at different k 's and in black we show the result of a numerical fit of type $\omega_l \propto k^{\alpha_l} (k - 1)^{\beta_l}$. The values for α_l , β_l are given in Equation (5.48).

of the system leading to close encounters and collisions. For, from Equation (5.35), we see that the fraction of the synodic frequency that resonates with the resonant frequencies ω gets smaller with increasing k ; therefore, since the resonant frequencies ω increase with m_{pl} , at higher k one needs a smaller m_{pl} for a secondary resonance to be crossed.

In order to estimate exactly when a regime of secondary resonances is encountered, by (5.35) we should equate the fraction of the synodic frequency $\delta\lambda'_{1,2}/k$ to $\mathbf{h} \cdot \omega$, for some $\mathbf{h} \in \mathbb{Z}^4$; recall moreover that the strongest secondary resonances will appear for low integers $h_1, \dots, h_4 \in \mathbb{Z}$. The expression for $\delta\lambda'_{1,2}/k$ is easy, since it is approximately

$$\frac{\delta\lambda'_{1,2}}{k} \simeq \frac{1}{k^2} n_1, \quad (5.47)$$

as we are in the $k : k - 1 - k : k - 1$ chain; here n_1 is the (mean) mean motion of the inner planet.

The determination of the dependence of ω on k is not as straightforward, and still needs further analytical investigation. The first approach we follow is purely numerical: we use the scheme of Subsection 5.3.4 applied to different values of k . We fix the planetary mass at $m_{\text{pl}} = 10^{-5} M_*$, since the scaling of ω with m_{pl} was already investigated in Figures 5.6e and 5.6f (we checked that they are valid also for different mean motion resonance indices k). Then, to be consistent with our m_{pl} vs. e_2 stability maps (cfr. Figure 5.5), we should also fix the resonant equilibrium point $\bar{\mathbf{p}}_{\text{eq}} = (\Psi_{1,\text{eq}}^{(1)}, \Psi_{2,\text{eq}}^{(1)}, \Delta\gamma_{1,2,\text{eq}}, \Delta\gamma_{2,3,\text{eq}})$ so that the resulting equilibrium $e_{2,\text{eq}}$ is equal for all k . With this choice, we find the frequencies ω corresponding to the chosen m_{pl} and the calculated $\bar{\mathbf{p}}_{\text{eq}}$ as explained in Subsect. 5.3.4. The result is plotted in Figure 5.14 (cfr. the coloured dots). The fact that the frequencies, for a given mass, grow with k again goes in the direction of destabilising a resonant chain earlier (i.e. at smaller planetary masses) for higher k . In fact, not only the resonant sub-synodic frequency (5.47) becomes slower, but the libration frequencies become faster. Thus, given the dependence of the libration frequencies on $m_{\text{pl}}^{2/3}$ (at small e), a smaller value of m_{pl} is required to encounter a secondary resonance.

Then, we attempt to fit the different curves for ω_l , $l = 1, \dots, 4$ to k . Since k always appears together with $k - 1$ in all formulæ associated with a $k : k - 1$ resonance, it is natural to search for a fit of the form $k^{\alpha_l} (k - 1)^{\beta_l}$ for some α_l, β_l . Doing so, we get for the four resonant frequencies ω_l

$$\begin{aligned} \alpha_1 &\simeq 0.33, \quad \beta_1 \simeq 1.2 \\ \alpha_2 &\simeq -0.47, \quad \beta_2 \simeq 1.9 \\ \alpha_3 &\simeq -0.35, \quad \beta_3 \simeq 1.4 \\ \alpha_4 &\simeq -0.43, \quad \beta_4 \simeq 1.4; \end{aligned} \quad (5.48)$$

the goodness of the fit is shown by the black dots in Figure 5.14, which follow perfectly the values of the resonant frequencies ω at different k . The relationship between (α_1, β_1) and (α_2, β_2) should be clear: since ω_1 is the highest frequency related to the resonant angle for the inner pair and ω_2 for the outer pair, and since we are in a $k : k - 1$ chain, the two frequencies are almost a $(k - 1)/k$ away from each other. To understand the scaling law for ω_1 , one may attempt to use the simple two-planet model for the inner pair (e.g. [Batygin and Morbidelli(2013)a, Batygin(2015)]), ignoring the perturbation of the outer planet. A similar fitting to powers of k and $k - 1$ of the value of ω_1 for one resonant pair does yield a qualitatively similar result: $\alpha_1 \simeq 0.28$, $\beta_1 \simeq 1.2$; however, the scaling for the second

degree of freedom associated to the difference of pericentres yields a scaling which is not consistent with (5.48). Notice that in the case of two resonant planets, [Batygin(2015)] gives a scaling for the resonant frequency ω_1 in terms of k , $k-1$ and $f_{\text{res}}^{(j)}$ (the Laplace coefficients that determine the strength of each resonant term, cfr. Equation (5.9)); however, the frequency ω_1 that is considered in [Batygin(2015)] is the one at the value of the angular momentum at which the separatrix first appears, so their fit is not directly translatable to the exponents in (5.48), since these are calculated for the frequencies at constant $e_{2,\text{eq}}$. A concise analytical treatment of the needed scaling laws will be the subject of future work. Nevertheless, using the numerical scaling for ω_l we can give an estimate for the mass at which a 3-planet $k=4$ resonant chain should become unstable, given the value of the planetary mass for which this happens in the case $k=3$. Let us consider for simplicity the value of ω_1 as a reference, since it is the highest resonant frequency (however, low-order combinations of all resonant frequencies combined can also play a role). Going from $k=3$ to $k=4$ at a given mass, ω_1 increases by a factor of 1.8, while n_1/k^2 decreases by a factor $(4/3)^2$. So, to cross a secondary resonance, $m_{\text{pl}}^{2/3}$ has to be $\simeq (4/3)^{-2}/1.8$ times smaller. This gives, for the case $k=4$, a mass that is $((4/3)^{-2}/1.8)^{3/2} \simeq 0.17$ times that for an instability in the $k=3$ chain, which was $m_{\text{pl}} \sim 1.3 \times 10^{-3}$. This gives a value of $\simeq 2 \times 10^{-4}$, which is to a factor of two the one found in our $(N+1)$ -body simulations, $\simeq 4 \times 10^{-4}$.

5.4 N Planets

We sketch below how the results found in the previous section can be generalised to the case of $N \geq 3$ equal-mass planets in a given $k : k-1$ mean motion resonance chain. We begin by recalling that, as pointed out by [Matsumoto et al.(2012)] (see also the results from [Izidoro et al.(2019)]), the critical mass for stability of a resonant chain decreases with N and, for the same reasoning presented in Subsect. 5.3.1, this should not be the case if the origin of the instability were due to close encounters as in the two-planet case. Therefore, one must investigate the dynamical origin of these instabilities, as we did in the previous section for $N=3$.

We start introducing the Hamiltonian $\mathcal{H}^* = \mathcal{H}_{\text{kepl}} + \mathcal{H}_{\text{res}} + \mathcal{H}_{\text{syn}}$, where \mathcal{H}_{res} contains the resonant interactions between all $N-1$ pairs of neighbouring planets, and \mathcal{H}_{syn} contains terms of type $\cos(\lambda_i - \lambda_{i+1})$, $i=1, \dots, N-1$; for both \mathcal{H}_{res} and \mathcal{H}_{syn} we will consider interaction terms up to order one in the eccentricities, as we did in the previous section. We then make use of a canonical transformation analogous to (5.12): we introduce the resonant angles $\psi_1^{(i)} = k\lambda_{i+1} - (k-1)\lambda_i + \gamma_i$ and the angles $\delta\gamma_{i,i+1} = \gamma_i - \gamma_{i+1}$ for each planet pair, $i=1, \dots, N-1$ (this gives $2(N-1)$ resonant degrees of freedom), then we have the synodic angle $\delta\lambda_{1,2} = \lambda_1 - \lambda_2$, and finally a $\gamma'_N = -\gamma_N$ which will not appear in the Hamiltonian (its conjugated action will again be the total orbital angular momentum).

We can immediately generalise the result of Subsection 5.3.4 and state that the $2(N-1)$ purely resonant degrees of freedom are Lyapunov stable at low amplitude of libration around the resonant equilibrium point for any number of planets N . For, when adding an outer resonant pair to the system with the same resonance index k the Hamiltonian simply repeats itself, since to first order in the eccentricities we are only considering the mutual planetary perturbations due to immediately neighbouring planets and the structure of each term is the same, namely (5.8). So, each planet is either the inner or outer planet, or a middle planet as in the case already considered of a three-planets system. Therefore, all resonant libration frequencies will always have the same sign, and the reasoning of Subsection 5.3.4 stands.

As in the case of three resonant planets, we thus conclude that the instability must be due to an interaction between the synodic degree of freedom and the purely resonant degrees of freedom. Then, it is natural to investigate when a regime of secondary resonances analogous to (5.33) and (5.36) can be encountered. To answer this question, we proceeded analytically following the steps of Subsect. 5.3.5.2. We introduce a generating Hamiltonian χ_{syn} which eliminates the synodic contribution \mathcal{H}_{syn} , so χ_{syn} in Delaunay variables will have harmonic terms $\sin(\lambda_i - \lambda_{i+1})$, $i=1, \dots, N-1$. Transforming $\mathcal{H}^* = \mathcal{H}_{\text{kepl}} + \mathcal{H}_{\text{res}} + \mathcal{H}_{\text{syn}}$ with the Lie series generated by χ_{syn} eliminates \mathcal{H}_{syn} to first order in m_{pl} (the planetary mass for all planets), but introduces new terms to order 2 in m_{pl} (among which the most important is $\{\{\mathcal{H}_{\text{kepl}}, \chi_{\text{syn}}\}, \chi_{\text{syn}}\}$, like in the case $N=3$); these newly introduced terms will contain a fraction of the synodic angle $\delta\lambda_{1,2}$, and we are interested in the smallest fraction of $\delta\lambda_{1,2}$ that appears. Like in the case of three planets, the term $(m_{\text{pl}}^2/2)\{\{\mathcal{H}_{\text{kepl}}, \chi_{\text{syn}}\}, \chi_{\text{syn}}\}$ combines together all synodic angles $\lambda_i - \lambda_{i+1}$. Notice that in the new coordinates $\psi_1^{(i)}$, $\delta\gamma_{i,i+1}$ and $\delta\lambda_{1,2}$, each $\lambda_i - \lambda_{i+1}$ can be written as $\lambda_i - \lambda_{i+1} = \left(\frac{k-1}{k}\right)^{i-1} (\lambda_1 - \lambda_2) = \left(\frac{k-1}{k}\right)^{i-1} \delta\lambda_{1,2}$ plus terms including $\psi_1^{(j)}$ and $\delta\gamma_{j,j+1}$. However we do not need to keep track of the $\psi_1^{(j)}$'s and $\delta\gamma_{j,j+1}$'s since we are only interested in the way the angle $\delta\lambda_{1,2}$ appears in the $\mathcal{O}(m_{\text{pl}}^2)$ terms. The smallest fraction of $\delta\lambda_{1,2}$ will be generated by combining the synodic angles relative to the two outermost pairs $\lambda_{N-2} - \lambda_{N-1}$

and $\lambda_{N-1} - \lambda_N$, since already they contain the smallest fraction of $\delta\lambda_{1,2}$. Multiplying them together (using $\cos(a)\cos(b) = \frac{1}{2}(\cos(a-b) + \cos(a+b))$) yields a harmonic term of type

$$\cos\left(\left(\left(\frac{k-1}{k}\right)^{N-3} - \left(\frac{k-1}{k}\right)^{N-2}\right)\delta\lambda_{1,2} + \dots\right), \quad (5.49)$$

where the $+\dots$ terms represents a combination of $\psi_1^{(j)}$'s and $\delta\gamma_{j,j+1}$'s, which again we are not interested in. Therefore, the lowest synodic frequency that appears in the $\mathcal{O}(m^2)$ term is

$$\frac{1}{k}\left(\frac{k-1}{k}\right)^{N-3}\delta\lambda_{1,2} \simeq \frac{1}{k^2}\left(\frac{k-1}{k}\right)^{N-3}n_1; \quad (5.50)$$

this equation is the generalisation to $N \geq 3$ of Equation (5.47). This is the fraction of the synodic frequency which can resonate with the libration frequencies ω_l of the resonant degrees of freedom. Since ω_l increase with m_{pl} (as $\omega \sim m_{\text{pl}}^{1/2}$ or $m_{\text{pl}}^{2/3}$ according to the eccentricities), there will be a critical mass after which a regime of secondary resonances is encountered, which can excite the system and cause its instability. Since the factor $\frac{1}{k}\left(\frac{k-1}{k}\right)^{N-3}$ multiplying $\delta\lambda_{1,2}$ decreases with N and with k , the conclusion is that *the regime of secondary resonances between synodic and resonant degrees of freedom is encountered at lower masses for increasing k and/or increasing N , and therefore the critical mass $(m_{\text{pl}}/M_*)_{\text{crit}}$ allowed for stability decreases with N and with k* . This gives an analytical explanation to the numerical findings of [Matsumoto et al.(2012)].

The takeaway is that we now have a better dynamical understanding of the origin of the instabilities observed in the numerical experiments. As pointed out in Subsect. 5.3.6, in order to make a quantitative prediction of the onset of such instabilities in terms of the planetary masses for an arbitrary number of planets N and resonant index k , we still need to find the dependence of the libration frequencies ω_l on k and N in addition to m_{pl} . We can then equate ω_l to (5.50) in order to obtain an equation for the critical mass for stability in terms of k and N . In particular, it is still not clear if the scaling law of ω_l in terms of k and $k-1$ changes significantly with N ; this will be the subject of future work. Once this aspect is worked out and we are able to make a more precise prediction on the onset of instabilities in resonant chains, we also plan to check its validity by running a set of numerical experiments with different values of N and k .

Chapter 6

Extreme secular excitation of eccentricity inside mean motion resonance

In this chapter we discuss how planetary instabilities and collisions can be at the origin of a relevant mechanism for a different astrophysical context: the observed pollution of the atmospheres of White Dwarfs. Spectroscopic studies of a large sample of cool, hydrogen-rich White Dwarfs have established a minimum frequency of 30% for the pollution phenomenon in these objects ([Zuckerman et al.(2003), Koester et al.(2014)], see also [Farihi(2016)] for a review). In cold White Dwarfs, heavy elements should rapidly sink ([Fontaine and Michaud(1979), Vauclair and Fontaine(1979)]) leaving behind only Hydrogen or Helium. Thus, external sources must be responsible for any photospheric metals. The most commonly accepted explanation is that these metals originate from tidally disrupted planetesimals ([Debes and Sigurdsson(2002), Jura(2003)]). In essence, planetesimals perturbed into highly eccentric orbits pass within the stellar Roche limit¹ (which is of the order of the solar radius R_{\odot}) and are torn apart by gravitational tides; subsequent collisions reduce the fragments to dust; the latter produce an infrared excess and slowly rain down onto the stellar surface, which generates the observed atmospheric pollution.

As we mentioned in Section 1.3, bottom-up planetesimal formation by accretion processes in the same fashion as described in Subsect. 1.2.2 is unlikely to be an active process in the post-disc phase around old objects like White Dwarfs. Therefore, the presence of a large population of small bodies must be explained in another way. It is conceivable that in earlier stages of their lives, these stars hosted compact planetary systems such as the resonant chains described in the earlier chapters of this thesis. Then, the decrease of stellar mass during the star’s life can be seen as an implementation in nature of the numerical experiments of Chapter 5, where the planets’ mutual interactions become stronger, until a planetary instability is reached. The inferred planetesimal population in the late stages of these stars would be the effect of the generation of debris in the resulting planetary collisions. Obviously, for this model to work, these planetesimals then have to be “pushed” by planetary perturbations to achieve orbits that are eccentric enough to pass within the star’s Roche limit $\sim R_{\odot}$. Given the ubiquity of the White Dwarf pollution phenomenon, a robust mechanism of extreme eccentricity excitation of planetesimals is needed (e.g. [Bonsor et al.(2011), Debes et al.(2012), Petrovich and Muñoz(2017), Mustill et al.(2018), Veras et al.(2018)]). In this chapter (based on [Pichierri et al.(2017)]) we investigate one possible mechanism: the extreme secular excitation of the eccentricity of small bodies which reside in specific mean motion resonances with a slightly eccentric outer planetary perturber.

¹The *Roche limit* or *Roche radius* of a primary body is the distance d_R within which the self-gravity of a second body is surpassed by the tidal forces exerted by the first, so that the secondary body (which is usually smaller) gets disintegrated. In the rigid-body approximation, both bodies are approximately spheres with masses M and m and radii R and r for the primary and secondary respectively. Writing $d \gg r$ for the distance between the two, we equate the tidal force $F_{\text{tidal}} = \mathcal{G}M/d^2 - \mathcal{G}M/(d+r)^2 \simeq (2\mathcal{G}M/d^3)r$ applied by the primary to the self-gravity force $F_{\text{self}} = \mathcal{G}m/r^2$ of the secondary [Armitage(2015)], which yields a Roche limit of $d_R \simeq (2M/m)^{1/3}r$. This can be expressed in terms of the densities ρ_M and ρ_m of the primary and secondary respectively as $d_R \simeq (2\rho_M/\rho_m)^{1/3}R$ so the radius r of the secondary does not appear.

6.1 Small bodies driven into star-grazing orbits by planetary perturbations

Over the last 30 years it has become clear that planetary perturbations can force asteroids into such highly eccentric orbits that they collide with the Sun. There is also growing evidence that planetesimals may fall into their parent stars or suffer tidal disruption.

In the Solar System, Sun-grazing long-period comets (e.g. the famous Kreutz group; [Marsden(1967)]) have been known for a long time, but these objects are expected to come from the Oort cloud on orbits that are already highly eccentric, which means that planetary perturbations only play a minor role in driving their final Sun-grazing eccentricities. But in 1994, [Farinella et al.(1994)], following the evolution of the known near-Earth objects with numerical simulations, discovered that asteroids frequently collide with the Sun. The original source of near-Earth asteroids is the asteroid belt, so in this case planetary perturbations must play a major role in removing the object's initial angular momentum. Mean motion resonances with Jupiter and a secular resonance with Saturn were identified as the main mechanisms capable of pushing the asteroid's eccentricity to high values, far more effective than planetary close encounters. [Gladman et al.(1997)], again with numerical simulations, showed that more than 70% of the objects initially in the ν_6 secular resonance with Saturn or the 3:1 mean motion resonance with Jupiter eventually collide with the Sun.

The collision of small bodies with the central star is not an oddity of our Solar System. [Ferlet et al.(1987)] and [Lagrange et al.(1987)] proposed that the red-shifted Ca II and Na I absorption lines observed in β Pictoris were due to infalling evaporating bodies (see also [Beust et al.(1989), Beust et al.(1990), Beust et al.(1991)]). The frequency of such events, on a characteristic timescale of a few years, suggests that the infalling bodies were on short-period orbits, similar to asteroids or short-period comets in the Solar System. In recent years, many more young star systems have been observed to possess Doppler-shifted, transient absorption line features similar to β Pic, suggesting that infalling small bodies may be a common phenomenon (e.g. [Sorelli et al.(1996), Welsh and Montgomery(2013), Greaves et al.(2016)]).

The observed atmospheric pollution of White Dwarfs can also most likely be explained by infalling planetesimals, whose orbits are driven very close to the star by planetary perturbation. These astrophysical contexts have revived the interest in mean motion resonances with eccentric planets as a generic mechanism for pumping the eccentricities of small bodies from ~ 0 to ~ 1 , i.e. for driving planetesimals into the central star.

Analytic celestial mechanics shows that mean motion resonances with a planet on a *circular* orbit only cause an oscillation of the small body's semi-major axis coupled with a moderate oscillation of the eccentricity and with the libration of the angle $k\lambda - k'\lambda'$ (where λ and λ' are the mean longitudes of the small body and of the planet, respectively, and the integer coefficients k and k' define the $k' : k$ resonance; [Henrard and Lemaître(1983), Lemaître(1984)]). However, if the perturbing planet has a finite eccentricity, inside a mean motion resonance there can be a dramatic secular evolution; the eccentricity of the small body can undergo large excursions correlated with the precession of the longitude of perihelion ([Wisdom(1983), Wisdom(1985), Henrard and Caranicolas(1990)]).

These pioneer works used a series expansion of the Hamiltonian in power laws of the eccentricities of the perturbed body (e) and of the planet (e'), and focused specifically on the case of the 3:1 resonance with Jupiter. A few years later, [Moons and Morbidelli(1993), Moons and Morbidelli(1995)] developed a semi-analytic study of the dynamics in mean motion resonances using a first-order expansion in e' but no series expansions in e . This way, they were able to follow the evolution of the small body to arbitrarily high eccentricities. This approach is valid only for small values of e' and moreover for $e > e'$. Motivated by the [Farinella et al.(1994)] numerical results, Moons and Morbidelli focused on the specific case of the Solar System, including the effects of Saturn on the orbital evolution of Jupiter in addition to their combined perturbation to the asteroid. In this framework, they established the existence of overlapping secular resonances inside the 4:1, 3:1, 5:2, and 7:3 mean motion resonances, which can push the eccentricity of the small body to unity.

In a more general context, [Beust and Morbidelli(1996)] investigated the secular dynamics in mean motion resonances with a single planet with various (albeit moderate) eccentricities. Again, they considered an expansion in e' to the first order, and no expansion in the eccentricity of the perturbed body. Of all the resonances, they found that 4:1 is the most powerful in pushing the eccentricity of the small body from ~ 0 to ~ 1 , provided that $e' \gtrsim 0.05$. In contrast, the 3:1 resonance only generates large oscillations in the eccentricity of the small body, but they are insufficient to produce star-grazing orbits, at least for planet eccentricities up to 0.1. Because of the linear expansion in e' , [Beust and Morbidelli(1996)] could not determine the threshold planetary eccentricity that generates the star-grazing phenomenon for small bodies initially on quasi-circular orbits in the 3:1 resonance.

In this chapter we revisit the problem of the eccentricity evolution of small bodies inside mean motion resonances with an eccentric planet using a semi-analytic approach. In order to go beyond the works cited above, we

do not expand the Hamiltonian in the eccentricity of either the small body or the perturber. In this way, our study is valid for all eccentricities and also in the $e < e'$ regime. Our work is not the first to avoid expansions in e' (e.g. [Beaugé et al.(2006), Michtchenko et al.(2006), Sidorenko(2006)]). We use the adiabatic principle (already invoked in [Wisdom(1985)]) to disentangle the motion related to the libration of $k\lambda - k'\lambda'$ from the secular motion relating eccentricity and longitude of perihelion. To remain relatively simple, our analysis is performed in the limit of small amplitude of libration in the mean motion resonance.

This chapter is structured as follows. In Section 6.2, we develop the analytic formalism for the study of the secular dynamics at the core of mean motion resonances, without series expansions. This results in the averaged Hamiltonian with two degrees of freedom (6.9). In Section 6.3 we lay out the method for studying the dynamics given by the averaged Hamiltonian, using the theory of adiabatic invariance; we also discuss the limit of validity of this method. In Section 6.4 we also include a post-Newtonian term, describing the fast precession of the longitude of perihelion at large eccentricity due to General Relativity. Our results are presented in Section 6.5. We first neglect the effect of General Relativity; in this case the secular evolution is independent of the planet’s mass, and only the timescale of the secular evolution depends on it. We focus in particular on the 4:1, 3:1, and 2:1 resonances, and for each of these resonances we evaluate what planetary eccentricities are needed to lift bodies from initially quasi-circular orbits to star-grazing ones, if it is ever possible. When this is the case, we then introduce the post-Newtonian correction, which makes the secular dynamics at high eccentricity dependent on the planetary mass. Thus, we determine – for the resonances and the planetary eccentricities previously considered – the minimal planetary mass required to achieve the star-grazing phenomenon. In addition, we provide in the Appendix D a Mathematica notebook implementing our model so that the reader can compute the secular dynamics in the desired resonances with the desired planets. The conclusions of this chapter are summarised in Section 6.6.

6.2 Planetary Hamiltonian

We start with the Hamiltonian for the restricted planar three-body problem, Equation (2.86). By denoting with \mathbf{r} and $\dot{\mathbf{r}}$ the Cartesian coordinates and momenta of the perturbed test particle (“small body”), and using a prime for the perturber (“planet”), the Hamiltonian (2.86) reads:

$$\begin{aligned} \mathcal{H} &= \mathcal{H}_{\text{kepl}} + \mathcal{H}_{\text{pert}} \\ &= \frac{1}{2} \|\dot{\mathbf{r}}\|^2 - \frac{\mathcal{G}M_*}{\|\mathbf{r}\|} - \mathcal{G}m' \left(\frac{1}{\Delta} - \frac{\mathbf{r} \cdot \mathbf{r}'}{\|\mathbf{r}'\|^3} \right), \end{aligned} \quad (6.1)$$

where M_* is the mass of the star, m' is the mass of the perturber, and $\Delta = \|\mathbf{r} - \mathbf{r}'\|$ is the distance between the test particle and the perturber. We introduce for the perturbed particle the canonical modified Delaunay action-angle variables $(\Lambda, \Gamma, \lambda, \gamma)$, given by²

$$\begin{aligned} \Lambda &= \sqrt{\mathcal{G}M_* a}, & \lambda &= \ell + \varpi, \\ \Gamma &= \sqrt{\mathcal{G}M_* a(1 - \sqrt{1 - e^2})}, & \gamma &= -\varpi, \end{aligned} \quad (6.2)$$

where, as usual, a is the semi-major axis, e is the eccentricity, λ is the mean longitude, $\ell = E - e \sin E$ is the mean anomaly, and ϖ is the longitude of pericentre of the test mass, obtained from the Cartesian coordinates through (2.76). The perturber is assumed to follow a given Keplerian orbit, so \mathbf{r}' is a function of time; its Cartesian coordinates can also be expressed in terms of orbital elements (a', e', ℓ', ϖ') using Equation (2.76) (with primed quantities). In order to make the system autonomous, we extend the phase space (cfr. Subsect. 2.1.2.1) by introducing for the perturber

$$\Lambda', \quad \lambda' = \ell' + \varpi' = n'(t - t_0), \quad (6.3)$$

where $n' = \sqrt{\mathcal{G}(M_* + m')/a'^3}$ is the mean motion of the perturber. We assume that the perturber does not precess, so without loss of generality we set $\varpi' = 0$. Now the autonomous Hamiltonian of the system reads

$$\mathcal{H}(\Lambda, \Gamma, \Lambda', \lambda, \gamma, \lambda') = -\frac{\mathcal{G}^2 M_*^2}{2\Lambda^2} + n'\Lambda' + \mathcal{H}_{\text{pert}}(\Lambda, \Gamma, \lambda, \gamma, \lambda'; e', \varpi' = 0), \quad (6.4)$$

²Recall that in the restricted problem the Delaunay set for the massless particle is obtained from (2.82) eliminating the factor μ from the actions and putting the mass to zero, cfr. the end of Subsect. 2.2.1.

where the perturbation part $\mathcal{H}_{\text{pert}}$ is to be written in terms of the newly defined variables. We note that it depends parametrically on the arbitrary values of e' and $\varpi' = 0$.

We now consider the test particle to be close to an inner mean motion resonance with the outer perturber. In other words, we assume $kn - k'n' \sim 0$, where $n = \sqrt{\mathcal{G}M_*/a^3}$ is the mean motion of the test particle for some positive integers k, k' , such that $k' > k$. In order to study the resonant dynamics, it is possible to introduce a set of canonical resonant action-angle variables:

$$\begin{aligned} S &= \Gamma, & \sigma &= \frac{k'\lambda' - k\lambda + (k' - k)\gamma}{(k' - k)}, \\ P &= \frac{k' - k}{k}\Lambda + \Gamma, & \nu &= \frac{-k'\lambda' + k\lambda}{(k' - k)} = -\sigma + \gamma, \\ \tilde{\Lambda}' &= \Lambda' + \frac{k'}{k}\Lambda, & \tilde{\lambda}' &= \lambda'. \end{aligned} \tag{6.5}$$

The historical reason for adopting these variables is that for $e' = 0$ there is no harmonic term in ν in the Hamiltonian and thus P is a constant of motion. The reason why the critical resonant angle σ is not simply defined as $k'\lambda' - k\lambda + (k' - k)\gamma$ is explained in [Lemaitre(1984)] and is due to the d'Alembert rules (cfr. Subsect. 2.2.2.1): the coefficient of the terms $\cos[l(k'\lambda' - k\lambda + (k' - k)\gamma)]$ in the Fourier expansion of the perturbing Hamiltonian is proportional to $e^{|k' - k|}$ for small values of e . Thus, for small eccentricities the Hamiltonian is a polynomial expression in $e \cos \sigma$ and $e \sin \sigma$, and the apparent singularity at $e = 0$ can be removed.

Using the variables (6.5), the Keplerian part of the Hamiltonian takes the form

$$\mathcal{H}_{\text{kepl}}(S, P, \tilde{\Lambda}') = -\mathcal{G}^2 M_*^2 \frac{(k' - k)^2}{2k^2(P - S)^2} + n' \left[\tilde{\Lambda}' - \frac{k'}{(k' - k)}(P - S) \right]. \tag{6.6}$$

At this point, we average the Hamiltonian over the fast angles; as in Chapters 3 and 4, this is equivalent to a perturbative elimination of the non-resonant harmonics, up to first order in the mass of the perturber (cfr. Subsect. 2.3.1). From a computational point of view, a remark is in order. The Cartesian components given by (2.76) applied to the perturbed and the perturber are expressed in terms of the eccentric anomalies E, E' . Thus, it would be necessary to invert Kepler's equation $\lambda - \varpi = \ell = E - e \sin E$ (Equation (2.73)) to obtain $E = E(\lambda)$, and similarly for $E' = E'(\lambda')$. If e' is not too large, as in the case of the family of equilibrium points computed in Chapter 3 in the non-expanded case, the latter inversion is not problematic. However the eccentricity e of the test particle can reach high values, and solving the Kepler equation for the test particle becomes numerically cumbersome. Therefore, it is advisable to retain the dependence on the eccentric anomaly E , use the differential relationship $d\lambda = (1 - e \cos E) dE$, and integrate over E instead. This is more convenient because the dependence of λ on E is given through Kepler's equation by an explicit formula. We also note that λ is related to λ' through σ by $\lambda' = [k\lambda - (k' - k)(\gamma - \sigma)]/k'$. In summary, using the resonant relationship and Kepler's equation one obtains E' from λ' , λ' from λ , and λ from E , so that the averaging over E eliminates the short periodic dependence of the Hamiltonian. By doing so, the canonical angle λ' vanishes from the averaged Hamiltonian, and $\tilde{\Lambda}'$ becomes a constant of motion, so that the term $n'\tilde{\Lambda}'$ can be dropped from (6.6).

Proceeding this way, after the averaging procedure the perturbation $\mathcal{H}_{\text{pert}}$ reduces to

$$\mathcal{H}_{\text{res}}(S, P, \sigma, \nu) := \frac{1}{2\pi k'} \int_0^{2\pi k'} \mathcal{H}_{\text{pert}} \cdot (1 - e \cos E) dE; \tag{6.7}$$

it is important to note that we integrate over E from 0 to $2\pi k'$ instead of just 2π because, as already pointed out in Section 3.1, only after k' revolutions of the test particle around the star (which correspond to k revolutions of the outer perturber) does the system attain the initial configuration, thus recovering the complete periodicity of the Hamiltonian. The integral (6.7) can be solved numerically. In our code we use a Mathematica function with an imposed relative accuracy of 10^{-10} . For the Keplerian part we just write

$$\bar{\mathcal{H}}_{\text{kepl}}(S, P) := -\mathcal{G}^2 M_*^2 \frac{(k' - k)^2}{2k^2(P - S)^2} - n' \frac{k'}{(k' - k)}(P - S). \tag{6.8}$$

The averaged Hamiltonian then becomes

$$\bar{\mathcal{H}}(S, P, \sigma, \nu) := \bar{\mathcal{H}}_{\text{kepl}} + \mathcal{H}_{\text{res}}. \tag{6.9}$$

This two degree of freedom system is not integrable in general, unless further approximation is made.

6.3 Studying the averaged Hamiltonian

We now intend to study quantitatively the dynamics given by the Hamiltonian (6.9). This can be seen as an integrable system (i.e. the Keplerian part), to which a small perturbation of order $\mu = m'/M_* \ll 1$ is added.

We begin by noticing that $\bar{\mathcal{H}}_{\text{kepl}}$ only depends on $P - S$, so it is convenient to introduce the canonical variables

$$\begin{aligned} \Sigma &= S - P, & \sigma, \\ P, & & p = \sigma + \nu = \gamma, \end{aligned} \tag{6.10}$$

making $\bar{\mathcal{H}}_{\text{kepl}}$ a function of Σ alone. The location of exact resonance is given by the value $\Sigma = \Sigma_{\text{res}}$ such that

$$\frac{\partial \bar{\mathcal{H}}_{\text{kepl}}}{\partial \Sigma}(\Sigma_{\text{res}}) = 0, \quad \text{i.e. } \Sigma_{\text{res}} = -(\mathcal{G}M_*)^{2/3} \frac{(k' - k)}{(k^2 k' n')^{1/3}}, \tag{6.11}$$

which is simply $n = n_{\text{res}} = (k'/k)n'$. The expansion of $\bar{\mathcal{H}}_{\text{kepl}}$ in $\Delta\Sigma = \Sigma - \Sigma_{\text{res}}$ starts with a quadratic term in $\Delta\Sigma$. Since the perturbation \mathcal{H}_{res} is a function of (Σ, P, σ, p) and is of order μ , the dynamics in the canonical pair of variables (Σ, σ) near Σ_{res} is equivalent to that of a pendulum with Hamiltonian of the form $(\Delta\Sigma)^2 + \mu \cos \sigma$, so its frequency is of order $\sqrt{\mu}$. On the other hand, the dynamics in the canonical pair (P, p) is slower, with a characteristic frequency of order μ . We can therefore apply the adiabatic principle and study the dynamics in (Σ, σ) with fixed (P, p) , and then the dynamics in (P, p) keeping constant the action integral

$$J = \oint \Sigma d\sigma, \tag{6.12}$$

which is the adiabatic invariant of the dynamics ([Henrard(1993)], see also Subsect. 2.3.2).

We now explain this procedure in more detail. Once the values of P and p have been fixed, $\bar{\mathcal{H}}$ reduces to a one degree of freedom Hamiltonian in (Σ, σ) and parametrized by (P, p) , which we denote by $\bar{\mathcal{H}}_{(P,p)}(\Sigma, \sigma)$. This Hamiltonian is therefore integrable, so we can study its dynamics by plotting its level curves. We note however that by fixing P we can obtain Σ from e and vice versa, so we can also use $(e \cos \sigma, e \sin \sigma)$ as independent variables. Although these variables are not canonical, they have the already mentioned advantage that for small e the Hamiltonian is a polynomial in $(e \cos \sigma, e \sin \sigma)$, so the level curves do not have a singularity at $e = 0$. In addition, the plot of the level curves does not require the use of canonical variables. We show examples of these plots in the case of the 4:1 resonance in Figure 6.1.

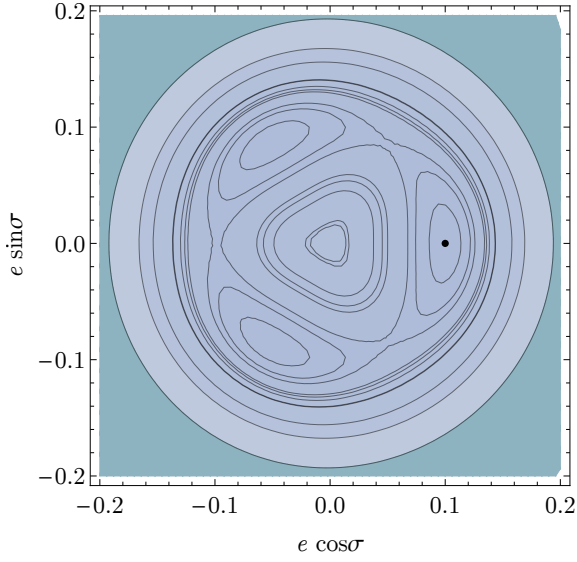
In principle, the dynamics can be studied for any value of J . Once the cycle of $\bar{\mathcal{H}}_{(P,p)}(\Sigma, \sigma)$ corresponding to the considered value of J through (6.12) is identified, the full Hamiltonian $\bar{\mathcal{H}}(\Sigma, \sigma, P, p)$ is averaged over the cycle, as explained in [Henrard(1993)], leading to a new one degree of freedom Hamiltonian $\bar{\mathcal{H}}(P, p; J)$. This Hamiltonian is integrable, and the resulting dynamics in (P, p) describes the secular evolution of the small body inside the mean motion resonance with the perturber.

In this work we vastly simplify this procedure by limiting ourselves to the case $J \rightarrow 0$, i.e. the limit of small libration amplitude in the mean motion resonance. In this limit, the cycle in (Σ, σ) described by $\bar{\mathcal{H}}_{(P,p)}$ shrinks to the stable equilibrium point. Thus, there is no need to average the full Hamiltonian over a cycle: $\bar{\mathcal{H}}(P, p; J = 0)$ is obtained by evaluating $\bar{\mathcal{H}}$ on the stable equilibrium point of $\bar{\mathcal{H}}_{(P,p)}$ in the variables e and σ . We note that by having fixed P , we are effectively linking the semi-major axis a to the eccentricity e , via the relation

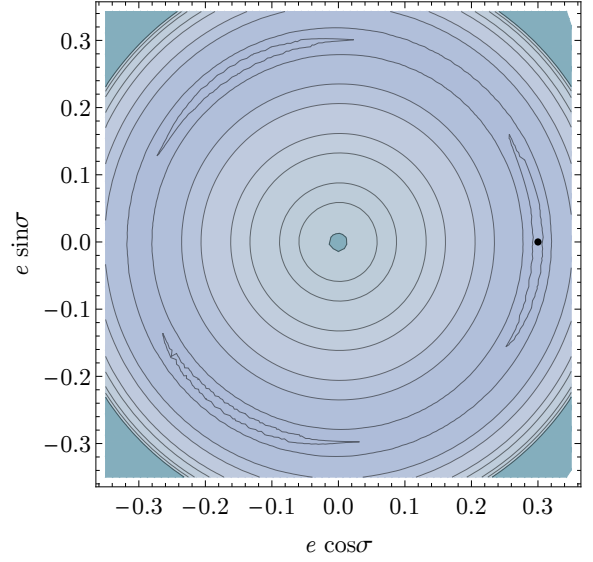
$$a = \frac{P^2}{\mathcal{G}M_* \left(k'/k - \sqrt{1 - e^2} \right)^2}; \tag{6.13}$$

therefore, we recover the equilibrium values a_{eq} of the semi-major axis as well.

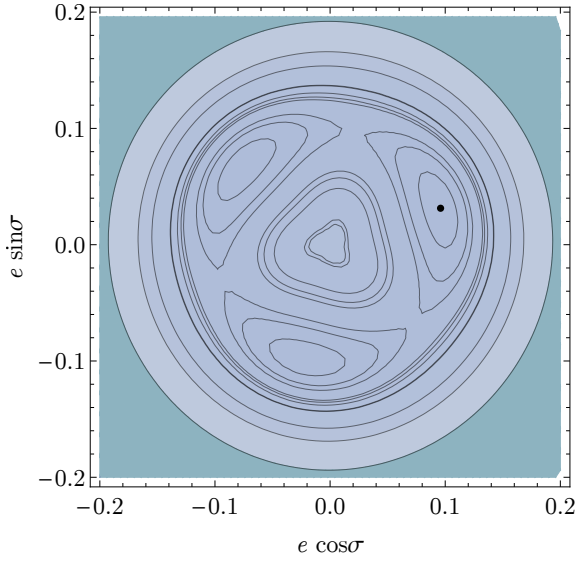
We show an example of this calculation in Figure 6.2, for the 2:1, 3:1, and 4:1 resonances. It is worth pointing out that the equilibrium points in the (e, a) diagram deviate away from the Keplerian resonant value $a_{\text{res}} = a'(k/k')^{2/3}$ as $e \rightarrow 0$. This is especially evident in the case of first-order resonances, $|k - k'| = 1$, as we already discussed in Chapters 3 and 4. In this case, for $e > e'$ the main harmonic in the Hamiltonian is $e \cos \sigma$, i.e. $\sqrt{\Gamma} \cos \sigma$, from (6.2) and expansion for small e . Because $\dot{p} = \partial \mathcal{H} / \partial \Gamma$, this harmonic gives $\dot{p} \propto 1/\sqrt{\Gamma} \sim 1/e$, which grows considerably as e approaches zero; therefore, in order to maintain $\dot{\sigma} = [k'\dot{\lambda}' - k\dot{\lambda} + (k' - k)\dot{p}]/(k' - k) \sim 0$, it is necessary to have $k'\dot{\lambda}' - k\dot{\lambda} \approx 0$ i.e. $a/a' \approx (k/k')^{(2/3)}$. For resonances of order $|k' - k| > 1$ the main harmonic in the Hamiltonian for $e > e'$ is $e^{|k' - k|} \cos \sigma$, i.e. $\Gamma^{|k' - k|/2} \cos \sigma$. Therefore, the first derivative in Γ is not singular for $e \sim \sqrt{\Gamma} \rightarrow 0$. However, for $e < e'$ the main harmonic dependent on e is $e^{|k' - k| - 1} e \cos[(k' - k)\sigma - (k' - k - 1)(p + \varpi')]$, which



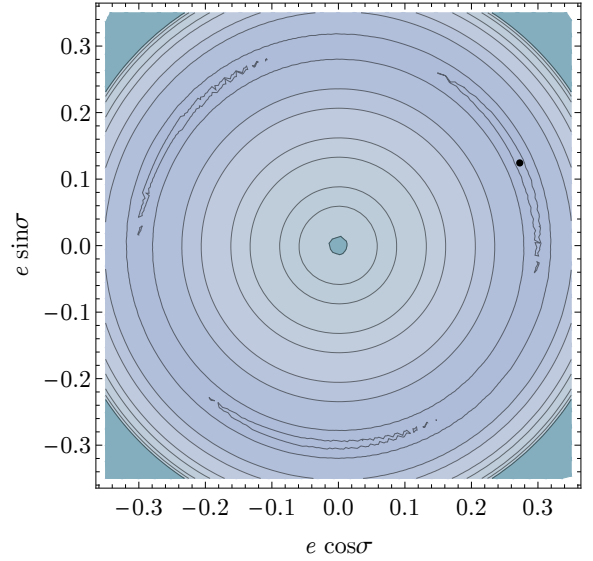
(a) $P = 1.893, p = 0$.



(b) $P = 1.919, p = 0$.



(c) $P = 1.893, p = \pi/8$.



(d) $P = 1.919, p = \pi/8$.

Figure 6.1: Level plots of the Hamiltonian $\bar{\mathcal{H}}_{(P,p)}(\Sigma, \sigma)$ on the $(e \cos \sigma, e \sin \sigma)$ plane for different values of P and p . This is the case of $k' = 4, k = 1$, with $e' = 0.1, a' = 1$ AU, and $\mu = 10^{-3}$ for the perturber (in units where $\mathcal{G}M_* = 1$). The black dot in each panel indicates the position of the stable equilibrium point that is found by our algorithm. The function $\bar{\mathcal{H}}_{(P,p)}$ is periodic in σ with period $2\pi/(k' - k)$, so there will always be $k' - k$ equivalent stable equilibria one rotation away from each another. We note that e_{eq} increases with P , while p has the effect of simply rotating the diagram.

gives a contribution to \dot{p} proportional to $1/e$, and the same reasoning applies. Indeed, in the case of inner mean motion resonance, a_{eq} always attains values that are slightly less than the Keplerian a_{res} as $e \rightarrow 0$, as shown in Figure 6.2. We must note, however, that the deviation of the equilibrium points away from the resonant value a_{res} indicates a rapid precession of the pericentre ϖ . This means that our assumption that p and P remain constant is no longer valid. It breaks down when their motion evolves with a frequency of order $\sqrt{\mu}$, i.e. of the same order as the frequency of the Σ, σ evolution. When $\dot{p} \sim \sqrt{\mu}$, the equilibrium semi-major axis of the test particle deviates from the Keplerian value by the amount of order $(2/3)(\sqrt{\mu}/k)(a_{\text{res}})^{5/2}$. Thus, we can determine the lower limit in eccentricity for the validity of our approach as the value of e at which the equilibrium point a_{eq} deviates away from a_{res} by more than this quantity. In this work, we will focus mainly on resonances of order higher than 1 because

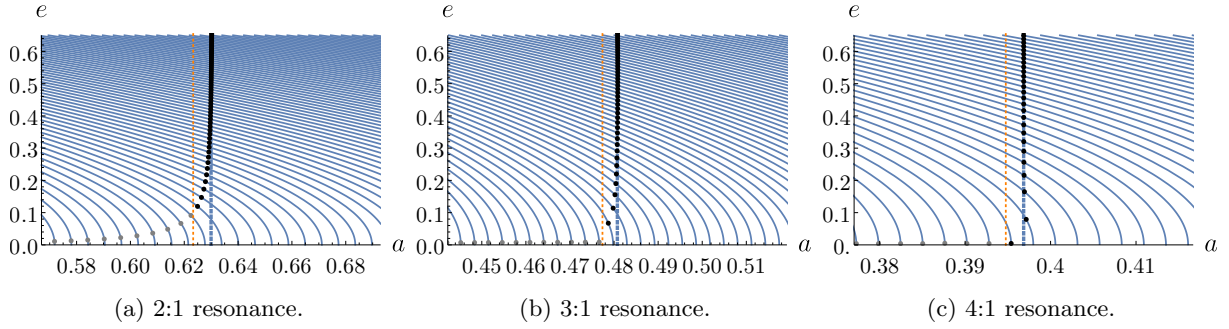


Figure 6.2: Level curves of P on the (a, e) plane for the case of the 2:1, 3:1, and 4:1 resonances with $a' = 1$ AU for the perturber (in units where $\mathcal{G}M_* = 1$). The solid lines depict equation (6.13), where the numerical value of P increases from left to right. The vertical thick dashed lines indicate the location of exact Keplerian resonance, $a_{\text{res}} = a'(k/k')^{2/3}$. The dots represent the equilibrium values for the eccentricity and the semi-major axis on different level curves of P , while the arbitrary value of ϖ remains fixed. Here we used $e' = 0.2$ and $\mu = 10^{-3}$. We note that the equilibrium points deviate away from exact resonance at low eccentricities, which is particularly evident in the case of first-order resonances (the 2:1 resonance in this case; see text for details). Since this deviation is linked to a faster precession of the pericentre $\varpi = -p$, the value of e at which this effect becomes higher than $(2/3)(\sqrt{\mu}/k)(a_{\text{res}})^{5/2}$ yields a lower bound in e above which our approach is valid. The orange dashed line indicates a deviation from the exact resonance of this amount. We thus colour-coded the equilibrium points using black for those that fall above this lower limit in eccentricity, and grey for those that fall below it: for the latter, the fast change in p does not allow us to consider the pair (P, p) as slowly evolving variables.

they are much more efficient in pushing the eccentricity e from ~ 0 to ~ 1 (see Section 6.5). In this case, for $e < e'$ our approach is valid down to very small values of the eccentricity.

We have implemented this scheme in a Mathematica notebook, which is included in Appendix D. Let us now briefly explain the steps in our calculation, which ultimately yields the level curves of the Hamiltonian $\bar{\mathcal{H}}(P, p; J = 0)$ on the $(e \cos \varpi, e \sin \varpi)$ plane, thereby describing the secular evolution of the small body inside the mean motion resonance with the perturber, in the limit of $J = 0$. First, we consider a fixed value of $P = P^*$. For some given value of ϖ , we can find the (stable) equilibrium point in the $(e \cos \sigma, e \sin \sigma)$ plane in the following manner. If $\varpi = \varpi_0 = 0$, the Hamiltonian (6.9) contains only cosines of $(k' - k)\sigma$ (and its multiples) so that its extrema in σ are found at $2\pi l/(k' - k)$ and $(2\pi l + \pi)/(k' - k)$, $l \in \mathbb{Z}$. Taking for example $\sigma = \sigma_0 = 0, \pm\pi$, we can write the Hamiltonian (6.9) as $\bar{\mathcal{H}}(e, P^*, \sigma_0, \varpi_0)$ and we can find its maximum as a function of the eccentricity. The fact that $\bar{\mathcal{H}}$, as a function of e , must have a maximum at the resonance can be seen from (6.8), which clearly has a maximum in $\Sigma = S - P$ at Σ_{res} (defined in (6.11)). Then, because $\frac{\partial^2 \bar{\mathcal{H}}}{\partial \Sigma^2} = \frac{\partial^2 \bar{\mathcal{H}}}{\partial S^2}$ and S is monotonic in e , $\bar{\mathcal{H}}$ must have a maximum in e . We call e_{max} the value of the eccentricity for which $\bar{\mathcal{H}}$ is maximal. We must now check that this is in fact the stable equilibrium point, i.e. that in σ_0 the function $\bar{\mathcal{H}}(e_{\text{max}}, P^*, \sigma, \varpi_0)$ of σ has a maximum (and not a minimum). If this is not the case, we can repeat the calculation with $\sigma = \pi/(k' - k), \pi/(k' - k) + \pi$. Although in principle the maximum in σ could be away from this axis (because of the higher order harmonics in $(k' - k)\sigma$), in practice in all the cases we studied this procedure effectively yields, for the given value of $P = P^*$ and for $\varpi = \varpi_0 = 0$, the stable equilibrium point in (e, σ) , denoted by $(e_{\text{eq}}, \sigma_{\text{eq}})$. We note from Figure 6.1 that e_{eq} increases with the value P^* .

Following the procedure described above, we can assign to the Hamiltonian $\bar{\mathcal{H}}(P^*, \varpi_0; J = 0)$ the value $\bar{\mathcal{H}}(e_{\text{eq}}, P^*, \sigma_{\text{eq}}, \varpi_0)$ on the point $(e_{\text{eq}} \cos \varpi_0, e_{\text{eq}} \sin \varpi_0)$. We also note that from the equilibrium value e_{eq} , it is possible to obtain the corresponding a_{eq} through equation (6.13). When ϖ is not zero, the diagram in the $(e \cos \sigma, e \sin \sigma)$ plane is, to a good approximation³ for most values of e , simply rotated by a quantity related to ϖ , so that the equilibrium values of the eccentricity and the semi-major axis do not change substantially, but only σ_{eq} changes (see Figure 6.1). This way, it is possible to obtain the equilibrium value for σ by finding the maximum in σ of the function $\bar{\mathcal{H}}(e_{\text{eq}}, P^*, \sigma, \varpi)$ for the fixed value of ϖ . It is worth noticing that in order to assign to the point $(e_{\text{eq}} \cos \varpi, e_{\text{eq}} \sin \varpi)$ the appropriate value of the Hamiltonian, we are only interested in the $\max_{\sigma \in [0, 2\pi]} \bar{\mathcal{H}}(e_{\text{eq}}, P^*, \sigma, \varpi) = \max_{\sigma \in [0, 2\pi/(k' - k)]} \bar{\mathcal{H}}(e_{\text{eq}}, P^*, \sigma, \varpi)$ for the fixed value of ϖ , not in the actual value σ_{eq} of σ where the maximum is attained. However, we need to check that σ_{eq} changes smoothly with P^* and ϖ . If this were not the case, a bifurcation would occur, which would invalidate the assumption that the amplitude of

³We have checked that in the 4:1 resonance e_{eq} changes only by $\lesssim 0.1\%$ with the rotation of ϖ , down to $e_{\text{eq}} \sim 0.05$, for $e' = 0.1$.

libration remains small. We have checked that this happens only in the case of the 3:1 resonance in a point on the $\varpi = 0$ axis (e.g. at $e \simeq 0.35$ in Figure 6.7(b)). We note that this point is never crossed during the secular evolution because it appears as a centre of libration.

By letting P vary, i.e. effectively by allowing e_{eq} to vary, we obtain the level curves of the Hamiltonian $\bar{\mathcal{H}}(P, p; J = 0)$ in the variables $(e \cos \varpi, e \sin \varpi)$. We present several examples in Section 6.5, where we show level curves of $\bar{\mathcal{H}}$ for different resonances and different values of e' .

6.4 Effect of short-range forces

When the eccentricity of the test mass reaches values close to 1, so that the osculating ellipse becomes narrower and narrower, the periastron distance from the star $a_{\text{peri}} = a(1 - e)$ becomes considerably small. At this point, the effect of various short-range forces may become important and must be considered. One such short-range force arises from General Relativity, with the post-Newtonian contribution to the test particle's Hamiltonian given by

$$\mathcal{H}_{\text{GR}} = \frac{\mathcal{G}M_*}{a} \left(\frac{\mathcal{G}M_*}{ac^2} \right) \left(\frac{15}{8} - \frac{3}{\sqrt{1 - e^2}} \right), \quad (6.14)$$

where c is the speed of light ([Krivov(1986)]). We note that the 15/8 term only gives the General Relativity correction to the mean motions, while the $1/\sqrt{1 - e^2}$ term gives the correction to the precession of the pericentre. Since we are only interested in the latter and we have averaged over the mean motion, we drop the former. Another short-range force arises from the rotational bulge of the central star, with the Hamiltonian given by

$$\mathcal{H}_{\text{rot}} = -\frac{\mathcal{G}M_*R_*^2J_2}{2a^3(1 - e^2)^{3/2}}, \quad (6.15)$$

where R_* is the stellar radius, and $M_*R_*^2J_2$ is the rotation-induced quadrupole moment of the star. To assess the importance of these short-range forces, we compare \mathcal{H}_{GR} and \mathcal{H}_{rot} to Φ_0 , the characteristic tidal potential produced by the planetary perturber on the test particle,

$$\Phi_0 \equiv \frac{\mathcal{G}m'a^2}{a'^3}. \quad (6.16)$$

We find

$$\begin{aligned} \frac{|\mathcal{H}_{\text{GR}}|}{\Phi_0} &\simeq 10^{-2} \left(\frac{M_*}{M_\odot} \right)^2 \left(\frac{m'}{M_\oplus} \right)^{-1} \left(\frac{a'}{a} \right)^3 \left(\frac{a}{1 \text{ AU}} \right)^{-1} \frac{1}{(1 - e^2)^{1/2}} \\ &\simeq 1.7 \left(\frac{M_*}{M_\odot} \right)^2 \left(\frac{m'}{M_\oplus} \right)^{-1} \left(\frac{n}{4n'} \right)^2 \left(\frac{a}{1 \text{ AU}} \right)^{-1/2} \left(\frac{a_{\text{peri}}}{R_\odot} \right)^{-1/2}, \end{aligned} \quad (6.17)$$

$$\begin{aligned} \frac{|\mathcal{H}_{\text{rot}}|}{\Phi_0} &\simeq \frac{k_{q*}\hat{\Omega}_*^2}{2} \left(\frac{M_*}{m'} \right) \left(\frac{R_*}{a} \right)^2 \left(\frac{a'}{a} \right)^3 \frac{1}{(1 - e^2)^{3/2}} \\ &\simeq 0.086 \left(\frac{k_{q*}}{0.01} \right) \left(\frac{P_*}{10 \text{ days}} \right)^{-2} \left(\frac{R_*}{R_\odot} \right)^5 \left(\frac{m'}{M_\oplus} \right)^{-1} \left(\frac{n}{4n'} \right)^2 \left(\frac{a}{1 \text{ AU}} \right)^{-1/2} \left(\frac{a_{\text{peri}}}{R_\odot} \right)^{-3/2}, \end{aligned} \quad (6.18)$$

where $a_{\text{peri}} = a(1 - e)$, and we use $J_2 = k_{q*}\hat{\Omega}_*^2 = k_{q*}\Omega_*^2R_*^3/(GM_*)$, with $\Omega_* = 2\pi/P_*$ the stellar rotation rate. Clearly, for most main-sequence stars (with $P_* \gtrsim 2$ days) and White Dwarfs, $|\mathcal{H}_{\text{rot}}|$ is negligible compared to $|\mathcal{H}_{\text{GR}}|$. We neglect \mathcal{H}_{rot} in the remainder of our analysis.

It is straightforward to include \mathcal{H}_{GR} into the scheme outlined in Section 6.3 as we simply need to add the value $\mathcal{H}_{\text{GR}}(a_{\text{eq}}, e_{\text{eq}})$ to the value of the planetary Hamiltonian. This could change the dynamics of the system considerably at sufficiently high eccentricity. In fact, up to this point, the perturber's mass (rescaled by the star's mass) μ has played a role in setting the amplitude of libration in Σ (or a, e) in the Hamiltonian $\bar{\mathcal{H}}_{(P,p)}$, and in setting the frequency of libration around the stable equilibrium point. However, the dynamics described by $\bar{\mathcal{H}}(P, p; J = 0)$ does not depend on the perturber's mass because both P and p appear only in the part of the Hamiltonian derived from \mathcal{H}_{res} , where μ is a multiplying parameter. Thus, the evolution of e as a function of $\varpi = -p$ does not depend on μ , only the timescale of this evolution does (and scales as $1/\mu$).

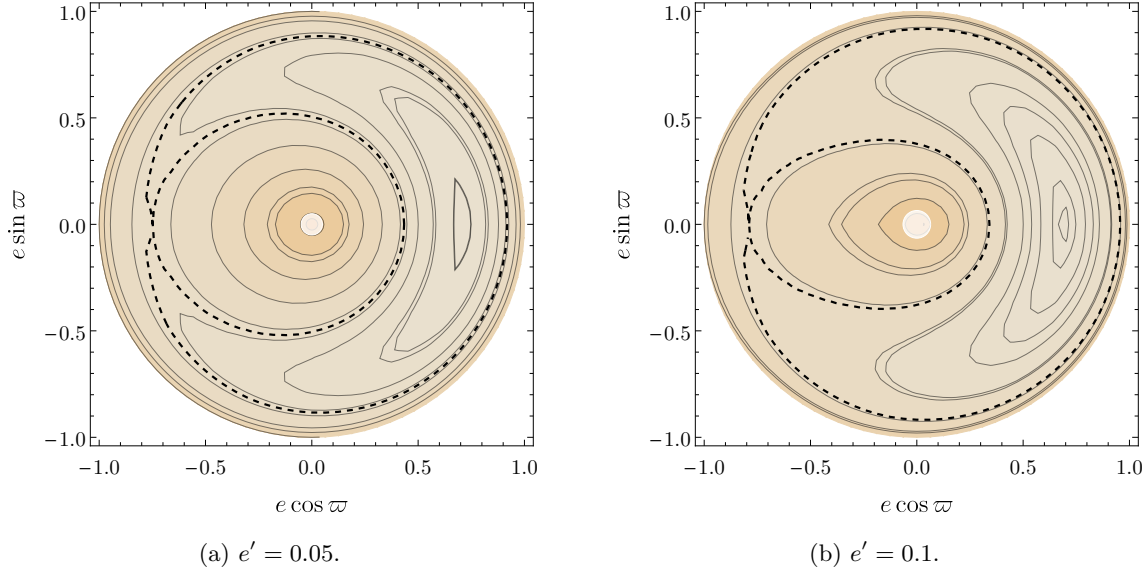


Figure 6.3: Level curves of the Hamiltonian $\bar{\mathcal{H}}$ on the $(e \cos \varpi, e \sin \varpi)$ plane for the 2:1 mean motion resonance with an outer perturber for low values of e' ($=0.05$ and 0.1 , both with $\varpi' = 0$). The General Relativity effect is not included. Lighter colours indicate a higher value of the Hamiltonian. The white shaded discs centred at the origin indicate the regions where the adiabatic method is not valid (see Section 6.3), i.e. where our calculations do not necessarily reflect the true dynamics of the system. The dark dashed line indicates a set of critical orbits which separate the phase space into a circulation zone near the origin, a libration zone near the stable equilibrium point at $\varpi = 0$, and an outer circulation region. All orbits with initially low eccentricities do not experience an appreciable increase in e .

With the addition of the General Relativity term in the Hamiltonian, the dynamical behaviour of the system will in general depend on μ . Indeed, \mathcal{H}_{GR} is independent of μ , and is dependent on P :

$$\mathcal{H}_{\text{GR}}(\Sigma, P, \sigma, p) = \frac{3\mathcal{G}^4 M_*^4}{c^2} \frac{(k' - k)^4}{k^3 \Sigma^3 (kP - (P + \Sigma)k')}. \quad (6.19)$$

Thus, the actual evolution of P (i.e. of e_{eq} if $J = 0$) as a function of p (i.e. ϖ) depends on the value of μ .

Another way to understand this is that the General Relativity potential has the effect of keeping the eccentricity constant while the pericentre $\varpi = -p$ precesses (because $\dot{p} = \frac{\partial \mathcal{H}_{\text{GR}}}{\partial P} = -\frac{3\mathcal{G}^4 M_*^4}{c^2} \frac{(k' - k)^5}{k^3 \Sigma^3 (kP - (P + \Sigma)k')^2} < 0$ while $\dot{P} = 0$, $\dot{\Sigma} = 0$). In contrast, in the restricted three-body problem (see previous section) the precession of the pericentre is coupled with the variation in the eccentricity. Since the mass of the perturber μ appears in the planetary potential as a multiplicative factor in the perturbation, but not in the General Relativity potential, it will play the role of a parameter regulating which of the two dynamics in the $(e \cos \varpi, e \sin \varpi)$ plane is dominant. The smaller μ is, the more the General Relativity contribution will prevail, and the less efficient the planet will be in pumping the eccentricity of the test particle; the bigger μ is, the less the \mathcal{H}_{GR} contribution will be apparent.

6.5 Results

In Figures 6.3, 6.4, and 6.5 we show the level curves of the Hamiltonian $\bar{\mathcal{H}}$ (see Section 6.3) on the $(e \cos \varpi, e \sin \varpi)$ plane for the 2:1, 3:1, and 4:1 resonances, respectively, with low values of the eccentricity of the perturber, $e' = 0.05$ and $e' = 0.1$. The General Relativity effect is not included in these figures. The white shaded discs centred at the origin (barely visible in Figure 6.5) indicate the regions where the adiabatic method is not valid (see section 6.3); in these regions our calculations do not necessarily reflect the true dynamics of the system.

We note in Figure 6.5 how even for low values of e' the 4:1 resonance is extremely effective in driving the eccentricity of the test particle from $e \sim 0$ to $e \sim 1$. Indeed, there is only a small portion of the phase space that allows orbits starting with low eccentricities to circulate near the origin ($e = 0$). In the case of $e' = 0.05$ only some orbits with moderate initial eccentricities, i.e. $e > 0.2$ and initial $\varpi \sim 0$, actually librate around the stable

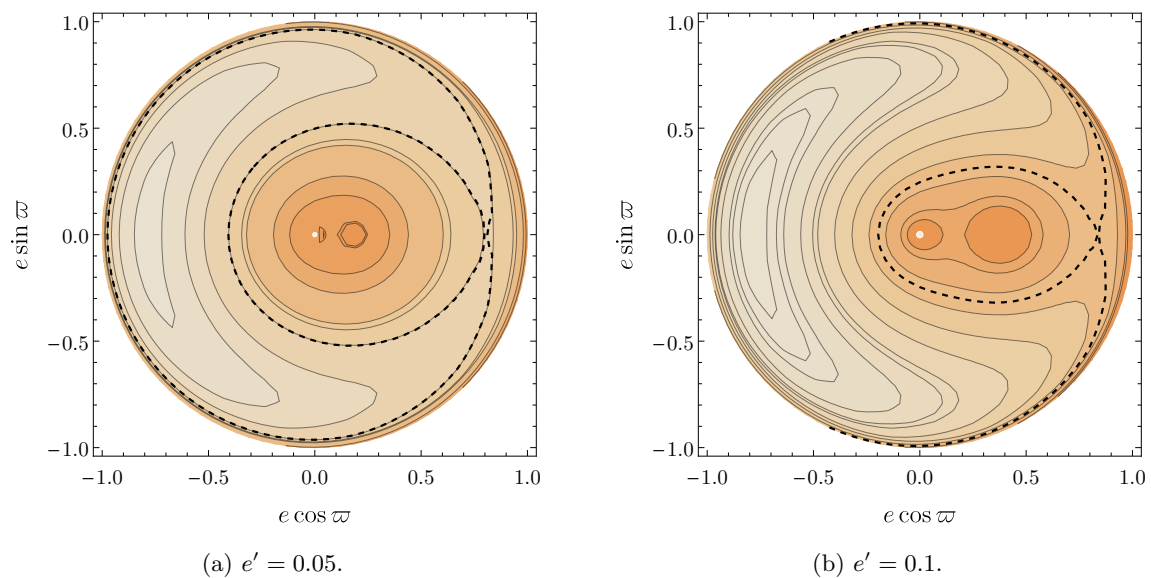


Figure 6.4: Same as Figure 6.3, but for the 3:1 mean motion resonance with an outer perturber.

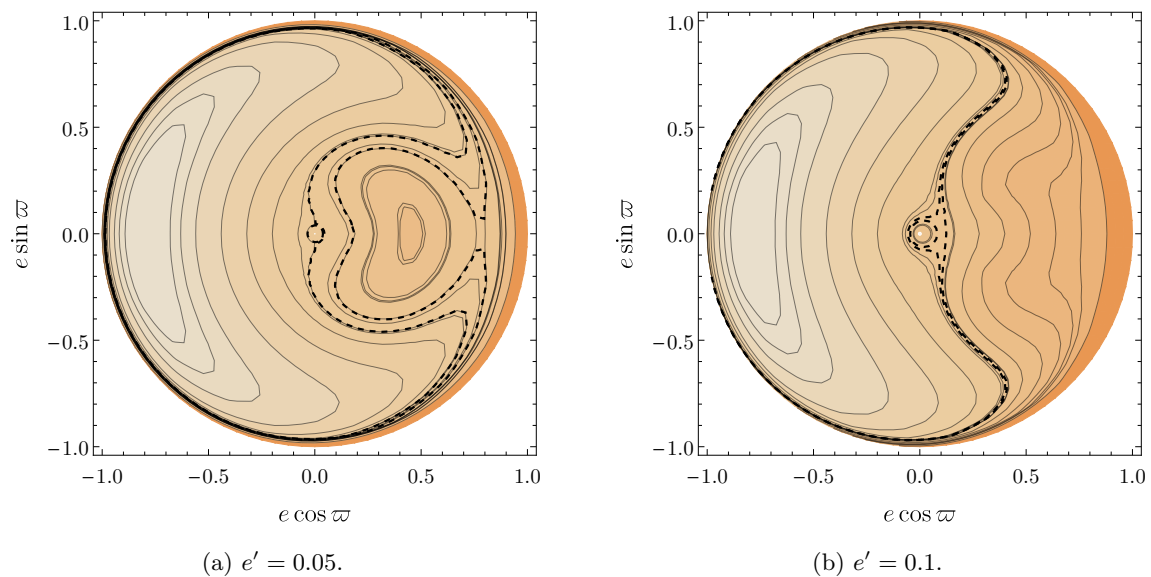


Figure 6.5: Same as Figure 6.3, but for the 4:1 mean motion resonance with an outer perturber. In contrast to Figures 6.3 and 6.4, orbits with small initial eccentricities can be driven to $e \sim 1$.

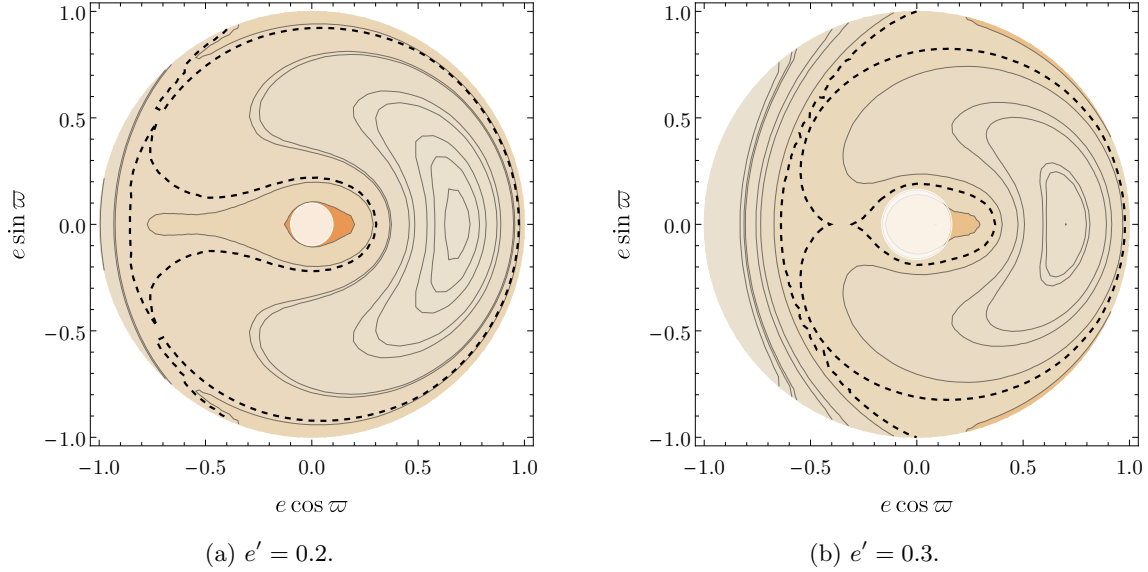


Figure 6.6: Level plots of the Hamiltonian $\bar{\mathcal{H}}$ on the $(e \cos \varpi, e \sin \varpi)$ plane for the 2:1 mean motion resonance with an outer perturber with modest eccentricities ($e' = 0.2$ and $e' = 0.3$, both with $\varpi' = 0$). All orbits with initially low eccentricities do not experience a large increase in e .

equilibrium point at $\varpi = 0$, $e \sim 0.4$, while for $e' = 0.1$, all orbits sufficiently distant from the origin eventually end up at $e \sim 1$. This is not the case for the other resonances. For the 2:1 resonance, we see from Figure 6.3 that all orbits with initial eccentricities up to ~ 0.4 and ~ 0.3 , for $e' = 0.05$ and $e' = 0.1$, respectively, remain confined around the equilibrium point near the origin. Another equilibrium point is present at $e \sim 0.7$, $\varpi = 0$, implying that whatever the initial values of ϖ even a higher initial eccentricity is not enough to push the test particle to a star-grazing orbit. Indeed, the presence of the separatrix (shown as a black dashed curve) does not allow any orbit with initial eccentricity lower than ~ 0.9 to move farther away from the origin. In the case of the 3:1 resonance, Figure 6.4 shows that eccentricities lower than 0.4 for $e' = 0.05$ and 0.2 for $e' = 0.1$ remain small, because the level curves librate around $\varpi = 0$. For $e' = 0.05$ a separatrix bounds the maximum attainable eccentricity as in the 2:1 resonance. This confirms the results in [Beust and Morbidelli(1996)].

Figures 6.6, 6.7, and 6.8 depict our results for high values of the perturber's eccentricity, $e' = 0.2$ and $e' = 0.3$. We find that for the 2:1 and 3:1 resonances, even these higher values of e' are not sufficient to generate star-grazing objects from $e \sim 0$. Although for some initial configurations it is possible to observe an excitation in the eccentricity (see e.g. the case of the 3:1 resonance in Figure 6.7(a), where particles with $e \sim 0.2$ and $\varpi = \pi$ may indeed reach $e \sim 1$), a modest/high initial eccentricity of the test particle is needed in order to eventually reach a value close to 1. On the other hand, Figure 6.8 shows that when the perturber's eccentricity is too high, the capability of the 4:1 resonance to raise the eccentricity of the test particle from ~ 0 to ~ 1 is diminished. In all cases (Figures 6.6 – 6.8), a separatrix confines all orbits close to the origin. We note that this separatrix occupies the region where the adiabatic method remains valid (see Section 6.3), i.e. outside the white shaded region in each plot. Therefore, any orbit with a small initial eccentricity remains confined to low values of e .

As we noted in Section 6.4, when the eccentricity of the test particle reaches sufficiently high values, the effect of the General Relativity term becomes important, and the mass parameter μ plays a crucial role in shaping the dynamics of the system. Led by our results shown in Figures 6.3-6.8, we restrict ourselves to the case of a test particle in the 4:1 mean motion resonance with the outer perturber, and we study the critical value μ_{crit} needed such that the periastron distance $a_{\text{peri}} = a(1 - e)$ reaches sufficiently small values, e.g. the radius of the central star or the star's Roche limit (which is $\sim R_{\odot}$, for White Dwarfs and asteroids with internal density about a few g cm^{-3}).

In Figure 6.9 we show the level curves of the Hamiltonian $\bar{\mathcal{H}}$ with $e' = 0.1$, on the $(\varpi, \log a_{\text{peri}})$ plane, both with and without the addition of the General Relativity contribution, for the case of $\mu = 3 \times 10^{-6}$. Here we choose the resonance location of the test particle a_{res} at 1 AU. We can clearly see that while in the purely planetary case the resonance is capable of pushing a test mass with a small initial eccentricity $e \sim 0.05$ into a star-grazing orbit, this does not hold true when \mathcal{H}_{GR} is introduced. In Figure 6.10 we repeat the calculation, this time with $\mu = 5 \times 10^{-5}$ and the same values for $a_{\text{res}} = 1$ AU and $e' = 0.1$, and we see that even with the General Relativity contribution,

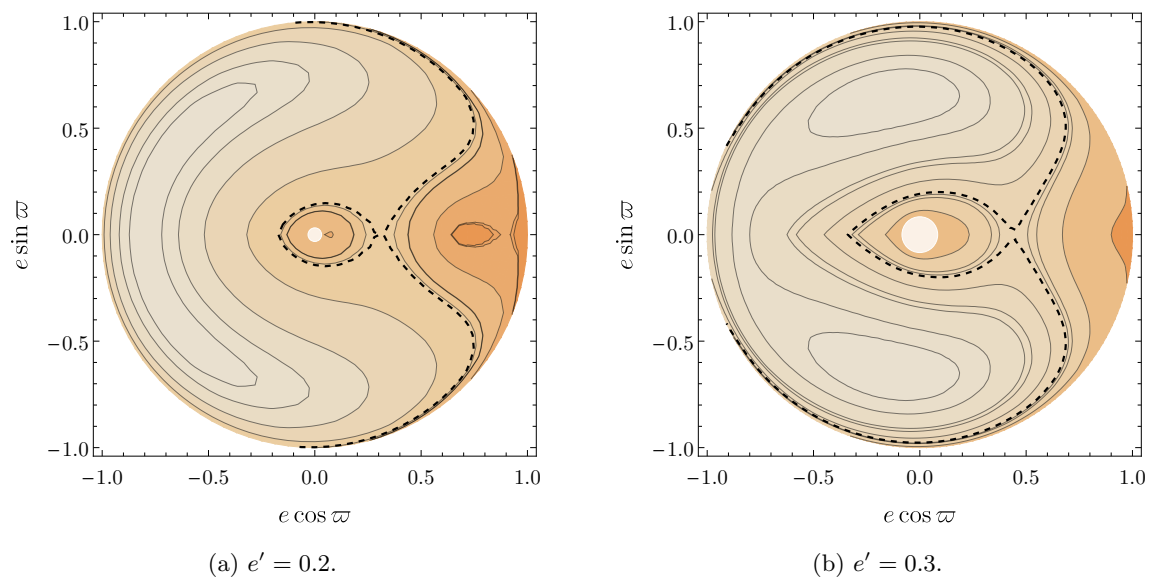


Figure 6.7: Same as Figure 6.6, but for the 3:1 mean motion resonance with an outer perturber.

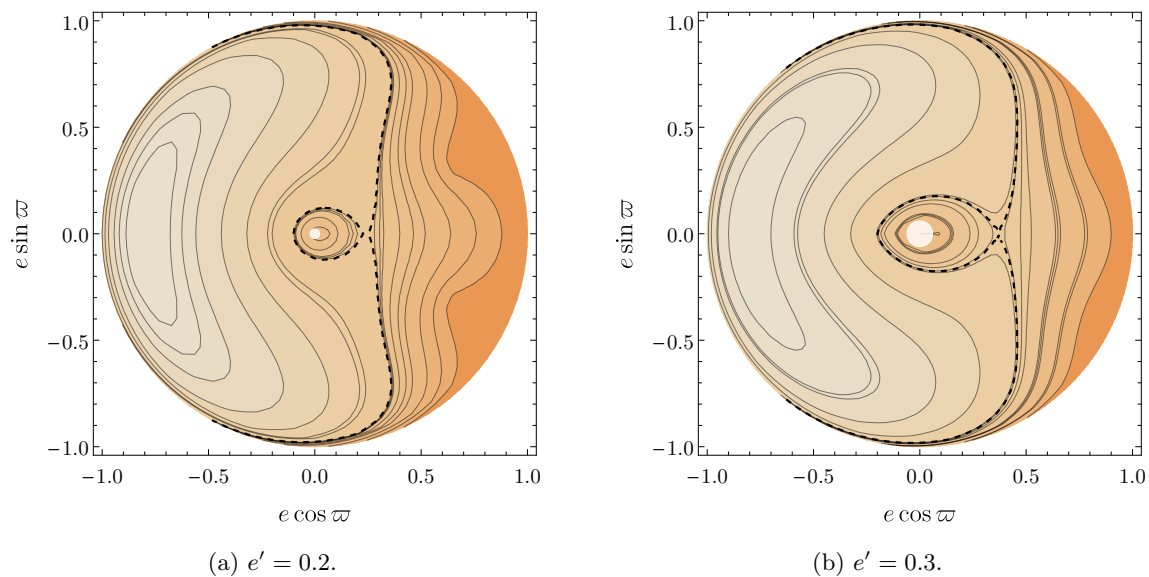


Figure 6.8: Same as Figure 6.6, but for the 4:1 mean motion resonance with an outer perturber. In contrast to Figure 6.5, orbits with initial $e \sim 0$ do not experience extreme eccentricity excitation.

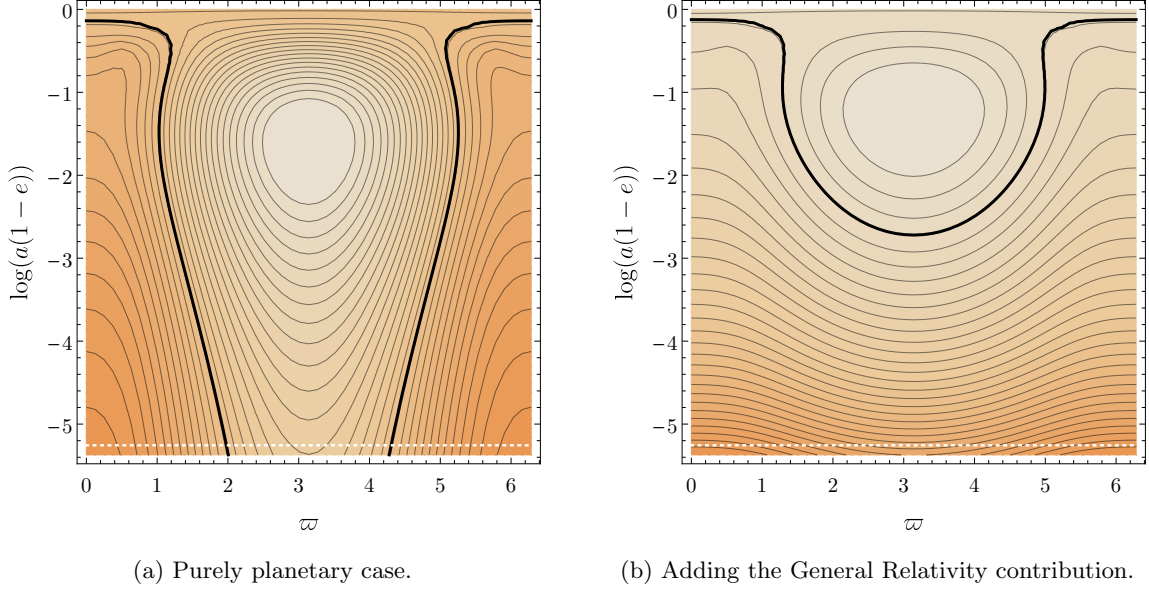


Figure 6.9: Level curves of the Hamiltonians $\bar{\mathcal{H}}$ (left panel) and $\bar{\mathcal{H}} + \mathcal{H}_{\text{GR}}$ (right panel) on the $(\varpi, \log a_{\text{peri}})$ plane for a test mass at $a_{\text{res}} = 1$ AU in 4:1 mean motion resonance with an outer perturber with $\mu = 3 \times 10^{-6}$, $\varpi' = 0$ and $e' = 0.1$. The mass of the parent star is set at $M_* = 1M_{\odot}$. The black solid line experiencing a significant change in a_{peri} indicates the trajectory with the initial conditions $\varpi = 0$ and $e = 0.05$. The lower edge of the plot is at the location of the radius of the star, here taken to be the radius of the Sun (R_{\odot}). The white dotted line indicates the location of the Roche limit, calculated using a density of the test particle of $\rho_{\text{tp}} = 2 \text{ g cm}^{-3}$. The addition of the General Relativity potential reduces drastically the efficiency of the planetary perturbation in driving the test particle to collide with the star.

test particles with initial small eccentricities are just about able to reach $a_{\text{peri}} \sim R_{\odot}$. Because the thick curve in Figure 6.10(b) is almost tangent to the bottom of the figure at $\varpi = \pi$, we deduce that the critical mass to achieve star-grazing orbits for this choice of a' and e' is close to 5×10^{-5} solar masses.

The critical perturber mass $\mu_{\text{crit}} = m'_{\text{crit}}/M_*$ can be estimated as follows. For a test particle near a given mean-motion resonance (4:1) with an external perturber (of given m', a', e'), the “secular” planetary Hamiltonian can be written schematically as

$$\bar{\mathcal{H}} = -\Phi_0 \hat{\mathcal{H}}(e, \varpi), \quad (6.20)$$

where

$$\Phi_0 \equiv \frac{\mathcal{G}m'a^2}{a'^3} \propto \frac{m'}{a}, \quad (6.21)$$

and $\hat{\mathcal{H}}$ is dimensionless. We note that in the above equation, a is really $a_0 = a'/4^{2/3}$ (the value of a in exact Keplerian resonance with the perturber). We assume that the test mass starts with an initial eccentricity $e_0 \ll 1$ at $\varpi = 0$. Its maximum eccentricity $e_{\text{max}}^{(0)}$ (achieved at $\varpi = \pi$) is determined by

$$\hat{\mathcal{H}}(e_0, 0) - \hat{\mathcal{H}}(e_{\text{max}}^{(0)}, \pi) = 0. \quad (6.22)$$

The superscript “(0)” in $e_{\text{max}}^{(0)}$ indicates that this maximum eccentricity is obtained without any short-range force effect.

Now we consider how \mathcal{H}_{GR} affects e_{max} . We write

$$\mathcal{H}_{\text{GR}} = -\frac{\Phi_{\text{GR}}}{\sqrt{1-e^2}}, \quad (6.23)$$

with

$$\Phi_{\text{GR}} \equiv \frac{3\mathcal{G}M_*}{a} \frac{\mathcal{G}M_*}{ac^2}. \quad (6.24)$$

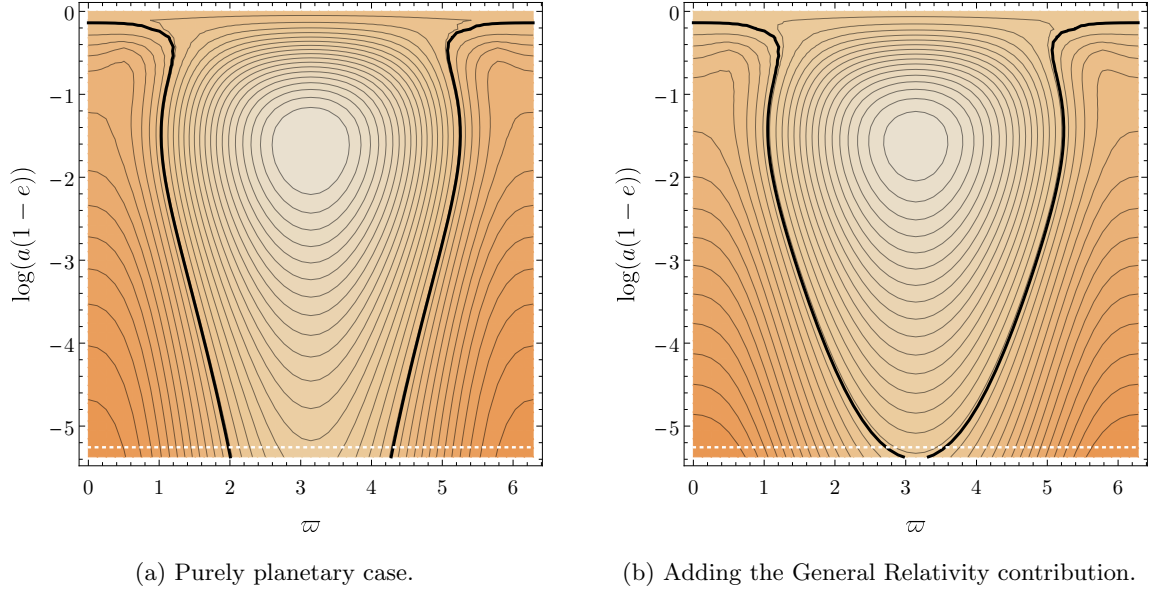


Figure 6.10: Same as in Figure 6.9, except for $\mu = 5 \times 10^{-5}$. In this case, a test mass starting at $\varpi = 0$ and $e = 0.05$ can fall into the star even considering the General Relativity contribution. The level curves of the purely planetary Hamiltonian do not change with different values of μ : as explained in the text, here μ only plays the role of setting the timescales of the evolution of the test particle, not the evolution itself.

Again, starting with an initial eccentricity $e_0 \ll 1$ at $\varpi = 0$, the maximum eccentricity e_{\max} of the test mass (achieved at $\varpi = \pi$) is estimated by

$$\Phi_0 \hat{\mathcal{H}}(e_0, 0) + \Phi_{\text{GR}} \simeq \Phi_0 \hat{\mathcal{H}}(e_{\max}, \pi) + \frac{\Phi_{\text{GR}}}{\sqrt{1 - e_{\max}^2}}. \quad (6.25)$$

Assuming $1 - e_{\max} \ll 1$, equation (6.25) becomes

$$\frac{|\mathcal{H}_{\text{GR}}|}{\Phi_0} = \frac{\Phi_{\text{GR}}}{\Phi_0} \frac{1}{\sqrt{1 - e_{\max}^2}} \simeq \hat{\mathcal{H}}(e_0, 0) - \hat{\mathcal{H}}(e_{\max}, \pi) =: f. \quad (6.26)$$

This shows that e_{\max} depends on various parameters through the ratio $\Phi_{\text{GR}}/\Phi_0 \propto M_*^2/(m'a)$.

Setting $a(1 - e_{\max}) = R_{\text{crit}}$ in equation (6.26), we obtain the critical perturber mass m'_{crit} that allows the test particle to reach a certain pericentre distance R_{crit} :

$$\begin{aligned} m'_{\text{crit}} &= \frac{3}{\sqrt{2}} \frac{1}{f} \frac{\mathcal{G} M_*^2}{c^2} \frac{1}{\sqrt{R_*}} a^{-1/2} \left(\frac{a(1 - e_{\max})}{R_*} \right)^{-1/2} \left(\frac{4}{1} \right)^2 \\ &\simeq 17 M_{\oplus} \left(\frac{f}{0.1} \right)^{-1} \left(\frac{M_*}{M_{\odot}} \right)^2 \left(\frac{a}{1 \text{ AU}} \right)^{-1/2} \left(\frac{R_{\text{crit}}}{R_{\odot}} \right)^{-1/2}. \end{aligned} \quad (6.27)$$

It is important to note that f in general depends on e_{\max} and thus is a complicated function of (R_{crit}/a) . However, we can calculate its numerical value in the case depicted in Figures 6.9 and 6.10, where we obtain $f \sim 0.1$.

6.6 Conclusions

In this chapter, we have revisited the problem of secular dynamics inside mean motion resonances in the restricted planar three-body problem in order to determine to what extent planetary perturbations can effectively drive small bodies into highly eccentric orbits, and cause them to fall into the star or suffer tidal disruption. This mechanism can be an efficient way to drive planetesimals generated as debris by post-instability planetary collisions close to their White Dwarf host, and explain the observed pollution in heavy elements of these stars' atmospheres. While

most previous works employed series expansion of the Hamiltonian in powers of the eccentricities or were limited by a first-order development in e' to the case of $e > e'$ and small e' (where e' and e are the eccentricities of the planetary perturber and the test particle, respectively), we do not perform any expansions, thus making our results valid for a wider range of orbital configurations. We make use of the principle of adiabatic invariance to reduce the two-degree-of-freedom Hamiltonian (6.9) to the integrable Hamiltonian $\bar{\mathcal{H}}$, which we study in the limit of vanishing amplitude of libration of $k'\lambda' - k\lambda$ in the $k' : k = 2:1, 3:1$ and $4:1$ mean motion resonances. We confirm the results of [Beust and Morbidelli(1996)], and show that for small e' ($\lesssim 0.1$) the $2:1$ and $3:1$ resonances are not able to push test particles in initially nearly circular orbits into star-grazing trajectories (Figures 6.3, 6.4), while the $4:1$ resonance is extremely effective (Figure 6.5). Moreover, we find that a higher value of e' ($=0.2-0.3$) does not change this picture for the $2:1$ and $3:1$ resonances (Figures 6.6, 6.7), but makes the $4:1$ resonance less effective by generating a larger stable region of circulation around $e \sim 0$ (Figure 6.8). Finally, in the cases where the resonance is strong enough to generate star-grazing objects, we include the General Relativity contribution to the Hamiltonian, which causes a fast precession of the pericentre while keeping the eccentricity constant, thereby suppressing the effectiveness of the planet's perturbation to generate extreme eccentricities (Figure 6.9). While the planetary mass only sets the timescales of the secular eccentricity evolution when the General Relativity effect is neglected, we note that it now plays an important dynamical role, as it regulates the relative contribution of the purely Newtonian evolution and the impact of the post-Newtonian term. We then obtain, for a specific choice of semi-major axis and eccentricity of the perturber, an estimate on the minimum planetary mass needed to drive eccentricity growth of the test particle from ~ 0 to ~ 1 . An approximate analytic expression for this critical mass is also obtained. In addition, we make available a Mathematica notebook (see Appendix D) which implements the calculations outlined in this chapter to allow the interested reader to examine the effect of secular dynamics inside mean motion resonances for other applications.

Chapter 7

Conclusions

In this thesis, I explored important aspects of planetary dynamics in mean motion resonance in the context of our current knowledge of the architecture of exoplanetary systems, with specific attention to the Super-Earth/Mini-Neptune population. These planets are extremely common around Sun-like stars, and therefore pose important constraints on planetary formation scenarios and subsequent dynamical evolution. I gave an introduction of the general picture of Planetary Science in Chapter 1, starting from the basic structure of protoplanetary discs and discussing the main steps of planetary formation. Then, I focused mainly on planet-disc interactions such as type-I migration and eccentricity damping, which can lead to the formation of chains of mean motion resonances. This astrophysical framework established the main motivation of my thesis: although the formation of resonances should be commonplace during the formation of Super-Earth/Mini-Neptune systems, most of the observed systems are not close to resonance. Therefore, throughout this work I investigated the process of resonant capture, some dynamical aspects of the evolution in resonance, and the stability of resonant chains.

After this first general introduction, I dedicated Chapter 2 to the description of the tools of Hamiltonian Mechanics, since it is the backbone of the analytical work contained in this text. Using this formalism, I recalled the main concepts and equations relevant to Celestial Mechanics, mainly to familiarise the reader with the notation but also to detail important technical aspects such as the development of the planetary disturbing function. Then, I introduced the basic methods of perturbation theory, which have been heavily used throughout the text, especially in Chapter 5. I also recalled the concept of the adiabatic invariant, which is also used regularly in the thesis, and applied it to describe the general theory of capture into resonance.

Having laid out the foundation for the thesis in the first two chapters, I discussed in Chapter 3 the well-understood process of capture of two planets into a first order mean motion resonance $k : k - 1$ by means of convergent migration in a protoplanetary disc. To do so, I gave an analytical description of the structure of resonant pairs using an unexpanded Hamiltonian which is therefore valid at arbitrary orbital eccentricities, in the planar approximation for simplicity. I drew the locations of the linearly stable resonant equilibrium points in terms of the semi-major axis ratios and eccentricities, for different values of the planetary masses and for different resonant indices k , and explored resonant dynamics at low amplitude of librations of the orbital parameters. I then illustrated how the planet-disc interaction naturally brings the system's configuration near one of these equilibrium points, and how the system subsequently follows adiabatically the curve of equilibria increasing the planets' eccentricities, until this effect is balanced by the eccentricity damping supplied by the disc. I also detailed the planets' evolution during the phase of capture into resonance using an approach that is compatible with the Hamiltonian framework and the adiabatic principle, which also yields an analytical prediction of the final equilibrium eccentricity of the captured states. These analytical investigations have been validated by numerical N -body simulations including the dissipative effects of the disc.

In Chapter 4, I considered the near-resonant population, and specifically the resulting evolution under dissipative forces such as tidal dissipation provided by the central star. Previous works have investigated these effects and concluded that the resulting eccentricity damping could explain the presence of near-resonant systems residing much wider from exact resonance than one would expect: the coupling between the semi-major axis and the eccentricities can indeed cause the semi-major axis ratios to grow. In this chapter, I extended this picture of the dissipative divergence of resonant orbits to the case of three-planet systems. I generalised the analytical description of the previous chapter to three planets, with both pairs residing in a first-order mean motion resonance, in the limit of small eccentricities. I thus drew equilibrium curves analogous to those presented in Chapter 3, and argued that if the observed orbital architecture of a system is found near one of these equilibrium points, this would be strongly suggestive of resonant capture and subsequent orbital divergence due to dissipative evolution. Thus, I showed how

one can measure in a statistical way to what extent the observed architecture of a given system is compatible with these physical processes, and applied this approach to actual systems from the near-resonant population. This technique can easily be applied to newly discovered planetary systems.

In Chapter 5, I tackled the main question which motivated this thesis: the onset of instability of resonant chains. I began by recalling that previous works demonstrated that the paucity of resonances in the exoplanets sample is not in contradiction with the scenario of capture into mean motion resonance during the disc phase, if post-disc instability rates are as high as 90% [Izidoro et al.(2017), Izidoro et al.(2019)]. Previous numerical investigations of the stability of resonant chains pointed out that there is a critical planetary mass above which the crossing time of resonant systems is comparable to that of non-resonant ones and the chains become unstable, and that this limit mass decreases with increasing number of planets and/or increasing index k of the resonance [Matsumoto et al.(2012)]. The dynamical origin of these instabilities had not been discussed. In Chapter 5, I thus investigated analytically and numerically the stability of resonant chains as a function of the planetary mass, kept equal for all planets for simplicity. From the numerical perspective, I used numerical experiments where I fictitiously increased the planetary mass to follow the low-amplitude regime until the onset of instability. I started the analysis of two resonant planets, relying on the general analytical treatment presented in Chapter 3. I found that, within reasonable values of the planetary eccentricities, secondary resonances between the frequency of libration of a resonant angle (which grows with the planetary mass) and the frequency of the fast synodic angle $\lambda_1 - \lambda_2$ (which is constant with the planetary mass) do not play a role in the observed instabilities. Then, I considered the effect of close encounters between planets, inspired by the mutual Hill radius stability criterion [Gladman(1993)]. I found that resonant planetary systems are more stable than those with randomly chosen orbital parameters, but that there is a critical distance after which the system goes unstable, which is a fraction of the usual distance d_{crit} for non-resonant systems. I also saw that for resonant systems with bigger amplitude of libration of the resonant angles this critical distance approaches more and more the usual distance d_{crit} . Then, I considered the case of three resonant planets. I showed that the instability for three planets occurs at smaller masses than in the two-planet case, which cannot be explained by close encounters alone, and I identified a novel dynamical mechanism which excites the amplitude of libration of the resonant degrees of freedom. The excited systems can then become unstable by suffering close encounters and collisions. Therefore, I investigated this phenomenon, using a simplified Hamiltonian which reproduced well the observed excitation of the system. Carrying out the calculation explicitly in the case $k = 3$, I showed that the observed excitation is due to a set of secondary resonances between a combination of the resonant frequencies and a fraction of the synodic frequency. I identified the specific secondary resonance that caused the effect in the numerical integrations, and built a simple integrable model for this resonance which captures qualitatively the dynamics until the excitation of the system is too severe, showing for example that there can be a capture into this specific resonance. I therefore proposed that in the numerical simulations the systems become unstable due to a crossing of this type of secondary resonances, which excites the planets' orbits and leads to a phase of close encounters and collisions. This gives a critical mass at which a regime of secondary resonances is encountered, and after which the system can be destabilised. This scheme can then be generalised to an arbitrary number of planets N and/or an arbitrary index of the first-order mean motion resonance k of the chain. I calculate for different N 's and k 's the lowest fraction of the synodic frequency that can resonate with the resonant frequencies, and showed that it decreases with N and k . Since the resonant frequencies grow with the planetary mass, the regime of secondary resonances between synodic and resonant degrees of freedom is encountered at lower masses for increasing k and/or increasing N , and therefore the critical mass allowed for stability decreases with N and with k . This gave an analytical explanation to the numerical findings of [Matsumoto et al.(2012)].

Finally, in Chapter 6, I argued that during the star's mass loss that characterises the last stages of stellar evolution, compact planetary systems around the progenitors of White Dwarfs can become unstable in a similar way as described in the previous chapter. The outcome of mutual collisions can be the generation of collisional debris. This debris can then be driven by planetary perturbations into highly eccentric orbits and cause them to fall into the star or suffer tidal disruption, which would explain the high rates of observed atmospheric pollution in White Dwarf atmospheres. I thus revisited the problem of secular dynamics inside mean motion resonance in the restricted planar three-body problem, using an unexpanded Hamiltonian which allows to probe arbitrarily high eccentricity values for the planetary perturber and the perturbed particle. I confirmed previous results which showed that the 4:1 mean motion resonance with a slightly eccentric perturber can be very efficient in driving initially vanishing eccentricities of the test particle to unity, while higher eccentricities for the perturber reduce this effect. Then, I also included a post-Newtonian term describing the fast precession of the longitude of perihelion at large eccentricity due to General Relativity, and showed that it can reduce the planet's ability to drive the small particle onto the star. Therefore, I determined the minimal planetary mass that is needed to recover the star-grazing phenomenon.

7.1 Future perspectives

During the three years which lead to the writing of this manuscript, I was exposed to different concepts and techniques, many of which were completely new to me, not coming from an astrophysics background. This allowed me to apply my previous knowledge to concrete problems in planetary dynamics, specifically the architecture of planetary systems. More importantly, this laid the grounds for future research in this field.

The key result of this thesis is the determination of a dynamical origin of instability of resonant chains, contained in Chapter 5. This fits extremely well in the current framework of planet formation and exoplanetary science, since it clarifies why the over-all flat period-ratio distribution shown in Figure 1.7 is not in contradiction with the current formation scenarios. Super-Earths/Mini-Neptunes can indeed form during the disc phase (which we expect given that some of them host gaseous envelopes), migrate to the inner edge of the disc and be captured in resonance (which is also expected), but they subsequently become unstable once the disc of gas is removed. This was first proposed by [Izidoro et al.(2017)], and this thesis gives an original and precise dynamical explanation for this mechanism, which was its main motivation. However, these results can be seen as a starting point rather than an end point.

The first improvement will be to perform a more detailed analysis of the different orbital configurations with larger N and k . The aim is to obtain a simple but accurate analytical prediction of the location of these secondary resonances, which would determine the limits of stability in the general case. One can also generalise this scheme to resonant chains with different resonant indices k along the chain. In this case, one can imagine that the most fragile resonant pairs are the ones with higher k , so it might be sufficient to test those and not the whole chain. Also different planetary masses can be considered. Notice in passing that our results are already compatible with observed resonant chains. For example, the Galileian satellites of Jupiter reside in a 2:1 – 2:1 chain, have a comparable mass (within a factor of 3), with the most massive being $\sim 8 \times 10^{-5}$ that of Jupiter, well within the limits of stability according to our criterion. Another example is Kepler-223, whose planets have a comparable mass and reside in a 4:3 – 3:2 – 4:3 chain. Using similar arguments to those presented at the end of Subsect. 5.3.6, the planetary mass above which we expect this chain to be unstable is of order 10^{-4} , and the planets have a mass of roughly 10^{-5} the mass of their host star. Moreover, now that we have a better grasp on a specific dynamical mechanism that can trigger instabilities, I plan to run a suite of numerical integrations like the ones presented in Chapter 5, targeted specifically to investigate the onset of instability at different N and k , to check the analytical prediction.

These advances should yield an even more robust understanding of the dynamics, and ultimately furnish a useful criterion directly applicable in the more general context of planetary architectures. This would be the next natural improvement. The aim of the analysis performed in Chapter 5 was to pinpoint the reasons for instability in the low-amplitude regime in the purely conservative case: this was the first necessary step in the dynamical investigation of the instabilities observed for example in the synthetic Super-Earth systems of [Izidoro et al.(2017), Izidoro et al.(2019)]. These simulations are where specific planetary formation scenario get tested, and constitute a less “protected” environment since a residual population of small planetary embryos is also interacting with the planets, which can be the case in actual planetary systems. First, since the mutual planetary perturbations should be the predominant effect, it would be pertinent to check how relevant the mechanism of the crossing of secondary resonances is in these different numerical simulations. A criterion of onset of instability specifically tailored to resonant chains of Super-Earths/Mini-Neptunes based on the crossing of secondary resonances would be extremely useful in computing which synthetic systems that are formed during the phase of planet formation and convergent migration remain stable and which do not. Then, the non-conservative effects can be taken into account, and could potentially enhance or inhibit the rates of instabilities of resonant chains. It will be fascinating to explore how all these effects combine to shape the formation and subsequent evolution of planetary systems. Finally, this scheme is not limited to the Super-Earth/Mini-Neptune population. For example, consider that the limit mass allowed for stability in the case of three planets is of order $\sim 10^{-3}M_*$, reduced to $\sim 10^{-4}M_*$ for chains more compact than the 3:2, as shown in Chapter 5. This may give an explanation for the apparent loneliness of hot Jupiters.

With a criterion for stability of resonant chains, it may even be possible to predict which stable chains can form in the first place during the first stage of planet formation, which cannot, and which may form but become unstable on very short timescales. Once we know that a specific configuration can be stable, and we have the analytical tools to understand its dynamics, one could study the conditions that can lead to such a configuration. The disc prescriptions used in Chapters 3 to 5 were very simple, as we only needed to capture the planets deep into resonance in order to subsequently study its stability. The same techniques can be expanded to a more accurate setup of the process of capture into resonance during the disc-phase, using the more realistic expressions for the migration and damping, exploring different disc surface densities and including other parameters such as turbulent

viscosity. These effects are expected to play a role in determining how compact the resonant chain is, and how deep in resonance the system finds itself. Matching these to observed resonant systems may give insights on the structure of inner regions of protoplanetary discs, which remains to this day poorly constrained. Another approach is to perform hydrodynamical simulations of multi-planetary systems under different disc parameters. This would allow to determine more precisely which resonant chains are preferred under which specific disc conditions.

The results of Chapter 5 gave some insights in the observed period ratio distribution of exoplanets shown in Figure 1.7, elucidating why there is an over-all broad distribution of non-resonant systems. Then, another aspect of this distribution that was considered in this thesis was the observed excess of systems just wide of exact commensurabilities. The results of Chapter 4 expanded on our knowledge of this population and imply that resonant systems may actually be more numerous than one might imagine simply by looking at the period ratio distribution. In this context, significant improvements in our understanding of the nature of exoplanetary systems will come from better characterising their orbital configuration. Specifically, a better quantification of the eccentricities and masses of near-resonant planets would be significant, as it is the key to confirm this hypothesis.

The theoretical aspects of planetary dynamics have improved significantly in the last decades, helped by observational improvements and analytical insights. This thesis is well placed in the growing field of planetary science: it is built on our accumulated knowledge, it contributes new insights to refine it, and offers interesting perspectives of future research. Meanwhile, current and future missions, such as Gaia, TESS and PLATO, will allow for a better characterisation of the demographics of exoplanets, and warrant our growing interest in the formation, architecture and evolution of planetary systems.

Bibliography

- [Antoniadou and Voyatzis(2014)] Antoniadou, K. I., Voyatzis, G. 2014. Resonant periodic orbits in the exoplanetary systems. *Astrophysics and Space Science* 349, 657.
- [Armitage(2010)] Armitage, P. J. 2010. *Astrophysics of Planet Formation*, 294 pp. ISBN 978-0-521-88745-8 (hardback). Cambridge, UK: Cambridge University Press.
- [Armitage(2015)] Armitage, P. J. 2015. Physical processes in protoplanetary disks. arXiv e-prints arXiv:1509.06382.
- [Arnold(1963)] V.I. Arnold: A theorem of Liouville concerning integrable problems of dynamics, *Sibirsk. Math. Zh.* 4 471–474 (1963).
- [Arnold(1978)] Arnold, V. I. 1978. *Mathematical methods of classical mechanics*. Graduate texts in mathematics.
- [Bailey and Batygin(2018)] Bailey, E., Batygin, K. 2018. The Hot Jupiter Period-Mass Distribution as a Signature of in situ Formation. *The Astrophysical Journal* 866, L2.
- [Baillié et al.(2015)] Baillié, K., Charnoz, S., Pantin, E. 2015. Time evolution of snow regions and planet traps in an evolving protoplanetary disk. *Astronomy and Astrophysics* 577, A65.
- [Barge and Sommeria(1995)] Barge, P., Sommeria, J. 1995. Did planet formation begin inside persistent gaseous vortices?. *Astronomy and Astrophysics* 295, L1.
- [Baruteau et al.(2014)] Baruteau, C., and 8 colleagues 2014. Planet-Disk Interactions and Early Evolution of Planetary Systems. *Protostars and Planets VI* 667.
- [Batygin(2015)] Batygin, K. 2015. Capture of planets into mean-motion resonances and the origins of extrasolar orbital architectures. *Monthly Notices of the Royal Astronomical Society* 451, 2589.
- [Batygin and Adams(2017)] Batygin, K., Adams, F. C. 2017. An Analytic Criterion for Turbulent Disruption of Planetary Resonances. *The Astronomical Journal* 153, 120.
- [Batygin and Morbidelli(2013)a] Batygin, K., Morbidelli, A. 2013. Analytical treatment of planetary resonances. *Astronomy and Astrophysics* 556, A28.
- [Batygin and Morbidelli(2013)b] Batygin, K., Morbidelli, A. 2013. Dissipative Divergence of Resonant Orbits. *The Astronomical Journal* 145, 1.
- [Batygin et al.(2015)] Batygin, K., Deck, K. M., Holman, M. J. 2015. Dynamical Evolution of Multi-resonant Systems: The Case of GJ876. *The Astronomical Journal* 149, 167.
- [Batygin et al.(2016)] Batygin, K., Bodenheimer, P. H., Laughlin, G. P. 2016. In Situ Formation and Dynamical Evolution of Hot Jupiter Systems. *The Astrophysical Journal* 829, 114.
- [Beaugé and Nesvorný(2012)] Beaugé, C., Nesvorný, D. 2012. Multiple-planet Scattering and the Origin of Hot Jupiters. *The Astrophysical Journal* 751, 119.
- [Beaugé et al.(2003)] Beaugé, C., Ferraz-Mello, S., Michtchenko, T. A. 2003. Extrasolar Planets in Mean-Motion Resonance: Apse Alignment and Asymmetric Stationary Solutions. *The Astrophysical Journal* 593, 1124.
- [Beaugé et al.(2006)] Beaugé, C., Michtchenko, T. A., Ferraz-Mello, S. 2006. Planetary migration and extrasolar planets in the 2/1 mean-motion resonance. *Monthly Notices of the Royal Astronomical Society* 365, 1160.

- [Beust and Morbidelli(1996)] Beust, H., Morbidelli, A. 1996. Mean-Motion Resonances as a Source for Infalling Comets toward β Pictoris. *Icarus* 120, 358.
- [Beust et al.(1989)] Beust, H., Lagrange-Henri, A. M., Vidal-Madjar, A., Ferlet, R. 1989. The beta Pictoris circumstellar disk. IX. Theoretical results on the infall velocities of CA II, AI III and MG II.. *Astronomy and Astrophysics* 223, 304.
- [Beust et al.(1990)] Beust, H., Lagrange-Henri, A. M., Madjar, A. V., Ferlet, R. 1990. The beta Pictoris circumstellar disk. X. Numerical simulations of infalling evaporating bodies.. *Astronomy and Astrophysics* 236, 202.
- [Beust et al.(1991)] Beust, H., Madjar, A. V., Lagrange-Henri, A. M., Ferlet, R. 1991. The beta Pictoris circumstellar disk. XI. New CA II absorption features reproduced numerically.. *Astronomy and Astrophysics* 241, 488.
- [Birnstiel et al.(2016)] Birnstiel, T., Fang, M., Johansen, A. 2016. Dust Evolution and the Formation of Planetesimals. *Space Science Reviews* 205, 41.
- [Bitsch et al.(2013)] Bitsch, B., Crida, A., Morbidelli, A., Kley, W., Dobbs-Dixon, I. 2013. Stellar irradiated discs and implications on migration of embedded planets. I. Equilibrium discs. *Astronomy and Astrophysics* 549, A124.
- [Bitsch et al.(2015)] Bitsch, B., Johansen, A., Lambrechts, M., Morbidelli, A. 2015. The structure of protoplanetary discs around evolving young stars. *Astronomy and Astrophysics* 575, A28.
- [Bitsch et al.(2018)] Bitsch, B., Morbidelli, A., Johansen, A., Lega, E., Lambrechts, M., Crida, A. 2018. Pebble-isolation mass: Scaling law and implications for the formation of super-Earths and gas giants. *Astronomy and Astrophysics* 612, A30.
- [Bitsch et al.(2019)] Bitsch, B., and 6 colleagues 2019. Formation of planetary systems by pebble accretion and migration: growth of gas giants. *Astronomy and Astrophysics* 623, A88.
- [Bonsor et al.(2011)] Bonsor, A., Mustill, A. J., Wyatt, M. C. 2011. Dynamical effects of stellar mass-loss on a Kuiper-like belt. *Monthly Notices of the Royal Astronomical Society* 414, 930.
- [Brasser et al.(2018)] Brasser, R., Matsumura, S., Muto, T., Ida, S. 2018. Trapping Low-mass Planets at the Inner Edge of the Protostellar Disk. *The Astrophysical Journal* 864, L8.
- [Brouwer & Clemence(1961)] Brouwer, D., & Clemence, G. M. 1961, *Methods of celestial mechanics*, Academic Press, New York
- [Chatterjee et al.(2016)] Chatterjee, S., Krantzler, S. O., Ford, E. B. 2016. Period Ratio Distribution of Near-Resonant Planets Indicates Planetesimal Scattering. *IAU Focus Meeting* 29A, 30.
- [Cossou et al.(2014)] Cossou, C., Raymond, S. N., Hersant, F., Pierens, A. 2014. Hot super-Earths and giant planet cores from different migration histories. *Astronomy and Astrophysics* 569, A56.
- [Cresswell and Nelson(2006)] Cresswell, P., Nelson, R. P. 2006. On the evolution of multiple protoplanets embedded in a protostellar disc. *Astronomy and Astrophysics* 450, 833.
- [Crida et al.(2008)] Crida, A., Sándor, Z., Kley, W. 2008. Influence of an inner disc on the orbital evolution of massive planets migrating in resonance. *Astronomy and Astrophysics* 483, 325.
- [Cuzzi et al.(1993)] Cuzzi, J. N., Dobrovolskis, A. R., Champney, J. M. 1993. Particle-Gas Dynamics in the Midplane of a Protoplanetary Nebula. *Icarus* 106, 102.
- [Cuzzi et al.(2008)] Cuzzi, J. N., Hogan, R. C., Shariff, K. 2008. Toward Planetesimals: Dense Chondrule Clumps in the Protoplanetary Nebula. *The Astrophysical Journal* 687, 1432.
- [Cresswell and Nelson(2008)] Cresswell, P., Nelson, R. P. 2008. Three-dimensional simulations of multiple protoplanets embedded in a protostellar disc. *Astronomy and Astrophysics* 482, 677.
- [Debes and Sigurdsson(2002)] Debes, J. H., Sigurdsson, S. 2002. Are There Unstable Planetary Systems around White Dwarfs?. *The Astrophysical Journal* 572, 556.

- [Debes et al.(2012)] Debes, J. H., Walsh, K. J., Stark, C. 2012. The Link between Planetary Systems, Dusty White Dwarfs, and Metal-polluted White Dwarfs. *The Astrophysical Journal* 747, 148.
- [Deck and Batygin(2015)] Deck, K. M., Batygin, K. 2015. Migration of Two Massive Planets into (and out of) First Order Mean Motion Resonances. *The Astrophysical Journal* 810, 119.
- [Deck et al.(2013)] Deck, K. M., Payne, M., Holman, M. J. 2013. First-order Resonance Overlap and the Stability of Close Two-planet Systems. *The Astrophysical Journal* 774, 129.
- [Delaunay(1867)] Delaunay C., 1867, *Théorie du mouvement de la Lune*. Mem. Acad. Sci.. 29, Paris, 1867
- [Delisle and Laskar(2014)] Delisle, J.-B., Laskar, J. 2014. Tidal dissipation and the formation of Kepler near-resonant planets. *Astronomy and Astrophysics* 570, L7.
- [Delisle et al.(2012)] Delisle, J.-B., Laskar, J., Correia, A. C. M., Boué, G. 2012. Dissipation in planar resonant planetary systems. *Astronomy and Astrophysics* 546, A71.
- [Delisle et al.(2015)] Delisle, J.-B., Correia, A. C. M., Laskar, J. 2015. Stability of resonant configurations during the migration of planets and constraints on disk-planet interactions. *Astronomy and Astrophysics* 579, A128.
- [Dullemond et al.(2018)] Dullemond, C. P., and 14 colleagues 2018. The Disk Substructures at High Angular Resolution Project (DSHARP). VI. Dust Trapping in Thin-ringed Protoplanetary Disks. *The Astrophysical Journal* 869, L46.
- [Dürmann and Kley(2015)] Dürmann, C., Kley, W. 2015. Migration of massive planets in accreting disks. *Astronomy and Astrophysics* 574, A52.
- [Ehrenreich et al.(2015)] Ehrenreich, D., and 10 colleagues 2015. A giant comet-like cloud of hydrogen escaping the warm Neptune-mass exoplanet GJ 436b. *Nature* 522, 459.
- [Ellis and Murray(2000)] Ellis, K. M., Murray, C. D. 2000. The Disturbing Function in Solar System Dynamics. *Icarus* 147, 129.
- [Fabrycky et al.(2014)] Fabrycky, D. C., and 21 colleagues 2014. Architecture of Kepler’s Multi-transiting Systems. II. New Investigations with Twice as Many Candidates. *The Astrophysical Journal* 790, 146.
- [Farihi(2016)] Farihi, J. 2016. Circumstellar debris and pollution at white dwarf stars. *New Astronomy Reviews* 71, 9.
- [Farinella et al.(1994)] Farinella, P., and 6 colleagues 1994. Asteroids falling onto the Sun. *Nature* 371, 315.
- [Fendyke and Nelson(2014)] Fendyke, S. M., Nelson, R. P. 2014. On the corotation torque for low-mass eccentric planets. *Monthly Notices of the Royal Astronomical Society* 437, 96.
- [Ferlet et al.(1987)] Ferlet, R., Hobbs, L. M., Madjar, A. V. 1987. The beta Pictoris circumstellar disk. V. Time variations of the CA II-K line.. *Astronomy and Astrophysics* 185, 267.
- [Fernandes et al.(2019)] Fernandes, R. B., Mulders, G. D., Pascucci, I., Mordasini, C., Emsenhuber, A. 2019. Hints for a Turnover at the Snow Line in the Giant Planet Occurrence Rate. *The Astrophysical Journal* 874, 81.
- [Ferraz-Mello(2007)] Ferraz-Mello, S. 2007. Canonical Perturbation Theories - Degenerate Systems and Resonance. *Astrophysics and Space Science Library*.
- [Fontaine and Michaud(1979)] Fontaine, G., Michaud, G. 1979. Diffusion time scales in white dwarfs.. *The Astrophysical Journal* 231, 826.
- [Fressin et al.(2013)] Fressin, F., and 8 colleagues 2013. The False Positive Rate of Kepler and the Occurrence of Planets. *The Astrophysical Journal* 766, 81.
- [Fulton et al.(2017)] Fulton, B. J., and 12 colleagues 2017. The California-Kepler Survey. III. A Gap in the Radius Distribution of Small Planets. *The Astronomical Journal* 154, 109.
- [Fulton and Petigura(2018)] Fulton, B. J., Petigura, E. A. 2018. The California-Kepler Survey. VII. Precise Planet Radii Leveraging Gaia DR2 Reveal the Stellar Mass Dependence of the Planet Radius Gap. *The Astronomical Journal* 156, 264.

- [Gillon et al.(2016)] Gillon, M., and 14 colleagues 2016. Temperate Earth-sized planets transiting a nearby ultracool dwarf star. *Nature* 533, 221.
- [Gillon et al.(2017)] Gillon, M., and 29 colleagues 2017. Seven temperate terrestrial planets around the nearby ultracool dwarf star TRAPPIST-1. *Nature* 542, 456.
- [Gladman(1993)] Gladman, B. 1993. Dynamics of Systems of Two Close Planets. *Icarus* 106, 247.
- [Gladman et al.(1997)] Gladman, B. J., and 9 colleagues 1997. Dynamical lifetimes of objects injected into asteroid belt resonances. *Science* 277, 197.
- [Goldreich and Schlichting(2014)] Goldreich, P., Schlichting, H. E. 2014. Overstable Librations can Account for the Paucity of Mean Motion Resonances among Exoplanet Pairs. *The Astronomical Journal* 147, 32.
- [Goldreich and Tremaine(1979)] Goldreich, P., Tremaine, S. 1979. The excitation of density waves at the Lindblad and corotation resonances by an external potential.. *The Astrophysical Journal* 233, 857.
- [Goldreich and Tremaine(1980)] Goldreich, P., Tremaine, S. 1980. Disk-satellite interactions.. *The Astrophysical Journal* 241, 425.
- [Goldreich and Ward(1973)] Goldreich, P., Ward, W. R. 1973. The Formation of Planetesimals. *The Astrophysical Journal* 183, 1051.
- [Goździewski et al.(2016)] Goździewski, K., Migaszewski, C., Panichi, F., Szuszkiewicz, E. 2016. The Laplace resonance in the Kepler-60 planetary system. *Monthly Notices of the Royal Astronomical Society* 455, L104.
- [Greaves et al.(2016)] Greaves, J. S., and 8 colleagues 2016. Gas and dust around A-type stars at tens of Myr: signatures of cometary breakup. *Monthly Notices of the Royal Astronomical Society* 461, 3910.
- [Hadden and Lithwick(2014)] Hadden, S., Lithwick, Y. 2014. Densities and Eccentricities of 139 Kepler Planets from Transit Time Variations. *The Astrophysical Journal* 787, 80.
- [Hadden and Lithwick(2017)] Hadden, S., Lithwick, Y. 2017. Kepler Planet Masses and Eccentricities from TTV Analysis. *The Astronomical Journal* 154, 5.
- [Hadjidemetriou(2002)] Hadjidemetriou, J. D. 2002. Resonant Periodic Motion and the Stability of Extrasolar Planetary Systems. *Celestial Mechanics and Dynamical Astronomy* 83, 141.
- [Hayashi(1981)] Hayashi, C. 1981. Structure of the Solar Nebula, Growth and Decay of Magnetic Fields and Effects of Magnetic and Turbulent Viscosities on the Nebula. *Progress of Theoretical Physics Supplement* 70, 35.
- [Henrard(1993)] Henrard, J. 1993, *The Adiabatic Invariant in Classical Mechanics*. *Dynamics Reported*, 117-235, Springer.
- [Henrard and Caranicolas(1990)] Henrard, J., Caranicolas, N. D. 1990. Motion near the 3/1 resonance of the planar elliptic restricted three body problem. *Celestial Mechanics and Dynamical Astronomy* 47, 99.
- [Henrard and Lemaître(1983)] Henrard, J., Lemaître, A. 1983. A Second Fundamental Model for Resonance. *Celestial Mechanics* 30, 197.
- [Henrard and Henrard(1991)] Henrard, J., Henrard, M. 1991. Slow crossing of a stochastic layer. *Physica D Non-linear Phenomena* 54, 135.
- [Henrard and Morbidelli(1993)] Henrard, J., Morbidelli, A. 1993. Slow crossing of a stochastic layer. *Physica D Nonlinear Phenomena* 68, 187.
- [Henrard et al.(1986)] Henrard, J., Lemaître, A., Milani, A., Murray, C. D. 1986. The Reducing Transformation and Apocentric Librators. *Celestial Mechanics* 38, 335.
- [Hernández et al.(2007)] Hernández, J., and 11 colleagues 2007. A Spitzer Space Telescope Study of Disks in the Young σ Orionis Cluster. *The Astrophysical Journal* 662, 1067.
- [Howard et al.(2012)] Howard, A. W., and 66 colleagues 2012. Planet Occurrence within 0.25 AU of Solar-type Stars from Kepler. *The Astrophysical Journal Supplement Series* 201, 15.

- [Izidoro et al.(2017)] Izidoro, A., and 7 colleagues 2017. Breaking the chains: hot super-Earth systems from migration and disruption of compact resonant chains. *Monthly Notices of the Royal Astronomical Society* 470, 1750.
- [Izidoro et al.(2019)] Izidoro, A., and 6 colleagues 2019. Formation of planetary systems by pebble accretion and migration: Hot super-Earth systems from breaking compact resonant chains. arXiv e-prints arXiv:1902.08772.
- [Jin and Mordasini(2018)] Jin, S., Mordasini, C. 2018. Compositional Imprints in Density-Distance-Time: A Rocky Composition for Close-in Low-mass Exoplanets from the Location of the Valley of Evaporation. *The Astrophysical Journal* 853, 163.
- [Johansen et al.(2015)] Johansen, A., Mac Low, M.-M., Lacerda, P., Bizzarro, M. 2015. Growth of asteroids, planetary embryos, and Kuiper belt objects by chondrule accretion. *Science Advances* 1, 1500109.
- [Jontof-Hutter et al.(2016)] Jontof-Hutter, D., and 9 colleagues 2016. Secure Mass Measurements from Transit Timing: 10 Kepler Exoplanets between 3 and 8 M_{\oplus} with Diverse Densities and Incident Fluxes. *The Astrophysical Journal* 820, 39.
- [Jost(1968)] R. Jost: Winkelund Wirkungsvariable für allgemeine mechanische Systeme, *Helvetica Physica Acta* 41, 965–968 (1968).
- [Jura(2003)] Jura, M. 2003. A Tidally Disrupted Asteroid around the White Dwarf G29-38. *The Astrophysical Journal* 584, L91.
- [Kanagawa et al.(2018)] Kanagawa, K. D., Tanaka, H., Szuszkiewicz, E. 2018. Radial Migration of Gap-opening Planets in Protoplanetary Disks. I. The Case of a Single Planet. *The Astrophysical Journal* 861, 140.
- [Keppler et al.(2018)] Keppler, M., and 124 colleagues 2018. Discovery of a planetary-mass companion within the gap of the transition disk around PDS 70. *Astronomy and Astrophysics* 617, A44.
- [Kley and Crida(2008)] Kley, W., Crida, A. 2008. Migration of protoplanets in radiative discs. *Astronomy and Astrophysics* 487, L9.
- [Kley and Nelson(2012)] Kley, W., Nelson, R. P. 2012. Planet-Disk Interaction and Orbital Evolution. *Annual Review of Astronomy and Astrophysics* 50, 211.
- [Koester et al.(2014)] Koester, D., Gänsicke, B. T., Farihi, J. 2014. The frequency of planetary debris around young white dwarfs. *Astronomy and Astrophysics* 566, A34.
- [Krivov(1986)] Krivov, A. V. 1986. Hamiltonian Equations of the Planetary N-Body Problem in the Post-Newtonian Approximation. *Soviet Astronomy* 30, 224.
- [Lagrange et al.(1987)] Lagrange, A. M., Ferlet, R., Vidal-Madjar, A. 1987. The beta Pictoris circumstellar disk. IV. Redshifted UV lines.. *Astronomy and Astrophysics* 173, 289.
- [Lambrechts and Johansen(2012)] Lambrechts, M., Johansen, A. 2012. Rapid growth of gas-giant cores by pebble accretion. *Astronomy and Astrophysics* 544, A32.
- [Lambrechts and Johansen(2014)] Lambrechts, M., Johansen, A. 2014. Forming the cores of giant planets from the radial pebble flux in protoplanetary discs. *Astronomy and Astrophysics* 572, A107.
- [Lambrechts et al.(2014)] Lambrechts, M., Johansen, A., Morbidelli, A. 2014. Separating gas-giant and ice-giant planets by halting pebble accretion. *Astronomy and Astrophysics* 572, A35.
- [Lambrechts et al.(2019)] Lambrechts, M., and 6 colleagues 2019. Formation of planetary systems by pebble accretion and migration: How the radial pebble flux determines a terrestrial-planet or super-Earth growth mode. arXiv e-prints arXiv:1902.08694.
- [Laskar(1985)] Laskar, J. 1985. Accurate methods in general planetary theory. *Astronomy and Astrophysics* 144, 133.
- [Laskar(1990)] Laskar, J. 1990. *Systèmes de Variables et Eléments. Modern Methods in Celestial Mechanics*, Comptes Rendus de la 13ème Ecole Printemps d’Astrophysique de Goutelas (France), 24-29 Avril, 1989. Edited by Daniel Benest and Claude Froeschle. Gif-sur-Yvette: Editions Frontieres, 1990., p.63 63.

- [Laskar(1997)] Laskar, J. 1997. Large scale chaos and the spacing of the inner planets.. *Astronomy and Astrophysics* 317, L75.
- [Laskar(2000)] Laskar, J. 2000. On the Spacing of Planetary Systems. *Physical Review Letters* 84, 3240.
- [Laskar and Boué(2010)] Laskar, J., Boué, G. 2010. Explicit expansion of the three-body disturbing function for arbitrary eccentricities and inclinations. *Astronomy and Astrophysics* 522, A60.
- [Lee and Peale(2002)] Lee, M. H., Peale, S. J. 2002. Dynamics and Origin of the 2:1 Orbital Resonances of the GJ 876 Planets. *The Astrophysical Journal* 567, 596.
- [Lemaitre(1984)] Lemaitre, A. 1984. High Order Resonances in the Restricted Three-Body Problem. *Celestial Mechanics* 32, 109.
- [Lesur(2018)] Lesur, G. 2018. Dynamics of protoplanetary discs (Dynamique des disques protoplanétaires), Habilitation à diriger des recherches présentée par Geoffroy Lesur à l’Institut de Planétologie et d’Astrophysique de Grenoble
- [Lin and Papaloizou(1986)] Lin, D. N. C., Papaloizou, J. 1986. On the Tidal Interaction between Protoplanets and the Protoplanetary Disk. III. Orbital Migration of Protoplanets. *The Astrophysical Journal* 309, 846.
- [Lin et al.(1996)] Lin, D. N. C., Bodenheimer, P., Richardson, D. C. 1996. Orbital migration of the planetary companion of 51 Pegasi to its present location. *Nature* 380, 606.
- [Liouville(1855)] Sur l’intégrations des équations différentielles de la dynamique, *Journal de Mathématiques pures et appliquées*, tome XX (1855).
- [Lissauer et al.(2011)] Lissauer, J. J., and 24 colleagues 2011. Architecture and Dynamics of Kepler’s Candidate Multiple Transiting Planet Systems. *The Astrophysical Journal Supplement Series* 197, 8.
- [Lithwick and Wu(2012)] Lithwick, Y., Wu, Y. 2012. Resonant Repulsion of Kepler Planet Pairs. *The Astrophysical Journal* 756, L11.
- [Lithwick et al.(2012)] Lithwick, Y., Xie, J., Wu, Y. 2012. Extracting Planet Mass and Eccentricity from TTV Data. *The Astrophysical Journal* 761, 122.
- [Luger et al.(2017)] Luger, R., and 32 colleagues 2017. A seven-planet resonant chain in TRAPPIST-1. *Nature Astronomy* 1, 129.
- [Mardling and Lin(2002)] Mardling, R. A., Lin, D. N. C. 2002. Calculating the Tidal, Spin, and Dynamical Evolution of Extrasolar Planetary Systems. *The Astrophysical Journal* 573, 829.
- [Marsden(1967)] Marsden, B. G. 1967. The sungrazing comet group. *The Astronomical Journal* 72, 1170.
- [Masset(2001)] Masset, F. S. 2001. On the Co-orbital Corotation Torque in a Viscous Disk and Its Impact on Planetary Migration. *The Astrophysical Journal* 558, 453.
- [Masset et al.(2006)] Masset, F. S., Morbidelli, A., Crida, A., Ferreira, J. 2006. Disk Surface Density Transitions as Protoplanet Traps. *The Astrophysical Journal* 642, 478.
- [Matsumoto et al.(2012)] Matsumoto, Y., Nagasawa, M., Ida, S. 2012. The orbital stability of planets trapped in the first-order mean-motion resonances. *Icarus* 221, 624.
- [Mayor and Queloz(1995)] Mayor, M., Queloz, D. 1995. A Jupiter-mass companion to a solar-type star. *Nature* 378, 355.
- [Mayor et al.(2011)] Mayor, M., and 13 colleagues 2011. The HARPS search for southern extra-solar planets XXXIV. Occurrence, mass distribution and orbital properties of super-Earths and Neptune-mass planets. arXiv e-prints arXiv:1109.2497.
- [Migaszewski(2015)] Migaszewski, C. 2015. On the migration of two planets in a disc and the formation of mean motion resonances. *Monthly Notices of the Royal Astronomical Society* 453, 1632.

- [Migaszewski(2016)] Migaszewski, C. 2016. On the migration of three planets in a protoplanetary disc and the formation of chains of mean motion resonances. *Monthly Notices of the Royal Astronomical Society* 458, 2051.
- [Millholland and Laughlin(2019)] Millholland, S., Laughlin, G. 2019. Obliquity-driven sculpting of exoplanetary systems. *Nature Astronomy* 3, 424.
- [Millholland et al.(2017)] Millholland, S., Wang, S., Laughlin, G. 2017. Kepler Multi-planet Systems Exhibit Unexpected Intra-system Uniformity in Mass and Radius. *The Astrophysical Journal* 849, L33.
- [Mills et al.(2016)] Mills, S. M., Fabrycky, D. C., Migaszewski, C., Ford, E. B., Petigura, E., Isaacson, H. 2016. A resonant chain of four transiting, sub-Neptune planets. *Nature* 533, 509.
- [Michtchenko et al.(2006)] Michtchenko, T. A., Beaugé, C., Ferraz-Mello, S. 2006. Stationary Orbits in Resonant Extrasolar Planetary Systems. *Celestial Mechanics and Dynamical Astronomy* 94, 411.
- [Michtchenko et al.(2008)] Michtchenko, T. A., Beaugé, C., Ferraz-Mello, S. 2008. Dynamic portrait of the planetary 2/1 mean-motion resonance - I. Systems with a more massive outer planet. *Monthly Notices of the Royal Astronomical Society* 387, 747.
- [Mizuno(1980)] Mizuno, H. 1980. Formation of the Giant Planets. *Progress of Theoretical Physics* 64, 544.
- [Moons and Morbidelli(1993)] Moons, M., Morbidelli, A. 1993. The Main Mean Motion Commensurabilities in the Planar Circular and Elliptic Problem. *Celestial Mechanics and Dynamical Astronomy* 57, 99.
- [Moons and Morbidelli(1995)] Moons, M., Morbidelli, A. 1995. Secular resonances inside mean-motion commensurabilities: the 4/1, 3/1, 5/2 and 7/3 cases.. *Icarus* 114, 33.
- [Morbidelli(1995)] Morbidelli, A. 1995, *Resonant structure and diffusion in hamiltonian systems*, Chaos and diffusion in Hamiltonian systems. Proceedings of the 4th workshop in astronomy and astrophysics of Chamonix, France, 7-12 February, 1994. Edited by Daniel Benest and Claude Froeschle. Published by Editions Frontiers (Paris), 1995, p.65
- [Morbidelli(2002)] Morbidelli, A. 2002, *Modern celestial mechanics : aspects of solar system dynamics*, by Alessandro Morbidelli. London: Taylor AMP Francis, 2002, ISBN 0415279399,
- [Morbidelli(2018)] Morbidelli, A. 2018. Accretion Processes. arXiv e-prints arXiv:1803.06708.
- [Morbidelli et al.(2008)] Morbidelli, A., Crida, A., Masset, F., Nelson, R. P. 2008. Building giant-planet cores at a planet trap. *Astronomy and Astrophysics* 478, 929.
- [Morbidelli et al.(2012)] Morbidelli, A., Lunine, J. I., O'Brien, D. P., Raymond, S. N., Walsh, K. J. 2012. Building Terrestrial Planets. *Annual Review of Earth and Planetary Sciences* 40, 251.
- [Mulders et al.(2018)] Mulders, G. D., Pascucci, I., Apai, D., Ciesla, F. J. 2018. The Exoplanet Population Observation Simulator. I. The Inner Edges of Planetary Systems. *The Astronomical Journal* 156, 24.
- [Müller et al.(2018)] Müller, A., and 45 colleagues 2018. Orbital and atmospheric characterization of the planet within the gap of the PDS 70 transition disk. *Astronomy and Astrophysics* 617, L2.
- [Murray & Dermott(1999)] Murray, C. D., & Dermott, S. F. 1999, *Solar system dynamics* by C.D. Murray and S.F. McDermott. (Cambridge, UK: Cambridge University Press), ISBN 0-521-57295-9 (hc.), ISBN 0-521-57297-4 (pbk.),
- [Mustill et al.(2018)] Mustill, A. J., Villaver, E., Veras, D., Gänsicke, B. T., Bonsor, A. 2018. Unstable low-mass planetary systems as drivers of white dwarf pollution. *Monthly Notices of the Royal Astronomical Society* 476, 3939.
- [Neishtadt(1999)] Neishtadt A. (1999) On Adiabatic Invariance in Two-Frequency Systems. In: Simó C. (eds) *Hamiltonian Systems with Three or More Degrees of Freedom*. NATO ASI Series (Series C:Mathematical and Physical Sciences), vol 533. Springer, Dordrecht
- [Neishtadt et al.(2008)] Neishtadt A., Vainchtein D., Vasiliev A. (2008) Adiabatic Invariance in Volume-Preserving Systems. In: Borisov A.V., Kozlov V.V., Mamaev I.S., Sokolovskiy M.A. (eds) *IUTAM Symposium on Hamiltonian Dynamics, Vortex Structures, Turbulence*. IUTAM Bookseries, vol 6. Springer, Dordrecht

- [Newton(1687)] Newton, I. 1687. *Philosophiae Naturalis Principia Mathematica*.
- [Obertas et al.(2017)] Obertas, A., Van Laerhoven, C., Tamayo, D. 2017. The stability of tightly-packed, evenly-spaced systems of Earth-mass planets orbiting a Sun-like star. *Icarus* 293, 52.
- [Ogihara et al.(2015)] Ogihara, M., Morbidelli, A., Guillot, T. 2015. A reassessment of the in situ formation of close-in super-Earths. *Astronomy and Astrophysics* 578, A36.
- [Ormel and Shi(2013)] Ormel, C., Shi, J.-M. 2013. The Flow Pattern around Low-Mass Planets. *Protostars and Planets VI Posters*.
- [Owen and Wu(2017)] Owen, J. E., Wu, Y. 2017. The Evaporation Valley in the Kepler Planets. *The Astrophysical Journal* 847, 29.
- [Paardekooper and Mellema(2006)] Paardekooper, S.-J., Mellema, G. 2006. Halting type I planet migration in non-isothermal disks. *Astronomy and Astrophysics* 459, L17.
- [Papaloizou and Szuszkiewicz(2005)] Papaloizou, J. C. B., Szuszkiewicz, E. 2005. On the migration-induced resonances in a system of two planets with masses in the Earth mass range. *Monthly Notices of the Royal Astronomical Society* 363, 153.
- [Papaloizou and Terquem(2010)] Papaloizou, J. C. B., Terquem, C. 2010. On the dynamics of multiple systems of hot super-Earths and Neptunes: tidal circularization, resonance and the HD 40307 system. *Monthly Notices of the Royal Astronomical Society* 405, 573.
- [Petigura et al.(2013)] Petigura, E. A., Howard, A. W., Marcy, G. W. 2013. Prevalence of Earth-size planets orbiting Sun-like stars. *Proceedings of the National Academy of Science* 110, 19273.
- [Petit et al.(2018)] Petit, A. C., Laskar, J., Boué, G. 2018. Hill stability in the AMD framework. *Astronomy and Astrophysics* 617, A93.
- [Petrovich and Muñoz(2017)] Petrovich, C., Muñoz, D. J. 2017. Planetary Engulfment as a Trigger for White Dwarf Pollution. *The Astrophysical Journal* 834, 116.
- [Pichierri et al.(2017)] Pichierri, G., Morbidelli, A., Lai, D. 2017. Extreme secular excitation of eccentricity inside mean motion resonance. Small bodies driven into star-grazing orbits by planetary perturbations. *Astronomy and Astrophysics* 605, A23.
- [Pichierri et al.(2018)] Pichierri, G., Morbidelli, A., Crida, A. 2018. Capture into first-order resonances and long-term stability of pairs of equal-mass planets. *Celestial Mechanics and Dynamical Astronomy* 130, 54.
- [Pichierri et al.(2019)] Pichierri, G., Batygin, K., Morbidelli, A. 2019. The role of dissipative evolution for three-planet, near-resonant extrasolar systems. *Astronomy and Astrophysics* 625, A7.
- [Poincaré(1892)] Poincaré, H. 1892, *Les méthodes nouvelles de la mécanique céleste*, Gauthier-Villars, Paris, 1892
- [Poincare & Fichot(1905)] Poincare, H., & Fichot, E. 1905, *Leçons de mécanique céleste professées à la Sorbonne*, Gauthier-Villars, Paris, 1905-10
- [Pollack et al.(1996)] Pollack, J. B., Hubickyj, O., Bodenheimer, P., Lissauer, J. J., Podolak, M., Greenzweig, Y. 1996. Formation of the Giant Planets by Concurrent Accretion of Solids and Gas. *Icarus* 124, 62.
- [Pousse et al.(2017)] Pousse, A., Robutel, P., Vienne, A. 2017. On the co-orbital motion in the planar restricted three-body problem: the quasi-satellite motion revisited. *Celestial Mechanics and Dynamical Astronomy* 128, 383.
- [Ramos et al.(2017)] Ramos, X. S., Charalambous, C., Benítez-Llambay, P., Beaugé, C. 2017. Planetary migration and the origin of the 2:1 and 3:2 (near)-resonant population of close-in exoplanets. *Astronomy and Astrophysics* 602, A101.
- [Rivera et al.(2010)] Rivera, E. J., Laughlin, G., Butler, R. P., Vogt, S. S., Haghighipour, N., Meschiari, S. 2010. The Lick-Carnegie Exoplanet Survey: a Uranus-Mass Fourth Planet for GJ 876 in an Extrasolar Laplace Configuration. *The Astrophysical Journal* 719, 890.

- [Robert et al.(2018)] Robert, C. M. T., Crida, A., Lega, E., Méheut, H., Morbidelli, A. 2018. Toward a new paradigm for Type II migration. *Astronomy and Astrophysics* 617, A98.
- [Rogers(2015)] Rogers, L. A. 2015. Most 1.6 Earth-radius Planets are Not Rocky. *The Astrophysical Journal* 801, 41.
- [Safronov(1969)] Safronov, V. S. 1969, *Evolution of the Protoplanetary Cloud and Formation of the Earth and the Planets*, English translation, NASA TT F-677 (1972).
- [Sessin and Ferraz-Mello(1984)] Sessin, W., Ferraz-Mello, S. 1984. Motion of two planets with periods commensurable in the ratio 2:1 solutions of the hori auxiliary system. *Celestial Mechanics* 32, 307.
- [Sidorenko(2006)] Sidorenko, V. V. 2006. Evolution of asteroid orbits at the 3 : 1 their mean motion resonance with Jupiter (planar problem). *Cosmic Research* 44, 440.
- [Simon et al.(2016)] Simon, J. B., Armitage, P. J., Li, R., Youdin, A. N. 2016. The Mass and Size Distribution of Planetesimals Formed by the Streaming Instability. I. The Role of Self-gravity. *The Astrophysical Journal* 822, 55.
- [Sorelli et al.(1996)] Sorelli, C., Grinin, V. P., Natta, A. 1996. Infall in Herbig Ae/Be stars: what NA D lines tell us.. *Astronomy and Astrophysics* 309, 155.
- [Tamayo et al.(2017)] Tamayo, D., Rein, H., Petrovich, C., Murray, N. 2017. Convergent Migration Renders TRAPPIST-1 Long-lived. *The Astrophysical Journal* 840, L19.
- [Terquem and Papaloizou(2007)] Terquem, C., Papaloizou, J. C. B. 2007. Migration and the Formation of Systems of Hot Super-Earths and Neptunes. *The Astrophysical Journal* 654, 1110.
- [Turner et al.(2014)] Turner, N. J., and 6 colleagues 2014. Transport and Accretion in Planet-Forming Disks. *Protostars and Planets VI* 411.
- [Vauclair and Fontaine(1979)] Vauclair, G., Fontaine, G. 1979. Convective mixing in helium white dwarfs.. *The Astrophysical Journal* 230, 563.
- [Veras et al.(2018)] Veras, D., Xu, S., Rebassa-Mansergas, A. 2018. The critical binary star separation for a planetary system origin of white dwarf pollution. *Monthly Notices of the Royal Astronomical Society* 473, 2871.
- [Ward(1992)] Ward, W. R. 1992. Coorbital Corotation Torque. *Lunar and Planetary Science Conference* 23, 1491.
- [Ward(1997)] Ward, W. R. 1997. Protoplanet Migration by Nebula Tides. *Icarus* 126, 261.
- [Weiss et al.(2013)] Weiss, L. M., and 17 colleagues 2013. The Mass of KOI-94d and a Relation for Planet Radius, Mass, and Incident Flux. *The Astrophysical Journal* 768, 14.
- [Weiss et al.(2018)] Weiss, L. M., and 12 colleagues 2018. The California-Kepler Survey. V. Peas in a Pod: Planets in a Kepler Multi-planet System Are Similar in Size and Regularly Spaced. *The Astronomical Journal* 155, 48.
- [Welsh and Montgomery(2013)] Welsh, B. Y., Montgomery, S. 2013. Circumstellar Gas-Disk Variability Around A-Type Stars: The Detection of Exocomets?. *Publications of the Astronomical Society of the Pacific* 125, 759.
- [Williamson(1936)] J. Williamson, 1936, *On the algebraic problem concerning the normal forms of linear dynamical systems*, *Amer. J. of Math.* 58, 141?163 (1936).
- [Winn and Fabrycky(2015)] Winn, J. N., Fabrycky, D. C. 2015. The Occurrence and Architecture of Exoplanetary Systems. *Annual Review of Astronomy and Astrophysics* 53, 409.
- [Wintner(1934)] A. Wintner, 1934, *On the linear conservative dynamical systems*, *Annali di Matematica Pura ed Applicata*, ser. 4, tomo 13 (1934-1935).
- [Wisdom(1983)] Wisdom, J. 1983. Chaotic behavior and the origin of the 3/1 Kirkwood gap. *Icarus* 56, 51.
- [Wisdom(1985)] Wisdom, J. 1985. A perturbative treatment of motion near the 3/1 commensurability. *Icarus* 63, 272.

- [Wisdom(1986)] Wisdom, J. 1986. Canonical Solution of the Two Critical Argument Problem. *Celestial Mechanics* 38, 175.
- [Wolszczan and Frail(1992)] Wolszczan, A., Frail, D. A. 1992. A planetary system around the millisecond pulsar PSR1257 + 12. *Nature* 355, 145.
- [Wright et al.(2012)] Wright, J. T., Marcy, G. W., Howard, A. W., Johnson, J. A., Morton, T. D., Fischer, D. A. 2012. The Frequency of Hot Jupiters Orbiting nearby Solar-type Stars. *The Astrophysical Journal* 753, 160.
- [Wu and Lithwick(2013)] Wu, Y., Lithwick, Y. 2013. Density and Eccentricity of Kepler Planets. *The Astrophysical Journal* 772, 74.
- [Xu et al.(2018)] Xu, W., Lai, D., Morbidelli, A. 2018. Migration of planets into and out of mean motion resonances in protoplanetary discs: overstability of capture and non-linear eccentricity damping. *Monthly Notices of the Royal Astronomical Society* 481, 1538.
- [Youdin and Goodman(2005)] Youdin, A. N., Goodman, J. 2005. Streaming Instabilities in Protoplanetary Disks. *The Astrophysical Journal* 620, 459.
- [Zuckerman et al.(2003)] Zuckerman, B., Koester, D., Reid, I. N., Hünsch, M. 2003. Metal Lines in DA White Dwarfs. *The Astrophysical Journal* 596, 477.

Appendix A

Integrable approximation for two-planet mean motion resonant dynamics

In this appendix, I sketch the reduction of the averaged Hamiltonian $\bar{\mathcal{H}}$ expanded to first order in the eccentricities and inclinations, for two planets of mass m_1, m_2 in a $k : k - 1$ mean motion resonance. The derivation yields a 1 d.o.f. Hamiltonian with the same structure as an Andoyer Hamiltonian $\mathcal{H}_{\text{And},1}$ (cfr. (2.56)), and is based on [Sessin and Ferraz-Mello(1984)] and [Batygin and Morbidelli(2013)a, Batygin(2015)].

We start with the Hamiltonian (3.2), that I rewrite here for readability:

$$\bar{\mathcal{H}} = \mathcal{H}_{\text{kepl}} + \mathcal{H}_{\text{res}}. \quad (\text{A.1})$$

The resonant Hamiltonian \mathcal{H}_{res} expanded to first order in the eccentricities and inclinations reads (cfr. Subsect. 2.2.2.1)

$$\mathcal{H}_{\text{res}} = -\frac{\mathcal{G}m_1m_2}{a_2} \left(f_{\text{res}}^{(1)} e_1 \cos(k\lambda_2 - (k-1)\lambda_1 + \gamma_1) + f_{\text{res}}^{(2)} e_2 \cos(k\lambda_2 - (k-1)\lambda_1 + \gamma_2) \right) + \mathcal{O}(e^2, I^2); \quad (\text{A.2})$$

dropping the higher order terms naturally makes the problem a planar one. Introducing modified Delaunay variables $(\Lambda_i, \Gamma_i, \lambda_i, \gamma_i)$, Equation (2.98), the Keplerian part $\mathcal{H}_{\text{kepl}}$ takes the usual form

$$\mathcal{H}_{\text{kepl}} = -\frac{\mathcal{G}^2(M_* + m_1)^2\mu_1^3}{2\Lambda_1^2} - \frac{\mathcal{G}^2(M_* + m_2)^2\mu_2^3}{2\Lambda_2^2}, \quad (\text{A.3})$$

while resonant Hamiltonian \mathcal{H}_{res} expanded to first order in the eccentricities and inclinations is

$$\begin{aligned} \mathcal{H}_{\text{res}} = & -\frac{\mathcal{G}^2 M_* m_1 m_2^3}{\Lambda_2^2} \left(f_{\text{res}}^{(1)} \sqrt{\frac{2\Gamma_1}{\Lambda_1}} \cos(k\lambda_2 - (k-1)\lambda_1 + \gamma_1) \right. \\ & \left. + f_{\text{res}}^{(2)} \sqrt{\frac{2\Gamma_2}{\Lambda_2}} \cos(k\lambda_2 - (k-1)\lambda_1 + \gamma_2) \right), \end{aligned} \quad (\text{A.4})$$

where we used the approximation $\Gamma_i \simeq \Lambda_i e_i^2 / 2$ (cfr. Equation (3.10)). The coefficients $f_{\text{res}}^{(1)}$ and $f_{\text{res}}^{(2)}$ depend (weakly) on the semi-major axis ratio (cfr. Subsect. 2.2.2.1); as in Subsect. 3.1.1, since the two terms in parenthesis in (A.4) are already of order $\sqrt{\Gamma} = \mathcal{O}(e)$, we evaluated Λ_i on the nominal values of the semi-major axes \bar{a}_i corresponding to the Keplerian approximation, and the coefficients f_{res} become constants. We notice that $f_{\text{res}}^{(1)} < 0$ and $f_{\text{res}}^{(2)} > 0$ [Murray & Dermott(1999)].

Now, we introduce for (Λ_i, λ_i) the change of variable ([Sessin and Ferraz-Mello(1984)], see also Equation (3.5))

$$\begin{aligned} \Theta &= \Lambda_2/k, & \theta &= k\lambda_2 - (k-1)\lambda_1, \\ \mathcal{K} &= \Lambda_1 + \frac{k-1}{k}\Lambda_2, & \kappa &= \lambda_1. \end{aligned} \quad (\text{A.5})$$

The newly defined angle κ does not appear explicitly in the Hamiltonian, making its conjugated action \mathcal{K} a constant of motion; we discussed in Section 3.1 its significance with respect to the nominal semi-major axes \bar{a}_i . Unlike the

derivation of Section 3.1 (which was valid for unexpanded Hamiltonians), we now take a different path. The modified Delaunay variables (Γ_i, γ_i) are changed to mixed secular cartesian coordinates

$$\begin{aligned} x_i &= \sqrt{2\Gamma_i} \cos \gamma_i, \quad y_i = \sqrt{2\Gamma_i} \sin \gamma_i, \quad \text{i.e.} \\ \Gamma_i &= \frac{1}{2}(x_i^2 + y_i^2), \quad \gamma_i = \text{atan2}(y_i, x_i), \end{aligned} \quad (\text{A.6})$$

where y are the coordinates and x the conjugated momenta. With this, the resonant Hamiltonian becomes

$$\mathcal{H}_{\text{res}} = -(\alpha_1 x_1 + \alpha_2 x_2) \cos \theta + (\alpha_1 y_1 + \alpha_2 y_2) \sin \theta, \quad (\text{A.7})$$

where

$$\alpha_i = \frac{\mathcal{G}^2 M_*^2 m_1 m_2^3}{(M_* + m_2) \Lambda_2^2} \times \frac{f_{\text{res}}^{(i)}}{\sqrt{\Lambda_i}}, \quad i = 1, 2, \quad \alpha_1 < 0, \quad \alpha_2 > 0, \quad (\text{A.8})$$

are constants that describe the strength of the two harmonics. Then, we introduce another change of coordinates: the rotation¹ [Henrard et al.(1986), Wisdom(1986)]

$$\begin{aligned} u_1 &= \frac{\alpha_1 x_1 + \alpha_2 x_2}{\sqrt{\alpha_1^2 + \alpha_2^2}} & v_1 &= \frac{\alpha_1 y_1 + \alpha_2 y_2}{\sqrt{\alpha_1^2 + \alpha_2^2}}, \\ u_2 &= \frac{\alpha_2 x_1 - \alpha_1 x_2}{\sqrt{\alpha_1^2 + \alpha_2^2}} & v_2 &= \frac{\alpha_2 y_1 - \alpha_1 y_2}{\sqrt{\alpha_1^2 + \alpha_2^2}}, \end{aligned} \quad (\text{A.9})$$

where v are the coordinates and u the conjugated momenta. The resonant Hamiltonian becomes

$$\mathcal{H}_{\text{res}} = \sqrt{\alpha_1^2 + \alpha_2^2} (-u_1 \cos \theta + v_1 \sin \theta). \quad (\text{A.10})$$

The rotation (A.9) allows to successfully reduce the number of degrees of freedom to 1: introducing

$$\begin{aligned} \Phi_i &= \frac{1}{2}(u_i^2 + v_i^2), \quad \phi_i = \text{atan2}(v_i, u_i), \quad \text{i.e.} \\ u_i &= \sqrt{2\Phi_i} \cos \phi_i, \quad v_i = \sqrt{2\Phi_i} \sin \phi_i. \end{aligned} \quad (\text{A.11})$$

we get

$$\mathcal{H}_{\text{res}} = -\sqrt{\alpha_1^2 + \alpha_2^2} \sqrt{2\Phi_1} \cos(\theta + \phi_1), \quad (\text{A.12})$$

a Hamiltonian where neither ϕ_2 nor Φ_2 enter explicitly. Now we just need to call $\theta + \phi_1 =: \psi_1$, and complete the change of coordinates²:

$$\begin{aligned} \Psi_1 &= \Phi_1, & \psi_1 &= \theta + \phi_1, \\ \Psi_2 &= \Phi_2, & \psi_2 &= \theta + \phi_2, \\ \Omega &= \Theta - \Phi_1 - \Phi_2, & \omega &= \theta, \\ \mathcal{K}, & & \kappa. & \end{aligned} \quad (\text{A.13})$$

We see that the three last angles do not enter in the the Hamiltonian, which in this set of canonical variables becomes

$$\bar{\mathcal{H}} = -\frac{\mathcal{G}(M_* + m_1)^2 \mu_1^3}{2(\mathcal{K} + (1-k)(\Psi_1 + \Psi_2 + \Omega))^2} - \frac{\mathcal{G}(M_* + m_2)^2 \mu_2^3}{2(k(\Psi_1 + \Psi_2 + \Omega))^2} - \sqrt{\alpha_1^2 + \alpha_2^2} \sqrt{2\Psi_1} \cos(\psi_1), \quad (\text{A.14})$$

i.e. an integrable 1 d.o.f. Hamiltonian system in (Ψ_1, ψ_1) with integrals of motion (i.e. parameters) $\Psi_2, \Omega, \mathcal{K}$. It is interesting to write what these variables are in terms of the original orbital elements. Working backwards through

¹The idea is that \mathcal{H}_{res} depends on x_i and y_i only through $\alpha_1 x_1 + \alpha_2 x_2$ and $\alpha_1 y_1 + \alpha_2 y_2$ (the coefficients of $\cos \theta$ and $\sin \theta$) which, up to a renormalisation, form a canonical pair: they therefore become u_1 (the momentum) and v_1 (the position) respectively; the remaining two variables are obtained by completing the canonical change of variable.

²I keep the names of the variables used in [Batygin and Morbidelli(2013)a, Batygin(2015)], but these are different from the variables that we used in Chapters 3 to 5.

the changes of variables, in the approximation $\Gamma_i \simeq \Lambda_i e_i^2/2$ valid at small eccentricities one gets:

$$\begin{aligned}\Psi_1 &= \frac{e_1^2 \alpha_1^2 \Lambda_1 + e_2^2 \alpha_2^2 \Lambda_2 + 2e_1 e_2 \alpha_1 \sqrt{\Lambda_1} \alpha_2 \sqrt{\Lambda_2} \cos(\varpi_1 - \varpi_2)}{2(\alpha_1^2 + \alpha_2^2)}, \\ \Psi_2 &= \frac{e_1^2 \alpha_2^2 \Lambda_1 + e_2^2 \alpha_1^2 \Lambda_2 - 2e_1 e_2 \alpha_2 \sqrt{\Lambda_1} \alpha_1 \sqrt{\Lambda_2} \cos(\varpi_1 - \varpi_2)}{2(\alpha_1^2 + \alpha_2^2)}, \\ \Omega &= \frac{\Lambda_2}{k} - \Lambda_1 \frac{e_1^2}{2} - \Lambda_2 \frac{e_2^2}{2}, \\ \mathcal{K} &= \Lambda_1 + \frac{k-1}{k} \Lambda_2.\end{aligned}\tag{A.15}$$

One notices that in this approximation $\Omega + \mathcal{K} = \mathcal{L}$ the angular momentum, and that $\Psi_1 + \Psi_2 = (\Lambda_1 + \Lambda_2) - \mathcal{L} = \mathcal{A}$ the (planar) angular momentum deficit (AMD), which is conserved away from mean motion resonance (i.e. in the secular domain, [Laskar(1997), Laskar(2000)]). A final simplification, which allows to cast the Hamiltonian in the form of an Andoyer Hamiltonian, can be made if one considers small deviations of the semi-major axes around their nominal values \bar{a}_i . It is convenient to do so starting from the expression of $\mathcal{H}_{\text{kepl}}$ in terms of Λ_i and carry out the series of transformation of variables outlined above. We introduce $\delta\Lambda_i = \Lambda_i - \bar{\Lambda}_i$ and develop each Keplerian term $-(\mathcal{G}^2(M_* + m_i)^2 \mu_i^3)/(2\Lambda_i^2)$ to order two in $\delta\Lambda_i$, which yields $4\bar{n}_i \Lambda_i - \frac{3}{2} \bar{h}_i \Lambda_i^2$ (up to some constant terms), where $\bar{n}_i := (\mathcal{G}^2(M_* + m_i)^2 \mu_i^3)/\bar{\Lambda}_i^3 \equiv \sqrt{\mathcal{G}(M_* + m_i)}/\bar{a}_i^3$ is the nominal mean motion, and $\bar{h}_i := \bar{n}_i/\bar{\Lambda}_i \equiv 1/(\mu_i \bar{a}_i^2)$ is the inverse moment of inertia of a circular orbit (cfr. a similar calculation in the case of three planets, Equations (4.9) and (4.10)). Therefore the Keplerian part can be approximated as

$$\mathcal{H}_{\text{kepl}} \simeq 4(\bar{n}_1 \Lambda_1 + \bar{n}_2 \Lambda_2) - \frac{3}{2} (\bar{h}_1 \Lambda_1^2 + \bar{h}_2 \Lambda_2^2).\tag{A.16}$$

Introducing now the coordinates (A.13) (and removing unimportant constant terms involving \mathcal{K}) the Hamiltonian becomes

$$\bar{\mathcal{H}} = 3(k-1)\bar{h}_1 \mathcal{K} (\Psi_1 + \Psi_2 + \Omega) - \frac{3}{2} (\bar{h}_1 (k-1)^2 + \bar{h}_2 k^2) (\Psi_1 + \Psi_2 + \Omega)^2 - \sqrt{\alpha_1^2 + \alpha_2^2} \sqrt{2\Psi_1} \cos(\psi_1).\tag{A.17}$$

One recognises the functional form of an Andoyer Hamiltonian $\mathcal{H}_{\text{And},1}$, cfr. (2.56). Equation (A.17) can also be made to depend on a single parameter $\tilde{\delta}$ to cast it in the simplified form (2.57). To do this, one can rescale all the actions and the Hamiltonian by $\eta = \left(\frac{\alpha_1^2 + \alpha_2^2}{3^2 (\bar{h}_1 (k-1)^2 + \bar{h}_2 k^2)} \right)^{1/3}$:

$$\tilde{\mathcal{H}} = \bar{\mathcal{H}}/\eta, \quad \tilde{\Psi}_1 = \Psi_1/\eta, \quad \tilde{\Psi}_2 = \Psi_2/\eta, \quad \Omega = \tilde{\Omega}/\eta, \quad \tilde{\mathcal{K}} = \mathcal{K}/\eta.\tag{A.18}$$

After dropping unimportant terms independent on $\tilde{\Psi}_1$, the Hamiltonian becomes

$$\tilde{\mathcal{H}} = 3\eta \left((k-1)\bar{h}_1 \tilde{\mathcal{K}} - (\bar{h}_1 (k-1)^2 + \bar{h}_2 k^2) (\tilde{\Psi}_2 + \tilde{\Omega}) \right) \tilde{\Psi}_1 + 3\eta (\bar{h}_1 (k-1)^2 + \bar{h}_2 k^2) (-\tilde{\Psi}_1^2/2 - \sqrt{2\tilde{\Psi}_1} \cos(\psi_1)),\tag{A.19}$$

so the coefficient in front of the $\tilde{\Psi}_1^2$ term equals half that multiplying $\sqrt{2\tilde{\Psi}_1} \cos(\psi_1)$, and both are proportional to $3\eta (\bar{h}_1 (k-1)^2 + \bar{h}_2 k^2)$. Then one rescales the Hamiltonian and the time variable by this $3\eta (\bar{h}_1 (k-1)^2 + \bar{h}_2 k^2)$. Finally, introducing

$$\tilde{\delta} = \frac{\left((k-1)\bar{h}_1 \tilde{\mathcal{K}} - (\bar{h}_1 (k-1)^2 + \bar{h}_2 k^2) (\tilde{\Psi}_2 + \tilde{\Omega}) \right)}{(\bar{h}_1 (k-1)^2 + \bar{h}_2 k^2)},\tag{A.20}$$

and calling $\tilde{\psi}_1 = \psi_1$ one arrives at

$$\tilde{\mathcal{H}} = \tilde{\delta} \tilde{\Psi}_1 - \frac{1}{2} \tilde{\Psi}_1^2 - \sqrt{2\tilde{\Psi}_1} \cos(\tilde{\psi}_1),\tag{A.21}$$

which has the desired form (2.56), up to a change of signs. This Hamiltonian is given in dimensionless form: the quantity η (which has units of angular momentum) encapsulates all of the information regarding how the dynamics scales with mass ratios and physical sizes of the orbits [Batygin and Morbidelli(2013)a, Batygin(2015)]. Since $\tilde{\Psi}$ is proportional to the eccentricity squared and during the disc phase the effect of the disc is to damp the eccentricities faster than the planets migrate, cfr. Subsect. 3.2.1, during capture in mean motion resonance the action $\tilde{\Psi}$ is initially small. As in Subsect. 2.3.3, this means that $\tilde{\delta}$ measures the proximity to the desired $k : k-1$ resonance. Notice that during convergent migration, $\tilde{\delta}$ is positive [Batygin(2015)]. Since the coefficient in front of $\tilde{\Psi}_1^2$ in (A.21) is negative, by Subsection 2.3.3 mean motion resonance capture is ensured by the adiabatic principle for small amplitude orbits.

Appendix B

Reduced Hamiltonian to a common planetary mass factor for three resonant planets

In the course of Chapter 4 we made implicit use of a reduced Hamiltonian which incorporates the planetary masses through a common planet-to-star mass factor \tilde{m} . In this appendix, we detail the construction of this Hamiltonian and its use in the chapter.

Consider three planets, whose physical parameters are labelled 1, 2, and 3 for the inner, middle and outer planet respectively, orbiting around a star of mass M_* on the same plane. Suppose that the planets are (close to) a chain of mean-motion resonance, with nominal semi-major axes \bar{a} and that the deviations of the semi-major axes from the nominal values are small, and assume that the eccentricities are small enough, so that an analysis to first order in e is valid. These are the working assumptions throughout Section 4.2. Having fixed the planet-planet mass ratios $m_1/m_2 = \beta_1$ and $m_2/m_3 = \beta_2$, we introduce the average planet-star mass ratio

$$\tilde{m} = \frac{m_1 + m_2 + m_3}{3M_*} = \frac{m_1(1 + \beta_1^{-1} + \beta_1^{-1}\beta_2^{-1})}{3M_*}. \quad (\text{B.1})$$

Inverting this expression we easily get all planetary masses in terms of \tilde{m} ,

$$\begin{aligned} m_1 &= c_1 \tilde{m} := \frac{3\beta_1\beta_2 M_*}{1 + \beta_2 + \beta_1\beta_2} \tilde{m}, \\ m_2 &= c_2 \tilde{m} := \frac{3\beta_1 M_*}{1 + \beta_2 + \beta_1\beta_2} \tilde{m}, \\ m_3 &= c_3 \tilde{m} := \frac{3M_*}{1 + \beta_2 + \beta_1\beta_2} \tilde{m}, \end{aligned} \quad (\text{B.2})$$

with coefficients c depending on M_* , β_1 and β_2 only.

We introduce the modified Delaunay action-angle variables $(\Lambda_i, \Gamma_i, \lambda_i, \gamma_i)$ as in (2.98), but we rescale the actions by the common mass factor \tilde{m} : this gives the following definition for the Λ 's (we maintain the same notation as the non-rescaled actions for simplicity)

$$\begin{aligned} \Lambda_1 &= \frac{3\beta_1\beta_2 M_*}{1 + \beta_2 + \beta_1\beta_2} \sqrt{\mathcal{G}M_* a_1} = c_1 \sqrt{\mathcal{G}M_* a_1}, \\ \Lambda_2 &= \frac{3\beta_1 M_*}{1 + \beta_2 + \beta_1\beta_2} \sqrt{\mathcal{G}M_* a_2} = c_2 \sqrt{\mathcal{G}M_* a_2}, \\ \Lambda_3 &= \frac{3M_*}{1 + \beta_2 + \beta_1\beta_2} \sqrt{\mathcal{G}M_* a_3} = c_3 \sqrt{\mathcal{G}M_* a_3}, \end{aligned} \quad (\text{B.3})$$

and the same formal definition of $\Gamma = \Lambda e^2/2$ at lowest order in e . We now introduce the Hamiltonian for the problem, that is the sum of the Keplerian Hamiltonian (4.5) and the resonant interaction Hamiltonian (4.6) to first order in e . However since we have rescaled the actions by \tilde{m} , in order for the Hamilton equations to be conserved we must also rescale the Hamiltonian itself by \tilde{m} . As in Section 4.2, since we are not considering large deviations

in the semi-major axes from their nominal values, and since the resonant Hamiltonian is already of order $\mathcal{O}(e)$, we evaluate the resonant Hamiltonian on the nominal values $\bar{\Lambda}$ defined from \bar{a} using (B.3). It is then easy to see that the rescaled Keplerian Hamiltonian takes the form

$$\mathcal{H}_{\text{kepl}} = - \sum_{i=1}^3 \frac{c_i^3}{2} \left(\frac{\mathcal{G}M_*}{\Lambda_i} \right)^2, \quad (\text{B.4})$$

and is therefore independent of \tilde{m} , while the rescaled resonant part will have a multiplicative coefficient \tilde{m} :

$$\begin{aligned} \mathcal{H}_{\text{res}} = \tilde{m} \left[- \frac{\mathcal{G}^2 M_* c_1 c_2^3}{\Lambda_2^2} \left(f_{\text{res}}^{(1,1)} \sqrt{\frac{2\Gamma_1}{\Lambda_1}} \cos(k^{(1)}\lambda_2 - (k^{(1)} - 1)\lambda_1 + \gamma_1) \right. \right. \\ \left. \left. + f_{\text{res}}^{(2,1)} \sqrt{\frac{2\Gamma_2}{\Lambda_2}} \cos(k^{(1)}\lambda_2 - (k^{(1)} - 1)\lambda_1 + \gamma_2) \right) + \right. \\ \left. - \frac{\mathcal{G}^2 M_* c_2 c_3^3}{\Lambda_3^2} \left(f_{\text{res}}^{(1,2)} \sqrt{\frac{2\Gamma_2}{\Lambda_2}} \cos(k^{(2)}\lambda_3 - (k^{(2)} - 1)\lambda_2 + \gamma_2) \right. \right. \\ \left. \left. + f_{\text{res}}^{(2,2)} \sqrt{\frac{2\Gamma_3}{\Lambda_3}} \cos(k^{(2)}\lambda_3 - (k^{(2)} - 1)\lambda_2 + \gamma_3) \right) \right]. \quad (\text{B.5}) \end{aligned}$$

From here, the sequence of changes of variables detailed in Section 4.2 can be performed using the same formal definitions for the new rescaled variables.

Already from the Hamiltonian written in terms of the rescaled variables Λ and $\Gamma \propto e^2$ one can see the following. Assuming a fixed equilibrium value of the semi-major axes (that is, of the Λ 's), a change in the planet-star mass factor \tilde{m} will have the only effect to rescale the equilibrium values of all $\sqrt{\Gamma} \propto e$ by the same quantity. In this configuration, the equilibria of the semi-major axis ratios $(a_2/a_1)_{\text{eq}}$ and $(a_3/a_2)_{\text{eq}}$ remain independent of \tilde{m} .

Appendix C

Some useful Mathematica code snippets for perturbation theory

Calculate the Poisson bracket $\{\dots\{\{f, g\}, g\}, \dots, g\}$ of f vs. g , i times:

```
IthPoissonBracket[f_, g_, p_List, q_List, i_Integer] /; Length[p] == Length[q] :=
  If[i == 1,
    Chop[D[f, {q}].D[g, {p}] - D[f, {p}].D[g, {q}]],
    IthPoissonBracket[IthPoissonBracket[f, g, p, q, 1], g, p, q, i - 1]
  ];
```

Select a harmonic from a Poisson-expression of type $I^m \begin{Bmatrix} \sin \\ \cos \end{Bmatrix}(\phi)$:

```
SelectHarmonic[
  PoissonExpr_] /; (! FreeQ[Last[1. PoissonExpr], Cos] || !
  FreeQ[Last[1. PoissonExpr], Sin]) :=
  Identity @@ Last[PoissonExpr];
```

Obtain the generating Hamiltonian which eliminates a perturbation term \mathcal{H}_1 in a Hamiltonian \mathcal{H} whose integrable part is $\mathcal{H}_0 = \boldsymbol{\omega} \cdot \mathbf{I}$ (linear in the actions):

```
\[Chi]generator[H0_, H1_, p_List, q_List] /; Length[p] == Length[q] :=
Module[
  {local\[Omega]vect, local\[Chi], localxtmp, localH1tmp, locali,
  localH1Expand, localITOT, localsmalldivisor},
  local\[Omega]vect = D[H0, {p}];
  localH1Expand = H1 // Expand;
  If[FreeQ[Head[localH1Expand], Plus],
    (* If H1 is only one addend *)
    localsmalldivisor = D[SelectHarmonic[H1], {q}].local\[Omega]vect;
    local\[Chi] = -(localH1Expand/localsmalldivisor) /. {Sin -> Cos,
    Cos -> Sin},
    (* Else if H1 contains multiple addends *)
    localITOT = Length[List @@ (localH1Expand)];
    For[locali = 1, locali <= localITOT, locali++,
      localH1tmp = (List @@ (localH1Expand))[[locali]];
      localsmalldivisor = D[SelectHarmonic[localH1tmp], {q}].local\[Omega]vect;
      localxtmp[
        locali] = -(localH1tmp/localsmalldivisor) /. {Sin -> Cos,
        Cos -> Sin};
      local\[Chi] = Sum[localxtmp[locali], {locali, 1, localITOT}];
    ];
  ];
local\[Chi]
```

Transform a Hamiltonian \mathcal{H} with the Lie series transformation given by a generating Hamiltonian χ , up to order equal to a given order:

```
TransformHWith\[Chi][H_,\[Chi]_, p_List, q_List, Order_Integer] /;
```

```

Length[p] == Length[q] := Module[
{localorder},
Chop[(H +
Sum[1/Factorial[
localorder] (IthPoissonBracket[H, \[Chi], p, q,
localorder]) // TrigExpand // Chop, {localorder, 1,
Order})] // TrigReduce]
];

```

Appendix D

Mathematica code used in Chapter 6

```
ClearAll["Global`*"]
(*This notebook is meant to accompany the article: "Extreme Secular Excitation of Eccentricity
  Inside Mean Motion Resonance: Driving Small Bodies into Star-Grazing Orbits by Planetary
  Perturbations", by G. Pichierri, A. Morbidelli & D. Lai.

Article Reference Number: AA/2017/30936

Key Words: Celestial Mechanics\[Dash]Planets and satellites:dynamical evolution and stability\[
  Dash]Minor planets ,asteroids:general\[Dash]Stars:white dwarfs\[Dash]Methods:analytical
*)

(*A note on notation*)
(*In the following, a and e will refer to semi-major axes of the test mass, while ap and ep will
  refer to those of the planetary perturber (in the article, the notation a' and e' is used:
  you can read the p in ap as prime).
The same notation is used for the angles \[CurlyPi] (the longitude of pericenter) and \[Lambda] (
  the mean longitude).
In short, all quantities with a p at the end will refer to the perturber (such as Mp, the mass of
  the perturber).
Also, k and kp will denote the integers that define the resonance: np:n=k:kp, where n and np are
  the mean motions of the two bodies.
Code units are such that G*M_Star=1, where G is the Gravitational constant and M_Star the mass of
  the central star.*)
(*This notebook generates in one stroke the level curves of the Hamiltonian denoted by Overscript
  [Overscript[H, _], _](N,p; J=0) in the article and the Hamiltonian Overscript[Overscript[H, _
  ], _]+ Subscript[H, GR], both on the (e cos\[CurlyPi], e sin\[CurlyPi]) plane and the (\[
  CurlyPi],Log[a(1-e)]) plane (Figures 3–10). A simplified version of Figure 2 is also obtained
  *)
(*Introduce the Hamiltonian (2.1)*)
(*Define the Keplerian Hamiltonian*)
HKep=-1/(2L^2) + np Lp;
(*Introduce the perturbation in cartesian coordinates*)
\[CapitalDelta]=Sqrt[(x-xp)^2+(y-yp)^2]; (*Distance between planet and test particle*)
\[CapitalDelta]p= (xp^2+yp^2)^(3/2);(*Distance between planet p and star*)
HPert=-Mp(1/ \[CapitalDelta] - (x xp + y yp)/\[CapitalDelta]p);(*the perturbing Hamiltonian of
  the restricted three-body problem*)
(*In the following commented text we simply recall in a self-contained fashion the canonical
  variables that will be used.*)
(*Canonical modified Delaunay variables, formulas (2.3), (2.4)*)
(*
(*Actions*)
P=Sqrt[a](1-Sqrt[1-e^2]); (*P=L-G*)
L=Sqrt[a];
Lp; (* Lp(=L' in the article) is a dummy variable to make the Hamiltonian autonomous*)

(*Conjugated Angles*)
p=-\[CurlyPi];
\[Lambda];
\[Lambda]p;
*)
```

```

(*In addition there is a  $\lambda_p$  (=  $\lambda'$  in the article) which is a parameter, since the
  outer planet does not precess*)
(*These are the cartesian coordinates as functions of orbital elements*)

(*
In the following EE = eccentric anomaly;
x=Cos[ $\lambda$ ] * a * (Cos[EE]-e)-Sin[ $\lambda$ ] * a * Sqrt[1-e^2] * Sin[EE];
y=Sin[ $\lambda$ ] * a * (Cos[EE]-e)+Cos[ $\lambda$ ] * a * Sqrt[1-e^2] * Sin[EE];

xp=Cos[ $\lambda_p$ ] * ap * (Cos[EEp]-ep)-Sin[ $\lambda_p$ ] * ap * Sqrt[1-ep^2] * Sin[EEp];
yp=Sin[ $\lambda_p$ ] * ap * (Cos[EEp]-ep)+Cos[ $\lambda_p$ ] * ap * Sqrt[1-ep^2] * Sin[EEp];
 $\lambda_p$ =0; (*WLOG: outer planet does not precess, take its perihelion at 0*)
*)
(*Canonical resonant variables, formula (2.6) in the article*)
(*
(*Actions*)
S=P;
NN=(kp-k)/k L+P; (*called N in the article*)
Lptilda=(kp/k)L+ Lp;

(*Conjugated Angles*)
 $\lambda$  = (kp  $\lambda_p$  - k  $\lambda$  + (kp-k)p)/(kp-k);
 $\lambda$  = - $\lambda$  + p // Simplify;
 $\lambda_p$ ;
*)

(*Invert the transformation on the actions; get the Keplerian part of the Hamiltonian*)
Solve[{S=P, NN==(kp-k)/k L+S, Lptilda==(kp/k)L+ Lp}, {L, Lp, P}] // Simplify
HKepl=HKepl // %[[1]]
{{L->(k (-NN+S))/(k-kp), Lp->(k Lptilda-kp (Lptilda-NN+S))/(k-kp), P->S}}
-((k-kp)^2/(2 k^2 (-NN+S)^2))+(np (k Lptilda-kp (Lptilda-NN+S)))/(k-kp)
(*Get e from S, a*)
Solve[S== Sqrt[a](1-Sqrt[1-e^2]), e] // Simplify
(*Get a from NN, S*)
Solve[NN== (kp-k)/k Sqrt[a]+S, a]
{{e->-Sqrt[(((2 Sqrt[a]-S) S)/a)]}, {e->Sqrt[(((2 Sqrt[a]-S) S)/a)]}
{{a->(k^2 (NN-S)^2)/(k-kp)^2}}
(*Get a=a(N, e)*)
aFromAndNN=Solve[NN==(kp-k)/k Sqrt[a] +Sqrt[a](1-Sqrt[1-e^2]), a][[1]] // Simplify
{a->(k^2 (-(-1+e^2) k^2+2 Sqrt[1-e^2] k kp+kp^2) NN^2)/((-1+e^2) k^2+kp^2)^2}
(*Fix perturber: THESE CAN BE MODIFIED BY THE USER*)
ap=1/(k/kp)^(2/3); (*In AU*)
np=1/Sqrt[ap^3];
Mp=10^(-4);
ep=.1;

(*Choose the resonance: THESE CAN BE MODIFIED BY THE USER*)
kp=4;
k=1;
ares=ap * (k/kp)^(2/3); (*Resonant location of a*)
(*Write the Cartesian coordinates in terms of the orbital parameters*)
x=Cos[ $\lambda$ ] * a * (Cos[EE]-e)-Sin[ $\lambda$ ] * a * Sqrt[1-e^2] * Sin[EE];
y=Sin[ $\lambda$ ] * a * (Cos[EE]-e)+Cos[ $\lambda$ ] * a * Sqrt[1-e^2] * Sin[EE];

 $\lambda$ =0;
xp=Cos[ $\lambda_p$ ] * ap * (Cos[EEp]-ep)-Sin[ $\lambda_p$ ] * ap * Sqrt[1-ep^2] * Sin[EEp];
yp=Sin[ $\lambda_p$ ] * ap * (Cos[EEp]-ep)+Cos[ $\lambda_p$ ] * ap * Sqrt[1-ep^2] * Sin[EEp];

(*Write EEp=EEp( $\lambda_p$ ) from Kepler's eq*)
BessMax=50;
EEp= $\lambda_p$ +Sum[2/n BesselJ[n, n ep] Sin[n  $\lambda_p$ ], {n,1,BessMax}];

(*Link all the angles to EE=eccentric anomaly (on which we average),  $\lambda$ ,  $\lambda_p$ *)
 $\lambda$ =(kp-k) $\lambda$  + k  $\lambda_p$ +(kp-k) $\lambda$ /kp;
 $\lambda$ =EE-e Sin[EE]+ $\lambda$ ; (* by Kepler's eq.*)
(*Now we can get the averaged perturbation, i.e. equation (2.8) in the article*)
HPertAveraged[sigma_, ecc_, varpi_, semia_]:=1/(2 Pi kp) NIntegrate[(HPert*(1-e Cos[EE])) // {e-> ecc,
   $\lambda$ ->sigma,  $\lambda_p$ ->varpi, a->semia }, {EE,0,2 Pi kp}, PrecisionGoal->10, AccuracyGoal
  ->10];
HPertAveraged[.1,.1,0,ares](*Test that it returns a numerical value*)
-0.0000413709

```

```

If [kp-k==1,arif=98/100ares, arif=ares]; (*arif is used to sample some values of NN in the MAIN
LOOP below. If we are in the case of an inner first order resonance we always need to sample
NN on values of a a bit to the left of the resonant value. For high ep this might also be
necessary for higher order resonances. The penultimate line of this code generates the curve
such as that in Figure 2 in the article, which allows one to check whether arif might have to
be adjusted.
The following two arrays are the ones that store the values for such plot.*)

eEqArray={}; (*Array of equilibrium values for e*)
aEqArray={}; (*Array of equilibrium values for a*)

ValueHamiltonianArray={}; (*Here we store the data in the form (e cos\[CurlyPi], e sin\[CurlyPi],
HPl) where HPl is the value of the purely planetary Hamiltonian: this will be plotted in the
last line of the code.*)
SampleArray={};(*Here we store the values of the Hamiltonian on the e cos\[CurlyPi] axis, to
produce a more readable contour plot*)

ValueHamiltonianArray2={};
(*Here we store the data in the form (\[CurlyPi], Log[a(1-e)], HPl) where HPl is the value of the
purely planetary Hamiltonian: this will be plotted in the last line of the code.*)

ValueHamiltonianGRArray={}; (*Here we store the data in the form (e cos\[CurlyPi], e sin\[CurlyPi
], HGR) where HGR is the value of the Hamiltonian including the General Relativity
contribution. This will be plotted in the last line of the code.*)
SampleArrayGR={};(*Here we store the values of the Hamiltonian on the e cos\[CurlyPi] axis, to
produce a more readable contour plot*)

ValueHamiltonianGRArray2={};
(*Here we store the data in the form (\[CurlyPi], Log[a(1-e)], HGR) where HGR is the value of the
Hamiltonian including the General Relativity contribution: this will be plotted in the last
line of the code.*)

c=(3 10^5)/(30); (*Speed of light in code units*)
RStar=0.00464913034; (*Radius of sun in AU. This can be set at the desired critical distance from
the star*)

Monitor[(*Monitor progress to show Progress Indicator*)
L1GridSize=15; (*Number of steps of the MAIN LOOP, to obtain the (e cos\[CurlyPi], e sin\[CurlyPi
], H) plots*)
L2GridSize=15; (*Number of steps on second loop, to obtain the (\[CurlyPi], Log[a(1-e)], H) plots
with values of a(1-e) close to RStar. This can be set to zero by the user if such plot is
not needed*)
l1=0;l2=0;(*Initialize to 0 the number of steps of the two plots, simply for the Progress
Indicator to work*)

(*MAIN LOOP on the values of NN*)
For[l1=0, l1<L1GridSize+1, l1++,
Clear[e,\[Sigma],\[CurlyPi],NN];

erif=l1/L1GridSize; (*Give a reference value for the eccentricity, to calculate a fixed value of
NN*)
NN=(kp-k)/k Sqrt[arif] +Sqrt[arif](1-Sqrt[1-erif^2]);

Clear[eEq,aEq];

(*We start with \[CurlyPi]=0*)
\[CurlyPi]0=0;
(*At this value of \[CurlyPi], equilibrium points in the (e*cos\[Sigma], e*sin\[Sigma]) diagram
are on the e*cos\[Sigma] axis, i.e. \[Sigma]=0,\[Pi];
OR on the axis \[Sigma]=\[Pi]/(kp-k),\[Pi]/(kp-k)+\[Pi] (plus any integer multiple of 2\[Pi
]/(kp-k) by the periodicity of the Hamiltonian in \[Sigma]*)

aFuncteThroughNN[ecc_]= NN^2/((kp-k)/k+1-Sqrt[1-ecc^2])^2;
SFrome[ecc_]:=Sqrt[aFuncteThroughNN[ecc]](1-Sqrt[1-ecc^2]);
HKeplAveraged[ecc_]:=-((kp-k)^2/(2k^2 (NN-SFrome[ecc])^2)-np kp/(kp-k) (NN-SFrome[ecc]));
(*the np*Lptilda contribution is irrelevant after averaging; this is tantamount to setting
Lptilda=0*)

(*We now get H_(NN,\[CurlyPi]0) (e, \[Sigma]*)
HAveragedSigmaEcc[sigma_,ecc_]:=1/(2 Pi kp)NIntegrate[(((HPert//.{aFromeAndNN}{[1]})*(1-e Cos[EE])
)/. {e->ecc, \[Sigma]->sigma, \[CurlyPi]->0}, {EE,0,2 Pi kp},PrecisionGoal->10,AccuracyGoal

```

```

->10]+HKeplAveraged[ecc];

(*Sample the Hamiltonian on the  $e \cos \sigma$  axis, i.e.  $\sigma=0, \pi$ *)
GridSizeEcc=Max[{400, Ceiling[600 erf]}];
tArray={};
ValuesArrayEcc={};
For[i=0, i<GridSizeEcc+1, i++,
t=-1 +2 i/GridSizeEcc;
\Xi=t;
\Eta=0;
AppendTo[tArray, t];

e=Sqrt[\Xi^2 + \Eta^2];
If[e==0, \Sigma=0, \Sigma=ArcTan[\Xi, \Eta]]; (*The ArcTan function is indeterminate when
both inputs are zero; in this case we set \Sigma=0*)
value=HAveragedSigmaEcc[\Sigma, e];
AppendTo[ValuesArrayEcc, value];
];
Clear[e, \Sigma, t, \Xi, \Eta];
ToMaximiseEcc=Interpolation[Transpose[{tArray, ValuesArrayEcc}]];

MaximumEcc=FindMaximum[ToMaximiseEcc[t], {t, Max[erf, 0.01], -1, 1}, Method->"Newton", PrecisionGoal
->10, AccuracyGoal->10];

tMax=t /. MaximumEcc[[2]];
eMax=Abs[tMax]; (*Candidate stable equilibrium point for e*)
(*Note: MaximumEcc[[1]] is the value of the function (i.e. averaged hamiltonian) on the point of
maximum. MaximumEcc[2] is the value of the independent variable (i.e. the eccentricity) where
the maximum of the function is located*)
aMax=aFuncThroughNN[eMax];

(*We need to check that this is the stable equilibrium: we need to check that for this eMax the
Hamiltonian in  $\sigma=0, \pi$  has a local maximum; if it has a local minimum than this is the
unstable equilibrium, so in the  $(e \cos \sigma, e \sin \sigma)$  diagram instead of looking at
the  $e \cos \sigma$  axis (i.e.  $\sigma=0, \pi$ ) we look for  $\sigma=\pi/(kp-k), \pi/(kp-k)+\pi$ *)

If[kp-k>1, (*In the case of first order resonance this check is not needed*)
FLAG=True; (*This flag will be turned to false iff we have in fact found the stable equilibrium
point in the  $(e \cos \sigma, e \sin \sigma)$  diagram*)
If[tMax > 0, (*Then we should look in the direction  $\sigma=0$  rather than  $\pi$ *)
If[
HPertAveraged[0, eMax, 0, aMax] >=HPertAveraged[\pi/(kp-k), eMax, 0, aMax], FLAG=False],
(*Note. On both sides of the inequality there would be an equal contribution of HKeplAveraged[
eMax] to the full Hamiltonian, the calculation of which we can clearly avoid*)
(*Else we should look in the direction  $\sigma=\pi$  rather than 0*)
If[HPertAveraged[\pi, eMax, 0, aMax]>=HPertAveraged[\pi/(kp-k), eMax, 0, aMax], FLAG=False]
];

If[FLAG, (*Then we must put ourselves in the case  $\sigma=\pi/(kp-k), \pi/(kp-k)+\pi$ *)
tArray={};
ValuesArrayEcc={};
For[i=0, i<GridSizeEcc+1, i++,
t=-1 +2 i/GridSizeEcc;
\Xi=t Cos[\pi/(kp-k)];
\Eta=t Sin[\pi/(kp-k)];
AppendTo[tArray, t];

e=Sqrt[\Xi^2 + \Eta^2];
If[e==0, \Sigma=0, \Sigma=ArcTan[\Xi, \Eta]];

value=HAveragedSigmaEcc[\Sigma, e];
AppendTo[ValuesArrayEcc, value];
];
Clear[e, \Sigma, t, \Xi, \Eta];
ToMaximiseEcc=Interpolation[Transpose[{tArray, ValuesArrayEcc}]];
MaximumEcc=FindMaximum[ToMaximiseEcc[t], {t, erf, -1, 1}, Method->"Newton", PrecisionGoal->10,
AccuracyGoal->10];

eMax=Abs[t /. MaximumEcc[[2]]];
];

```

```

];
(*Now we have found the stable equilibrium point in the eccentricity*)
eEq=eMax;
If [eEq<1,
AppendTo [eEqArray ,eEq];
aEq=aFuncThroughNN [eEq];
AppendTo [aEqArray ,aEq];

Lq=Log [aEq(1-eEq)];(*the natural logarithm of q=a(1-e) the pericenter distance*)

(*We store the value of the Hamiltonian in the arrays*)
HPl=MaximumEcc [1];
AppendTo [ValueHamiltonianArray , {eEq Cos[\[CurlyPi]0], eEq Sin[\[CurlyPi]0], HPl}];
AppendTo [SampleArray , HPl];
AppendTo [ValueHamiltonianArray2 , {\[CurlyPi]0, Lq, HPl}];
AppendTo [ValueHamiltonianArray2 , {2Pi, Lq, HPl}];

HamiltonianGR=-3 (1/aEq) (1/(aEq c^2))1/Sqrt[1-eEq^2];
HGR=HPl+HamiltonianGR;
AppendTo [ValueHamiltonianGRArray , {eEq Cos[\[CurlyPi]0], eEq Sin[\[CurlyPi]0], HGR}];
AppendTo [SampleArrayGR , HPl];
AppendTo [ValueHamiltonianGRArray2 , {\[CurlyPi]0, Lq, HGR}];
AppendTo [ValueHamiltonianGRArray2 , {2Pi, Lq, HGR}];

(*Now for different values of \[CurlyPi] we search for the value of \[Sigma] that maximizes the
Hamiltonian, under the assumption that the equilibrium eccentricity is the same as that
previously found for \[CurlyPi]0=0*)
GridSizeVarpi=Max[{20, 2*Ceiling[50 eEq]}];
For [j=1, j<GridSizeVarpi, j++,
\[CurlyPi]j= 2Pi j/GridSizeVarpi;
HAveragedSigma[sigma_]:=1/(2 Pi kp)NIntegrate [(HPert*(1-e Cos[EE]))/.{e-> eEq, \[Sigma]->sigma, a
-> aEq, \[CurlyPi]->\[CurlyPi]j}, {EE,0,2 Pi kp}, PrecisionGoal->10, AccuracyGoal->10] +
HKeplAveraged [eEq];

ValuesArraySigma={};
GridSizeSigma=50;
For [b=0, b<GridSizeSigma+1, b++,
\[Sigma]=(2 Pi/(kp-k)) b/GridSizeSigma;
value=HAveragedSigma [\[Sigma]];
AppendTo [ValuesArraySigma , value];
];

(*We store the value of the Hamiltonian in the arrays*)
HPl=Max [ValuesArraySigma];
AppendTo [ValueHamiltonianArray , {eEq Cos[\[CurlyPi]j], eEq Sin[\[CurlyPi]j], HPl}];
If [j==Floor [GridSizeVarpi/2], AppendTo [SampleArray ,HPl]];
AppendTo [ValueHamiltonianArray2 , {\[CurlyPi]j, Lq, HPl}];

HamiltonianGR=-3 (1/aEq) (1/(aEq c^2))1/Sqrt[1-eEq^2];
HGR=HPl+HamiltonianGR;
AppendTo [ValueHamiltonianGRArray , {eEq Cos[\[CurlyPi]j], eEq Sin[\[CurlyPi]j],HGR}];
If [j==Floor [GridSizeVarpi/2], AppendTo [SampleArrayGR ,HGR]];
AppendTo [ValueHamiltonianGRArray2 , {\[CurlyPi]j, Lq,HGR}];
];
];
];

(*Second loop in Log(a(1-e)). This allows to sample the Hamiltonian at high values of the
eccentricity. This loop can be avoided by setting L2GridSize to 0 earlier in the code*)
LqMax=Lq;
LqMin=Log [RStar];
HKeplAveragedAtAres=-1/(2ares)-1/ares; (*The value of the Keplerian part of the Hamiotonian at
the location of exact resonance, see below.
Note: By setting Lptilda to zero as we did above we obtain for the constant term np Lp the value
-1/a*)

For [l2=1, l2<L2GridSize+1,l2++,
Lq=LqMax + l2/L2GridSize (LqMin-LqMax); (*In this loop we also choose to follow the steps with
increasing eccentricity, i.e. with decreasing Lq=Log[a(1-e)]. Note that we started with l2=1
because the calculation at Lq=LqMax has already been performed*)

```

```

(*Note: we know that for high values of e the equilibrium point will be found at aEq=ares.
Therefore we avoid the calculation of aEq. This allows us to use the previously defined value
HKeplAveragedAtAres for the Keplerian Hamiltonian*)
q=Exp[Lq];(*q = ares (1-e)*)
eEq=1-q/ares;
aEq=ares;
For[j=0, j<GridSizeVarpi, j++,
\[CurlyPi]j=2 Pi j/GridSizeVarpi; (*We need to find, for each value of \[CurlyPi] in the interval
[0,2\[Pi]), the equilibrium point in \[Sigma], but unlike in the previous loop the edge case
of 0 is still to be considered. This is why we start from j=0 here*)

ValuesArraySigma={};
For[b=0, b<GridSizeSigma+1, b++,
\[Sigma]=(2 Pi/(kp-k)) b/GridSizeSigma;
AppendTo[ValuesArraySigma, HPertAveraged[\[Sigma], eEq, \[CurlyPi]j, aEq]+HKeplAveragedAtAres];
];

(*We store the value of the Hamiltonian in the arrays*)
HPl=Max[ValuesArraySigma];
AppendTo[ValueHamiltonianArray2, {\[CurlyPi]j, Lq, HPl}];
If[j==0, AppendTo[ValueHamiltonianArray2, {2 Pi, Lq, HPl}]];

HamiltonianGR=-3 (1/aEq) (1/(aEq c^2))1/Sqrt[1-eEq^2];
HGR=HPl+HamiltonianGR;
AppendTo[ValueHamiltonianGRArray2, {\[CurlyPi]j, Lq, HGR}];
If[j==0, AppendTo[ValueHamiltonianGRArray2, {2 Pi, Lq, HGR}]];
];
];

(*Run one last round for the purely planetary case, in the edge case of e=1*)
++l2; (*This is simply to show the Progress Indicator more precisely*)
eEq=1;
aEq=ares;
Lq=Log[aEq(1-eEq)];
NN=(kp-k)/k Sqrt[aEq] +Sqrt[aEq](1-Sqrt[1-eEq^2]);

GridSizeVarpi=Max[{20, 2*Ceiling[50 eEq]}];
For[j=0, j<GridSizeVarpi, j++,
\[CurlyPi]j= 2Pi j/GridSizeVarpi;
HAveragedSigma[sigma_]:=1/(2 Pi kp)NIntegrate[(HPert*(1-e Cos[EE]))/.{e-> eEq, \[Sigma]->sigma, a
-> aEq, \[CurlyPi]->\[CurlyPi]j}, {EE,0,2 Pi kp}, PrecisionGoal->10, AccuracyGoal->10] +
HKeplAveragedAtAres;
\[Sigma]Array={};
ValuesArraySigma={};
GridSizeSigma=50;
For[b=0, b<GridSizeSigma+1, b++,
\[Sigma]=(2 Pi/(kp-k)) b/GridSizeSigma;
value=HAveragedSigma[\[Sigma]];
AppendTo[\[Sigma]Array, \[Sigma]];
AppendTo[ValuesArraySigma, value];
];

(*We store the value of the Hamiltonian in the arrays*)
HPl=Max[ValuesArraySigma];
AppendTo[ValueHamiltonianArray, {eEq Cos[\[CurlyPi]j], eEq Sin[\[CurlyPi]j], HPl}];
If[j==Floor[GridSizeVarpi/2], AppendTo[SampleArray, HPl]];
AppendTo[ValueHamiltonianArray2, {\[CurlyPi]j, Lq, HPl}];
If[j==0, AppendTo[ValueHamiltonianArray2, {2Pi, Lq, HPl}]];
];
Clear[eEq, aEq, NN],
ProgressIndicator[Dynamic[(11+12)/(L1GridSize+L2GridSize+1.5)]]]
da=(2/3)(Sqrt[Mp]/k)(ares)^(5/2);
acrit=ares-N[da]
Show[
ListPlot[Transpose@{aEqArray, eEqArray}, PlotRange->{{.9 ares, 1.1 ares}, {0,1.2}}, PlotStyle->
Black],
ListPlot[{{ares, 0}, {ares, 1}}, Joined-> True, PlotStyle-> {Dotted, Blue}],
ListPlot[{{acrit, 0}, {acrit, 1}}, Joined-> True, PlotStyle-> {Dotted, Orange} ]
]
ListContourPlot[ValueHamiltonianArray, Contours->SampleArray, PlotRange->All, FrameLabel->{"e cos
\[CurlyPi]" , "e sin(\[CurlyPi])"}]

```

```

ListContourPlot[ValueHamiltonianArray2, Contours-> 30, FrameLabel->{"\[CurlyPi]", "Log[a(1-e)]"}]

ListContourPlot[ValueHamiltonianGRArray, Contours->SampleArrayGR, PlotRange->All, FrameLabel->{"e
cos(\[CurlyPi])", "e sin(\[CurlyPi])"}]

ListContourPlot[ValueHamiltonianGRArray2, Contours-> 30, FrameLabel->{"\[CurlyPi]", "Log[a(1-e)
]"}]

```


Appendix E

List of symbols and notations

In this Appendix I list the symbols that are used consistently throughout the thesis. All other symbols may change of meaning depending on the context.

Bold symbols usually refer to vectors, so $\mathbf{x} = (x_1, \dots, x_n)$ (thought as a column vector)

\mathbb{R} is the set of real numbers

\mathbb{N} are the natural numbers, \mathbb{N}_0 are the natural numbers including 0

\mathbb{Z} are the integers

\mathbb{T} is the torus, $\mathbb{T} = \mathbb{R}/2\pi\mathbb{Z}$

i is the imaginary unity

$\langle f \rangle_\phi := \frac{1}{T} \int f d\phi$ is the average of a function f periodic with period T with respect to an angle ϕ

\bullet is a placeholder for any variable/function (e.g. $(\bullet)^2 + 1$ represents the function $f(x) = x^2 + 1$)

\mathcal{H} is an Hamiltonian function

χ is a generating Hamiltonian

$\exp(tL_{\mathbf{X}})$ is the lie series operator for a field \mathbf{X}

N is the number of planets in a planetary system

\mathcal{G} is the gravitational constant

M_* is the stellar mass in a planetary system

m (lowercase m) is the mass of planets, e.g. $m_1, m_2, m_3, m_{\text{pl}}$ etc.

$\mu = \frac{mM_*}{M_* + m}$ is the reduced mass of a body of mass m orbiting around a star of mass M_*

a is the semi-major axis of an orbiting body

e is the eccentricity of an orbiting body

λ is the mean longitude of an orbiting body

ϖ is the longitude of pericentre of an orbiting body

$\gamma = -\varpi$

Λ is either $\mu\sqrt{\mathcal{G}(M_* + m)a} \sim m\sqrt{\mathcal{G}M_*a}$ or the rescaled $\sqrt{\mathcal{G}M_*a}$

$\Gamma = \Lambda(1 - \sqrt{1 - e^2}) \sim \Lambda e^2/2$ and may be the usual or rescaled action depending on Λ

\mathcal{L} is the (orbital) angular momentum, or the specific angular momentum depending on the definition of the actions

k is the index of a $k : k - 1$ mean motion resonance, or the index of an Andoyer Hamiltonian $\mathcal{H}_{\text{And},k}$

$\bar{\mathcal{H}}$ is the averaged Hamiltonian near mean motion resonance

τ_{mig} is the migration timescale, from disc-planet interaction, defined as $\dot{\log \mathcal{L}} = -1/\tau_{\text{mig}}$

τ_a is the semi-major axis change timescale, from disc-planet interaction, defined as $\dot{\log a} = -1/\tau_a$

τ_e is the eccentricity damping timescale, from disc-planet interaction, defined as $\dot{\log e} = -1/\tau_e$

M_\oplus is the mass of the Earth

M_\odot is the mass of the Sun

ω_l is the libration frequencies around a resonant equilibrium point, $l = 1, \dots, 2(N - 1)$